Constraining neutrino interaction parameters using the T2K off-axis near detector ND280 with a 4π solid angle sample selection

By YONGHENG XU, M.Sc.

A Thesis Submitted to the School of Graduate Studies in the Partial Fulfillment of the Requirements for the Degree of

Ph.D.

in

Particle Physics

Lancaster University
Lancaster, England, United Kingdom

Abstract

The Tokai-to-Kamioka (T2K) experiment is a long-baseline neutrino study designed to measure neutrino oscillation parameters, including $\theta_{13}, \theta_{23}, \Delta m^2_{32}$, and δ_{CP}. In the experiment, a proton beam is directed at a carbon target, generating a neutrino flux that is first measured by the Near Detector at 280 m (ND280) at the Japan Proton Accelerator Research Complex (J-PARC) on Japan's east coast and subsequently measured by the Super-Kamiokande (SK) detector, located 295 km away. By comparing the data from both detectors, researchers can extract crucial information about neutrino oscillation parameters.

Previously in the ND280 measurements, only charged-current neutrino interaction events featuring a forward-going final-state muon were employed. This thesis presents a novel approach by developing a set of selection criteria for charged-current events with muons in any direction relative to the neutrino flux. This advancement is achieved using time-of-flight information between ND280 sub-detectors. A correction was also developed to compensate for known data-simulation discrepancy.

Ten new subsamples have been created, and their associated systematic uncertainties have been assessed. These samples have been tested in the T2K near detector fitter, BANFF, resulting in improved constraints for numerous parameters compared to previous samples, as evidenced by test runs and validations. This will ultimately lead to an improved understanding of the neutrino oscillation parameters.

Acknowledgements

First and foremost, I would like to express my heartfelt gratitude to my supervisor, Laura Kormos. As an international student with no background in experimental particle physics, I faced significant challenges in grasping the intricacies of large-scale particle physics experiments. Your invaluable guidance and mentorship have been instrumental in bridging this gap for me. I have truly cherished our countless conversations on T2K, physics, life, and a myriad of other topics.

I also want to extend the thanks to other past and present Lancaster T2K people, from Helen O'Keeffe, Alex Finch, Matt Lawe, Tom Dealtry, Joe Walsh, Tristan Doyle, Menai Lamers-James and Adam Speers. You made Lancaster such a wonderful place to work as a PhD student.

I am grateful for the opportunity to work with the wonderful team at T2K, who are a group of truly amazing people. Throughout the course of this project, I have received invaluable help and guidance from a number of T2K members. I would like to extend my sincere thanks to Helen OKeeffe and Dave Hadley for their advice and guidance during the design phase of the selection process, and to Alexander Izmaylov and Alex Finch for their tireless assistance with c++ coding, debugging, and systematic error analysis. Additionally, I would like to express my gratitude to Joe Walsh, Tristan Doyle, and Kamil Skwarczyski for their efforts in integrating the project into the BANFF fitting framework. I am especially indebted to Ciro Riccio, whose unwavering support has been critical in every aspect of this work, including the development of the fitter mechanism, the evaluation of systematic errors, and even the search for my next job.

Finally, I would like to thank my family members, my partner Jing, and my parents, for all kind of support and encouragement during these years as a PhD student at Lancaster.

Contents

List of Figures

List of Tables

Glossary

2p2h Two-Particle-Two-Hole. 18, 168

BabyMIND Magnetised Iron Neutrino Detector . 51

BANFF Beam And ND280 Flux extrapolation task Force. 152

BrECal Barrel Electromagnetic Calorimeter. 48

BWD Backward. 88

CC-DIS Charged-Current Deep Inelastic Scattering. 18

CC-Res Charged-Current Resonant. 18

CCQE Charged-Current Quasi-Elastic. 18

DsECal Downstream Electromagnetic Calorimeter. 48, 61

ECal Electromagnetic Calorimeter. 36, 47

FGD Fine-Grained Detector. 36

FHC Forward Horn Current. 31

FSI Final State Interaction. 21, 173

FV Fiducial Volume. 92

FWD Forward. 88

HABWD High Angle Backward. 88

HAFWD High Angle Forward. 88

highland High Level Analysis ND280. 80

IH Inverted Hierarchy. 27

INGRID nteractive Neutrino GRID. 34

J-PARC Japan Proton Accelerator Research Complex. 28

LINAC LINear ACcelerator. 29

MC Monte Carlo. 21, 176

MF Mean Field. 164

MPPC Multi-Pixel Photon Counter. 36

MR Main Ring. 29

ND280 Near Detector at 280m. 1

NH Normal Hierarchy. 27

P0D π^0 Detector. 36

PDF Parton Distribution Function. 20

PID Particle IDentification. 93

PMT Photon Multiplier Tube. 39

POT Protons on Target. 32

psyche Propagation of Systematics and Characterization of Event. 80

RCS Rapid Cycling Synchroton. 29

RHC Reverse Horn Current. 31

RMM Readout Merger Module. 39

SCM Secondary Clock Module. 60

SF Spectral Function. 21

SK Super-KamiokaNDE. 1

SMRD Side Muon Range Detector. 36

SPP Single Pion Production. 169

T2K Tokai-to-KaimokaNDE experiment. 1, 28

TFB Trip-T Frontend Board. 39

ToF A Markov Chain MC fitter. 156, 190

ToF Time of Flight. 58, 79

TPC Time Projection Chamber. 36

WAGASCI WAter-Grid-And-SCIntillator. 51, 52

WLS WaveLength Shifting fibre. 36

Declaration of Authorship

This thesis represents either my own work or the output of collaborative research conducted by the T2K collaboration, of which I have been an member of since 2019 till as of when this thesis is written, spring 2023. None of the material in this thesis has been previously submitted for the purpose of obtaining a higher degree. Any works that were not authored by me have been explicitly referenced.

The core part of this work involved developing a 4π solid angle sample selection for the T2K ND280 detector. The author was primarily responsible for this work, with assistance from other T2K collaborators. This included designing the selection algorithm for ND280 data, evaluating systematic uncertainties, and correcting time-of-flight information which was crucial for the 4π selection. The author also explored potential enhancements for the ND280 sample selection in the BANFF fitting framework.

The time-of-flight correction was developed in collaboration with other T2K collaborators, including Sam Jenkins, Helen O'Keffe, Philip Litchfield, and Alexander Izmalov. The systematic evaluation discussed in Chapter 6 was conducted within the ND280 selection and systematics group. The fit validation introduced in Chapter 7 was performed within the near detector fitting group.

In addition to conducting research for this thesis, the author participated in several T2K studies. In 2021, during the peak of the COVID-19 pandemic, the author served as an online shifter for the monitoring and maintenance of INGRID data collection. Recently, the author has taken charge of the heavy neutral lepton study at ND280, which aims to set constraints on sterile neutrinos using the detector.

Furthermore, the author contributed to T2K's near detector upgrade work, specifically in the assembly of the super fine-grained detector, which involved inserting, cutting, and testing optical fibers. The author also played an active role in developing and maintaining ND280 analysis and fitting software, particularly Highland2 and BANFF.

Chapter 1

Introduction

In 2012, the Higgs boson was discovered at the Large Hadron Collider by the ATLAS and CMS experiments [1, 2], completing the last piece of the standard model of particle physics and marking a significant milestone in modern science. However, this discovery is far from the end of physics, as numerous unsolved problems persist, even in the field of particle physics. Neutrinos are directly linked to many of these problems, including neutrino mass, which is not accounted for in the standard model. Another unresolved issue is the baryonic matter-antimatter asymmetry in our universe [3, 4]. Neutrino oscillation, if it exhibits matter-antimatter asymmetry, would indicate leptonic Charge-Parity (CP) violation [4], potentially explaining the universe's asymmetry in conjunction with quark-sector CP violation. Therefore, the study of neutrinos is crucial to advancing particle physics, and to comprehending the universe in which we leave.

Various neutrino experiments have been developed to address questions in neutrino physics, including the Tokai-to-Kamiokande (T2K) experiment [5]. T2K is a long-baseline neutrino oscillation experiment that measures neutrino oscillation parameters by firing a proton beam at a carbon target to produce a neutrino flux. The experiment then measures the flavour distribution of the neutrino flux at two locations: one close to the target, named the Near Detector at 280m (ND280), and another 295 kilometers away, Super-Kamiokande (SK). This allows for the determination of the extent of the neutrinos' oscillation during their journey from the near detector to the far detector. ND280 is primarily a scintillator-based detector, while SK is a water-Cherenkov detector. At both detectors, only neutrino charged-current interactions are considered as oscillation signals, where a charged lepton of the same weak flavour as the incoming neutrino is produced, such as a muon in the case of an incoming muon neutrino.

While SK analyses consider events with incident muons traveling in any direction, the ND280 only includes events with forward-going muons. This thesis describes the development of a 4π solid angle selection for ND280 to enable a more accurate comparison of data between the near and far detectors, including the design of its cuts, the evaluation of systematic errors and the results of test anaylses using the new 4π subsamples.

The thesis is organised as follows: Chapter 2 provides an overview of the current understanding of neutrino physics. Chapter 3 introduces the T2K experiment and its hardware. Chapter 5 details the full-solid angular event selection at ND280. Chapter 4 discusses the time-of-flight correction for Run 8 data, essential for the 4π analysis. Chapter 6 estimates the systematic errors in sample selection due to ND280 detector effects. Chapter 7 explains the ND280 model, encompassing the beam model, neutrino-nuclei interaction model, and detector response model, as well as the fitting process for the model to data and how the inclusion of the 4π sample improves fitting results. Chapter 8 summarises the results, provides an outlook for upcoming upgrades in the following years, and offers concluding remarks.

Chapter 2

Theory

The standard model of particle physics consolidates our understanding of fundamental particles within a quantum field theory framework. It comprises 17 elementary particles: six spin-half quarks, three spin-half charged leptons, three spin-half neutral leptons which are referred to as neutrinos, four spin-one gauge bosons, and a spin-zero Higgs boson, as shown in Fig. 2.1. The model features three types of interactions, each occurring between spin-half fermions and mediated by a spin-one gauge boson:

- The strong interaction, described by Quantum Chromodynamics (QCD) theory, arises from a non-Abelian $SU(3)$ symmetry. Only quarks participate in this interaction, which is mediated by gluons. The strong interaction binds quarks together to form mesons or baryons and holds protons and neutrons together to create nuclei. Quark-bound states that are involved in strong interactions are referred to as hadrons; two-quarks states are called mesons and three-quark states are called baryons. On the contrary, fermions that do not participate in strong interactions are addressed as leptons.

- The electromagnetic interaction, mediated by photons, can be characterised by an Abelian $U(1)$ gauge theory. Particles that participate in this interaction, such as charged leptons and quarks, appear charged. The electromagnetic interaction serves as the fundamental force that binds electrons to nuclei to create atoms, unites atoms to establish molecules, and constitutes the foundation for friction.

- The weak interaction, mediated by W and Z bosons, is described by a non-Abelian $SU(2)$ gauge theory within the Standard Model. All fermions, including quarks,

charged leptons, and neutrinos, can participate in weak interactions. The weak interaction is commonly observed in atomic radioactivity and the fission of atoms.

The Higgs boson, the only spin-zero particle in the Standard Model, gives rise to the masses of many particles through the Higgs mechanism. The electromagnetic and weak interactions have been successfully unified in the electroweak interaction theory [6, 7, 8]. However, incorporating gravity into the quantum field theory framework remains an unresolved issue, as it necessitates a spin-two mediator that leads to inevitable divergence in calculations [9, 10]. Consequently, a quantum field theory encompassing gravity is one of the most pressing open questions in theoretical physics. A summary of all known elementary particles is illustrated below in Fig. 2.1.

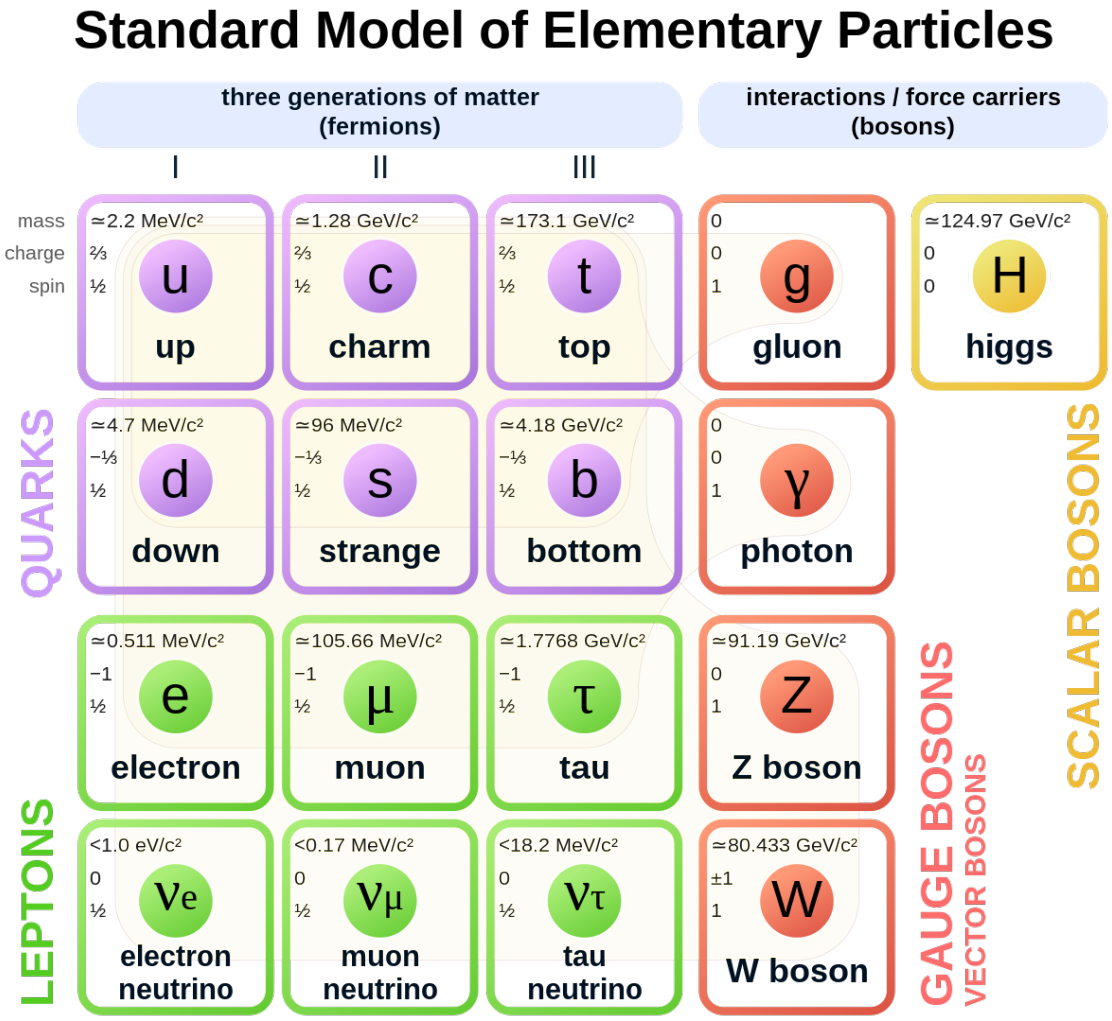

FIGURE 2.1: The standard particles of particle physics, to the best of human knowledge. The purple boxes are the quarks, the green boxes are the letpons, red boxes gauge bosons and the only yellow box is the Higgs boson. The fundamental characteristics of each particle, including their mass, spin and charge, are given at the top left corner of each particle's box [1]. Since free quarks have never been observed experimentally, their masses are not measured, but instead determined by watching their influence on hadronic properties. This figure is from [11].

In the Standard Model, neutrinos are neutral leptons that interact only weakly with other fermions. There are three flavours of neutrinos: ν_e, ν_μ, and ν_τ, each of which

[1]The term 'generation' arises from the fact that heavier particles can decay into lighter similar particles. Tauons decay into muons, which subsequently decay into electrons, making muons the daughter of tauons, and electrons the granddaughter of tauons, hence three generations in the charged lepton family. This is not the case for neutrinos, but given the association between charged leptons and neutrinos, the lepton generation is still relevant.

couples exclusively to a specific generation of charged lepton through charged-current weak interactions. The electroweak theory, developed by Weinberg, Salam, and Glashow [6, 12, 13], successfully explains weak interactions, predicting the existence of $W^{\pm}$ and Z^0 bosons as well as their coupling to neutrinos and other fermions.

Initially, the electroweak theory posited that neutrinos were massless. However, subsequent solar neutrino experiments demonstrated that neutrinos oscillate among flavours [14], necessitating a small but nonzero mass. This revelation opened the door to physics beyond the standard model.

This chapter offers a brief introduction to the history and theoretical understanding of neutrinos. The first section provides a historical overview of neutrino physics, while the second section offers a concise introduction to the electroweak theory of neutrinos. The focus of this thesis is neutrino oscillation, which is discussed in the third section. The fourth section introduces neutrino-nucleus interactions, which are relevant to subsequent chapters. Finally, the fifth section highlights some outstanding questions that will require future theoretical and experimental efforts to answer.

2.1 History of neutrinos

The discovery of neutrinos can be traced back to the study of atomic β decay. When the existence of neutrinos was unknown to contemporary scientists, atomic β decay appeared to be a two-body final state process, in which a fixed momentum of outgoing electrons was expected. Instead, a continuous electron energy spectrum was observed [15], seemingly violating the conservation of momentum. To preserve this fundamental symmetry in physics, Pauli suggested the existence of a light, neutral particle [16]. Fermi later developed a theory incorporating Pauli's postulated particle into β decays, naming the particle "neutrino" [17]. Another triumph of Fermi's theory was the discovery of inverse β decay, in which an antineutrino interacts with a proton to create a neutron and an electron.

The existence of neutrinos was first confirmed by Cowan and Reines in 1956 [18], before a formal theory for them was developed. The weak interaction theory, developed by Glashow [6], Salam [13], and Weinberg [12] in the 1960s, predicted that neutrinos interact also with other charged leptons, such as muons and taus. Muon neutrinos were

discovered in 1962 at the Brookhaven national laboratory [19], while tau neutrinos were not discovered until 2000 by the DONUT experiment [20].

The Standard Solar Model (SSM), which describes the internal cycle of particle interactions inside the sun, predicts that the sun emits a neutrino flux detectable on Earth via inverse β decay experiments. Davis first conducted this experiment in 1968, observing only half of the neutrinos predicted by the SSM [21]. Later experiments, including SAGE [22] and Kamiokande [23], confirmed this deficit, leading to the solar neutrino problem. The SNO experiment was the first to simultaneously measure both charged-current interactions, in which muon and tau processes were forbidden due to low energy, and neutral-current interactions, which could detect muon and tau neutrinos, in 2001. The deficit persisted in charged-current event rates, while the neutral-current event rate was consistent with SSM predictions [24].

This implied that while the total number of neutrinos still adhered to the SSM prediction, their weak flavours somehow changed. In 1957, Pontecorvo had suggested that neutrinos might change between neutrino and antineutrino [25]. He later proposed that their weak flavors could also change due to the mismatching between weak and mass eigenstates [26], and a mathematical formalism was proposed by Maki, Nakagawa, and Sakata in 1962 [27], from which a sine-function-like behavior of neutrino disappearance probability as a function of neutrino energy over distance can be predicted. This phenomenon of neutrinos changing their flavors in-flight later became known as neutrino oscillation. In 2007, the KamLAND experiment measured the survival probability of an electron neutrino as a function of neutrino energy over distance, and the results were in good agreement with the neutrino oscillation theory [14].

2.2 Neutrinos in the standard model

In the Glashaw-Weinberg-Salam theory of weak interaction [6, 7, 8], the only interaction neutrinos participate in is the electro-weak interaction. The theory starts from a global $SU(2) \bigotimes U(1)_Y$ gauge symmetry acting upon ferimon fields. Consider the following electron Lagrangian:

$$\mathcal{L} = i\bar{E}\gamma^\mu \partial_\mu E = i(\bar{E}_L \gamma^\mu \partial_\mu E_R + \bar{E}_R \gamma^\mu \partial_\mu E_R) \tag{2.1}$$

where E_R, E_L are the left-handed and right-handed scalar component of the electron fermion field, eigenstate of the project operators $\frac{1\pm\gamma^5}{2}$. γ^μ are the four Dirac matrices that form the Clifford algebra $\{\gamma^\mu, \gamma^\nu\} = 2g^{\mu\nu}I$, in which $g^{\mu\nu}$ is the metric tensor chosen to be diag$(1, -1, -1, -1)$ in this thesis, and $\gamma^5 \equiv i\gamma^0\gamma^1\gamma^2\gamma^3$. A global $U(1)$ transformation of the form $E_L \rightarrow E_L e^{i\alpha Y}$ or $E_R \rightarrow E_R e^{i\alpha Y}$, where Y represents the representation-dependent $U(1)$ generator and α is a real parameter driving the transformation, leaves the fields' equations of motion unchanged when derived from the corresponding Lagrangian. Consequently, both the left-handed and right-handed fields remain invariant under such $U(1)$ gauge transformations, signifying that the theory described by this Lagrangian exhibits an explicit global $U(1)$ symmetry.

Less obviously, the Lagrangian is also invariant under $SU(2)$ transformations in the form of

$$E_{L,R} \longrightarrow E'_{L,R} = e^{i\alpha^a\tau^a} E_{L,R}$$

where τ^a are the three $SU(2)$ generators mixing the left-hand and right-hand field components. α^a is the coefficienct of the generators, usually referred to as charges. Promoting the global symmetries to local gauge symmetries, the derivative then has to become a covariant derivative to guarantee local gauge symmetry:

$$D_\mu E_{L,R} = (\partial_\mu - i\frac{1}{2}\tau^a A^a_\mu - i\frac{1}{2}g'Y B^\mu)E_{L,R} \tag{2.2}$$

In Eq. 2.2, A^a_μ are the associated $SU(2)$ gauge bosons, τ^a are the $SU(2)$ generators, and g the coupling constant for the $SU(2)$ interaction. Similarly, B_μ is the $U(1)_Y$ gauge boson, Y is the $U(1)$ generator, and g' the gauge boson coupling constant to the fermion sector. This expression is algebraic; the explicit mathematical form is to be determined by the selection of representation. By chosing different representation or generator eigenstates, different particles and theories can be described.

To describe the real physical particles, for the left-handed charged lepton field we choose the representation where T^3 have eigenvalues of $-\frac{1}{2}$, and Y also $-\frac{1}{2}$; for the right-handed field, we choose the representation where $U(1)$ eigenvalue is -1, and T^3 eigenvalue is 0.

The covariant derivative for the left-handed and right-handed field is then:

$$D_\mu E_L = (\partial_\mu - i\frac{1}{2}g\tau^a A^a_\mu + i\frac{1}{2}g'B^\mu)E_L$$
$$D_\mu E_R = (\partial_\mu + ig'B^\mu)E_R$$

As there is currently no experimental evidence for right-handed neutrinos, this chapter will utilise the left-handed field to illustrate its points. The left-handed field transforms in the $n = 1/2$ representation of the $SU(2)$ group, also known as the weak isospin group in analogy with kaons [10, 28]. The vector E_L can be expressed as a two-component object:

$$E_L = ((\nu_e)_L, e_L)^T \tag{2.3}$$

where the first component describes the physical electron neutrinos and the second component describes the charged electrons. Expanding the covariant derivative of the left-handed field, it becomes

$$D_\mu E_L = \left[\partial_\mu + i\frac{1}{2}\begin{pmatrix} gA^3_\mu + g'B_\mu & g(A^1_\mu - iA^2_\mu) \\ g(A^1_\mu + iA^2_\mu) & -gA^3_\mu + g'B_\mu \end{pmatrix}\right]\begin{pmatrix} (\nu_e)_L \\ e_L \end{pmatrix}. \tag{2.4}$$

B_μ couples to both the neutrino field and the electron field, and hence it is not possible to interpret this particle as the physical photon. Steven Weinberg proposed a rotation [29] in the form of:

$$\begin{aligned} W^\pm_\mu &= \frac{1}{\sqrt{2}}[A^1_\mu - (\pm iA^2_\mu)], \\ Z^0_\mu &= \frac{1}{\sqrt{g^2 + g'^2}}(-gB_\mu + g'A^3_\mu), \\ Y_\mu &= \frac{1}{\sqrt{g^2 + g'^2}}(g'B_\mu - gA^3_\mu). \end{aligned} \tag{2.5}$$

With those rotations, electrons couple to the $W^\pm, Z^0$ and Y fields, while neutrinos couple only to $W^\pm$ and Z^0, exactly as how things happen in the physical world. The Y boson can be interpreted as photon carrying electromagnetic force.

It is now possible to rewrite the electron neutrino part of the standard model Lagrangian in terms of redefined gauge bosons and currents:

$$\mathcal{L} = \bar{E_L} D_\mu \gamma^\mu E_L = \bar{E}_L(i\gamma^\mu\partial_\mu)E_L + g(W^+_\mu J^{\mu+}_W + W^-_\mu J^{\mu-}_W + Z^0_\mu (J^0)^\mu) \tag{2.6}$$

where $J_W^{\pm}$ and J^0 are respectively the charged and neutral fermion currents that couple to $W^{\pm}$ and Z^0 bosons, and $W^{\pm}\mu$ are the charged weak force carrying bosons defined in 2.5. The explicit forms of the currents can be derived from the definition of the covariant derivative with some algebra [10, 28]. The results are

$$\begin{aligned} J_W^{+\mu} &= \frac{1}{\sqrt{2}}(\bar{\nu_e})_L \gamma^\mu e_L, \\ J_W^{-\mu} &= \frac{1}{\sqrt{2}}\bar{e}_L \gamma^\mu (\nu_e)_L, \\ J^{0\mu} &= \frac{1}{\cos\theta_w}[\bar{\nu_e}_L \gamma^\mu (\nu_e)_L + \bar{e}_L \gamma^\mu (-\frac{1}{2} + \sin^2\theta_w) e_L + \bar{e}_R \gamma^\mu \sin^2\theta_w e_R], \end{aligned} \tag{2.7}$$

where θ_w is the weak mixing angle, which is defined as $\cos\theta_w \equiv m_W/m_Z$, the ratio between W boson mass and Z boson mass. All terms in Eq. 2.7 that do not involve neutrinos are omitted for simplicity[2] . Feynman diagrams examplifying fundamental weak interactions are shown in Fig. 2.2.

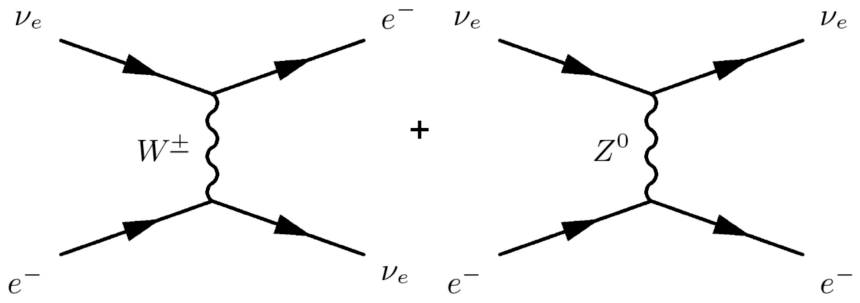

FIGURE 2.2: Feynman diagrams showing neutrino weak interactions. The initial state particles are on the left and final state particles are on the right. The left panel shows the charged-current interaction between two currents, and the right panel shows an example of a neutral current interaction.

For low-energy interactions, it is often easier to use the traditional Vector-Axial vector (V-A) form. The interaction vertex between fermions and gauges bosons are expressed as the sum of a vector current and a axial vector current. The vector vertex function is γ^μ as in quantum electrodynamcis, while that for the axial vector vertex is $\gamma^\mu\gamma^5$, where

[2]For an actual process mediated by $W^{\pm}$ or Z^0 to happen, the gauge boson propagation terms $\frac{1}{4}(F^a_{\mu\nu})^2$ are required, which are omitted for simplicity. The mass terms of W and Z in forms of $W^{+\mu}W^-_\mu$, $Z^\mu Z_\mu$ can be introduced to the theory through coupling to the scalar Higgs boson field [30, 31]. A Yukawa coupling to the Higgs field and subsequent spontaneous symmetry breaking also gives rise to charged lepton masses [32, 33, 34], but not to neutrino masses, which remains an open question in particle physics. See Section. 2.5 for more discussion on this topic.

$\gamma^5 = i\gamma^0\gamma^1\gamma^2\gamma^3$. The charged-current interaction can then be written as

$$\bar{f}\frac{-ig_W}{2\sqrt{2}}\gamma^\mu(1-\gamma^5)f \tag{2.8}$$

for charged-current interactions mediated by a $W^\pm$ boson and

$$\bar{f}\frac{-ig_Z}{2\sqrt{2}}\gamma^\mu(c_V - c_A\gamma^5)f \tag{2.9}$$

for neutral current interactions mediated by Z bosons. In the equations above, f and $\bar{f}$ are dirac spinors for the initial and final state fermions, g_Z and g_W are the coupling strengths for Z and $W^\pm$ bosons, respectively. The constants c_V and c_A dominate the coupling strength to vectors and pseudovectors and is dependent on the interacting particles. Table. 2.1 provides a full overview of the V-A form coupling strengths to all fermions in the standard model: Luckily, the weak and electromagnetic coupling constants are related by

Ferimion	c_V	c_A
Neutrinos	$\frac{1}{2}$	$\frac{1}{2}$
Charged Leptons	$-\frac{1}{2} + 2\sin^2\theta_w$	$-\frac{1}{2}$
u, c, t	$\frac{1}{2} - \frac{4}{3}\sin^2\theta_w$	$\frac{1}{2}$
d, s, b	$-\frac{1}{2} + \frac{2}{3}\sin^2\theta_w$	$-\frac{1}{2}$

TABLE 2.1: Table summarising Z^0 vector and axial-vector coupling to different fermion fields. Table adapted from [35].

the weak mixing angle θ_w defined earlier, and [6]:

$$g_W = \frac{g_e}{\sin\theta_w}, \quad g_Z = \frac{g_e}{\sin\theta_w\cos\theta_w} \tag{2.10}$$

where $g_e = \sqrt{4\pi\alpha}$ is the QED coupling constant $\alpha \simeq 1/137$ is the fine structure constant. The mass of $W^\pm$ and Z are also related by θ_w as $M_W = \cos\theta_w M_Z$. All of these are predictions of the GWS weak interaction model, and are in good agreement with experimental observations. The current best measurement of θ_w is nearly $\frac{\pi}{6}$[36].

2.3 Neutrino oscillation

The term neutrino oscillation refers to the phenomenon that, unlike the charged leptons, the weak eigenstates and mass eigenstates of neutrinos do not perfectly match, causing its

flavour composition to change as they travel through space. The idea was first proposed by Pontecorvo [25, 26]. It is conventional to label the weak eigenstates as $|\nu_e\rangle, |\nu_\mu\rangle, |\nu_\tau\rangle$ and the mass eigenstates as $|\nu_1\rangle, |\nu_2\rangle, |\nu_3\rangle$ [3].

Assuming that they both form a complete basis of the Hilbert space, one can always decompose one basis into a superposition of another [27, 38]:

$$|\nu_e\rangle = U_{e1}|\nu_1\rangle + U_{e2}|\nu_2\rangle + U_{e3}|\nu_3\rangle \tag{2.11}$$

where U_{e1}, U_{e2} and U_{e3} are complex constants. Maki, Nakagawa and Sakata proposed the lepton matrix form in order to link the mass eigenstates to the weak eigenstates [27]. The matrix is now commonly referred to as the PMNS matrix in honour of them alongside with Pontecorvo. It is then straightforward to write

$$\begin{pmatrix} \nu_e \\ \nu_\mu \\ \nu_\tau \end{pmatrix} = U_{\mathbf{PMNS}} \begin{pmatrix} \nu_1 \\ \nu_2 \\ \nu_3 \end{pmatrix} \tag{2.12}$$

where $U_{\mathbf{PMNS}}$ is the 3×3 mixing matrix of three weak flavours and three mass states. Consider a neutrino produced at a charged-current weak interaction vertex; it must be in a weak eigenstate, as required by the interaction term in the Lagrangian, say $|\nu_\mu\rangle$, at $t = 0$:

$$|\nu(0)\rangle = |\nu_\mu\rangle = U_{\mu1}|\nu_1\rangle + U_{\mu2}|\nu_2\rangle + U_{\mu3}|\nu_3\rangle. \tag{2.13}$$

As the masses of ν_1, ν_2, and ν_3 differ, their propagation in free space evolves at different rates over time. In order to determine the likelihood of finding each mass eigenstate at a particular space-time coordinate from the source, the next step is substituting the three-dimensional plane wave solution of the Schrödinger equation into each of the mass eigenstates:

$$|\nu_\mu(t)\rangle = \sum_i U_{\mu_i}(|\nu_i\rangle e^{-ip_i x}). \tag{2.14}$$

Here, $i = 1, 2, 3$ denotes the index of mass states, p_i represents the momentum four-vector of the ith neutrino mass-eigenstate, and x is the space-time coordinate where the neutrino

[3] Although there is no compelling theoretical reason to limit the number of flavours to three, however as the LEP Z decay width measurement shows that the number of light charged-leptons coupling is three [37], this thesis will proceed with the assumption that the number of weak flavours and mass eigenstates are both three.

state is to be determined. The notation $p_i x$ denotes the contraction of two four-vectors. By decomposing the mass eigenstates once more into weak eigenstates, the equation above turns into:

$$|\nu_\mu(t)\rangle = \sum_i U_{\mu i} e^{-ip_i x} (\sum_\alpha U^*_{\alpha i} |\nu_\alpha\rangle) \tag{2.15}$$

Where $i = 1, 2, 3$ is the index of mass eigenstates, and $\alpha = e, \mu, \tau$ is the index of weak eigenstates. The modulus squared of the sum of the coefficients of terms carrying a ν_μ index on the right hand side gives the probability of finding a ν_μ eigenstate at space time coordinate x:

$$P(\nu_\mu \to \nu_\mu) = |\sum_i U_{\mu i} (U_{\mu i})^* e^{-ip_i x}|^2 \tag{2.16}$$

which can be further simplified into

$$\begin{aligned} P(\nu_\mu \to \nu_\mu) &= 1 + \sum_i \sum_{j \neq i} Re\{U_{\mu_i} U^*_{\mu i} U_{\mu_j} U^*_{\mu j} [e^{-i(p_j - p_j)x} - 1]\} \\ &= 1 + \sum_i \sum_{j \neq i} |U_{\mu_i}|^2 |U_{\mu_j}|^2 Re\{[e^{-i(p_j - p_j)x} - 1]\} \end{aligned} \tag{2.17}$$

where the 1 comes from the fact that the PMNS matrix is unitary and the sum of its diagonal elements squared must be 1 to conserve probability. The sign in the exponential does not matter since only the real part matters, which does not depend on that sign. Assuming that the 0-components of the four momenta of the mass eigenstates differ, while the 1, 2, and 3 components are the same, i.e., $E_1 \neq E_2 \neq E_3$ while $\vec{p_1} = \vec{p_2} = \vec{p_3}$. For the simplicity of notation, hereafter the calculation will be demonstrated using mass eigenstate 1 and 2, without losing any generality, the real part in Eq. 2.17 can be further simplified into:

$$Re\{e^{i(p_1 - p_2)x} - 1\} = Re\{e^{i(p_1 - p_2)x}\} - 1 = \cos(p_1 x - p_2 x) - 1 \tag{2.18}$$

Using the conjecture that $\vec{p_1} = \vec{p_2} = \vec{p_3}$ and the definition that $p = |\vec{p_1}|$, Eq. 2.18 can be rewritten as

$$\cos(p_1 x - p_2 x) - 1 = \cos[(E_1 - E_2)T] - 1 = \cos\left(T\sqrt{p^2 + m_1^2} - T\sqrt{p^2 + m_2^2}\right) - 1 \tag{2.19}$$

where T is the time difference between the neutrinos production at $t = 0$ and its detection,

the 0 component of x. The fact that m_1 and m_2 are very small as compared to p enables the expansion of the square root:

$$\begin{aligned}\cos(p_1x - p_2x) - 1 &= \cos\left[Tp(1+\frac{m_1^2}{2p^2}) - Tp(1+\frac{m_2^2}{2p^2})\right] = \cos\left(T\frac{m_1^2-m_2^2}{2p}\right) - 1 \\ &= -2\sin^2\left(T\frac{m_1^2-m_2^2}{4p}\right)\end{aligned} \tag{2.20}$$

Neglecting the neutrino masses, and multiply both the numerator and denominator by c. Now that the denominator becomes $E_\nu = pc$, while on the numerator T becomes for $L = Tc$. The c cancels out, making the ratio now L/E with some coefficient, and the expression becomes

$$\Delta_{12} \equiv Re\{e^{i(p_1-p_2)x} - 1\} = -2\sin^2\left(\frac{(m_1^2-m_2^2)L}{4E_\nu}\right), \tag{2.21}$$

which can be easily found in any particle physics textbook. Substituting this back into Eq. 2.17 gives

$$P(\nu_\mu \to \nu_\mu) = 1 - \sum_i \sum_{j\neq i} |U_{\mu_i}|^2 |U_{\mu_j}|^2 \Delta_{ij} \tag{2.22}$$

This is the probability that a muon neutrino remains as a muon neutrino when detected at a given space-time coordinate x, or L for convenience in the cases of long-baseline accelerator neutrino experiments. This definition contains some approximations, but is enough to demonstrate the gist of the neutrino oscillation calculation, and to estimate the neutrino beam power E needed to achieve maximal oscillation probability at a detector placed at distance L. The reality is that there are relatively few facilities available for building neutrino beamlines and even fewer underground experiment facilities capable of hosting far detectors. As a result, the baseline distance, L, is typically constrained to a few discrete values by geographical and construction limitations making the neutrino energy, E, more flexible than L.

Parameter	Best fit value
$\sin^2\theta_{12}$	$0.304^{+0.012}_{-0.012}$
$\sin^2\theta_{23}$	$0.573^{+0.016}_{-0.020}$
$\sin^2\theta_{13}$	$0.02219^{+0.0006}_{-0.0006}$
δ_{CP}	$197^{+27}_{-24}\ ^\circ$
Δm^2_{21}	$7.42^{+0.21}_{-0.20} \times (10^{-5})$ eV^2
Δm^2_{31}	$2.517^{+0.26}_{-0.028} \times (10^{-3})$ eV^2

TABLE 2.2: The best global fit values for neutrino oscillation parameters, assuming normal mass ordering, $m_1 < m_2 < m_3$, which is favoured be current measurements [40].

Expanding Eq. 2.22 in full in terms of PNMS matrix elements gives [39]

$$
\begin{aligned}
P(\nu_\mu \to \nu_\mu) = 1 &- (4c_{13}^4 s_{23}^2 c_{23}^2 + 2s_{23}^2 s_{13}^2 c_{13}^2)\sin^2\Phi_{13} \\
&+ (4c_{13}^2(c_{12}^2 - s_{13}^2 s_{23}^2)s_{23}^2 c_{23}^2 + 4s_{12}^2 s_{23}^2 s_{13}^2 c_{13}^2 - 4c_{13}s_{23}c_{23}s_{12}c_{12}\cos\delta) \\
&\times (\frac{1}{2}\sin 2\Phi_{21}\sin 2\Phi_{13} + \sin^2\Phi_{21}\sin^2\Phi_{13}) \\
&- \{4s_{12}^2 c_{12}^2 c_{23}^2 (c_{12}^2 - s_{13}^2 s_{23}^2)^2 + 4s_{13}^2 s_{23}^2 c_{23}^2 (1 - 4\cos\delta^2 s_{12}^2 c_{12}^2) \\
&+ 16 s_{12}^2 c_{12}(c_{12}^2 - s_{12}^2)s_{23}c_{23}(c_{23}^2 - s_{23}^2)\cos\delta \\
&- 8c_{12}2s_{13}c_{13}2s_{23}c_{23}s_{12}c_{12}\cos\delta s_{23}^2 s_{12}^2 \\
&\} \times \sin^2\Phi_{21},
\end{aligned}
\tag{2.23}
$$

where $\Phi_{ij} = \frac{(m_i^2 - m_j^2)L}{4E_\nu}$, $c_{ij} = \cos\theta_{ij}, s_{ij} = \sin\theta_{ij}$. The best measurements of neutrino oscillation parameters from global fit as of when this thesis was written is given in Table. 2.2. In practice, a simplified form of Eq. 2.23 is useful to roughly estimate the property

of an experiment:

$$P(\nu_\mu \to \nu_\mu) = 1 - (4c_{13}^4 s_{23}^2 c_{23}^2 + 4s_{13}^4 c_{13}^2)\sin^2\Phi_{31} + \text{higher order terms} \tag{2.24}$$

Between the parenthesis, the second term is suppressed by a s_{13}^2 factor, which is close to 0 as in Table. 2.2, hence its contribution is smaller than the first term and it is considered as the next-to-leading order term, while the first term is the leading-order term. A similar calculation gives the probability of the ν_e appearance:

$$\begin{aligned} P(\nu_\mu \to \nu_e) = {} & 4c_{13}^2 s_{13}^2 s_{23}^2 \Phi_{21} \\ & + 8c_{13}^2 s_{12} s_{13} s_{23}(c_{12}c_{23}\cos\delta - s_{12}s_{13}s_{23})\cos\Phi_{32}\sin\Phi_{31}\sin\Phi_{21} \\ & - 8c_{13}^2 c_{12}c_{23}s_{12}s_{13}s_{23}\sin\delta\sin\Phi_{21}\sin\Phi_{32}\sin\Phi_{32} \\ & + 4s_{12}^2 c_{13}^2(c_{12}^2 c_{23}^2 + s_{12}^2 s_{23}^2 s_{12}^2 - 2c_{12}c_{23}s_{12}s_{23}s_{13}\cos\delta)\sin^2\Phi_{21}. \end{aligned} \tag{2.25}$$

Again, the first term contributes most and is considered as the leading order term. The dependence on the **CP** violation phase angle arises from the δ dependence, especially in the thrid term.

2.3.1 Matter effect

The neutrino oscillation calculation presented in Eq. 2.22 assumes that neutrinos travel through a vacuum. However, in the T2K experiment, neutrinos pass through the earth's crust on their way from the beam line to the far detector, and the interactions between neutrinos and the crustal matter have an impact on the neutrino oscillation probabilities. All three flavours of neutrinos interact with electrons and nuclei in atoms via neutral-current interactions. Additionally, electron neutrinos can interact with electrons via charged-current interactions.

To account for these effects on neutrino oscillation, Wolfenstein [41], Mikheyev and Smirnov [42] proposed a correction, which became known as the MSW effect. In the case of T2K, the matter effect's impact on the ν_e appearance probability is given by:

$$-8c_{13}^2 s_{13}^2 s_{23}^2(1 - 2s_{13}^2)\frac{aL}{4E}\cos\Phi_{32}\sin\Phi_{31}, \tag{2.26}$$

where $a = 2\sqrt{2}G_F n_e E$, $G_F = 4.54 \times 10^{-14}$ J$^2(\frac{hc}{2\pi})^3$ is the Fermi constant, and n_e is the electron density of the material. At T2K, $L = 295$ km and E is centered at 600 MeV. In the case of the ν_μ disappearance probability, the matter effect is even smaller and considered a higher-order term.

2.4 Neutrino-target interaction

The GSW weak-interaction theory, presented in Section 2.2, primarily describes neutrino interactions with other elementary particles, such as charged leptons and quarks. However, constructing a quark target for experiments is currently unfeasible, and even developing a hydrogen target necessitates significant advancements in technology.

The primary T2K neutrino targets are composed of oxygen and carbon [5]. Both of these atoms consist of bound states containing more than 10 nucleons, which in turn are bound states of up and down quarks. Calculating differential cross sections for such intricate processes and predicting the kinematics of final state particles is beyond the scope of modern quantum field theory, necessitating the use of effective models in the prediction of neutrino interaction event rates.

For the T2K experiment, the charged-current interaction, which results in the production of a charged lepton, is the only type of interaction of interest. The reconstruction algorithm employs the properties of the produced charged lepton to infer those of the incoming neutrino. The predicted neutrino interaction cross section with carbon as a function of neutrino energy is shown in Fig. 2.3. On the other hand, neutral-current interactions do not yield an easily detectable charged lepton, and thus contribute to the background for neutrino-oscillation analyses, although T2K made measurements of neutral-current neutrino interaction cross sections.

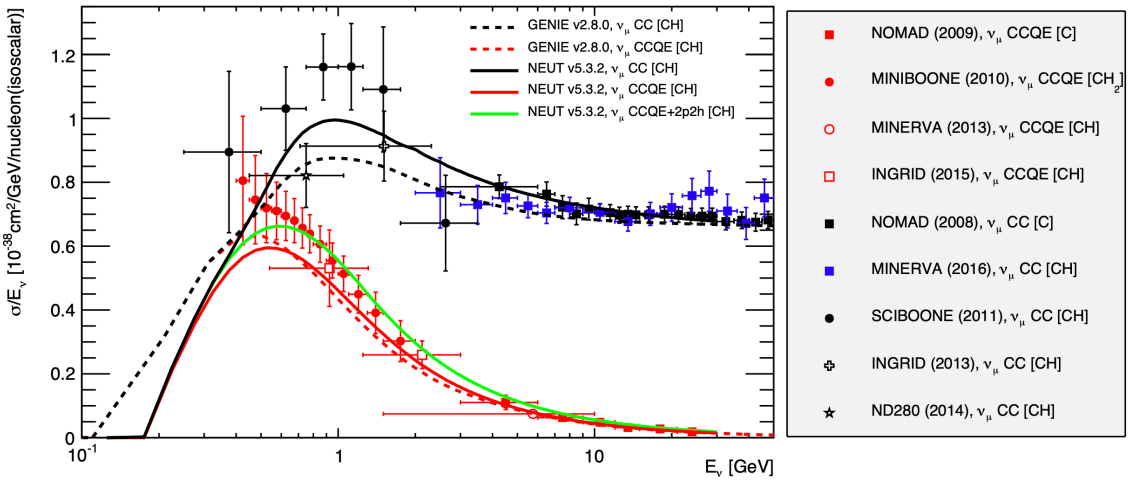

FIGURE 2.3: Neutrino-carbon scattering cross section as a function of incident neutrino energy. The colourful solid lines shows the theoretical prediction made by neutrino event generator NEUT [43]. GENIE [44] results are shown in dashed lines. The dots and error bars show measured results from previous experiments[45, 46, 47, 48, 49, 50, 51, 52, 53]. This figure is adapted from [54].

2.4.1 Neutrino-nucleon interactions

Given that a nucleus comprises bound nucleons, it is essential to first model neutrino-nucleon interactions before examining their interaction with the entire nucleus. There are three primary modes of charged-current neutrino-nucleon interactions: Charged-Current Quasi-Elastic (CCQE), two-particle-two-hole interaction (2p2h), Charged-Current Resonant (CC-Res), and Deep-Inelastic (CC-DIS) interactions. Each of these three interaction modes is dominant in different neutrino energy regions, and leads to different final-state products. This subsection will discuss these interactions in ascending order of interaction energy, from low to high.

For neutrinos possessing energies below 1 GeV, their interactions with nuclei are predominantly characterised by CCQE interactions. Notably, this range encloses the energy range at which the T2K neutrino energy distribution peaks. In a CCQE interaction, both neutrinos and anti-neutrinos scatter off nucleons:

$$\begin{aligned} \nu_l + n &\longrightarrow l^- + p^+ \\ \bar{\nu}_l + p^+ &\longrightarrow l^+ + n \end{aligned} \tag{2.27}$$

where l is any of the three lepton flavours: e, μ, τ. This a two-body final state similar to

elastic scattering, hence the name quasi-elastic. A CCQE interaction produces a charged lepton that carries most of the energy of the incoming neutrino, but does not produce any final-state mesons. In such interactions, a neutrino interacts with a neutron in the nucleus, and produces a proton and a charged lepton in the final state. According to the quark model, the neutrino only interacts with a down quark in the neutron via the exchange of a W^+ boson. The incident neutrino transforms into a charged lepton with the same flavour, while a down quark in the nucleon converts to an up quark to maintain charge conservation. Consequently, the quark composition of the impacted nucleon shifts from down-down-up to down-up-up, resulting in the conversion of a neutron to a proton. In the case of an anti-neutrino, it transforms into a positively-charged lepton and converts the up quark within the proton to a down quark, thereby changing the proton into a neutron. An illustration of a neutrino CCQE interaction is shown in Fig. 2.4.

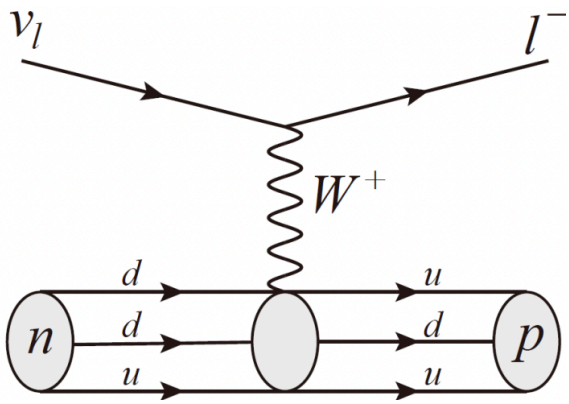

FIGURE 2.4: The Feynman diagram of a neutrino-nucleon CCQE interaction. The initial state particles are on the left, while the final state particles are on the right. This drawing is adapted from [55].

Another important type of quasi-elastic neutrino interaction is the two-particle-two-hole (2p2h) interactions. Similar to CCQE in many aspects, the main feature of 2p2h interactions is that the neutrino interacts with a nucleon pair instead of a single nucleon, causing two nucleons to be ejected from the nucleus instead of one. 2p2h interactions do not produce mesons and hence is similar to CCQE in terms of reconstructed event topology, but the additional nucleon makes the final state kinematics quite different.

Higher energy than the CCQE interaction is the CC-Res interaction, where a single pion is produced through inelastic excitation of the nucleon into a short-lived resonant

state. These processes can be written as:

$$\begin{aligned}
&\nu_l + p \longrightarrow l^- + \Delta^{++} \longrightarrow l^- + p^+ + \pi^+ \\
&\nu_l + n \longrightarrow l^- + \Delta^{+} \longrightarrow l^- + p^+ + \pi^0 \\
&\nu_l + n \longrightarrow l^- + n + \pi^+.
\end{aligned} \tag{2.28}$$

In many cases, there is a pion in the final state, therefore those pion-producing CC-RES interactions are also known as Single Pion Production (SPP) [4]. The CC-Res interactions dominate the energy region from 1 GeV to 10 GeV, where the DIS interaction becomes dominant. An example of an SPP event Feynman diagram is shown in Fig. 2.5.

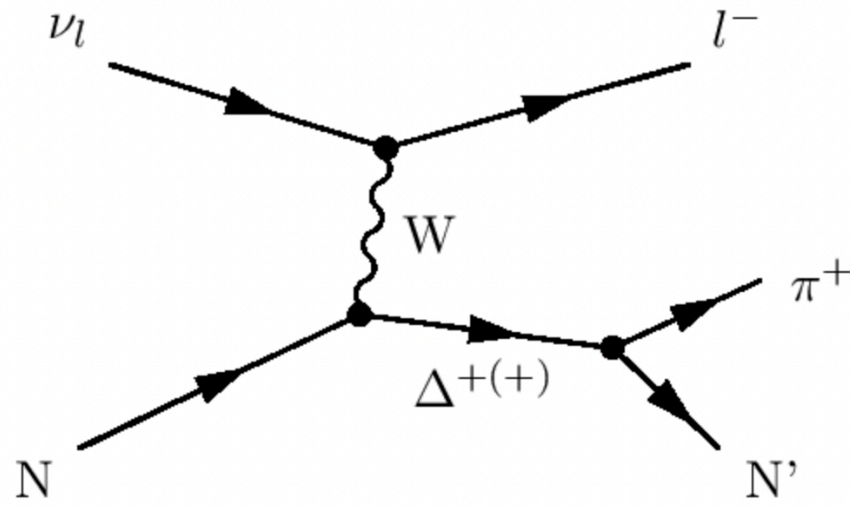

FIGURE 2.5: The Feynman diagram of a neutrino single pion production process. As compared with a quasi-elastic interaction, in this process a delta baryon is produced due to high incident neutrino energy, and subsequently decays into a pion. N' is the new nucleon, after its quark component changes in the interaction.

When the incident neutrino energy is greater than 10 GeV, CC-DIS becomes the dominant mode of neutrino-nucleus interactions. In those interactions, the momentum transfer is high enough to resolve the quark content of the target nucleon, producing hadronic jets subsequently. Parton distribution functions (PDFs), which give the probability of finding a parton carrying a specific quark type and momentum, are currently used to calculate

[4]It is worth noting that some CC-RES interactions do not produce pions, and some pion-producing reactions do not involve a median resonant particle. SPP and CC-RES overlaps by a lot, but not completely.

the cross section of such interactions. The computation of PDFs has been performed in detail using models based on quantum chromodynamics [56].

2.4.2 Neutrino-nucleus interactions

As previously noted, a neutrino-hydrogen experiment is not feasible with current technology, so all existing neutrino interaction experiments rely on heavier, more complex atoms for the majority of their target mass. In the case of the T2K far detector, oxygen constitutes the bulk of the target mass, while at ND280 oxygen and carbon constitute the majority of its target mass. This subsection outlines the neutrino-nucleus interaction model used in the Monte Carlo (MC) simulation of T2K, and several important augmentations to it.

Regardless, in addition to neutrino-nucleon interactions, the modeling process must account for the nucleus's structure, the motion of nucleons within the nucleus, and the trajectories of the final-state particles exiting the nucleus [57]. Currently, T2K uses the Spectral Function (SF) to model nucleon motion in its computation of neutrino-nucleus CCQE interactions, which is a semi-empirical model inspired by nuclear shell model, and built from experimental electron-neutron scattering data. Other neutrino More detailed discussions can be found in Sec. 7.3, and [58].

At T2K, the SF model is augmented with several corrections to produce a more accurate representation of neutrino-nucleus interactions. One important correction takes into account the Fermi motion of nucleons within a nucleus, which gives them a non-zero momentum even in the ground state. The lowest possible energy level allowed by Pauli's exclusion principle contains all nucleons in the ground state. However, for a neutrino to interact with a nucleon bound within the nucleus, it must carry enough energy to excite the nucleon to the next energy level. This requirement, known as Pauli blocking, prevents low-energy neutrino-nucleus interactions.

If a neutrino does successfully excite a nucleon and cause an interaction, the resulting products are affected by the nucleus as they leave it. In particular, hadrons may be absorbed or produced, and their momentum, charge, and type may be altered, whereas charged leptons are only affected electromagnetically. These effects are referred to as Final State Interactions (FSI).

The NEUT event generator [43], which is maintained by T2K collaborators, models all of the effects mentioned in this subsection. Furthermore, the relevant parameters have been implemented and fit to data in T2K.

2.5 Open questions in neutrino physics

Neutrino oscillation has become a widely accepted model among physicists, and over the years, the mixing angles have been measured with increasing precision. Despite these advances, there remain several open questions in neutrino physics that continue to puzzle researchers. These questions include the possible existence of Majorana fermions, the source of leptonic CP violation, the nature of sterile neutrinos, and the order of neutrino mass eigenvalues. This section will provide a brief introduction to these intriguing topics.

2.5.1 Majorana fermions

In modern quantum field theory, all other spin $\frac{1}{2}$ ferimons are considered as Dirac ferimons with mass term like

$$\mathcal{L}_{\text{Dirac}} = m(\bar{\psi}_L \psi_R + \bar{\psi_R} \psi_L)$$

in the Lagrangian [9, 10], where ψ_L and ψ_R are the left-handed and right-handed spinor. Standard model neutrinos, however, have no right-handed component and zero mass [10], so there is no such mass term for neutrinos. As experiments revealed that neutrinos possess small but non-zero mass, it became a problem to model how neutrinos acquire mass, and what their mass terms look like. The mass of Dirac fermions arises from their Yukawa coupling[5] to the Higgs field in forms such as:

$$g\phi^0 \psi \bar{\psi} \tag{2.29}$$

where ϕ^0 is the spin 0 Higgs boson field and ψ is the fermion field of interest. The coupling constant g determines how large the mass is. If neutrinos are indeed Dirac fermions which couple to the Higgs field and acquire mass through spontaneous symmetry breaking, this

[5] All bosons in the standard model have spin 1 and are hence vector bosons, except for the Higgs bosons, which have 0 spin. This means the Higgs field is a scalar field with only one component, hence the mathematical description for Higgs coupling to fermions is quite different from coupling to vector bosons. For instance, the dimension of the coupling constant and the normalisation are different from vector bosons. Hence, the Higgs coupling is considered a special sort of coupling, and named as Yukawa coupling in honour of Yukawa Hideki.

will require a very weak Yukawa coupling to the Higgs boson, which seems unphysical to many theorists [59, 60].

Alternatively, there is another possible way to write a Lorentz invariant mass term for neutrinos:

$$\mathcal{L}_{Majorana} = \bar{\psi_L}\sigma_2\psi_L,$$

where σ_2 is the charge-conjugation operator, hence the Majorana fermions are their own anti-particles. This is fine for composite particles like π^0, but if neutrinos are indeed Majorana they will break lepton number conservation.

A discernible implication of Majorana neutrinos' existence is that the neutrinos produced during β decay can be absorbed within the same process, allowing for neutrinoless double beta decay to occur, which is a phenomenon prohibited if neutrinos were Dirac fermions. A Feynman diagram for neutrinoless double β decay is shown in Fig. 2.6. Whether neutrinos are Majorana or Dirac remains to be determined by experiments, and many neutrinoless double β decay experiments are being conducted in search for such a process, including Kamland-ZEN and CUORE [61, 62, 63, 64].

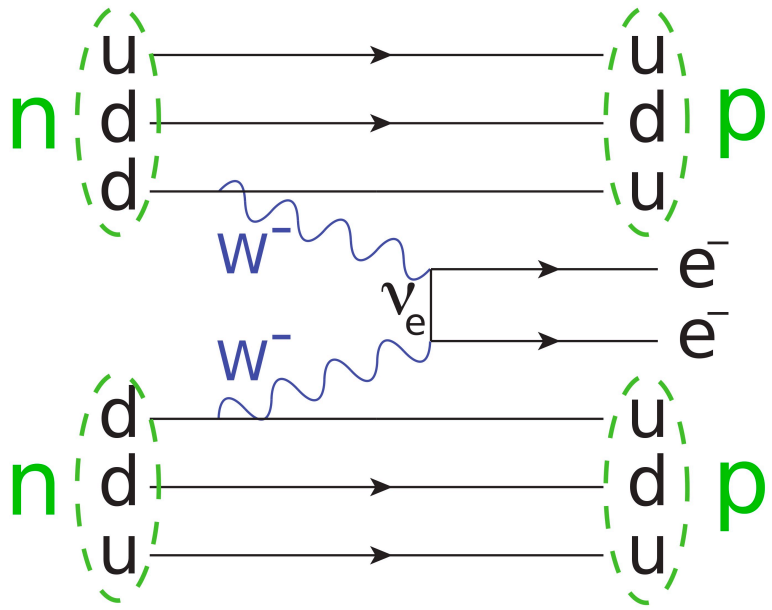

FIGURE 2.6: Feynman diagram of a neutrinoless double β decay. This drawing is adapted from [60]. The initial state particles are to the left, while the final state particles are to the right.

2.5.2 Leptonic CP violation

The **CP** transformation is a discrete transformation that combines both the charge conjugation transformation, **C**, and the parity transformation, **P**. For the field at space time coordindate $x = (x^0, \vec{x})$, those transformations are defined as below:

$$\begin{aligned} \mathbf{C}:&\mathbf{C}\{\psi(x)\} = \bar{\psi}(x) \\ \mathbf{P}:&\mathbf{P}\{\psi(x)\} = \psi(x^0, -\vec{x}) \end{aligned} \tag{2.30}$$

where $\psi(x)$ is some arbitrary field subject to the transformations, $\bar{\psi}(x)$ is its antiparticle. Mathematically, the standard model does not favour matter over anti-matter, but the baryonic universe is dominated by matter rather than anti-matter, raising the matter-antimatter asymmetry problem.

One possible source of such asymmetry is **CP** violation, i.e. certain interactions or processes on the elementary level are inclined more likely to happen for turning anti-particles into particles, than the other way around. Hadronic **CP** violation has been discovered in experiments [65, 66, 67], but it is not sufficient to explain the maximal asymmetry in our universe, which is dominated by matter. **CP** was regarded as a natural symmetry of our universe until 1964, when Cronin and Fitch *et al* discovered evidence of **CP** violation in neutral kaon decay experiments [68]. There are two groups of neutral kaons from empirical studies: the short lived kaons, K_S^0 and the long-lived kaons K_L^0. The mean life time of K_L^0 is 8.954×10^{-11} s, while that of K_L^0 is 5.116×10^{-8} s. Hence, the lifetime of K_L^0 is more than 500 times longer than that of K_S^0. Two main decay channels of neutral kaons are into pions:

$$K^0 \to \pi\pi\pi, \quad K^0 \to \pi\pi \tag{2.31}$$

Regardless of charge, pions are eigenstates of **CP** transformation whose eigenvalues are -1. Thus, the two pion final state is a **CP** eigenstate of +1, and the three pion state is -1. Since the three body decay is less likely to happen than a two body decay due to limited kinematic phase space volume and and extra vertex, it is natural to guess that K_L^0 only decays into three pions and is a **CP** eigenstate of -1, while K_S^0 decays into two pions and is a **CP** eigenstate of $+1$.

The experiment conducted in [68] built a 17.4 m decay tube so that after travelling down it for a long enough distance, the kaon beam becomes an arbitrarily homogenous K_L^0 beam. However, about 1/500 of K_L^0 were observed to decay into two pions, seemingly violating the conservation of **CP** symmetry.

In the context of neutrino oscillation and the PMNS matrix, the degree of **CP** violation is primarily determined by the **CP** violation phase angle, δ_{CP}. A non-zero value of δ_{CP} is expected to give rise to a matter-antimatter asymmetry. The T2K experiment compares the probability of a muon neutrino oscillating to an electron neutrino, and that of an anti-muon neutrino oscillating to an anti-electron neutrino. If $\delta_{\mathrm{CP}} = 0$, these two processes should have the same probability. T2K study yielded a confidence interval of δ_{CP} that does not include 0, indicating that **CP** violation also occurs in the leptonic sector [69].

2.5.3 Sterile neutrinos

Another open topic in neutrino physics is the sterile neutrinos. The decay width of Z^0 bosons indicates that there are only three weak eigenstates [70], but this does not necessarily rule out weakly-inactive neutrinos, or limit the number of neutrino mass eigenstates to three. In other words, the existence of other 'sterile' neutrinos cannot be ruled out yet, which do not couple to Z^0 and $W^{\pm}$. 'Active' standard model neutrinos can still oscillate into sterile states. In the Standard Model, there are three generations of quarks and leptons; however, no definitive limit has been established on the number of generations, nor is there a compelling reason to require an equal number of leptonic and quark generations, which is currently believed to be three.

A fourth generation of neutrinos were proposed as a natural candidate of dark matter [71], which is both easy to fit into the current standard model without breaking lepton universality, and provides competitive candidates to the 'hidden sector' particles. The LSND experiment first observed an excess of low energy electron neutrinos which hints the existence of such sterile neutrinos [72], which was later confirmed by MiniBooNE short-baseline experiment [73]. Later at the same site, the liquid-argone time projection chamber based MicroBooNE experiment was carried out, which did not observe such excess. It is not concluded yet whether those low-energy excess were due to sterile neutrinos, nor the academia has agreed on how to interpret the result of this series of experiments, as of when this thesis is written. T2K has also performed a search for light sterile neutrinos

using run 1-8 data, and no evidence for the mixing with a fourth type of neutrino was found in the analysis [74].

2.5.4 Neutrino masses

As discussed earlier in this chapter, experiments have confirmed that neutrinos have non-zero masses. Becuase the masses are minuscule, with an upper limit of 0.12 eV [75], they present a significant measurement challenge. For comparison, this upper limit is six orders of magnitude smaller than the mass of an electron [75].

While measuring the absolute mass of neutrinos is difficult, it is easier to measure the difference between their masses squared, denoted by Δm^2_{21} and Δm^2_{32}. Due to historical reasons, Δm^2_{21} is commonly refered to as the solar mass squared difference, Δm^2_{sol}, while Δm^2_{13} is the reactor difference Δm^2_{rec}, and Δm^2_{23} is the atmospheric difference Δm^2_{atm}. These parameters can be constrained by many neutrino oscillation experiments, including T2K, since the probability of neutrino oscillation depends on the mass squared difference, as shown in Eq. 2.22.

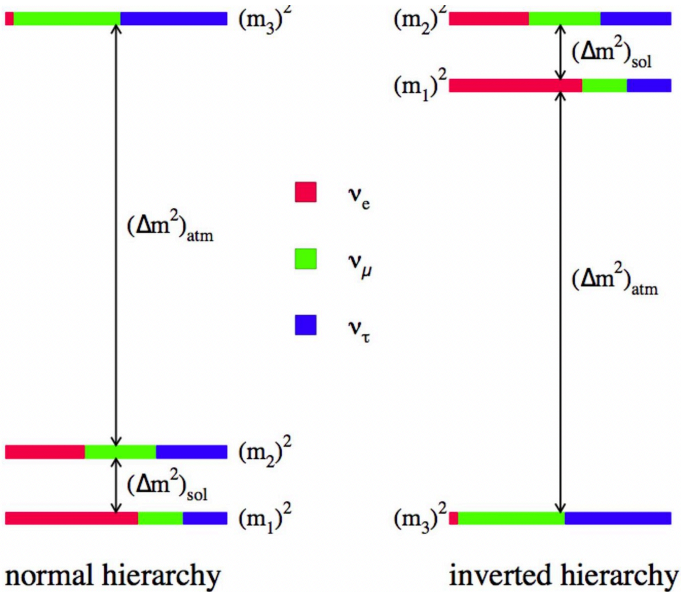

FIGURE 2.7: Two possible scenarios of neutrino mass ordering.

While neutrino oscillation analysis experiments are capable of measuring the differences between mass eigenvalues squared, they cannot directly constrain the sign of these differences or mass splittings. In such experiments, this information can only be inferred through complex fits, as the neutrino appearance or disappearance probability explicitly

depends only on the Δm^2. The KATRIN experiment, which analyses the tritum β decay energy spectrum, was built to measure the absolute mass of neutrino mass eigenstates [76].

Currently, the value of the atmospheric mass split Δm^2_{31} is measured to be approximately 2.5×10^{-5} eV^2, but the sign of this split remains undetermined [77]. Two possible scenarios, referred to as Normal mass Hierarchy (NH) ($m_1 < m_2 < m_3$) and Inverted mass Hierarchy (IH) ($m_3 < m_1 < m_2$), are demonstrated in Fig. 2.7.

Chapter 3

T2K Experiment

The Tokai-to-Kamioka (T2K) experiment is a long-baseline neutrino oscillation experiment that investigates neutrino oscillation physics through the disappearance of ν_μ or $\bar{\nu_\mu}$ and the appearance of ν_e or $\bar{\nu_e}$ [5]. The experiment takes place in northern Japan and involves producing a neutrino beam in the Japan Proton Accelerator Research Complex (J-PARC) on the east coast in Ibaraki prefecture, and measuring it twice: once at the ND280 near detector located 280 meters from the beam source in J-PARC, and a second time at the Super-Kamiokande (SK) far detector located in the mountains of Kamioka near the country's west coast. A schematic drawing of the geographical layout of the T2K experiment is shown in Figure 1. T2K provides constraints for neutrino-physics parameters, including θ_{13}, δ_{CP}, and m^2_{31}.

This chapter is structured as follows: The first subsection presents the T2K beam and off-axis detector, while the second subsection delves into the primary ND280 near detector, as well as other detectors within the J-PARC near detector complex. The third section focuses on the SK far detector.

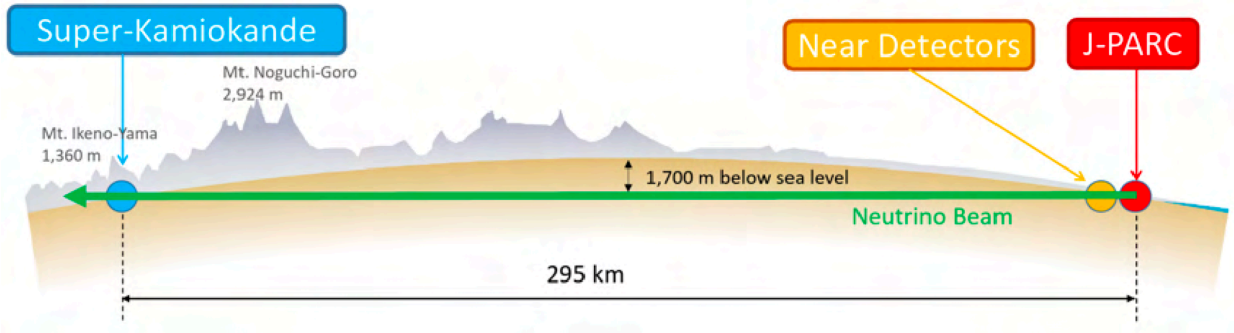

FIGURE 3.1: A schematic overview of the T2K experiment, showing the neutrino beam traveling from J-PARC to Super-Kamiokande.[5]

3.1 Beam

The T2K beam is generated through a multi-stage process, beginning with the acceleration of negatively charged hydrogen ions to 400 MeV in a LINear ACcelerator (LINAC). Next, a charge-stripping foil is employed to convert the ions into positively charged hydrogen ions, or protons. These protons are then injected into the J-PARC Rapid Cycling Synchrotron (RCS, which operates at a 25 Hz frequency and can accelerate the ions to up to 3 GeV. The RCS can hold up to two bunches of protons at a time, which are separated and accelerated to 30 GeV in the larger Main Ring (MR). The MR can hold up to eight bunches, which can be extracted to the neutrino beamline in short bursts.

In the T2K experiment, all eight bunches of protons are kicked into the neutrino beamline in a single turn by five kicker magnets. Each bunch lasts for 58 ns, with a 581 ns gap between bunches [78]. Timing data is transmitted via direct fiber link to the near detectors, and via GPS to the far detector, enabling precision beam neutrino event triggering. Protons can also be directed to a beam dump when necessary.

The T2K proton beamline leads the protons to a rod-shaped graphite target, which has a 2 cm diameter and a 90 cm length. Upon impact with carbon atoms, the protons produce a range of kaons and pions. To create a muon neutrino (or antineutrino) beam that is as pure as possible, T2K uses a series of electromagnetic horns to select hadrons of a specific mass carrying a particular charge. Flipping the horn polarity allows for the selection of hadrons with the opposite charge, and the subsequent production of a neutrino or antineutrino beam at will. An illustration of the T2K target system is shown in Figure 3.2.

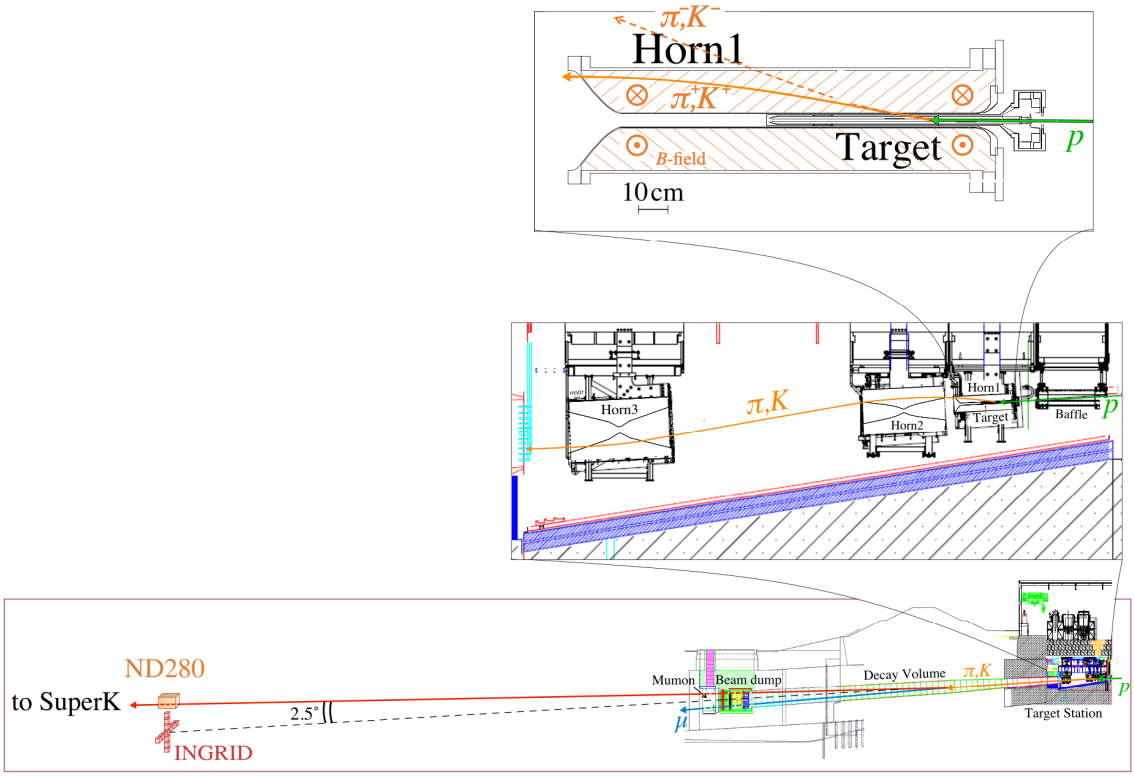

FIGURE 3.2: Schematic drawing of the T2K beamline. Charged hadrons of the required sign are focused via a series of electromagnetic horns, and directed onto a 100-m decay volume. Subsequently, a beam dump stops any charged particles, while allowing neutrinos to flow through and proceed to the near and far detectors.

The hadrons produced at the target then decays into neutrinos via various weak processes. Taking muon neutrinos as example, the dominant channels are

$$\pi^+ \longrightarrow \mu^+ + \nu_\mu \tag{3.1}$$

$$K^+ \longrightarrow \mu^+ + \nu_\mu \tag{3.2}$$

$$K^+ \longrightarrow \pi^0 + \mu^+ + \nu_\mu. \tag{3.3}$$

While pions can decay into electrons, these channels are heavily suppressed due to the light mass of electrons and the scarcity of right-handed helicity electrons, which are the only ones that can couple to the weak-interaction vertex[1]. Approximately 99.9% of π^+ decays

[1]For a spin-half fermion, a helicity eigenstate $F_\uparrow$ can be decomposed into chiral eigenstates F_L, F_R as $F_\uparrow = \frac{1}{2}(1 + \frac{p}{E+m})F_R + (1 + \frac{p}{E+m})F_L$. As shown in Eq. 2.6, the weak interaction vertex couples solely to left-handed chirality fermions. Electrons that are effectively massless at GeV scale, hence the chance to find a neutrino in a right-handed helicity eigenstate, which is the only allowed configuration allowed

occur via the $\mu^+ + \nu_\mu$ channel, while only 0.012% decay into $e^+ + \nu_e$ [75]. Furthermore, decay-product muons can themselves decay into electrons, contributing to the presence of electron neutrinos in the muon neutrino beam, along with intrinsic electron neutrinos originating from hadronic decays.

To produce a muon anti-neutrino beam, T2K can select negatively charged hadrons by flipping the polarity of the horns. The mode that produces muon neutrinos is conventionally called the Forward Horn Current (FHC), while the mode that produces muon anti-neutrinos is known as the Reverse Horn Current (RHC). T2K places a beam dump, which is a 75-tonne, water-cooled graphite block with 15 metal plates, at the end of the decay volume to absorb charged particles from proceeding to the ND280. Only muons with energy greater than 5 GeV can pass through the beam dump and reach the muon monitor behind [78].

3.1.1 Off-axis placement

An accelerator neutrino beam faces some hiccups that do not occur in charged particle beams: the neutrinos are electrically neutral and thus are impervious by the magnetic field. This makes the neutrino energy spectrum much wider than a proton or electron beam, and subsequently more difficult to simulate, as a range of incoming particle energy has to be considered, instead of a single defined energy.

One of the most notable features of T2K is its off-axis detector placement. The two primary detectors, ND280 and SK, are situated 2.5 degrees away from the beam axis, as shown in Fig. 3.3. By shifting the beam slightly off the far-detector direction, the neutrino energy spectrum shifts lower and has a narrower peak, providing T2K with a well-defined length-to-energy ratio.

T2K selected an off-axis angle of 2.5° such that the neutrino energy distribution peaks at 600 MeV, which maximises the ν_e appearance and ν_μ disappearance probabilities at the desired 295 km far detector distance. This energy region also leads to more CCQE events and fewer CC-Res and CC-DIS neutrino interactions in the data sample, making

by the conservation of angular momentum, from a left-handed chiral eigenstate, is very slim. For more discussions please refer to Chapter 11.6 in [55] and Chapter 9.4 in [35].

the signal selection easier. Moreover, the off-axis arrangement also narrows the neutrino energy spectrum and subsequently L/E, thereby making statistical inference easier.

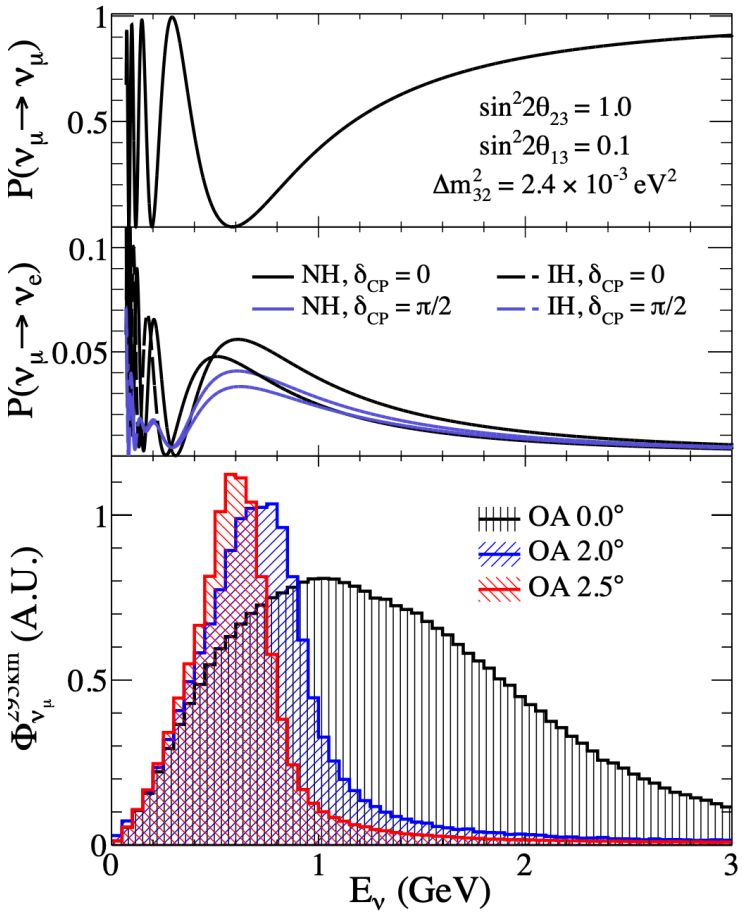

FIGURE 3.3: Top: T2K ν_μ survival probability at 295 km, as a function of neutrino energy. Middle: T2K ν_e appearance probabilities at 295 km as a function of neutrino energy. Probabilities in cases of maximal **CP** violation and no **CP** violation, NH and IH are drawn for comparison. Bottom: the neutrino energy distribution in different off-axis angle scenarios. The 'OA' in the top right corner stands for Off Axis. At the expense of total neutrino number, increasing the off-axis angle leads to a narrower neutrino energy distribution, making Monte Carlo simulation and data analyses easier. A 2.5° off-axis angle guarantees the maximum ν_μ disappearance and ν_e appearance probabilities at 295 km away from the neutrino source [5, 79]

Similar to the luminosity in collider experiments, T2K quantifies the amount of data using Protons On Target (POT), which is the number of protons delivered to the neutrino carbon graphite target. Naturally, POT is a quantity proportional to the number of data events useful to scale the number of events, just like luminosity. The accumulated POT

of T2K in both the FHC and RHC setting is shown in Fig. 3.4.

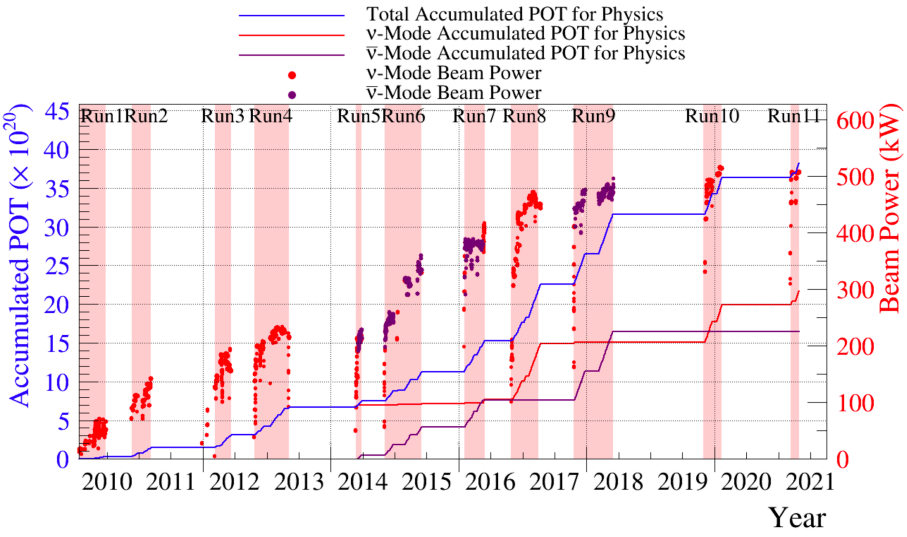

FIGURE 3.4: Accumulated protons delivered to the T2K target from the MR. The blue solid line shows the total POT, and each dot corresponds to a single run. The y coordinate of the dot represents the power of the beam. As of when this thesis is written, T2K has accumulated 3.8×10^{21} POT, in which 2.1×10^{21} are in FHC mode, and the rest 1.7×10^{21} are in RHC mode.

Many Monte Carlo simulations have been produced to predict the neutrino flux at the near and far detector, which requires knowledge of proton-carbon interactions. The neutrino flux at ND280 according to MC simulations in different configurations are shown in Fig. 3.5. NA61/SHINE data are used to constrain such models and predict the flux for T2K [80, 81]. At both the near and the far detector, FHC ν_μ beam has a greater than 90% purity, while the purity of the RHC $\bar{\nu}_\mu$ beam is usually around 60% due to bigger branching ratio of electronic hadron decays.

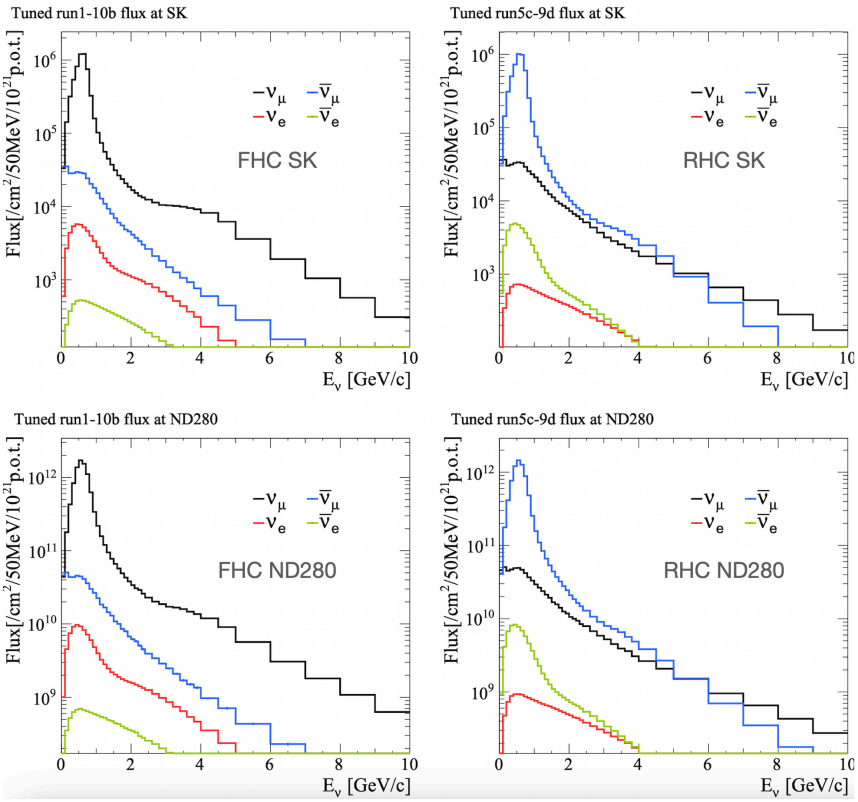

FIGURE 3.5: Top: The predicted T2K neutrino flux at Super-Kamiokande. Left panel is the FHC mode, and the right panel is the RHC mode. Bottom: The predicted T2K neutrino flux at ND280. Left panel is the FHC mode, and the right panel is the RHC mode[82].

3.2 INGRID

To measure the direction and intensity of the beam, T2K employs an on-axis iron-scintillator detector known as the Interactive Neutrino GRID (INGRID) [83]. INGRID consists of 14 identical modules that are arranged vertically and horizontally to form a cross, as illustrated in Fig 3.6. A photograph of the actual device is shown in Fig. 3.7. This configuration allows the relative intensity of the beam in each module to be detected, providing information on the direction of the beam. Over the years, two additional modules have been deployed in various configurations to enable measurements of the beam intensity off the vertical and horizontal axes.

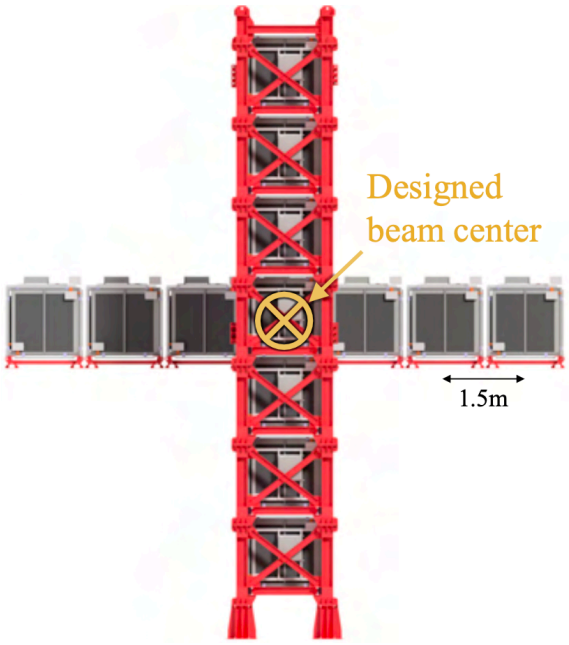

FIGURE 3.6: The arrangement of all 14 INGRID modules. Seven modules form a horizontal row, another seven form a vertical column, ending up in a cross. The center of the cross is on the neutrino beam center [83]. There are two overlapping modules at the beam center, one in the horizontal row, the other in the vertical column. Both arms of the cross are roughly 5 m long.

FIGURE 3.7: A photo of the horizontal INGRID modules taken by the author.

Each INGRID module consists of eleven tracking scintillator planes and nine iron target plates. The tracking scintillator planes are each constructed from two layers of optically separated plastic scintillator bars that are perpendicular to one another. WaveLength Shifting fibers (WLS) run through the center of each scintillator bar, which is mirrored at one end and read out by a Multi-Pixel Photon Counter (MPPC) at the other. To prevent charged particles from entering from the outside, scintillator veto planes are installed on both sides of INGRID. Fig. 3.8 provides an exploded view of an INGRID module.

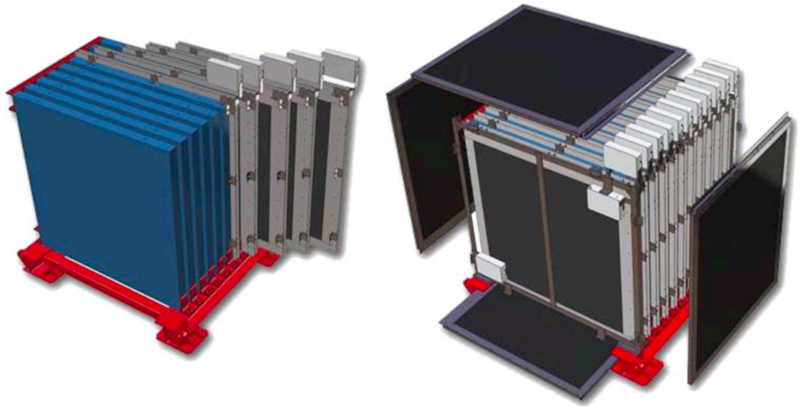

FIGURE 3.8: Exploded view of a single INGRID module. In the left plot, the blue panels are made in iron, while the grey ones are tracking scintillator planes made in plastic. In the right plot, the black panels are peripheral veto scintillator planes.

3.3 ND280

The Near Detector at 280m (ND280) is placed at 280 meters away from the target station, and is T2K's primary detector to measure the beam flux, neutrino energy spectrum and portion of different neutrino types. It also serves the purpose to constrain neutrino-nuclei interaction models [5]. Given its closeness to the target, the measurement at ND280 is seen as pre-oscillation.

ND280 is located on top of INGRID, positioned 2.5° away from the proton beam axis. The outermost part of the ND280 detector is the magnet system, which consists of an aluminum solenoid yoke and an iron flux return yoke recycled from the UA1 magnet [5]. Several subdetectors are situated inside the magnet, including the π^0 Detector (P0D), the Side Muon Range Detector (SMRD), the Fine Grained Detectors (FGDs), the Time Projection Chambers (TPCs), and the Electro-CALorimetry system (ECals). The SMRD

is installed within the magnet yoke, while the TPCs, P0D, FGDs, and downstream ECal all sit in a metal basket. Other ECal modules are installed between the magnet and the basket. The geometric arrangement of the ND280 subdetectors is shown in Fig. 3.9, and a photo of ND280 and in the near detector pit is presented in Fig. 3.10. Each of these subdetectors is designed to fulfill a specific function, which will be discussed in detail in the following sections.

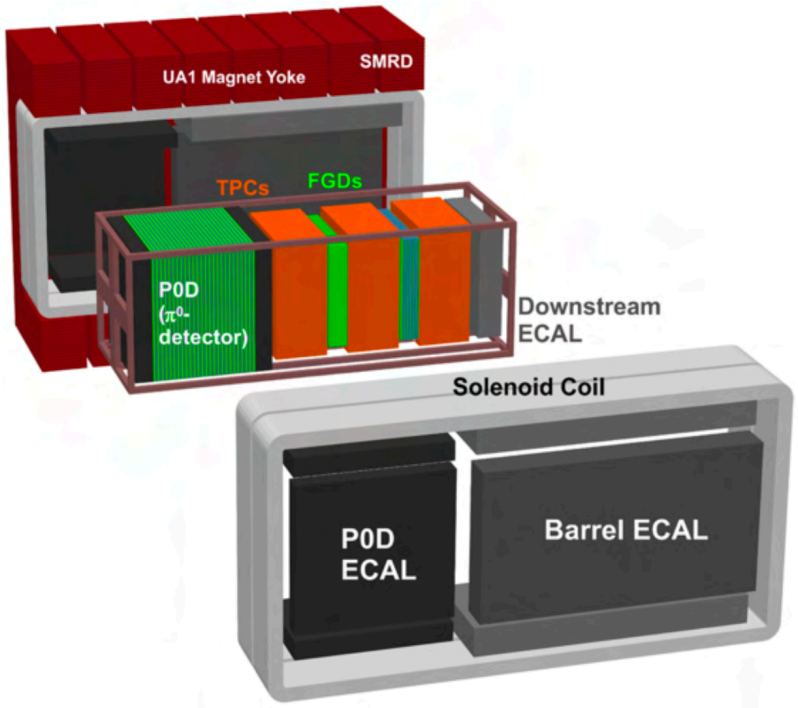

FIGURE 3.9: An exploded view of the ND280 detector. P0D, TPCs, FGDs and the downstream ECal all sit in a basket enclosed by the magnet system. The P0D is the most upstream detector, which is followed by three TPCs and two FGDs in a double sandwich order. The P0D and the two FGDs provide the target mass of ND280. TPCs are placed in between the target-mass providing detectors to track charged incident particles coming out of those detector. The TPCs and the FGDs make up the ND280 tracking volume, where most of T2K knowledge of ND280 track kinematics comes from. Wrappnig up the tracking volume and P0D is the ND280 ECal system, comprising the barrel and downstream ECal serving the tracking volume, and the P0D ECal for the P0D. All ECal modules except the downstream ECal are installed between the basket and the magnet. An additional ECal is installed after TPC3 for tracks exiting the tracking volume in that direction. Outside the ECal system there is the SMRD, which is installed in the magnet yoke.

.

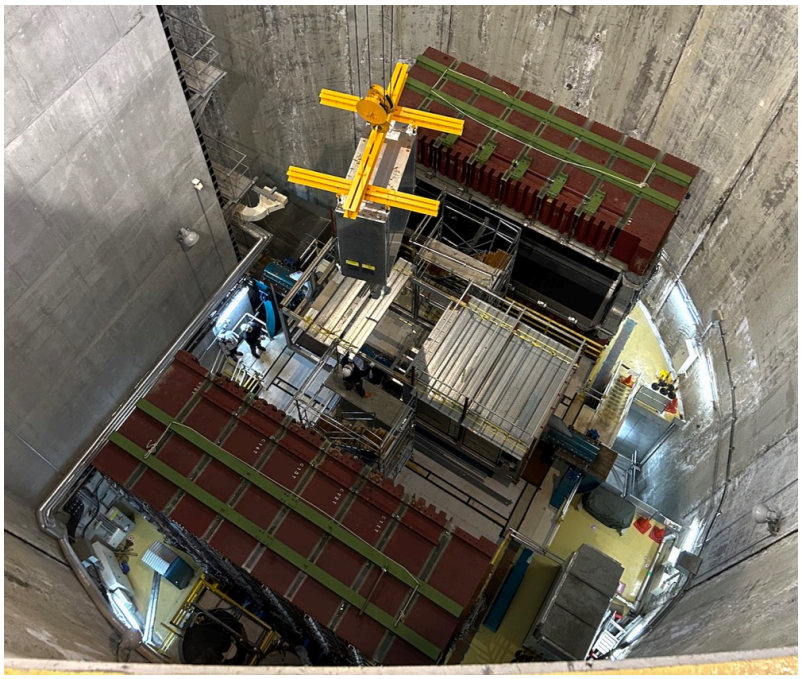

FIGURE 3.10: A photo of the ND280 detector taken by the author. The magnet is open, and the P0D module has been removed to make room for an upgrade.

3.3.1 Common components

Before jumping to the design of each of ND280 subdetectors, it is helpful to introduce the components that are shared by multiple subdetectors, especially the plastic scintillator bars and the multi-pixel detectors that read them.

1. **Scintillator bars**

   Many of ND280's subdetectors, such as the P0D, FGD, ECal, and SMRD (which uses scintillator slabs instead of bars), utilise long plastic scintillator bars or slabs with a central hole. WLSs are threaded through the hole, extending from one end to the other. In the case of SMRDs, the slabs feature a curved groove on their surface to minimise the distance between the WLS and the slab's surface. When a charged particle passes through the scintillator bar or slab, it deposits energy and excites the material via electromagnetic interaction. The excited material then de-excites, emitting photons that are collected by the WLS fibers and read out at the end of the fiber by the readout electronics, which will also be discussed in this section.

2. **Multi pixel photon counter**

The WLS fibers threaded through the scintillator bars in ND280's subdetectors are read out on at least one end by MPPCs produced by Hamamatsu Photonics. Compared to Photon Multiplier Tubes (PMTs), MPPCs are smaller in size and easier to integrate into detectors with limited space. Additionally, MPPCs are not affected by magnetic fields, making them particularly useful in ND280 where the physical size of the detectors is limited by the magnet system, and the readout systems operate in a strong magnetic field. A single MPPC chip is small, measuring 1.3 mm by 1.3 mm in area and containing 667 pixels. Each pixel is a photon diode with a voltage applied to it. When a photon enters, it produces an electron via the photoelectric effect, resulting in a current that is detectable by later electronics. As the MPPC contains a multitude of pixels, the number of pixels that see an induced current is proportional to the number of photons passing through the WLS and, ultimately, to the energy deposited by the traversing charged particle.

3. **Trip-T frontend boards**

   The MPPCs are connected to Trip-T Frontend Boards (TFBs), which control the voltage gains of the MPPCs to minimise temperature-dependent noise. Each TFB can control up to 16 MPPCs, and the TFB itself is read out by a Readout Merger Module (RMM), which can collect data from up to 48 TFBs. The ECal, P0D, and SMRD subdetectors all use TFBs and RMMs to acquire data. In contrast, the TPCs and FGDs use a different type of electronics known as data concentrator cards.

4. **Wavelength-shifting fibres**

   A Wavelength-Shifting Fiber (WLS) or wavelength-shifter is an optical fiber doped with a fluorescent material that absorbs photons at one wavelength and re-emits them at a longer, shifted wavelength. The fiber is designed to capture photons in a large active volume of the detector without the need for many photon detectors. It is useful in particle detectors as it allows for the detection of photons or at wavelengths or locations that are otherwise challenging to detect directly.

   In a scintillator-based detector, when a high-energy particle passes through the scintillating material, it produces a flash of light, or scintillation light. The WLS fiber is embedded in the scintillating material and captures the scintillation light. The fluorescent material in the fiber then re-emits the photons at a longer, more detectable wavelength. WLS fibers are also used to shift the frequency of photons to the part

of the spectrum that the photon detectors, such MPPCs used by ND280, are more sensitive to. In the ND280 detector, the P0D, FGD, ECal, and SMRD detectors all use WLS fibers to collect scintillation light.

3.3.2 Magnet

The momentum of a charged particle is commonly measured by determining the curvature of its trajectory in a magnetic field. To achieve this, the T2K experiment repurposed the UA1/NOMAD magnet system for the ND280.

The ND280 magnet provides a dipole magnetic field of 0.2 T perpendicular to the neutrino beam axis at a working current of 2.7 kA. The inner dimensions of the entire magnet are $7.0 \times 5.5 \times 3.6$ m^3, while the outer dimensions are $7.6 \times 5.6 \times 6.1$ m^3. The magnet is made up of two identical halves, each consisting of eight C-shaped iron flux return yokes, each of which is 48 mm thick and separated by 17 mm slits; in total, the magnet has 16 yokes. The SMRD system introduced in Sec. 3.3.7 is installed in those slits. The coils of the magnet are made of aluminium bars, each with a central hole for the cooling water to flow through. The total weight of the magnet system is 850 tonnes.

To accurately reconstruct the momentum of charged particles, a precise measurement of the magnetic field is essential. The ND280 experiment accomplished this by performing a meticulous measurement with a Hall probe at a magnetic field of 0.07 T, which was sufficient to scale up to the desired 0.2 T. The maps of the magnetic field strength are presented in Fig. 3.11. The final uncertainty of the magnetic field measurement is below 1‰, resulting in a sub 2% uncertainty on the muon momentum measurement in the energy peak region below 1 GeV [84].

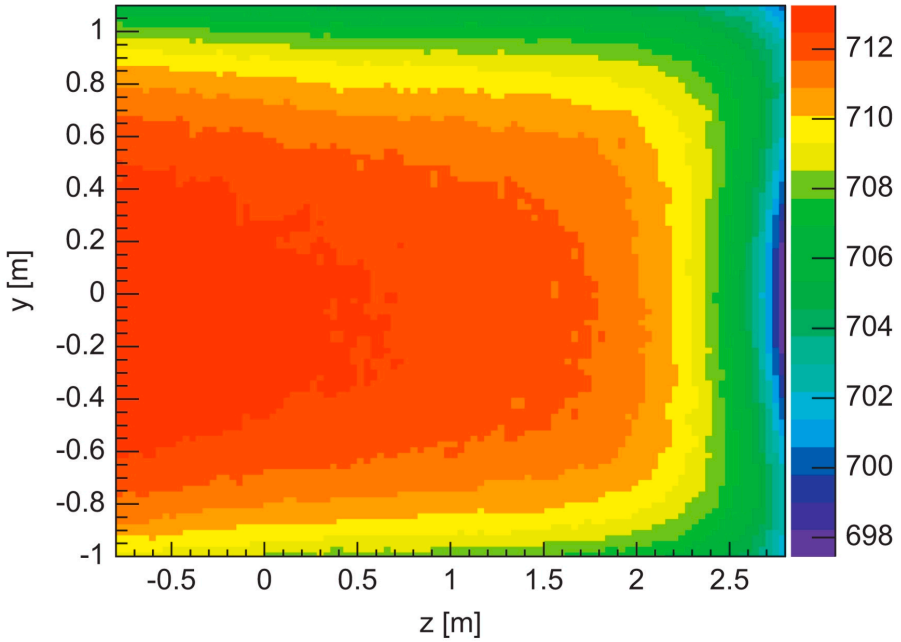

FIGURE 3.11: Magnetic field strength as viewed from the side, in the centre region of the ND280 tracker volume. The horizontal and vertical axis correspond to the spatial coordinates inside ND280. The color bar indicates the strength of the magentic field, unit in Gauss (10^{-4} T). The magnetic field uniformity is in general very good, and slightly stronger in the upstream part near P0D (left of the figure), and weaker near the downstream ECal (right of the figure). This figure is adapted from [84].

3.3.3 The pi-zero detector

The upstream-most subdetector of ND280 is the π^0 Detector (P0D), which is designed to measure the cross section of neutral-current neutrino-water interactions that produce a neutral pion, π^0, in the final state [5]. Since π^0s primarily decay into two photons [77], which are difficult to distinguish from electrons at Super-Kamiokande [85], if one of the pion decay photons cannot be reconstructed, the remaining photon can be easily mistaken for an electron, resulting in the event being misidentified as a charged-current ν_e event. The central part of P0D contains 26 scintillator modules, each of which features two planes of interleaved scintillator bars, a metal sheet, and a plane-shaped water bag. A photograph of a single P0D module can be found in Figure 3.12.

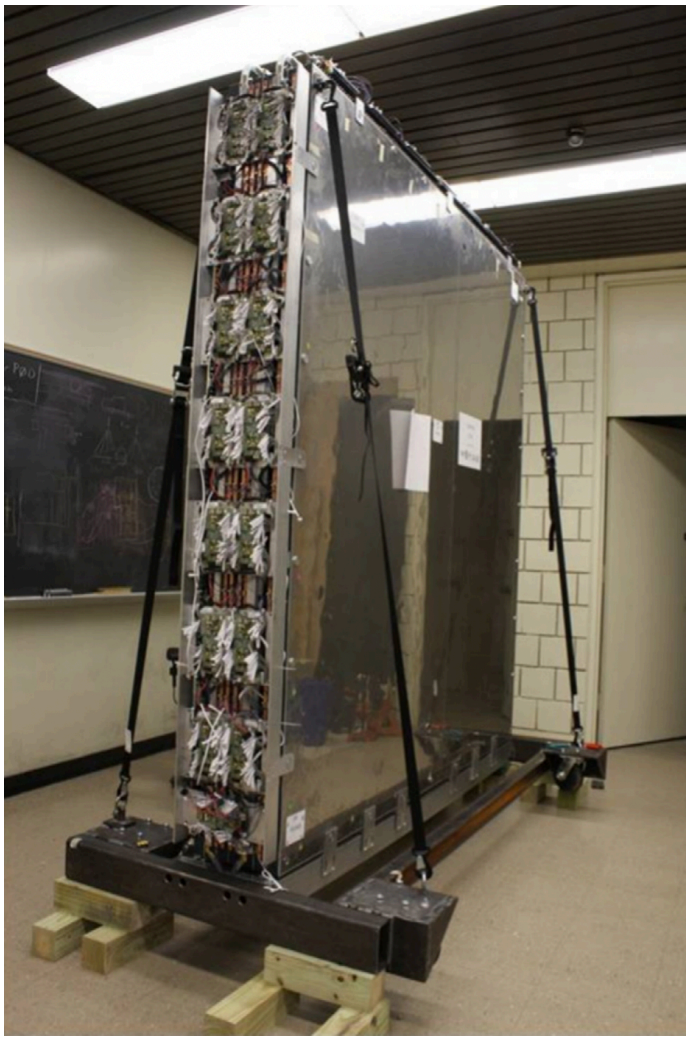

FIGURE 3.12: The photo of a single P0D module adapted from [86].

As shown in Fig. 3.13, the P0D can be further split into four regions, the upstream and the central ECal, the upstream and central water target. There are seven modules in the upstream ECal part, another seven in the upstream water target, 13 in the central water target and another 13 in the central ECal.

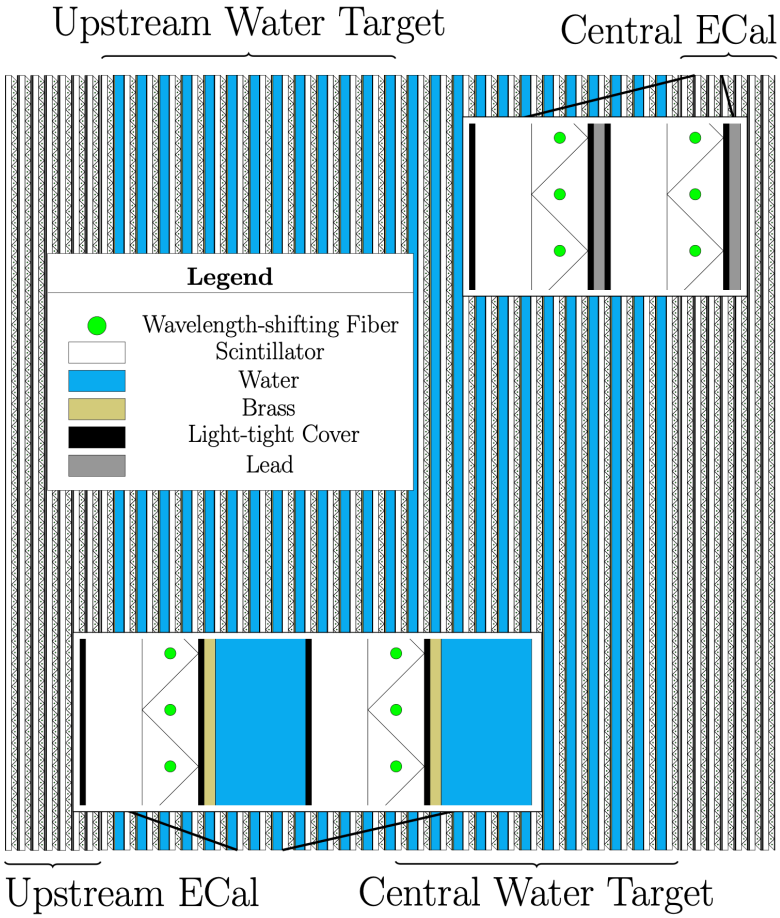

FIGURE 3.13: A schematic drawing of the P0D [5]. The beam comes in from the left hand side, and leaves on the right. Most upstream is the upstream ECal, then the upstream water targets, then the central water targets, finally the central ECals.

Each of the modules in the target module is made up by a scintillator plane, a layer of brass sheet, and a water bag. The brass sheets serve as veto planes to make sure which water bag the interaction happened in. The scintillator plane is made by two layers of perpendicular scintillator bars. Each scintillator plane has 134 vertical bars and 126 horizontal bars. The bars have triangular cross section with a wavelength shifting fibre threaded through a hole drilled in the center, and a layer of TiO_2 coating. The WLS is mirrored at one end, and read by MPPCs at the other. In the ECal modules, there is no water bag, and the brass sheets are replaced with lead sheets.

The water bags in the target region is refillable, which is designed to allow for comparison between water-in and water-out configurations. The difference in the P0D event rate with and without water in the bags enables T2K to measure neutral-current π^0 producing

neutrino-water event rates to a good precision, which is helpful in constraining systematic uncertainties at the SK far detector.

Throughout the experiment, the P0D did not prove to be very successful. Only the P0D components of tracks that met the selection criteria of the 4π sample were included in the oscillation analysis. As a result, the P0D will be replaced by a series of upgraded detectors, which will be briefly introduced in this thesis.

3.3.4 Fine-grained detector

Next to the P0D, along the beam direction, is the ND280 tracking volume, which comprises three TPCs and two FGDs arranged in a double-sandwich configuration. The two FGDs provide the target mass for the ND280 tracking volume and subsequently for T2K oscillation analysis [87].

The upstream FGD is referred to as FGD1 and is composed entirely of scintillator planes. The downstream FGD is referred to as FGD2 and features water bags as targets in its upstream portion and scintillator planes in its downstream half. Both FGDs are enclosed in a dark box. FGD scintillator bars, unlike those in P0D, have a square cross-section, with dimensions of $9.61 \times 9.61 \times \times 1864.3$ mm^3. Each scintillator layer consists of 192 bars arranged perpendicular to the plane of the adjacent layer. A scintillator bar contains a hole threaded with a wavelength-shifting fiber, which is mirrored at one end and read out by an MPPC at the other. The combination of two adjacent layers is often referred to as an XY module. All the XY modules are installed perpendicular to the neutrino beam axis, which is in the z direction. A picture of an XY module can be found in Fig. 3.14.

The MPPCs are installed on photonsensor busboards, which are screwed to the edge of XY modules. The front-end electronics are housed in minicrates mounted on the walls of the dark box. A schematic drawing of cross section view of FGD1 is shown in Fig. 3.15.

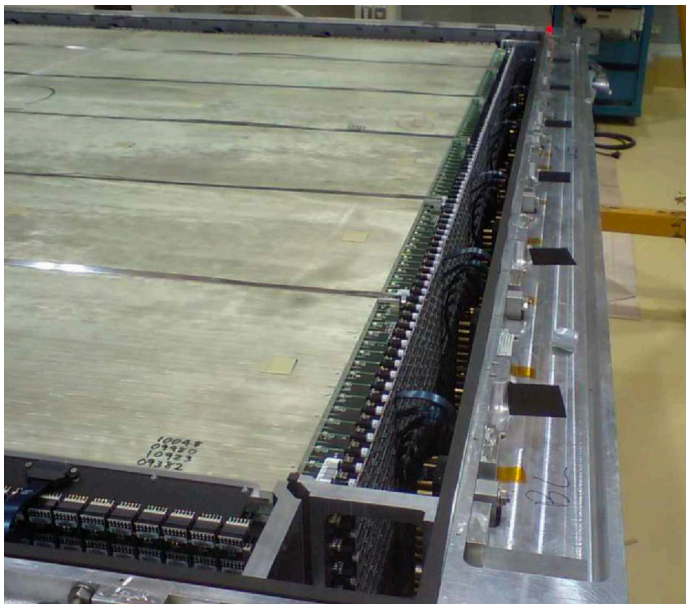

FIGURE 3.14: Picture of a FGD XY scintillator module.

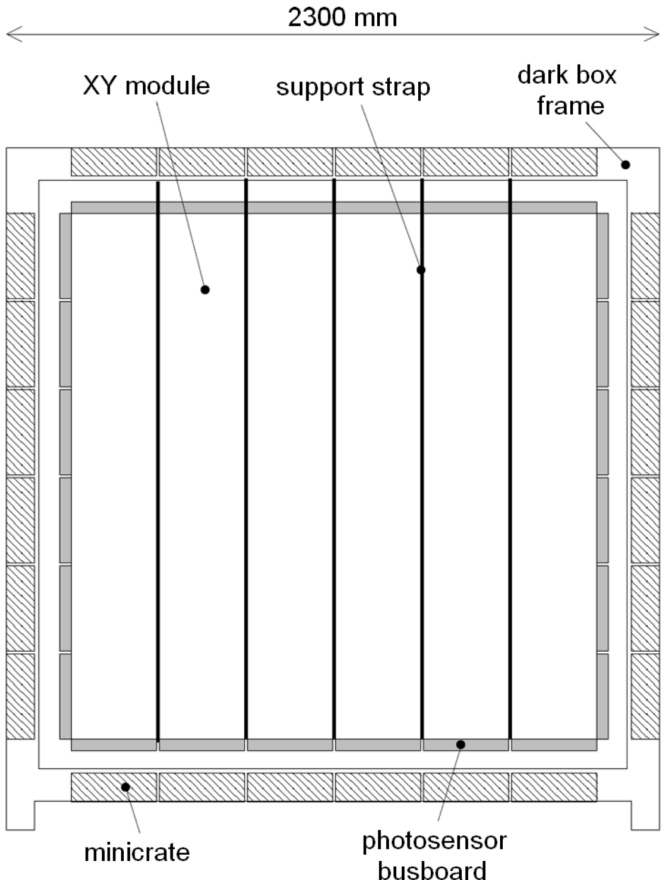

FIGURE 3.15: Cross-section view of FGD1, showing the locations of the scintillator modules, photosensors, support straps, electronics minicrates, and the dark box.

FGD1 has 15 XY modules, whereas FGD2 has only seven, as it has six 2.5 cm thick water layers between XY modules. Comparing FGD1 and FGD2 event rates allows for the extraction of differences in neutrino-carbon and neutrino-oxygen cross sections. The design of scintillator bars allows for a three-dimensional reconstruction of the track trajectory and vertex. However, when the event particle exits the tracking volume at a large angle relative to the beam direction, it may traverse only a small number of scintillator bars, sometimes only one, and the reconstruction accuracy of ND280 consequently degrades.

FGDs also play a role in particle identification, especially when the track stops in FGD and no TPC information is available. Charged particles lose energy when they pass through materials at different rates. The energy loss summed over the bars of a particle can be used to discriminate against different particle types. In practice, the energy loss rate is compared to different hypothetical particles, and the probability of the track being each hypothetical particle is calculated accordingly [87].

Fulfilling their desgin goals, the FGDs served as the primary neutrino interaction target in all T2K oscillation analyses so far until run 11. It performs well in reconstructing charged-current neutrino interaction vertices. However, reconstructing neutrons remains challenging.

3.3.5 Time projection chamber

The Time Projection Chambers (TPCs) in ND280 serve three functions: checking the curvature of charged particles in a magnetic field to determine their momenta, reconstructing charged particle tracks in three dimensions, and aiding in particle identification by monitoring the amount of ionization produced by traversing particles.

Three identical TPCs are located in the tracker volume, double-sandwiching the two FGDs. TPC1 is between the P0D and FGD1, TPC2 is between FGD1 and FGD2, and TPC3 is downstream of FGD2. Each TPC consists of a copper inner box that confines argon-based drift gas, which is divided into two parts by a central cathode. The inner box is fitted into an outer box that holds CO_2 gas for insulation. Both boxes are made from composite materials with a copper-clad coating. The inner cage has an 11.5-mm copper-strip pattern, with the electric voltage carefully set on each strip to create a uniform electric field in the same direction as the magnetic field between the cage wall and central cathode [88].

A schematic drawing of a ND280 TPC is shown in Fig. 3.16, and a photograph taken by the author of this thesis from the P0D side can be found in Fig. 3.17.

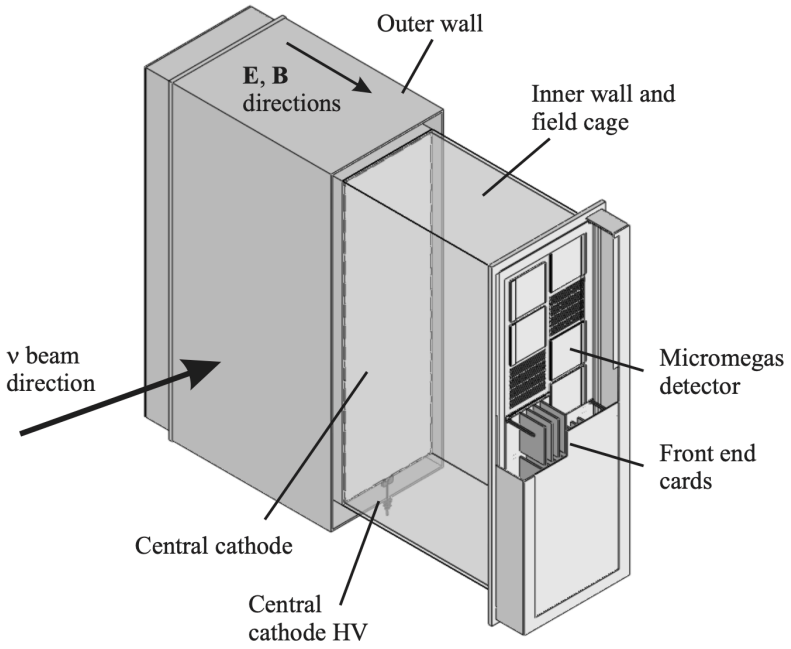

FIGURE 3.16: A schematic drawing of ND280 time projection chamber design. This figures is adapted from [88].

Each TPC is linked to two readout planes that are mounted on the inner cage wall. There are twelve 342× 359 mm^2 Micro-Pattern Gas Detectors (MicroMegas), which are finely segmented anode pads, in each readout plane. Each MicroMegas has 48 × 36 anode pads read out by printed circuits boards, allowing for precise reconstruction of charged particle tracks [88].

The TPCs fulfilled their design goals by providing the primary tracking capability for all T2K runs to date. Prior to the introduction of the 4π selection, it was necessary for all muon tracks to leave at least 18 TPC hits. With the implementation of the 4π selection, tracks with fewer than 18 TPC hits are now included in the high-angle samples of the oscillation analysis for the first time in T2K's history.

3.3.6 Electromagnetic calorimeter

The ND280 electromagnetic calorimeter (ECal) surrounds the tracker volume in a nearly hermetic manner and supplements the tracker in event reconstruction [89]. It measures the energy and direction of photon showers and distinguishes electrons, muons, and pions

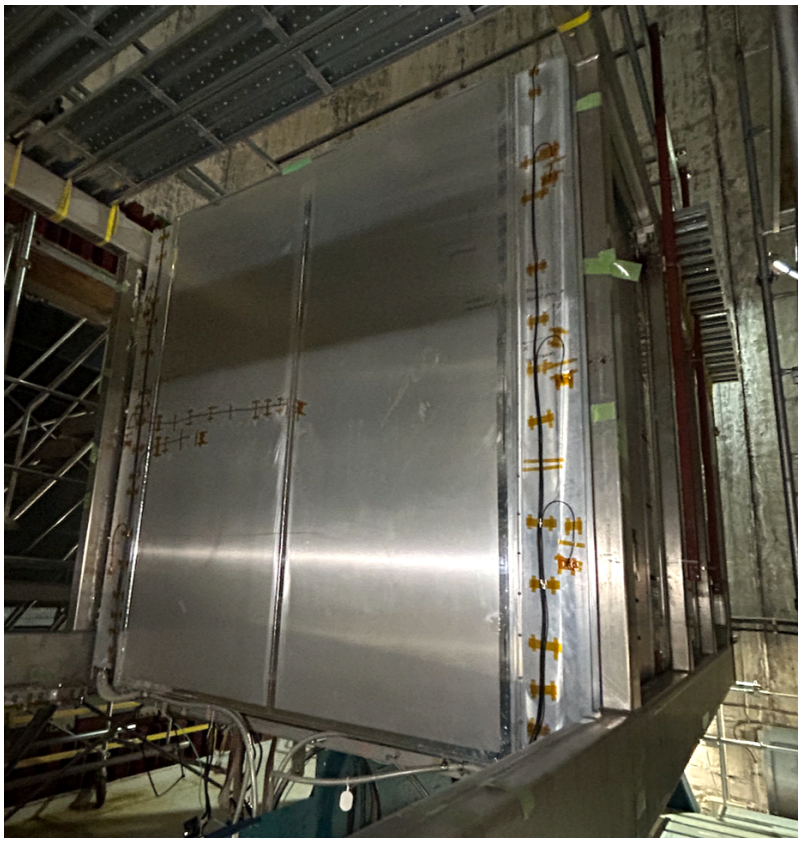

FIGURE 3.17: A photo of TPC1 taken from the upstream side, after the P0D had been removed.

based on shower shape. Its primary function is to identify and reconstruct π^0s from the tracker volume [90]. The ECal system also measures the photon momentum and detects charged particles leaving the trackers.

Similar to other ND280 scintillator detectors, the T2K ECals are built with layers of active scintillator bars threaded with a WLS fiber through a central hole, which is read on both ends by MPPCs connected to TFBs. Interleaved between the scintillator bars are lead absorber sheets.

The ND280 ECal comprises three parts: the P0D ECal, the Barrel ECal (BrECal), and the Downstream ECal (DsECal). The P0D ECal and Barrel ECal each have six modules, two vertical and four horizontal, while the downstream ECal has only one, bringing the total number to 13. The placement of the ECal modules is shown in Fig. 3.9. The downstream ECal sits in the basket after TPC3, while the P0D ECal and Barrel ECal are installed between the magnet and the basket.

All modules are built with scintillator-bar-made planes, although the design varies across modules. For instance, the top barrel ECal module is shown in Fig. 3.18.

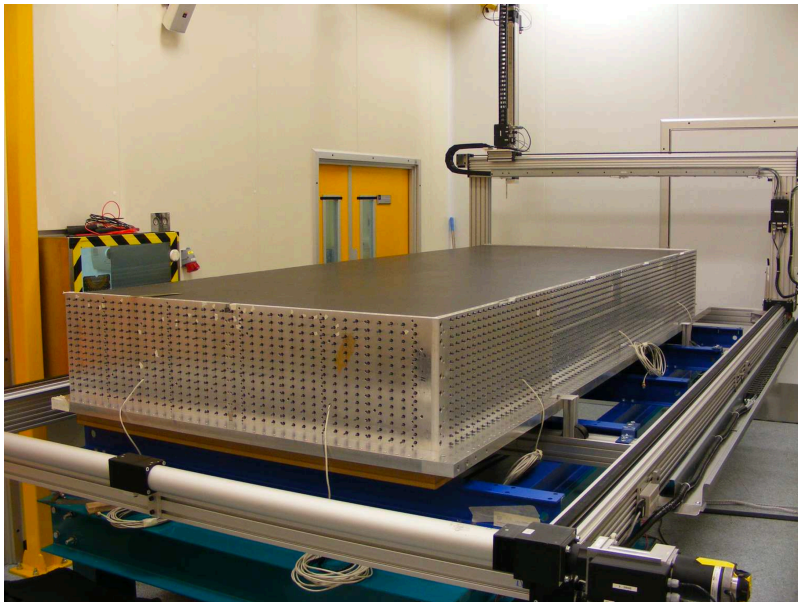

FIGURE 3.18: A 1.5×4 m^2 top ECal module under construction [5].

The P0D ECal is primarily responsible for detecting particles leaving the P0D. It can distinguish between tracks produced by minimal ionising particles such as muons or pions, and showers produced by lighter particles such as photons and electrons. To achieve this, there are two P0D ECal modules on top, two on the side, and two more under the ND280 basket's bottom, which allows for splitting when the magnet is open. Each P0D ECal module consists of six layers of scintillator bars arranged parallel to the beam axis. The lead sheets placed between the scintillator layers are 4.0 mm thick, providing a thickness of 4.3 electron radiation lengths (X_0) per layer. To fulfill their track and shower reconstruction purposes, the barrel and downstream ECal modules have more layers of scintillator bars than the P0D ECal: 31 layers in a barrel ECal module and 34 layers in a downstream ECal module. This allows thinner lead sheets (1.75 mm) to be used between scintillator bar layers while still providing enough X_0. The downstream ECal is $10.6X_0$, while the barrel ECal is $9.7X_0$. The downstream and barrel ECal scintillator bars, like in FGDs, are interleaved into layers, with bars in one layer perpendicular to the neighbouring layer. The barrel ECal layers are parallel with the beam axis, and the downstream ECal layers are perpendicular to it.

All ECal bars are read out by MPPCs from both ends with the only exception being the bars perpendicular to the beam direction, which is mirrored on one end and readout on another. A cable connects each MPPC to a TFB, which are mounted on cooling panels installed on the ECal module bulk head [90].

The ECal system is crucial in the reconstruction of neutral particles and plays a vital role in the identification of charged particles in all T2K runs and analyses conducted so far.

3.3.7 Side muon range detector

The Side Muon Range Detector (SMRD) system serves three functions: measuring the momentum of muons escaping the tracker volume at a high angle, acting as a cosmic ray trigger to prevent cosmic-muon events from being recorded, and identifying events occurring outside of the fiducial volume [91].

The former UA1 magnet comprises 16 flux return yokes, each consisting of 16 iron plates placed at an even distance of 17 mm from the next one. This configuration provides 15 available slits for inserting SMRD modules, with most yokes only having the three innermost slits occupied by SMRD modules. However, in yokes 6, 7, and 8, additional modules are installed to enhance the detection of particles leaving sideways. In total, the SMRD consists of 192 horizontally placed modules and 248 vertically placed modules.

Similar to the FGDs and the P0D, the active module of the SMRD is made up of plastic scintillators. Each SMRD module consists of several scintillator slabs, each of which is designed to match the size of the slits. A horizontal module comprises four slabs with dimensions of $7 \times 167 \times 875$ mm^3, while a vertical module consists of five counters with dimensions of $7 \times 175 \times 875$ mm^3. As the slabs are much wider than the bars used in FGDs or ECal modules, achieving a uniform response to signals across the surface of the counter requires a different approach. Instead of a straight hole down the middle, the WLS is threaded through a serpentine-shaped groove milled on the upper surface of the slab.

A picture of a single SMRD scintillator counter is shown in Fig. 3.19. The WLS is mirrored at one end, and read out by a MPPC on another.

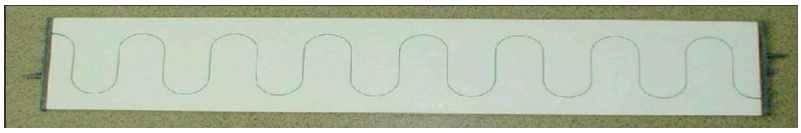

FIGURE 3.19: Photo of a ND280 SMRD scintillator counter. Unlike in other ND280 subdetectors, the WLS runs throguh the scintillator in a serpentine manner. A vertical scintillator has five such counters, and a horizontal has four.

The primary objective of the SMRD is to measure the momenta of muons generated in neutrino interactions and escaping the inner detectors at large angles relative to the neutrino beam. The 4π sample will for the first time in T2K history bring the SMRD components of reconstructed track into an oscillation analysis.

3.4 WAGASCI and BabyMIND

The main target mass provider of ND280, the fine-grained detectors, use either carbon in the scintillator bars or oxygen in the case of water as the target nuclei, whereas the SK far detector only uses oxygen. This difference in target nuclei requires a complex extrapolation of neutrino-nucleus interaction models and is a significant source of uncertainty in the oscillation study due to the differing characteristics of the nuclei. To address this issue, the T2K near-detector suite has recently added the WAter-Grid-And-SCIntillator detector (WAGASCI) [92] and a Magnetised Iron Neutrino Detector (BabyMIND) [93]. These detectors are located 1.5° away from the beam axis between INGRID and ND280, which enables T2K to explore a wider range of neutrino energies. A drawing of the WAGASCI and BabyMIND detector is shown in Fig. 3.20, and a photo can be found in Fig. 3.21.

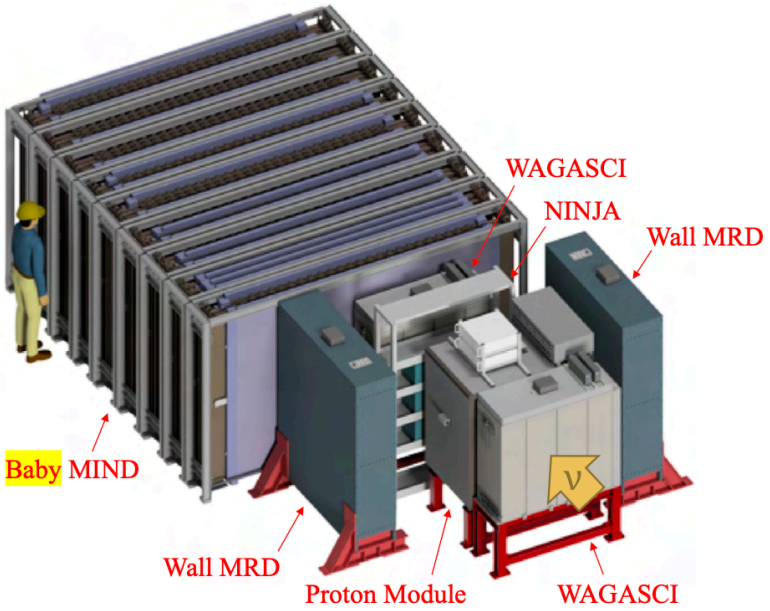

FIGURE 3.20: A schematic drawing of T2K WAGASCI and Baby-MIND detectors. WAGASCI is placed upstream, and BabyMIND is placed immediately downstream [92]. The NINJA detector in this drawing is not a part of T2K.

3.4.1 WAGASCI

The WAter-Grid-And-SCIntillator detector (WAGASCI) target water modules feature a 3D grid structure composed of thin scintillator bars, with water filling the cells between the bars. This design maximises the target material to total mass ratio in the modules, while also providing sufficient resolution for tracking particles. The hydrocarbon module was previously INGRID's proton module and is made up of scintillator planes surrounded by veto planes, similar to the INGRID modules. This module uses scintillator bars narrower than the INGRID modules to help track reconstruction. The vertical bars are $0.7 \times 21 \times 195$ cm^3 in dimension, and the horizontal ones are $0.7 \times 3 \times 288$ cm^3. The WAGASCI detector is equipped with Wall Muon Range Detectors (Wall-MRDs) on both sides of the core water and scintillator modules. These Wall-MRDs consist of alternating layers of magnetised iron and scintillator, enabling the identification and measurement of muon momenta. Placing the Wall-MRDs at a short distance from the target grid also allows for time-of-flight measurements.

3.4.2 BabyMIND

Immediately downstream of WAGASCI is the Baby Magnetised Iron Neutrino Detector (BabyMIND) detector [93, 94]. BabyMIND is a muon spectrometer dedicated to measure the momentum and charge of muons leaving WAGASCI target volume to a good precision. It consists of 33 magnetised iron plates and 18 scintillator planes. Early runs shows 97% POT collection efficiency and good muon momentum resolution in the range of $300 - 500$ MeV [94]. A photo of BabyMIND is shown in Fig. 3.21.

FIGURE 3.21: A photo of WAGASCI and BabyMIND taken by the author.

3.5 Super-Kamiokande as T2K far detector

The Super-Kamiokande (SK) detector serves as T2K's far detector to measure the flavour and momenta of T2K beam neutrinos that interact via charged-current neutrino-nuclei interactions. The measurements are then compared with predictions built from ND280

measurements to infer neutrino oscillation parameters. Situated at 295 km west of the J-PARC facility in the Hida prefecture, and 2.5° off the T2K beam axis, SK is a large water-Cherenkov detector situated in the Kamioka mine 1 km underground to suppress natural background from cosmic rays.

The Super-Kamiokande experiment itself was dedicated to measure neutrino flux from the sun and those produced by cosmic rays in the upper atmosphere. It has delivered competitive constraints on solar neutrino parameters, and also leads the measurement of proton decays since it started taking data in 1996 [85, 95, 96]. SK is also a part of the supernova early warning system [97].

Water-Cherenkov detectors are designed based on the fact that when a charged particle traverses a medium at a higher speed than the speed of light in that medium, the particle loses energy via emitting photons sideways at angle $\phi = \arccos \frac{c}{v\eta}$, where c is the speed of light in vaccum, v is the speed of the particle, and η is the index of refraction of the medium. For water, $\eta = 1.33$ [98]. c/η gives the speed of light in the medium. Cherenkov radiation is induced by charged particles polarising particles in the medium via electromagnetic interactions. The medium's particles de-excite by emitting photons in a cone pattern, which leaves a ring-shape image on the wall-mounted detectors. For a charged particle travelling slower than the speed of light, it still excites particles, but the emitted photons do not form a cone, and hence no ring in the detectors. A sketch of such radiation is shown in Fig. 3.22.

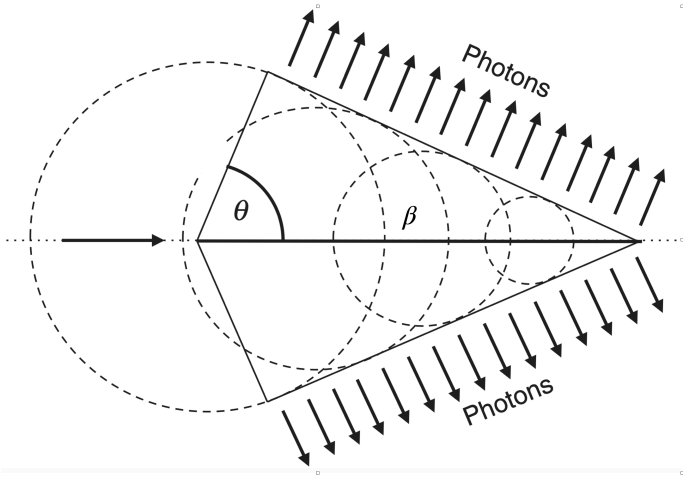

FIGURE 3.22: A schematic drawing of Cherenkov radiation. The particle travels in the medium from left to right at a higher speed than light, creating a cone of photons. This figure is from [55].

SK is a cylindrical water-Cherenkov detector with a radius of 19.4 m and a height of 41.2 m, containing 50,000 tonnes of ultra-pure water. The detector consists of two parts, the inner detector and the outer detector separated by a stainless steel cylinder with light-blocking black plastic coating. The outer detector has 1,885 Photon Multiplier Tubes (PMTs), each is 20 cm in diameter and is attached to wavelength-shifting planes, to detect and veto external background from entering the inner volume. The PMTs cover only 7% of the outer surface of the detector, but are capable of rejecting cosmic ray muons at close to 100% efficiency [85]. The inner detector has 11,129 inward-facing 50-cm PMTs instrumented on the walls and ceiling of the detector cylinder, which has a photo-coverage of over 40% of the inner surface, to detect Cherenkov radiation photons emitted by charged leptons produced in neutrino-water charged-current interactions.

The mass of a electron is only 511 keV [75]; hence, their trajectories are easily deflected by other particles along the path. The muon mass is over 100 MeV, meaning they have much greater inertia than electrons, and their trajectories are seldom affected by scattering off water molecules. such that the Cherenkov rings produced by electrons are usually less well-defined than those that are produced by muons, enabling particle identification by the fuzziness of the Cherenkov rings. Examples of an electron ring and a muon ring are shown in Fig. 3.23.

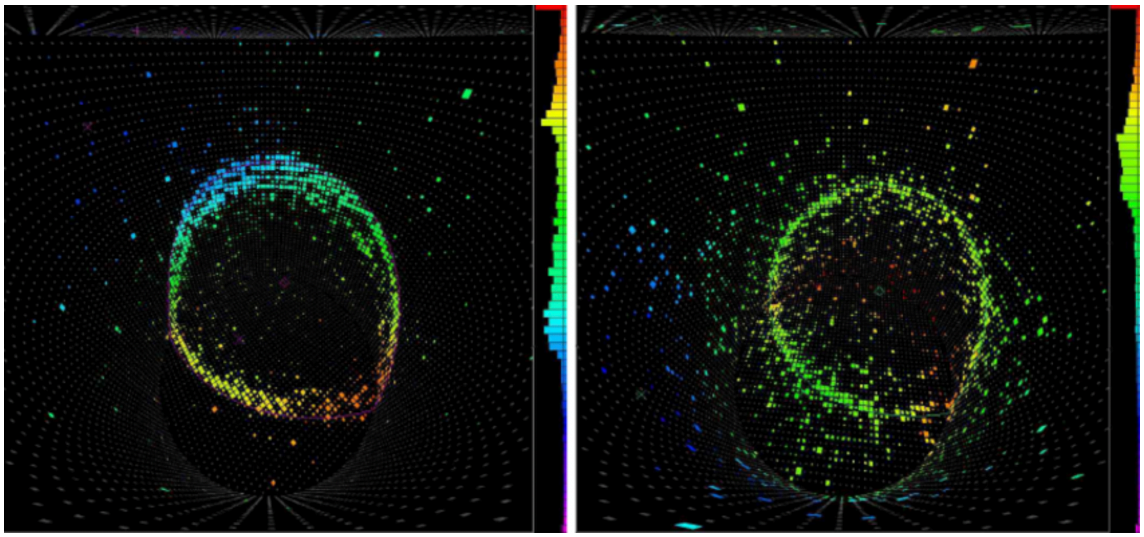

FIGURE 3.23: Left: a simulated SK reconstructed event identified as a muon. Right: a simulated SK event identified as an electron. Each colourful dot represents a inner detector PMT; the more photon the PMT collects, the warmer it colour appears. A muon-like event usually has a clearly defined ring, while in the electron-like event the ring is much more blurred. This figure is adapted from [96].

T2K beam neutrinos are in a state containing a non-zero ν_τ component when they reach SK, but the T2K neutrino energy spectrum peaks at 0.6 GeV, which is below the τ mass of 1.7 GeV. Hence, it is rare for the neutrino to bear enough energy to create an on-shell tauon in the final state. It is even harder for tauons to top the speed of light to produce Cherenkov rings, which would require even more energy. Tauons are also very short-lived with a half-life of 3×10^{-13} s and decay weakly into other charged particles including pions (58%), muons(17%) and electrons(17%) [75], making it nearly impossible to identify tauons at SK.

Since there is no magnet in SK, particle charges cannot be identified using the curvature of their trajectory; that is, the incident e^+ from an incoming $\bar{\nu}_e$ charged-current interaction cannot be separated from a e^- produced in a ν_e interaction. To be able to determine the charge, SK doped its ultra-pure water with gadolinium sulphate in 2020 [96], which will increase its neutron capture rate to up to 90%. An ^{155}Gd atom captures two neutrons to become a ^{157}Gd atom, and subsequently decays and emits detectable photons. Such a process is only possible for anti-neutrinos which produces neutrons in charged-current interactions. Neutrinos produce protons instead which cannot be captured by ^{155}Gd.

The main background at SK are pions and neutrons. As introduced in Sec. 2, neutrinos can also interact with atoms via neutral-current interactions by the exchange of a Z^0 boson. The incident neutrino does not turn into a charged lepton; hence, it is impossible to detect it or know its flavour. On the other hand, just like in charged-current interactions, the nuclei can still be excited and then de-excite by emitting hadrons in a resonant process, and the majority of such emissions are neutral pions, the decay product of which is hard to tell from electrons [85]. Therefore, the neutral current events are regarded as a background in T2K ν_e appearance analyses, and the ND280 P0D detector was built to study such processes in order to understand relevant systematic uncertainties.

Chapter 4

Time-of-flight correction for run8 MC

The Time-of-Flight (ToF) information is critical in creating the ND280 4π sample selection. However, during the run 8 ND280 data collection, a hardware issue caused a substantial discrepancy between the data and MC simulations in the ToF distribution [99]. To address this issue, the author of this thesis developed a two-step correction method based on existing corrections, which successfully reduced the discrepancy to an acceptable level.

Although the new correction method addressed the initial discrepancy, it introduced a source of systematic error. The author evaluated and quantified this error, which was then incorporated into the ND280 analysis software. This chapter provides a detailed description of the discrepancy's source, the development of the correction method, and the quantification of the induced systematic uncertainty. The run 8 information can now be used for any analysis, not just the one presented in this thesis.

4.1 Introduction

The ND280 reconstruction algorithm determines particle trajectories based on the charge and energy deposited in subdetectors, providing useful information for track geometry. However, determining the track's starting end is less efficient, particularly when the charge carried by the particle is unknown. When a track traverses two subdetectors, it is often easier to determine the track's direction using the time the particle spent traveling between them, or the Time-of-Flight ToF. Previous studies have proposed an algorithm that determines track direction using ToF information [54, 100].

This chapter is organised as follows: the next section defines ToF variables that will be used in the flipping algorithm, and the corrections applied to them. Sec. 4.3 describes briefly the data-MC discrepancy that necessitated the correction developed in this thesis. Sec. 4.4 details the design of the correction, and how the numbers are evaluated for. Finally, Sec. 4.5 explains the flipping algorithm, supplemented by Table. 4.2 that summarises all the flipping and correction values.

4.2 Time of flight at ND280

This section details how time of flight is defined between ND280 subdectors, how it is calibrated, and the run 8 data-MC discrepancy.

4.2.1 Time mark of ND280 subdetectors

Only the differnce of time is a measurable physical quantity. At ND280, time information is primarily obtained from hit time stamps, which are recorded when a hit is detected by the readout electronics. A single track usually passes through multiple subdetectors at ND280, and leaves multiple hits with corresponding time stamps in a single subdetector. It is necessary to combine time stamps from each subdetector module to create a "time mark" for that module. The travel time between subdetectors can then be determined by taking the difference between time marks from different subdetectors.

To construct the time mark for each subdetector module, a 3D linear function, or straight line, is fitted to the coordinates of all hits. This allows all hits to be utilised in the construction of the time mark.

$$\begin{aligned} x &= x_0 + t \times k_x \\ y &= y_0 + t \times k_y \\ z &= z_0 + t \times k_z \end{aligned} \tag{4.1}$$

where k_x, k_y and k_z are the slopes in three dimensions, and x_0, y_0, z_0 their intercepts. Next, this parametric function in Eq. 4.1 is evaluated at the coordinate of the first hit, X_1, to obtain T_1, and again at the coordinate of the final hit, X_2, to obtain T_2. The time

mark for a subdetector in ND280, $T_{\text{Subdetector}}$, is defined as [54]:

$$T_{\text{Subdetector}} \equiv \frac{T_1 + T_2}{2}. \tag{4.2}$$

Other options for the time mark have also been explored along the process of development, including the average of all time stamps in the subdetector, or simply T_1. It was found in sand muon control samples that the definition adopted by this thesis yields the samllest tail and RMS [100].

The definition of ToF between two subdetectors, for instance FGD2 and DsECal, is subsequently

$$\text{ToF}_{\text{FGD2-DsECal}} = T_{\text{DsECal}} - T_{\text{FGD2}} \tag{4.3}$$

This is the inter-subdetector ToF difference, later refered to as ToF value, or simply ToF for short, used in this thesis to estimate the direction of a track, and to which corrections are applied.

4.2.2 Calibration corrections

Before any high-level corrections are applied, two hardware calibration corrections are applied to the time stamps that are used to construct the time marks, which subsequently determines the inter-subdetector ToFs:

- *Light propagation time inside detectors and optical fibres*
  To correct for this effect, the distance the signal travels from the point of incident to the readout panel i.e. the distance it travels inside the WLS, is divided by the speed of light c, and the resulting ratio is subtracted from the time stamps.

- *Timing offset of subdetector SCMs*
  The timing offset of each subdetector's Secondary Clock Module SCM can be computed using a control sample of sand muons that pass through all subdetectors from the upstream direction. Assuming that all particles travel at the speed of light, the expected arrival time of these muons can be calculated for each subdetector (i.e., P0D, TPC, FGD, and DsECal). The offset for each subdetector's SCM is then determined by taking the difference between the expected arrival time and the measured data, which is corrected for light propagation. This process provides an

evaluated offset for each subdetector. Finally, the evaluated offset is applied to the time marks to ensure that the timing information is accurately synchronized across all subdetectors.

4.2.3 ToF topologies

After defining the inter-subdetector ToFs and applying low-level corrections, the ToFs are then used to re-evaluate the tracks' senses on a sub-detector pair basis, i.e. ToF topologies. This study considers a total of 24 such ToF topologies, all listed in Table 4.1.

It is worth mentioning not all possible subdetector pairs are included in the ToF sense check, as Table 4.1 shows. It only includes tracks that start in one of the FGDs and end in a non-TPC subdetector. The non-TPC subdetector is typically one of the ECal regions (ECal or DsECal), but not the P0D ECal. Additionally, subdetector pairs that are too far apart, such as FGD1-DsECal, have also been excluded due to low statistis and overlapping with other ToF topologies.

Table 4.1 lists various topologies, all of which involve at least one FGD and typically an ECal module. However, there are two special cases that don't involve an ECal: FGD1 to P0D, and FGD1 to FGD2. To categorise the subdetector pairs, the algorithm first separates them based on whether they start or end in the FGDs. Tracks that originates in the ECal and ends in the FGD have their own category. For FGD1-FGD2 tracks, if the track originates from FGD1, it belongs to the FGD1 to FGD2 topology regardless of whether it stops in FGD2 or not. If the track has time marks for both FGD1 and FGD2, but doesn't originate from FGD1, it will be classified under a special topology called FGD2 to FGD1.

Each subdetector pair involving an FGD and an ECal or P0D module is further divided into two categories: "track-like" and "shower-like". A track-like signal is defined as having more than one node in the non-FGD detector, while a shower-like signal leaves exactly one node. A note is a group of hits clustered together. However, please note that this definition does not apply to FGD1-FGD2 tracks, which can have any number of nodes.

FGD to BrECal ToF topologies are split into high-angle and low-angle. Similar to the 'high-angle' in the sample selection, here, a track being "high-angle" means that it has 18

or less TPC hits. On top of that, it is also required that the non-FGD end of the track lies either in the barrel ECal or in the SMRD.

Topology name	Starting	Finishing	hits non-FGD	hits TPC
FGD1-ECal Track	FGD1	BrECal	> 1	>18
FGD1-ECal Shower	FGD1	BrECal	1	>18
FGD1-DsECal Track	FGD1	DsECal	> 1	>18
FGD1-DsECal Shower	FGD1	DsECal	1	>18
P0D-FGD1 Track	P0D	FGD1	> 1	>18
P0D-FGD1 Shower	P0D	FGD1	1	>18
ECal-FGD1 Track	BrECal	FGD1	> 1	>18
ECal-FGD1 Shower	BrECal	FGD1	> 1	$\leq$18
FGD1-ECal high-angle Track	FGD1	BrECal	> 1	<=18
FGD1-ECal high-angle Shower	FGD1	BrECal	1	<=18
ECal-FGD1 high-angle Track	BrECal	FGD1	> 1	<=18
ECal-FGD1 high-angle Shower	BrECal	FGD1	1	<=18
FGD2-ECal Track	FGD2	BrECal	> 1	>18
FGD2-ECal Shower	FGD2	BrECal	1	>18
FGD2-DsECal Track	FGD2	DsECal	> 1	>18
FGD2-DsECal Shower	FGD2	DsECal	1	>18
ECal-FGD2 Track	BrECal	FGD2	> 1	>18
ECal-FGD2 Shower	BrECal	FGD2	> 1	>18
FGD2-ECal high-angle Track	FGD2	BrECal	> 1	<=18
FGD2-ECal high-angle Shower	FGD2	BrECal	1	<=18
ECal-FGD2 high-angle Track	BrECal	FGD2	> 1	<=18
ECal-FGD2 high-angle Shower	BrECal	FGD2	1	<=18
FGD1-FGD2	FGD1	FGD2	N/A	>18
FGD2-FGD1	FGD2	FGD1	N/A	>18

TABLE 4.1: List of all ToF topologies considered in this thesis. In this study, a total of 24 ToF topologies are included.

4.2.4 Gaussian correction

In previous studies [54, 101], MC track ToF values were smeared to reduce data-MC discrepancies. For a given ToF topology, the distribution of events' ToF values was assumed to be double-Gaussian-like, consisting of two Gaussian distributions: one for true forward-going tracks i.e those with corrected reconstruced sense, labeled with a plus sign +, and another for true backward-going tracks i.e. those with wrong reconstructed sense, labeled with a minus sign −. Mathematically, this can be written as:

$$\rho(t) = N^{+} \times n(t : \sigma_{+}, \mu_{+}) + N^{-} \times n(t : \sigma_{-}, \mu_{-}) \tag{4.4}$$

where t is the event's ToF; $\rho(t)$ is its event number density function; $N^{\pm}$ is the number of tracks in all events that belong to this ToF topology and are truly forward or backward; $n(t : \sigma_{\pm}, \mu_{\pm})$ is the Guassian probability density functions of true forward and backward functions in this ToF topology, centered at $\mu_{\pm}$ with a standard deviation of $\sigma_{\pm}$ respectively.

For each ToF topology, separate fits are performed for the double-Gaussian model using data and MC, respectively, yielding eight parameters: $\sigma_{\pm}^{\text{data, MC}}$ and $\mu_{\pm}^{\text{data, MC}}$ for both the forward (+) and backward (−) going tracks.

In order to correct the MC to match data, we then determine the distribution of the correction using the following expression:

$$\mu_{\pm}^{\text{corr}} = \mu_{\pm}^{\text{data}} - \mu_{\pm}^{\text{MC}}, \quad \sigma_{\pm}^{\text{corr}} = \sqrt{(\sigma_{\pm}^{\text{data}})^2 - (\sigma_{\pm}^{\text{MC}})^2} \tag{4.5}$$

During the study no case in which $(\sigma_{\pm}^{\text{data}})^2 < (\sigma_{\pm}^{\text{MC}})^2$ was found. Should there be any in future studies, a σ^{corr} value of 0 will be applied. The final expression of the correction for the X-Y topology is

$$T_{\text{X-Y}}^{\text{Corrected}} = T_{X-Y}^{\text{Nominal}} + C_{\text{X-Y}} \tag{4.6}$$

where C is the correction term generated from a normal distribution of parameters (μ_{+}^{corr}, σ_{+}^{corr}) if truly-forward or (μ_{-}^{corr}, σ_{-}^{corr}) if truly-backward, as defined in Eq. 4.5. $T_{\text{X-Y}}^{\text{Corrected}}$ is the corrected ToF value that will be used in the following analyses, and T_{X-Y}^{Nominal} is the raw ToF value from reconstruction as defined in Eq. 4.3 with all calibrations corrections in Sec. 4.2.2 applied.

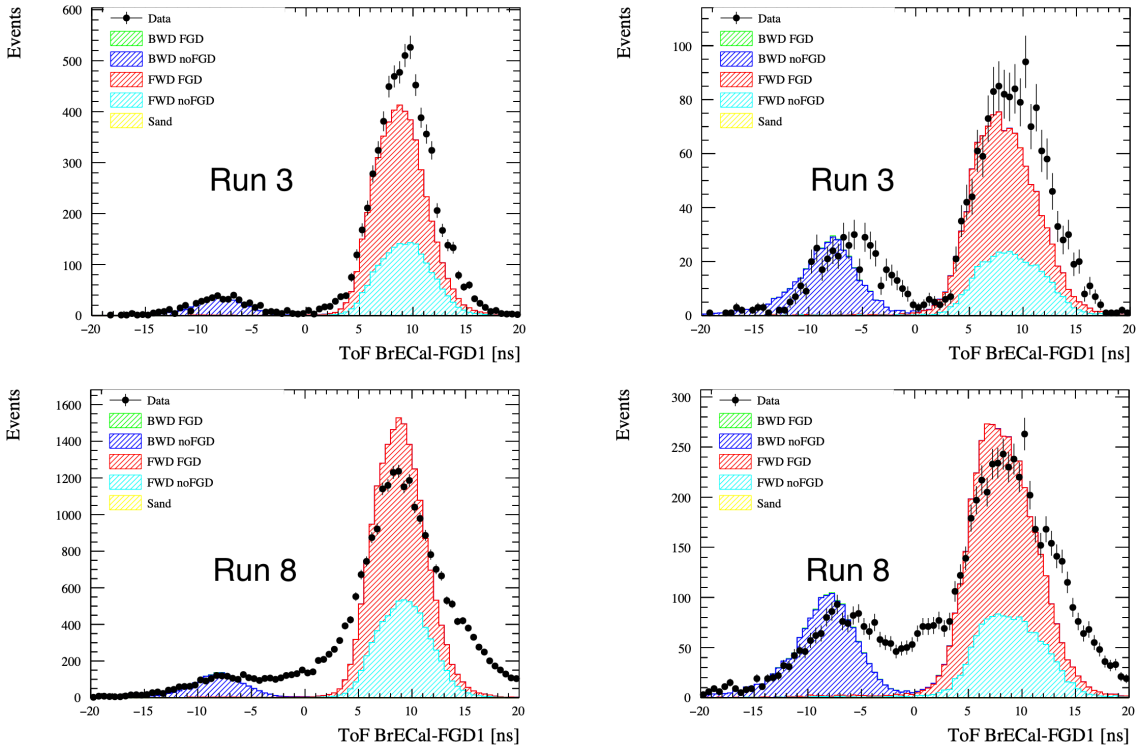

FIGURE 4.1: Run 3 and run 8 data ToF distribution for forward-going events between FGD1 and BrECal, with samples split into track-like and shower-like categories, after calibration corrections are applied. Colourful histograms are MC, while black dots are data. Top left: run 3 track-like. Top right: run 3 shower-like. Bottom left: run 8 track-like. Bottom right: run 8 shower-like.

4.3 Run 8 data-MC discrepancy

After sorting the tracks into 24 topologies and applying a Gaussian correction, it is now possible to compare the ToF distribution between MC simulation and data.

In earlier runs, the differences between the MC and data distributions were generally small. For example, in run3 (as shown in the top row of Fig. 4.1), the comparison reveals only minor discrepancies. However, in run8, a significantly larger data-MC discrepancy than in previous runs has been observed as in the bottom row of Fig. 4.1, which necessitates a new treatment.

4.4 Joint Gaussian - timeslip correction

To conduct a ToF-related study using run 8 data, the first step is to establish a reliable MC and a good understanding of the systematic uncertainties.

However, the ToF data distribution in run 8 differed significantly from the nominal MC expectation. To address this issue, the specific problem in run 8 needed to be identified, and a correction applied to the MC to account for this effect.

The traditional Gaussian-smearing correction, outlined in Sec. 4.2.4, was found to be insufficient [99]. A new hardware connection issue was identified as the potential source of the data-MC discrepancy, and a new correction was developed based on this discovery, in conjunction with the traditional Gaussian-smearing correction. This new approach successfully reduced the discrepancy to a similar level as in previous runs.

This section covers the hardware issue, the design of the correction, and the evaluation of correction parameters. The systematic error induced by this correction is discussed in Chapter 6, where all relevant systematic sources are addressed.

4.4.1 Physical motivation

During the control-sample calibration of Readout Merger Modules (RMMs), random time shifts of approximately ± 10 ns were observed, possibly due to an unstable connection between SCMs and RMMs. The SCMs and RMMs are connected using Xilinx RocketIO transceivers with a phase-lock loop frequency of 100 MHz. When the connection between TFBs and their SCMs is established, the timing between them can be shifted by up to 10 ns [99]. Such a 10 ns shift is commonly referred to as a 'time slip'. To emulate this effect and improve the accuracy of MC simulations, a ±10 ns shift is randomly applied to some events, which is called the time slip correction. This correction will be discussed in more detail in the following section.

4.4.2 Timeslip correction

The time slip effect described in Sec. 4.4.1 was not considered during MC production. To cover for this effect, a correction was developed as part of this thesis, and will be covered in detail in this section.

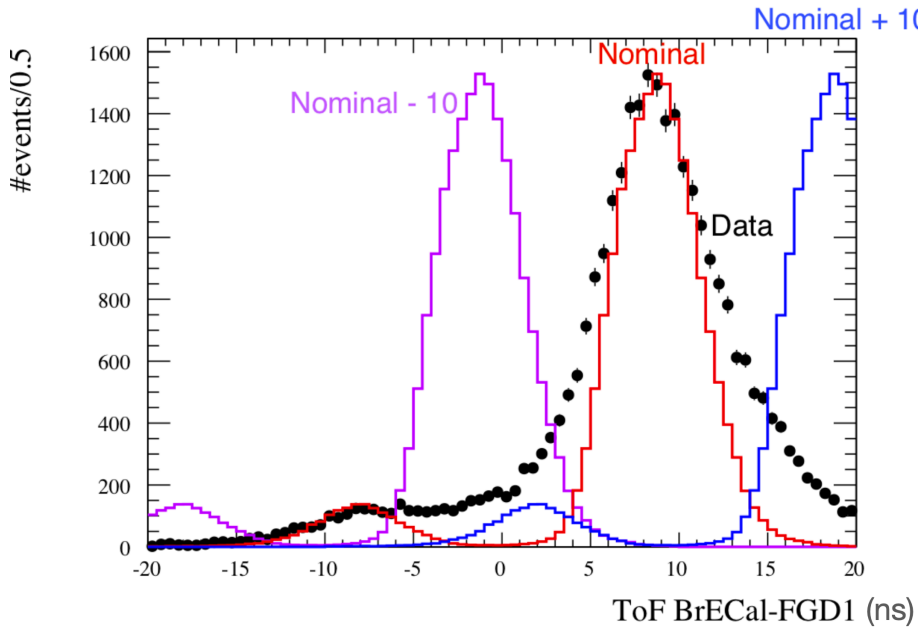

,

FIGURE 4.2: FGD1-BrECal low-angle forward topology ToF distribution in Monte Carlo for the nominal (red), and shifted (purple and blue) values. Data is given in black points. This figure is adapted from [99].

The time slips are modelled as follows: each ToF topology has a fraction f_1 of events that are affected by a +10 ns time slip, and another fraction f_2 affected by a −10 ns time slip [1] . For a ToF topology with a total of N events, it is possible to divide the events into three groups: E_0, which is not affected by any time slip and has a number of $N(1 - f_1 - f_2)$; E_1, which suffers from a +10 ns time slip and has a number of Nf_1; and E_2, which is affected by a −10 ns time slip and has a number of Nf_2. It is assumed that E_0, E_1, and E_2 all obey the same distribution.

Figure 4.2 shows E_0, E_1, and E_2 scaled to have the same area. The purple solid line represents E_2, the blue line represents E_1, and the red line represents the unaffected E_0. The corrected MC ToF distribution histogram can be obtained by stacking E_0, E_1, and E_2 together. The implementation of the model in psyche is simple: for each event with the ToF topology of interest, a random number f in $(0, 1)$ is generated from a uniform distribution. If $0 < f < f_1$, then the 10 ns is deducted from its relevant ToF value; if $f_1 < f < (f_1 + f_2)$, then 10 ns is added to its ToF value; if $(f_1 + f_2) < f < 1$ then the ToF value will not be changed. The problem now comes down to how to find values for

[1] Cases in which the time is shifted by two periods or more are found to be too rare to be worth including in the discussion.

f_1 and f_2, which will be explained in the next section.

4.4.3 Evaluation and application

Previously, the Gaussian correction parameters were evaluated using a double Gaussian fit, as described in Section 4.2.4. However, to optimise the Gaussian smearing parameters for the combined effect of both the Gaussian smearing and the time slip correction, it is necessary to re-evaluate the parameters for both the Gaussian correction and the time slip correction in a single fit. This section explains how the fit is performed for a given topology.

To correct each ToF topology using a combination of the two corrections, six independent parameters are required: two for the time slip correction (f_1 and f_2) and four for the Gaussian smearing ($\sigma_\pm$ and $\mu_\pm$). Assuming the value of σ is the same for both subdetectors, it is set that $\sigma_+ = \sigma_- = \sigma$ to reduce number of the degrees of freedom by one.

The Gaussian smearing correction is first applied to the nominal ToF distribution using the method introduced in Section 4.2.4, with parameters σ, μ_+, and μ_-. True forward tracks are corrected using σ and μ_+, while true backward tracks are corrected using σ and μ_-. Next, the time slip correction is applied to the Gaussian-smeared distribution, using f_1 and f_2. To accomplish this, the code creates two new distributions that are copies of the nominal distribution, each shifted by $+10$ and -10 ns and scaled to produce E_1 and E_2. The original distribution is scaled down by $(1 - f_1 - f_2)$ and stacked with the copy distributions to build the final corrected ToF distribution.

The goal of the fitter determines which corrected MC distribution is most similar to the data using a Pearson's binned χ^2 statistic:

$$\chi^2 = \sum_{i=1}^{N} \frac{(m_i - d_i)^2}{m_i}, \tag{4.7}$$

where m_i and d_i are the number of MC events and data events in the ith bin, respectively. N is the number of bins, in this study N=119. Across all topologies, a 119-bin uniform binning scheme is used in the building of histograms. The first bin starts at -30 ns, and the final bin ends at 29.5 ns; hence, each bin is 0.5 ns wide. The number of bins was intentionally odd to reduce numerical errors in the fitting.

The five-dimensional fitting is done in the following order: first the algorithm loops over all possible σ, $\mu_{\pm}$ in the 3D parameter space; then, at each point, the smearing correction to the nominal ToF is applied to the ToF histograms; next, the algorithm loops over f_1, f_2 using TFractionFitter [102] to find the pair that minimises χ^2 after a time slip correction has been applied according to the Gaussian-corrected ToF histogram. A flow chart showing the procedure of the whole fitting is shown in Fig. 4.3.

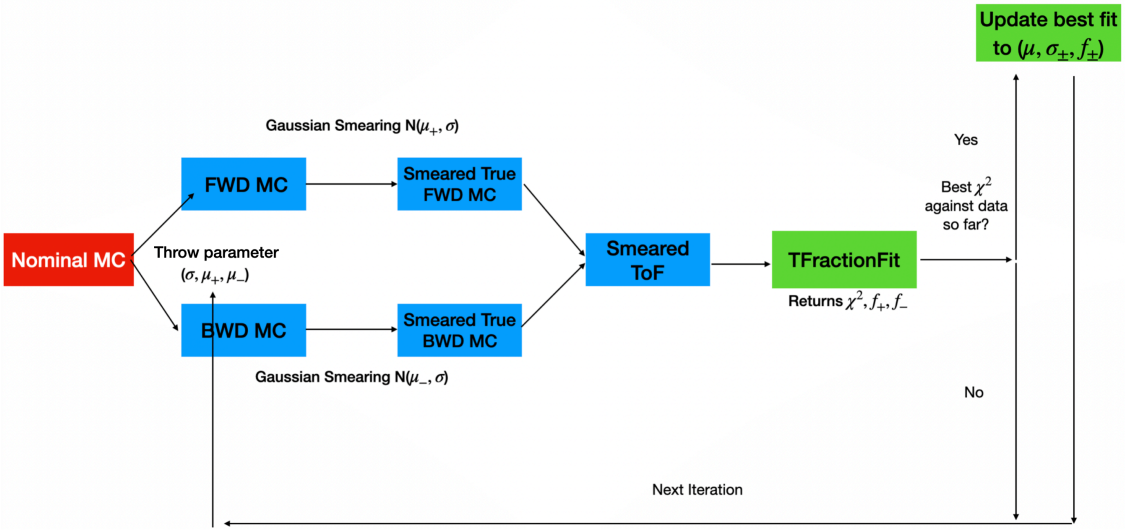

FIGURE 4.3: Flow chart detailing the program of the five-dimensional fit used in this analysis to find the best parameter for each ToF topology.

Applying Gaussian correction by convolving histograms: In principle, the canonical way to apply the Gaussian correction is event-wise, i.e. for each event, replace its raw ToF value, t_0, with

$$t = t_0 + c, \;\; c \sim N(\sigma, \mu^{\pm}) \tag{4.8}$$

where c is the correction obeying the normal distribution $N(\sigma, \mu)$, that is, the probability density function of c is

$$P(c) = \frac{1}{\sqrt{2\pi}\sigma} \exp\left(-\frac{(c-\mu)^2}{2\sigma^2}\right) \tag{4.9}$$

and rebuild the histogram using the corrected t instead of t_0. However, in the five-dimensional fit, there are three parameters for the Gaussian correction being scanned, such that applying the Gaussian correction in the event-wise way described in Eq. 4.8 is very computationally demanding. It can be shown mathematically that the sum of two normally-distributed random variables, a and b, is another normally distributed random

variable, whose probability distribution function can be obtained by convolving the two parent distributions [103]:

$$a \sim N(\sigma_a, \mu_a), b \sim N(\sigma_b, \mu_b) \tag{4.10}$$

$$\rho_a \otimes \rho_b = \rho_{a+b} \tag{4.11}$$

Hence, assuming that the ToF value distribution of forward going tracks and backward going tracks are Gaussianly distributed, it is possible to approximate the effect of a σ, μ smearing correction via the convolution of the Gaussianly distributed ToF with a Gaussian kernel generated using parameter σ, μ. Later in this section it will also be shown that the parameters obtained in this way are capable of correcting MC to a good likeness of data. The numerical convolution is done using the python numpy library [104].

Finding f_1 and f_2 using TFractionFitter: ROOT library TFractionFitter [102] is used in the second part to speed up the 5D fit. TFractionFitter is developed precisely to perform fraction fits. Assuming a target histogram is stacked by a group of sub-histograms, TFractionFitter is coded in Fortran to find the best fraction of each sub-histogram that minimises the χ^2 difference between their sum and the target histogram. The code takes a target distribution and a list of prior distributions as input, and returns the fractions of each prior distribution that will minimise the χ^2 of the stack computed against the target distribution. In this analysis, after the Gaussian correction is done using convolution, the corrected ToF distribution is translated to ± 10 ns, and these three distributions, E_0, E_1 and E_2, are used in TFractionFitter as prior inputs, with the data distribution being used as the target distribution. TFractionFitter returns the f_1, f_2 needed and its χ^2. For systematic uncertainty evaluation purposes, all f_1, f_2 and χ^2 are recorded. The $(\sigma, \mu_\pm)$ value group that has the smallest χ^2 given by the TFractionFitter, along with its f_1, f_2, is taken as the correction value for the ToF topology. For the later steps of the analysis, the rigid event-wise application of the Gaussian correction is used to create input. Examples of the effect of the joint Gaussian-Time slip correction can be seen in Fig. 4.4, 4.5, 4.6 and 4.7.

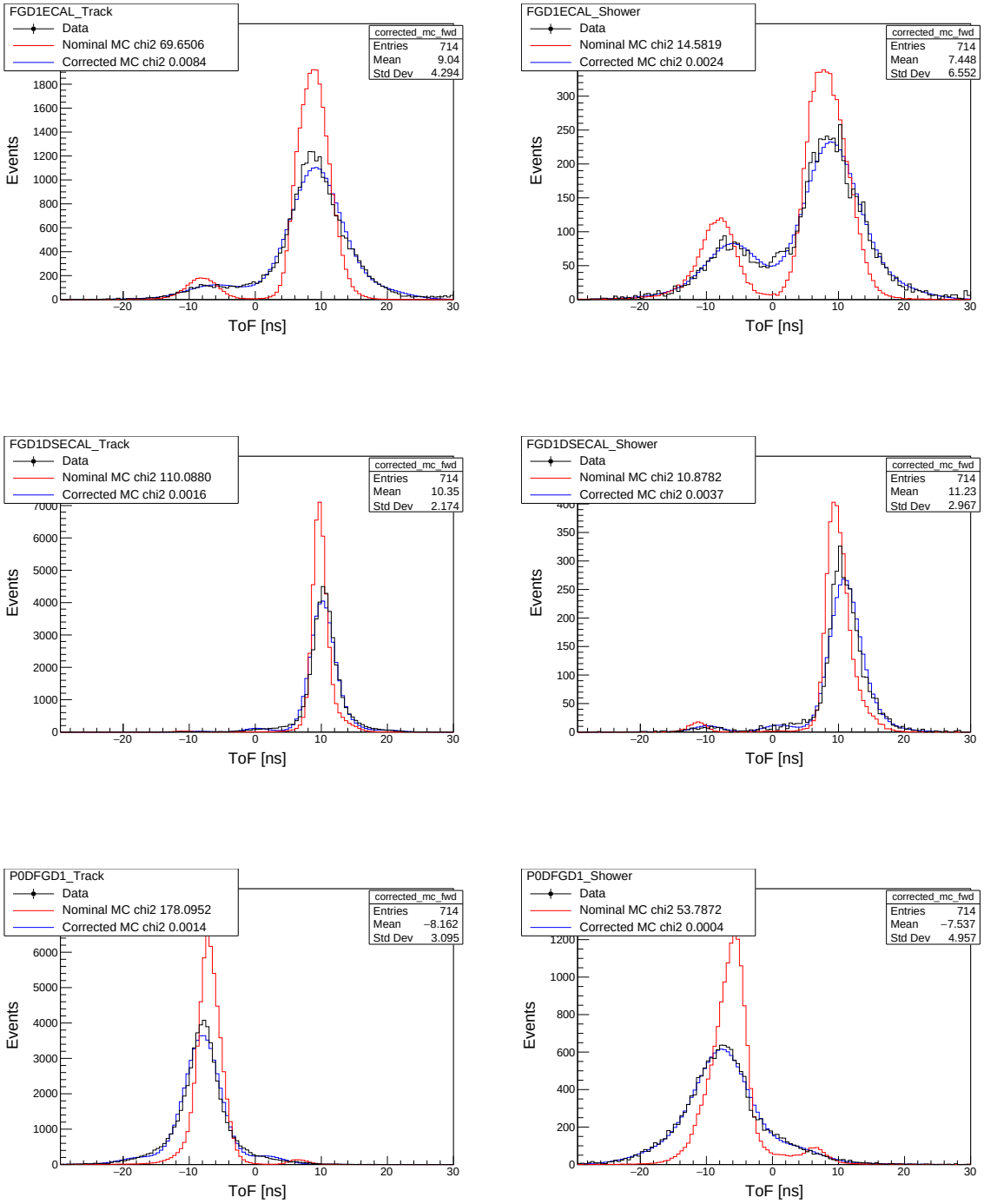

FIGURE 4.4: Corrected ToF value distributions of the first six FGD1 ToF topologies. The topologies' names are in the box at each plot's top left corner.

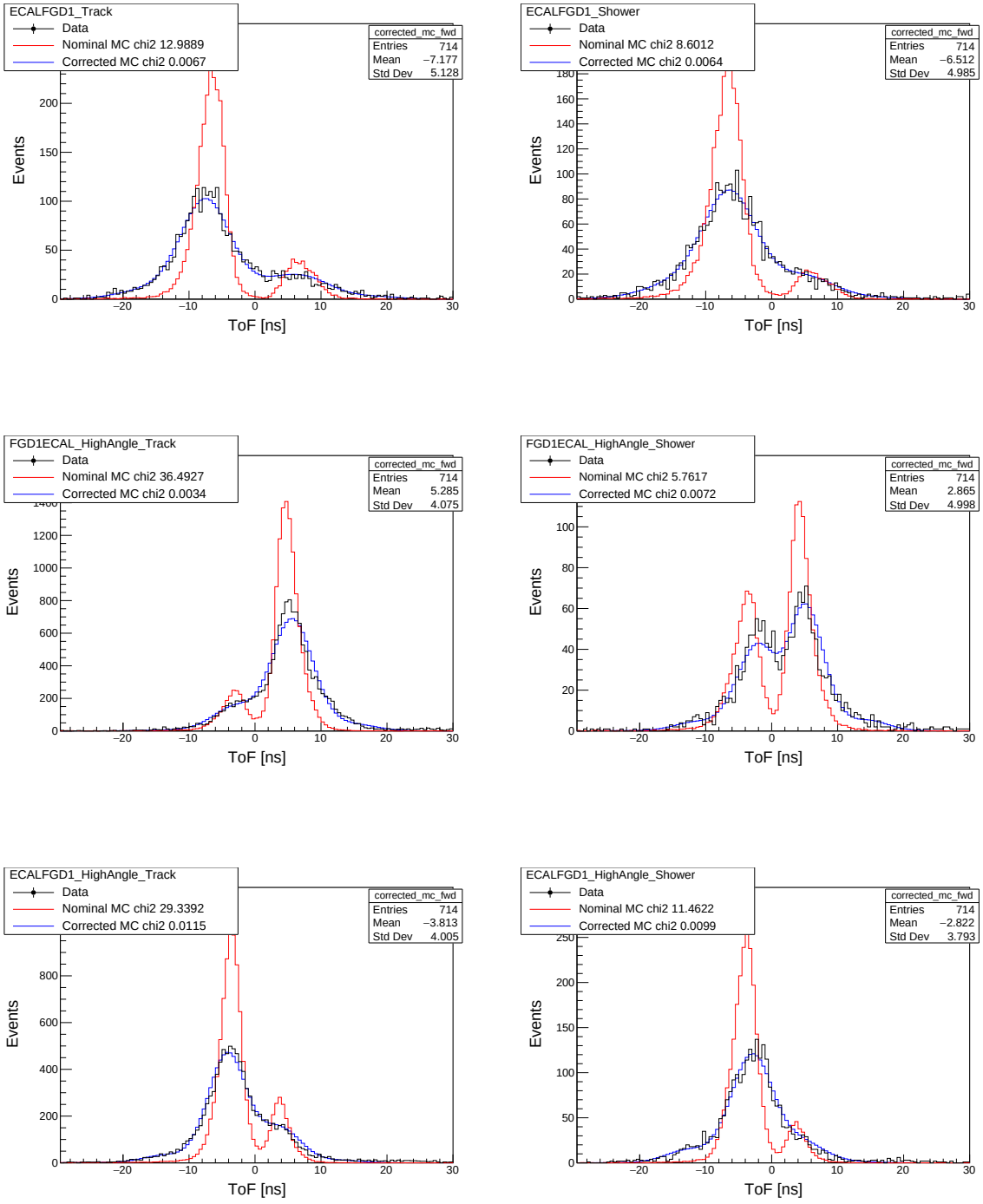

FIGURE 4.5: Corrected ToF value distributions of the rest of FGD1 ToF topologies. The topologies' names are in the box at each plot's top left corner.

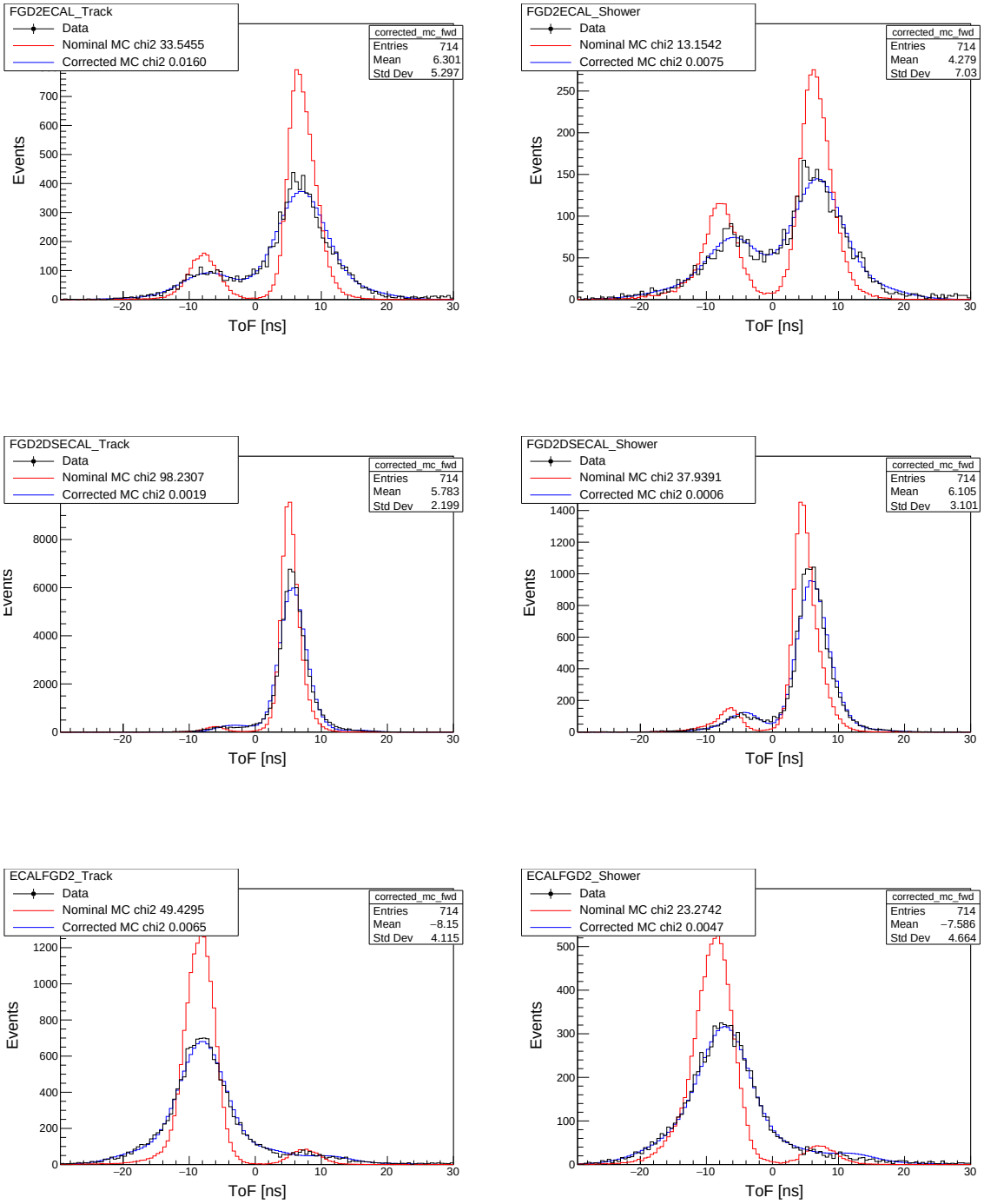

FIGURE 4.6: Corrected ToF value distributions of the first six FGD2 ToF topologies. The topologies' names are in the box at each plot's top left corner.

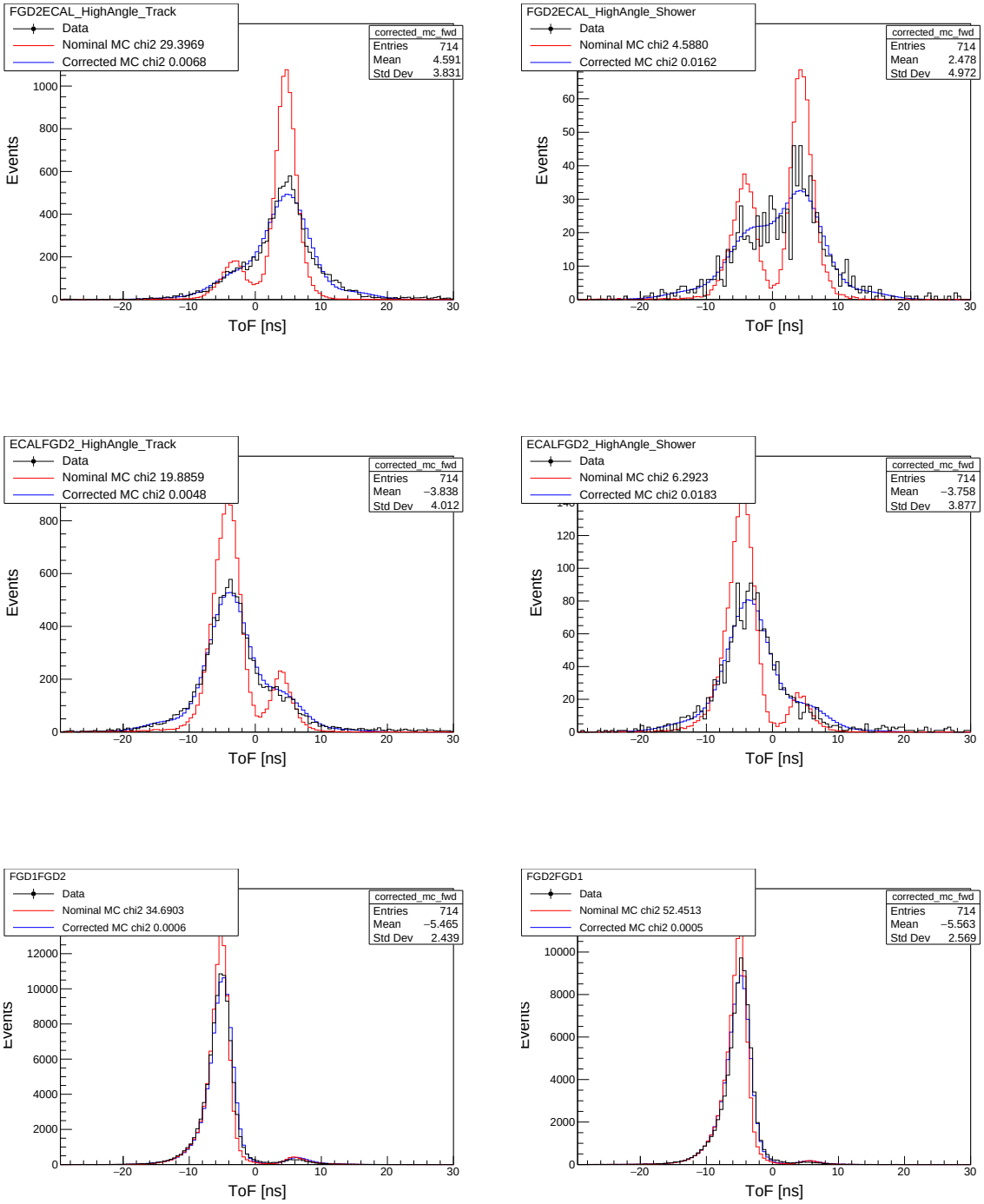

FIGURE 4.7: Corrected ToF value distributions of the last six FGD2 ToF topologies. The topologies' names are in the box at each plot's top left corner.

4.5 ToF track flipping

After the successful correction of the run 8 MC to closely match the collected data, the next step is to address the wrong directions, or 'senses', of ND280 tracks, using ToF measurements. A cut value is manually designed for each ToF topology according to its MC distribution. Backward tracks are identified as those with a smaller ToF value than the cut value, while forward tracks are those with a ToF value greator than the cut value.

The distribution of FGD1-ECal track-like ToF topologies, categorised by their true senses in MC, is shown in Fig. 4.9. A double-Gaussian distribution is visible, with the left peak containing mostly backward tracks and the right peak containing mostly forward tracks. Based on this distribution, a cut value of 0 ns is applied to this topology. In most ToF topologies, the double-Gaussian distribution is visible and well defined on different side of zero, and the cut is naturally placed at 0. However, in some cases, the double-Gaussian distribution is equivocal, and the cut is tuned to suppress out-of-fiducial-volume background. In the FGD1-P0D backward shower like topology, the two peaks are very close to each other, making it impossible to guarantee the purity. Thus, although the correction is also applied to this topology, it is not subject to the later sense check, and subsequently no track of this topology is considered for the backward-going subsamples.

If the nominal direction of a track differs from its ToF direction, the starting and ending positions of the track are swapped, and associated quantities such as charge are adjusted accordingly. Table 4.2 provides the correction parameters and cut values for all ToF topologies.

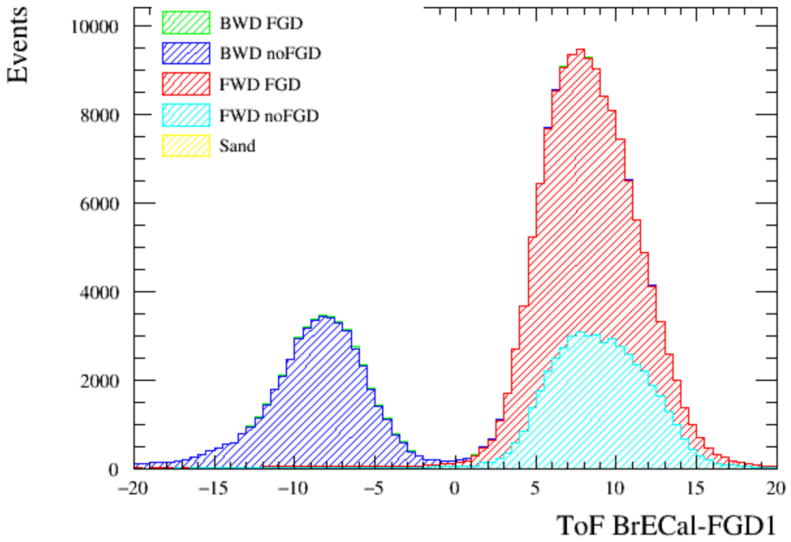

FIGURE 4.8: Distribution events of FGD1-Barrel ECal track like topology broken down to true direction in MC. The true forward tracks are shown in red (starting in FGD) and light blue (not in FGD), while the true backward tracks are shown in gree (starting in FGD) and blue (not in FGD). Two Gaussian peaks at some distance from each other are clearly visible in the plot. A cut value of 0 is selected for this topology.

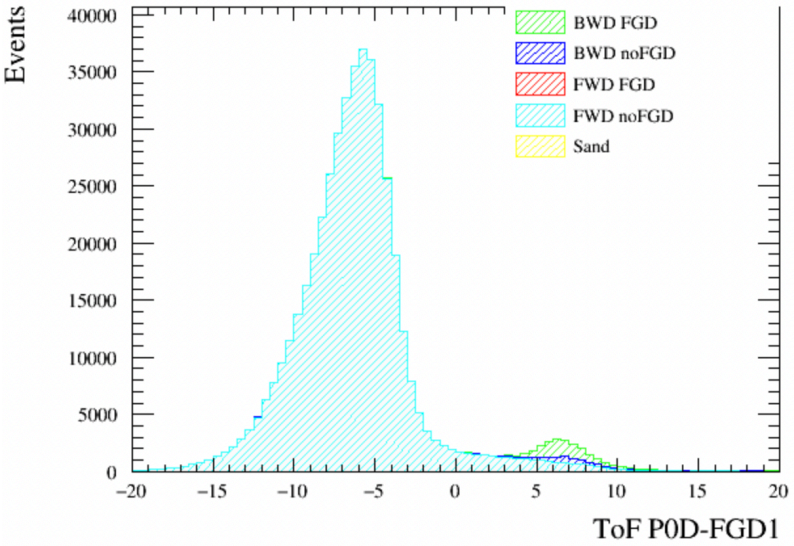

FIGURE 4.9: Distribution events of FGD2-P0D shower like topology broken down to true direction in MC. The true forward tracks are shown in red (starting in FGD) and light blue (not in FGD), while the true backward tracks are shown in green (starting in FGD) and blue (not in FGD). There is a long tail of the true forward samples, resulting in a huge OOFV background in the backward sample selected. This topology is therefore excluded from the selection.

ToF Topology	f_1	f_2	σ (ns)	μ_+ (ns)	μ_- (ns)	cut (ns)
Fgd1Fwd_ToF_ECal_FGD1_track	0.038	0.069	3.0	0.6	1.4	0
Fgd1Fwd_ToF_ECal_FGD1_shower	0.030	0.063	2.8	0.8	2.2	0
Fgd1Bwd_ToF_P0D_FGD1_track	0.040	0.036	1.4	0.8	3.4	1
Fgd1Bwd_ToF_P0D_FGD1_shower	0.036	0.011	1.4	1.2	1.8	1
Fgd1Bwd_ToF_ECal_FGD1_track	0.054	0.106	3.2	-0.8	1.4	1
Fgd1Bwd_ToF_ECal_FGD1_shower	0.068	0.080	3.4	0.6	0.2	2
Fgd1HAFwd_ToF_ECal_FGD1_track	0.031	0.046	2.6	1.0	0.8	0
Fgd1HAFwd_ToF_ECal_FGD1_shower	0.064	0.072	1.8	0.8	2.4	1
Fgd1HABwd_ToF_ECal_FGD1_track	0.055	0.064	2.4	0.0	-0.2	1
Fgd1HABwd_ToF_ECal_FGD1_shower	0.088	0.041	2.6	1.2	0.4	2
Fgd2Fwd_ToF_ECal_FGD2_track	0.037	0.054	3.2	0.2	0.6	-2
Fgd2Fwd_ToF_ECal_FGD2_shower	0.065	0.064	3.0	0.4	1.6	-2
Fgd2Fwd_ToF_DSECal_FGD2_track	0.030	0.011	1.4	0.6	5.0	-2
Fgd2Fwd_ToF_DSECal_FGD2_shower	0.015	0.014	1.4	1.2	2.6	-2
Fgd2Bwd_ToF_ECal_FGD2_track	0.059	0.093	2.8	0.4	4.0	2
Fgd2Bwd_ToF_ECal_FGD2_shower	0.059	0.084	3.0	1.6	4.0	1
Fgd2HAFwd_ToF_ECal_FGD2_track	0.051	0.058	2.6	0.6	1.2.	0
Fgd2HAFwd_ToF_ECal_FGD2_shower	0.100	0.050	2.6	0.4	1.8	0
Fgd2HABwd_ToF_ECal_FGD2_track	0.045	0.060	2.2	0.4	-0.2	1
Fgd2HABwd_ToF_ECal_FGD2_shower	0.044	0.057	2.4	1.4	0.4	2
Fgd1Fwd_ToF_FGD1_FGD2_track	0.002	0.000	0.8	0.4	-0.2	2
Fgd2Bwd_ToF_FGD2_FGD1_track	0.002	0.010	0.6	0.8	-4.8	2

TABLE 4.2: Summary of ToF correction values and cut value of all ToF topologies.

Chapter 5

Selecting 4π solid angle ν_μ charged-current sample at ND280

This chapter discusses the selection of ν_μ events in ND280 using Run 2, 3, 4, and 8 data in the FHC mode. In T2K, the primary goal of ND280 is to constrain flux and cross-section parameters used in the oscillation analysis, which helps improve our understanding of neutrino physics parameters.

Previous selections of ND280 data, as described in [69], only utilised events with forward-going muons, while the SK far detector selects events without angular preference due to its symmetric detector geometry. The comparison of the event distributions is shown in Fig. 5.1. ND280 samples show a distribution that halts at $\cos\theta = 0$, whereas the SK sample extends down to -1. To better compare ND280 data to SK data, it is necessary to introduce a 4π solid angle selection to the ND280 data samples. Furthermore, backward-going events have a high potential to provide better constraints on some of the neutrino-nuclei interaction cross-section parameters, as they are likely to have large momentum transfer.

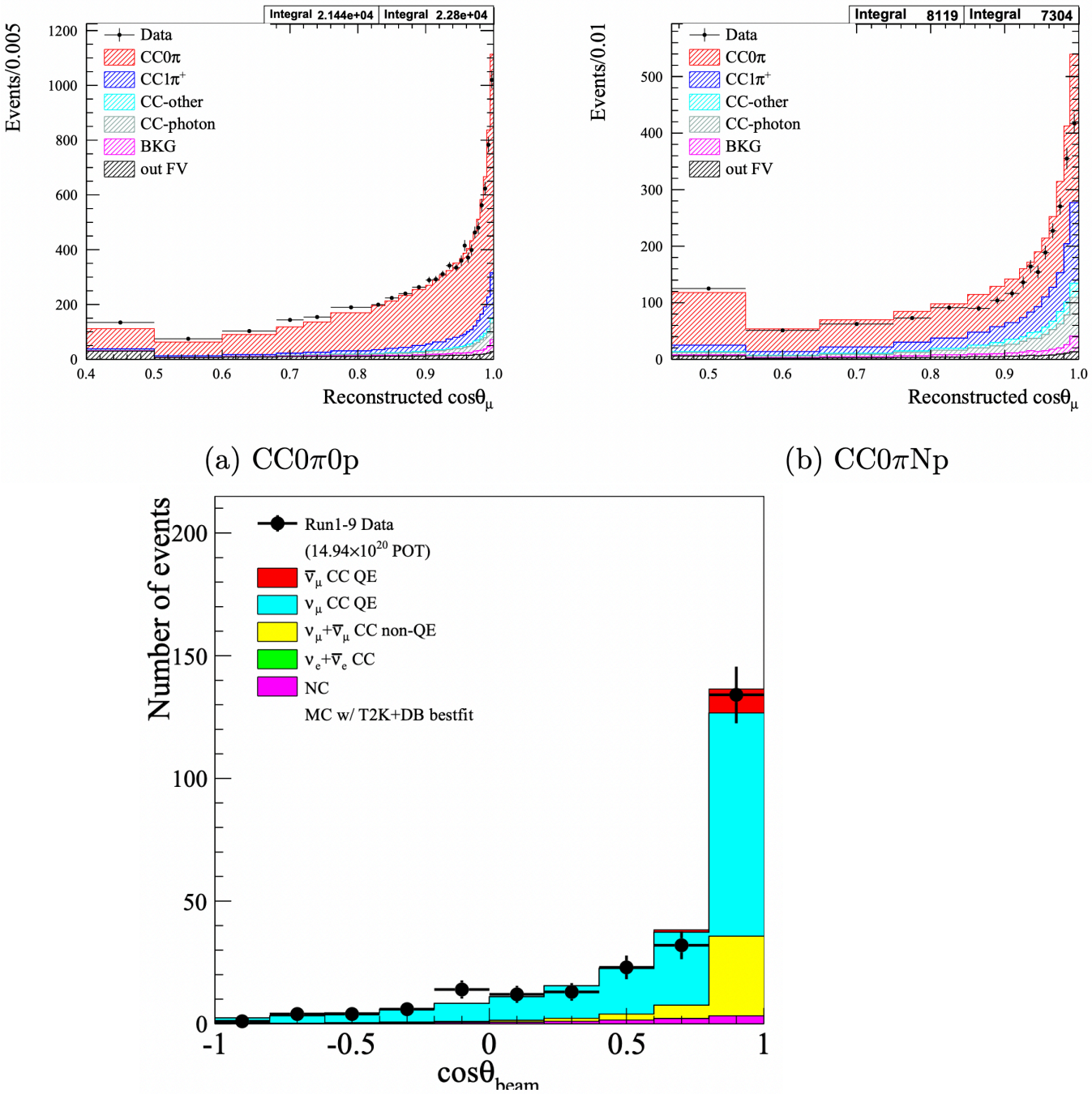

FIGURE 5.1: Top: the distribution of reconstructed muon ring direction $\cos\theta$ with respect to the ND280 neutrino flux axis for Run 2-9 events in the CC0π sample with no reconstructed proton (left) and with one or more reconstructed protons (right). This figure is from [105]. Bottom: the Super-Kamiokande distribution of reconstructed muon $\cos\theta$ with respect to the beam axis in the CC0π sample for Run 1-9. In each plot, the points are data, and the coloured histogram is Monte Carlo simulation. The figure is adapted from [106].

The work described in this chapter involves developing an ND280 sample selection of μ^- tracks with a 4π solid angle coverage. Previous ND280 samples assumed that all tracks are going forward, but instead in this selection the sense of a track was re-evaluated using its Time-of-Flight (ToF) information to find out backward going tracks. Charged-Current (CC) events were selected in FGD1 or FGD2 Fiducial Volume (FV) using methods similar to those introduced in [105]. The selected CC inclusive sample was then split into CC0Pi, CC1Pi, CCOther, and CCPhoton subsamples based on the presence or absence of photons and pions in the final state.

In the new sample selection presented in this chapter, new muon backward and high-angle CC0Pi subsamples are added. This is in addition to traditional muon forward-going subsamples. The CC0Pi forward and backward subsamples are also further divided by looking at the presence of protons.

The following is how this chapter is organised: The first section describes the data to which this selection applies. The second section goes over all of the corrections made to events. The third section explains the selection process in detail. Finally, the fourth section displays the selection results.

5.1 Input files to selection

The selection described in this chapter is a forward horn current (FHC) selection using ND280 data collected during runs 2, 3, 4, and 8. Run 1 is excluded from the analysis due to the absence of a barrel ECal. The analysis considers a total of 1.1602×10^{21} POT.

The accumulated POT is shown in Fig. 3.4, and a summary is provided in Table 5.1. More information on ND280 modeling and Monte Carlo (MC) simulation will be provided later in Chapter 7, but a brief introduction is given below. The details of the flux input used can be found in [80].

The MC files used in this analysis are generated using NEUT 5.4.0 [43], a neutrino-nucleus interaction generator developed and maintained by SK/T2K collaborators, for both magnet and sand neutrino interactions. The term “magnet MC” refers to simulated events that occur within ND280 subdetectors, while “sand MC” refers to those that occur outside. More description on NEUT and its modelling of neutrino-nucleus interactions will come in Sec. 7.3. The propagation of final-state particles in ND280 subdetectors is

Run number	Data POT (10^{20})	MC POT (10^{21})
Run 2 air	0.360	16.802
Run 2 water	0.434	12.038
Run 3 air	1.593	30.780
Run 4 air	1.789	36.122
Run 4 water	1.695	36.122
Run 8 air	4.150	44.532
Run 8 water	1.581	27.168
Total	11.602	203.563

TABLE 5.1: The table summarises the ND280 FHC runs used in this study [79], with POT for data and Monte Carlo simulations shown in separate columns. The 'Air' column indicates data taken with the water bags in P0D being empty, while the "Water" column represents data taken with the bags filled with water. The same sand muon Monte Carlo files, with 10.703×10^{20} POT, are used for all runs in this study.

simulated using GEANT4, a toolkit developed by CERN to simulate the propagation of particles through matter [107].

The response and event reconstruction are performed using the High Level Analysis ND280 (highland) package, which will be discussed in the next section of this chapter. All code described in this paragraph depends on CERN ROOT 5.34.34 [108], unless otherwise specified.

5.2 ND280 analysis with highland

The High Level Analysis ND280 (highland) and its core part, Propagation of Systematics and Characterization of Events (psyche), are crucial in many aspects of T2K physics analysis. They are used to select reconstructed ND280 events and propagate systematic errors, and play a major role in cross-section studies. Binned samples used as near detector fit inputs are selected using psyche.

To incorporate the new 4π samples, the highland/psyche software has been updated in various ways. These updates constitute an important part of the author's PhD work, and a detailed description will be given in this chapter. An overview of the organisation of highland sub-packages is shown in Fig. 5.2.

psyche is built against ROOT and provides all the core features mentioned, including event selection (handled by psycheSelection) and the propagation of systematic errors (handled by psycheSystematics). psycheSteering provides an API for other T2K software, such as the near detector fitters, to call and interact with. The data and MC files are read by psycheIO, which also applies corrections to events. The definition of ND280 detector and events is contained in psycheCore, psycheEventModel, psycheUtils, and psycheND280Utils.

Unlike psyche, highland is dependent on both ROOT and psyche. For each psyche package, there is a corresponding highland package containing features that are still in development, such as new sources or systematic uncertainties and corrections. Once a feature is considered mature, it moves to the parent psyche class. In addition, highland includes stand-alone physics packages that apply the selection to data and MC files and evaluate selection statistics, efficiency, purity, and systematic uncertainty. For each new sample selection, a new highland analysis package is developed. The numuCC4piMultiPiAnalysis package was developed for the sample selection discussed in this thesis.

Finally, there is the highlandTools package, which helps to make plots from the output of analysis packages.

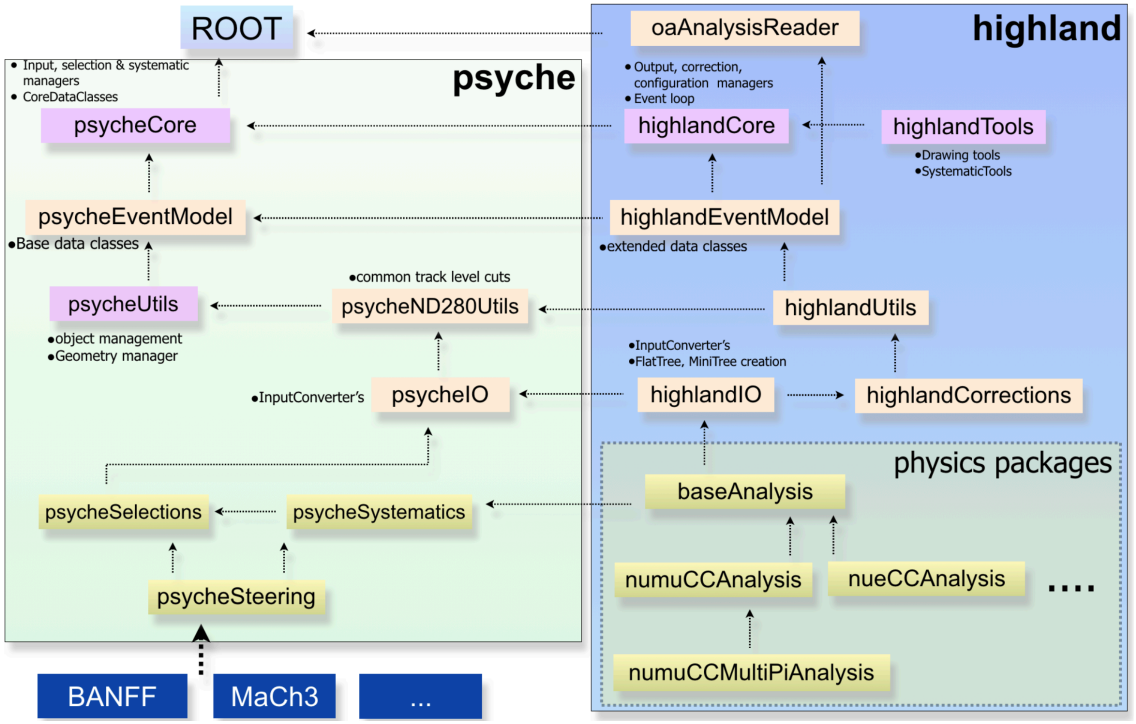

FIGURE 5.2: Organisation of major highland and psyche subpackages. Arrows in the drawing indicates collaboration between packages.

5.2.1 Input converting

Upon completion of the ND280 reconstruction, the reconstructed events at ND280 are saved in a format called oaEvent. The oaEvent format files contain raw data gathered by the detectors. While this is advantageous for calibration and reconstruction development purposes as it provides a comprehensive view, it is not optimal for actual physics analysis due to its substantial size and intricate file structure, which drags processing and is especially problematic when dealing with vast quantities. Consequently, it is essential to extract only the relevant information for event selection to prepare inputs for physics analyses.

In highland, this extraction is accomplished in two stages. First, oaEvent files are processed by oaAnalysisReader, a highland package, which converts the T2K proprietary oaEvent format into a ROOT processable format known as oaAnalysis files. Leveraging ROOT's file compression capabilities, the size of oaAnalysis files is typically reduced to only 1/4 of their parent oaEvent files. An oaAnalysis file contains several directories: HeaderDir, housing information on the relevant beam and data quality flags; ReconDir,

containing global reconstructed objects and local reconstructed objects for each subdetector; and TruthDir, found only in MC files, which holds truth information provided by NEUT.

Although the file size is already reduced by a factor of 4, oaAnalysis files are generally still too large for efficient highland analysis. Thus, it is beneficial to further extract features from oaAnalysis files and generate a more compact file format. highlandIO accomplishes this by converting oaAnalysis files into flattree files, which are typically less than 10% the size of oaAnalysis files, retaining only the necessary information for physics analysis while discarding most unused low-level data.

To ensure compatibility with the 4π samples introduced in this work, revisions were made to highlandIO and psycheIO. A notable discrepancy between highlandIO and psycheIO outputs was discovered in some of the new samples. The cause was traced back to previous versions of psyche, which did not consider P0D and ECal segments as no samples utilised these detectors at the time. However, these segments were included in highland to investigate sample selection possibilities. The author of this thesis introduced these features to psycheIO during the development of the 4π sample, successfully resolving the highland-psyche discrepancy.

5.2.2 Event corrections

Before using highland flattree files in any physics analysis, it is necessary to apply a series of corrections to reduce data-MC discrepancy. The psycheCorrections package applies these corrections to the flattree files when called by the highlandIO package. These corrections are based on known hardware failures or precise control-sample studies, and will be discussed in this section. In most cases, the MC is corrected to increase its resemblance to data, with the exception of dE/dx correction, were both MC and data are corrected to account for a known hardware issue.

In order to include run 8 data in the 4π oscillation analysis, a dedicated ToFCorrection subpackage was added to the psycheCorrections package. This subpackage will be introduced in Chapter 4. Additionally, there are other corrections that must be applied, which are listed below. For a more detailed description, please refer to [54].

- *Ignore right ECal*

  During runs 2, 3, and 4, the right ECal module was broken. To ensure that data and MC are treated consistently, information collected from these modules in both data and MC is excluded from this analysis. This correction is applied to all runs in order to treat the data uniformly.

- *TPC dE/dX corrections*

  TPC momentum reconstruction depends heavily on the magnetic field inside its volume, which were assumed to be uniform. However, measurements show that small uniformity exists. To address that, a correction is applied to reconstructed events in both data and MC. A more detailed discussion can be found in [84].

- *Momentum resolution*

  All MC reconstructed tracks have their momentum smeared by a factor of up to 40% to reduce data-MC discrepancy. The smearing factor is a function of the starting position of the track .

- *Momentum by range*

  Momentum by range is a technique used to measure a particle's momentum by analysing the distance it travels through a material. This method is particularly useful in cases where regular TPC momentum reconstruction is not possible, such as in high-angle events with few or no TPC hits.

  However, there are cases where the global ND280 reconstruction is unable to provide accurate momentum information using this technique. In such cases, the momentum by range correction is applied to recover the events and ensure that accurate momentum information is obtained.

5.2.3 Selecting events

After applying corrections in highlandIO, the next step in the analysis process is to use psycheSelection to apply event selection. psycheSelection filters highlandIO-produced flat-trees using a set of predefined criteria or "cuts". This selection process is applied to both data and MC.

The first use of psycheSelection is to produce input files for the near detector fit, called by OAGenweightApps. The near detector fit constrains neutrino physics parameters

by fitting the MC to the data and tuning model parameters to minimise the data-MC difference in the selected samples, which are the input files created using psycheSelection. A more detailed explanation of the near detector fit is provided in Chapter 7.

The output of psycheSelection can also be used in highland analysis packages to study selected sample purity, efficiency, and systematic uncertainty, as well as to develop new corrections or identify new sources of systematic uncertainties. A dedicated analysis package, ν_μ-charged-current-multiπ analysis (numuCC4piMultiPiAnalysis), was developed to study these characteristics of the 4π samples. The samples created by dedicated highland analysis packages can also be used to study the neutrino-nucleus interaction cross section, as in [54, 101].

All the results presented in this chapter and the following two chapters, Chapter 4 and Chapter 6, were obtained using psycheSelection and highland analysis packages that depend on it.

The systematic uncertainty on the number of events selected are also estimated using psyche software. The error sources considered, along with the error propagation algorithm, are presented in Chapter 6 of this thesis.

5.2.4 Systematic uncertainty propagation

In order to better constrain neutrino physics parameters, it is crucial to understand the uncertainties associated with the number of selected events. These uncertainties are caused by imperfect detector modeling, event reconstruction algorithms, and the event selection procedure itself. For example, uncertainties in the FGD mass value directly affect the total number of events observed in the FGDs, while uncertainties in magnetic field distortion impact the reconstructed momenta of charged particles and therefore indirectly affect the number of selected events, and may have events to migrate from one kinematic bin to another.

To evaluate these uncertainties, external studies and dedicated ND280 control samples are used. It is an important function of highland to propagate these uncertainties into an uncertainty on the number of events selected in the samples used for the near detector fit and cross-section studies.

In practice, systematic uncertainty propagation is usually performed by the highland analysis package of the selection for which the uncertainty is being evaluated, such as the oscillation analysis ν_μ CC 4π selection discussed in this thesis. The goal is to find the uncertainty on the number of events selected by the selection.

The error is evaluated using a 'toy experiment' method. The selection is performed multiple times on toy sets of MC simulation, with the parameters of the systematic uncertainty model randomly drawn according to their respective probability distribution functions. This process is performed many times, and each time, either the weight of the event change the same event may or may not be selected by the same selection cuts. Either way, the samples selected vary in toys. By looking at the variation in the number of selected events, it becomes possible to quantify the systematic uncertainty induced by detector effects.

The systematic uncertainties of the 4π sample are a key part of this thesis. To correctly incorporate the new samples, several new single systematic uncertainties sources are introduced. This includes the Time-of-Flight (ToF) error, the TPC-P0D matching efficiency, and the vertex backward migration error. The author re-evaluated the time-of-flight error in light of the new ToF correction and flipping, and included the later two error sources into the T2K near detector sample for the first time. The systematic errors will be covered in more detail in its dedicated Chapter 6, together with the highland software used to propagate the error on underlying parameters to error on number of selected events.

5.3 ν_μ charged current 4π Multi Pion Photon Proton Selection

The CC$4\pi - \gamma p^+$ selection, which creates the 4π sample input to T2K oscillation analysis, is developed from two existing psyche selections: the CCγp^+ selection and CC4π selection. Each of them is introduced below:

- **CCγp^+ Selection**

  This selection was developed by T. Doyle and K. Skwarczynski [109] in 2020 and used in the T2K 2022 oscillation analysis. It aims to select charged-current ν_μ events that feature a forward-going final-state muon. The selection splits these events into

five distinct subsamples: The CC0π0p sample, where there are no protons or pions in the final state; The CC0πNp sample, where there is at least one proton, but no pions in the final state; The CC1π sample, where there is exactly one pion, regardless of the number of protons; The CCOther sample, where there are two or more pions in the final state; The CCPhoton sample, where there is at least one photon or identified π^0 in the final state. π^0 are identified used a pair of electron and positron, as introduced in [110]. This sample was introduced to study neutrino interactions that produce π^0 events, which are an important background to the SK ν_e selection [111].

A schematic diagram of the this selection can be found in Fig. 5.3.

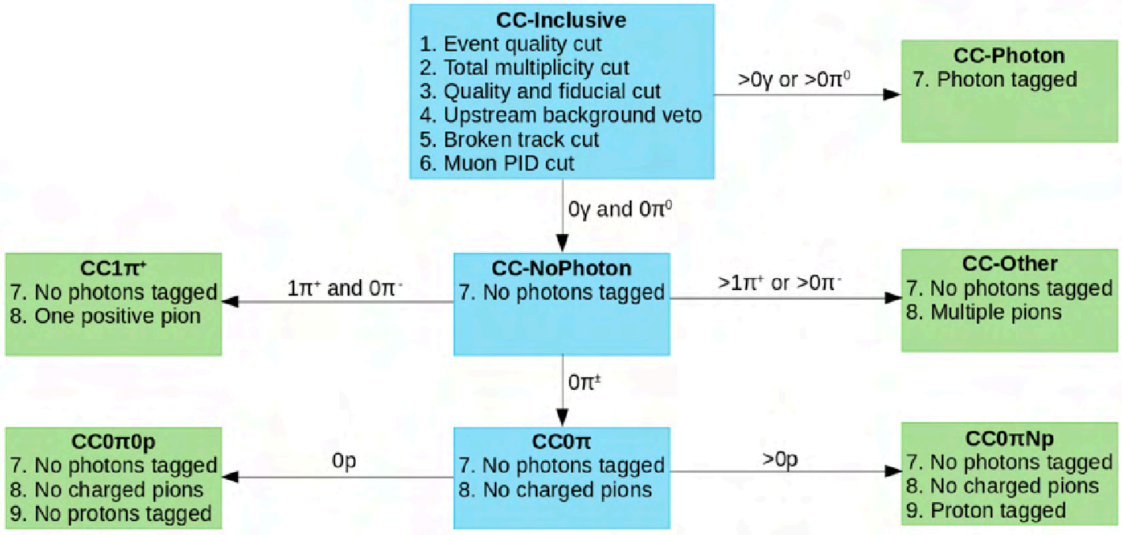

FIGURE 5.3: The flow chart of the ND280 CCγp^+ selection used in T2K oscillation analyses before the work described in the thesis is integrated. It involves multiple steps to identify neutrino interactions in the ND280 detector. The first step applies the traditional CC-inclusive selection used by T2K before 2015 to select a ν_μ charged-current inclusive sample. Next, the CC-inclusive sample is divided into five subsamples based on the criteria outlined in the chart. The intermediate samples are denoted by blue boxes, while the final samples that are used in physics analyses are indicated in green. The numbered items within each box represent the criteria imposed at each stage of the selection process. The figure has been adapted from [109].

- **CC4π Selection**

  This selection was developed in 2017 for cross-section study purpose [101]. The

selection process begins with the CC-inclusive sample, and instead of splitting it into five subsamples, it is divided into three based on the number of pions present: the CC0π sample, CC1π sample, and the CCOther sample. Each of these three samples is then further subdivided into four subsamples based on the direction of the final-state muon, resulting in a total of 12 subsamples in this selection. The four muon directions are categorized as forward (FWD), backward (BWD), high-angle forward (HAFWD), and high-angle backward (HABWD), as seen in Fig. 5.3.

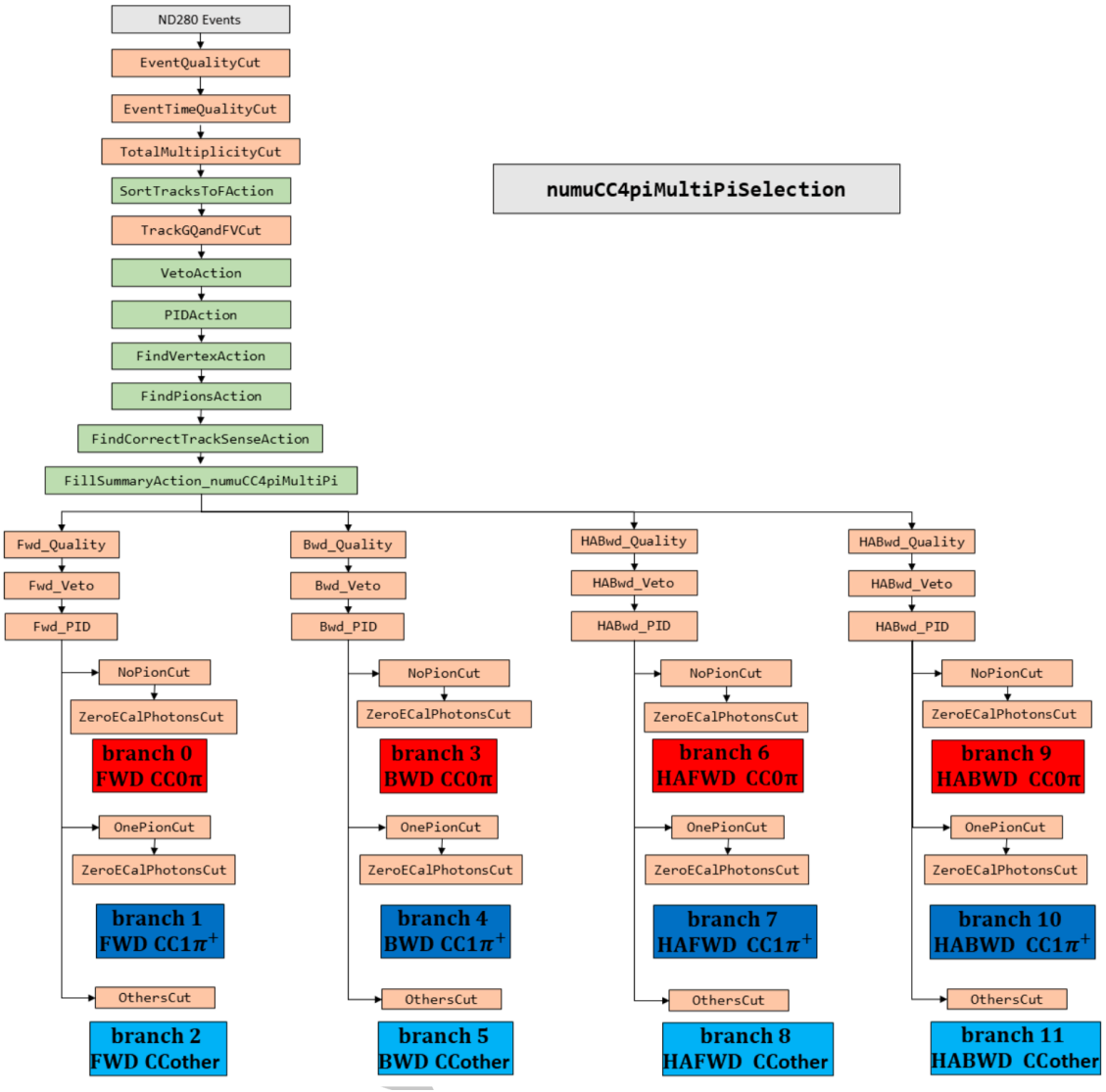

FIGURE 5.4: The flow chart of the ND280 CC4π selection, which involves multiple steps to identify neutrino interactions in the ND280 detector. The selected events are first subjected to a sense check to determine the true direction of the muon track - forward or backward - using inter-subdetector time of flight information. Next, a CC-inclusive sample is selected using traditional cuts, and then split into four directional samples: forward, backward, high-angle forward, and high-angle backward. Each of these directional samples is then further subdivided by the number of pions present, resulting in a total of 12 samples: CC0π, CC1π, and CCOther for each of the four directions. The figure has been adapted from [112].

Named as the CC4$\pi\gamma p^{+}$, or 'numuCC4piMultiPiPhotonProton' selection as named in the code, the oscillation analysis 4π selection outlined in this thesis draws from the key features of its two predecessors while incorporating modifications deemed necessary during

development.

Charged-current events exhibiting muon tracks in the backward and high-angle directions are exclusively considered for events without pions in the final state, specifically the CC0π subsamples: CC0π0p and CC0πNp. For the CC1π, CCOther, and CCPhoton subsamples, only events with forward-going muons are included in the selection. The sole exception is the CC1π high-angle forward sample, which is included due to its high purity and substantial number of selected events.

Owing to concerns regarding statistical and systematic uncertainty, the CC0π0p and CC0πNp samples do not differentiate between high-angle forward and high-angle backward samples. As a result, there are only two high-angle samples CC0π0p high-angle and CC0πNp high-angle rather than four, which brings the total number of CC0π samples to six. A flowchart illustrating the organisation of this selection and its corresponding subsamples is depicted in Fig. 5.5 and elaborated on in the subsequent text.

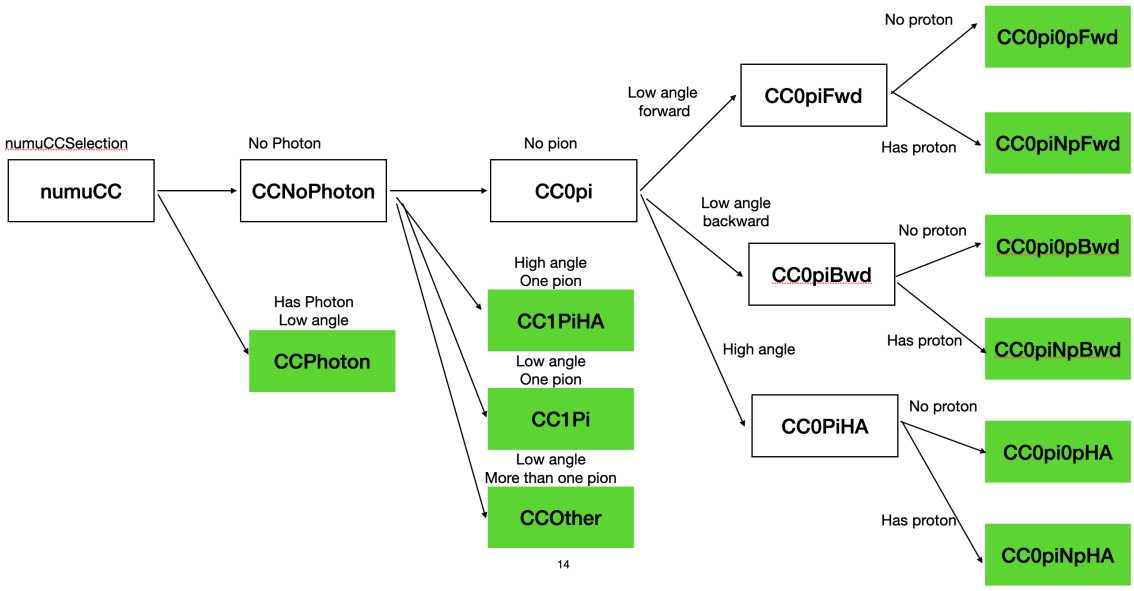

FIGURE 5.5: Flowchart of the ND280 CC4$\pi\gamma p^+$ selection process: Initially, a time of flight sense check, identical to the one used in the CC4π selection, is applied to all tracks for direction correction. Subsequently, a ν_μ CC sample is selected using standard cuts. The sample is then divided into a CCphoton sample and a CC No-photon sample based on the number of photons. The CC No-photon sample undergoes a pion number check, resulting in a CC1π sample, a CCOther sample, and a CC0π sample. The CC1π sample is further separated into a CC1π low-angle forward sample and a CC1π high-angle forward sample. Notably, events with a backward-going muon are excluded from the CC1π sample due to poor purity, unlike in CC0π samples. Finally, the CC0π sample is divided by muon direction and proton number into six samples: CC0π0p low-angle forward, CC0πNp low-angle forward, CC0π0p low-angle backward, CC0πNp low-angle backward, CC0π0p high-angle, and CC0πNp high-angle.

5.3.1 Common steps

The remainder of this chapter will focus on the cuts and outcomes of the novel CC4$\pi\gamma p^+$ selection. Due to the complex nature of this selection, a comprehensive explanation is provided in two distinct subsections: the current subsection discusses the common cuts applicable to all subsamples, while the following subsection elaborates on the particle identification, and the classification of events into their respective subsamples. Hereafter, to avoid confusion, a "sample" refers to the output psycheSelection creates, while a "subsample" is a group of events selected with certain features like number of pions or direction of the muon. A sample usually contain multiple subsamples. The CC4$\pi\gamma p^+$ sample developed as the main body of this thesis's work constitutes 10 subsamples.

- **ToF sense check**

  In previous ND280 samples, all tracks were considered forward-going, meaning that the more upstream end of a track was always regarded as the starting point, and the more downstream end as the finishing point. As mentioned earlier, constructing a 4π sample requires all tracks within an event to undergo a Time-of-Flight (ToF) sense check before applying any cuts. This check is performed using ToF information, and the underlying concept is straightforward: a forward-traveling particle should first pass through the upstream detector and then the downstream detector. Consequently, the timestamp recorded at the downstream detector should be greater than that recorded at the upstream detector, resulting in a positive timestamp difference.

  In principle, any track exhibiting a negative timestamp difference is deemed backward, indicating that it originated from the downstream detector and propagated in the reverse direction toward the upstream detector.[1] If a track is considered backward, its reconstructed starting and ending positions are swapped or 'flipped'. More details about the ToF treatment will follow in Chapter 4.

- **Event quality cut**

  This cut requires that events carries a satisfactory global ND280 data quality flag. Events occurring during T2K beam time windows are assigned such a flag. If an event takes place outside of the beam time window, it is automatically regarded as a background event and does not receive a good quality flag. The minimum time window under consideration is a beam bunch; all tracks occurring within a single bunch are considered to originate from the same event.

- **Total multiplicity cut**

  At least one reconstructed track is required in the event for the selection to work on. Introducing this cut speeds up the running of code significantly.

- **Fiducial volume cut**

  A fiducial volume (FV) refers to a specific region within the detector characterized by a high signal purity, where events occurring outside this region are considered as background. This cut requires that the track must begin within the FGD FV (FV). Different FV definitions are applied to various samples. For tracks containing

[1] In practice, to enhance purity, the flipping threshold is set to a non-zero value for certain ToF topologies. A comprehensive list of cutting values is provided in Table 4.2 in Chapter 4.

more than 18 TPC hits, the low-angle FV definition is used; whereas, for those with 18 or fewer TPC hits, the high-angle FV definition is employed. FGD1 and FGD2 share the same x and y FV definitions, differing only in their z values. This is because that for the high-angle samples, the most downstream XY module in each FGD is excluded from FV to suppress out-of-fiducial volume backgrounds. A comprehensive list of the fiducial volume definitions using ND280 coordinate system used in this analysis can be found in Table. 5.2. For a detailed explanation of the ND280 coordinate system, please refer to Appendix. A.

Sample name	x_{min}	x_{max}	y_{min}	y_{max}	z_{min}	z_{max}
FGD1 low-angle	-874.51	874.51	819.51	929.51	125.75	447.375
FGD1 high-angle	-874.51	874.51	819.51	929.51	125.75	437.255
FGD2 low-angle	-874.51	874.51	819.51	929.51	1483.75	1807.375
FGD2 high-angle	-874.51	874.51	819.51	929.51	1483.75	1797.255

TABLE 5.2: Fiducial volume definition of FGD1 low-angle, FGD1 high-angle, FGD2 low-angle and FGD2 high-angle samples in mm. The low-angle and high-angle FV differ by a small amount in z in order to suppress out-of-fiducial volume background.

In each FGD, high-angle tracks and low-angle tracks that survive the FV cut are further split into two groups each: the forward tracks, which have a greater ending z coordinate than starting, and the backward tracks, which do not. Before the next cut is applied, there are four groups of tracks: high-angle forward, high-angle backward, low-angle forward and low-angle backward.

- **Muon PID cut**

  In a single event, the negatively charged track with the largest momentum will be considered for the muon Particle IDentification (PID), which aims at selecting muons produced in ν_μ charged-current interactions. For low-angle tracks, a TPC PID algorithm is applied. TPCs can measure the energy deposit a candidate track leaves as a function of distance (dE/dx), and the measured values are compared to expectation values obtained from control sample studies and external researches. The measured values are contrasted with the expected values of muons, pions, protons, and electrons, and a pull value is computed for each hypothetical charged particle species

[101, 109]:

$$P^i = \frac{dE/dx_{measured} - dE/dx^i_{exp}}{\sigma_{dE/dx}} \tag{5.1}$$

Here, $dE/dx_{measured}$ and dE/dx^i_{exp} represent the measured energy loss rate in the TPC and the expected rate for particle type i. The denominator $\sigma_{dE/dx}$ signifies the uncertainty of the numerator. The likelihood of a candidate particle being of type i is then defined as:

$$\mathcal{L}_i = \frac{\exp(-(P^i)^2)}{\Sigma_j \exp(-(P^j)^2)} \tag{5.2}$$

where i, j denote the hypothetical charged particle indices. The summation in the denominator encompasses all particle types considered in the TPC PID. For positively charged tracks, μ^+, π^+, e^+, and p are considered, while for negatively charged tracks, only μ^-, e^- and π^- are in consideration. Another cut employed in the muon PID is

$$\mathcal{L}_{\mathbf{MIP}} = \frac{\mathcal{L}\mu + \mathcal{L}\pi}{1 - \mathcal{L}_p} > 0.05, \tag{5.3}$$

where MIP stands for Minimal Ionising Particles, a term used to discriminate against electrons. The distribution of L_μ and $L_{\mathbf{MIP}}$ can be found in Fig. 5.6.

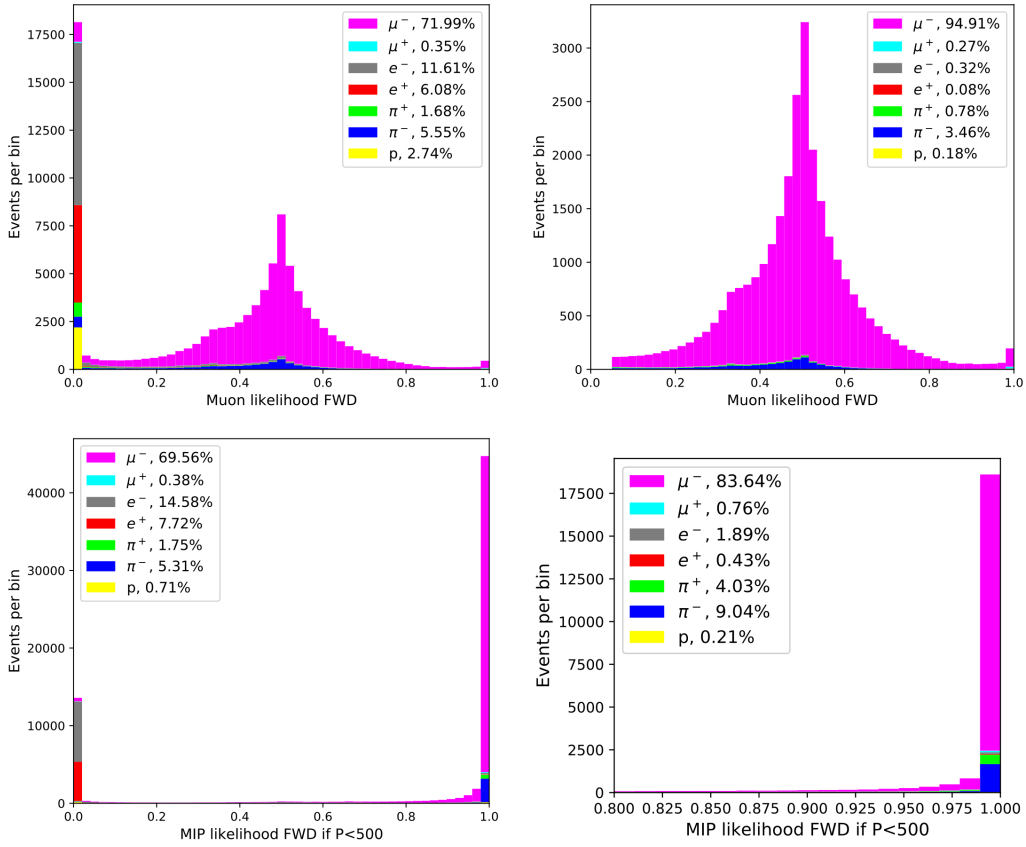

FIGURE 5.6: L_μ and $L_{\mathbf{MIP}}$ distributions in the forward going samples combined. This figure is adapted from [101].

In addition to the criteria mentioned above, different PID cuts are applied depending on the event muon's direction:

- ⋆ *Low-angle forward*: It is required that muon candidates originating from FGD1 with a momentum greater than 280 MeV do not stop in FGD2.
- ⋆ *Low-angle backward*: These muon candidates must satisfy $\mathcal{L}_{\mathbf{MIP}} > 0.65$ for those with $p < 200$ Mev, and $\mathcal{L}_\mu > 0.05$ for those with $p > 200$ MeV.
- ⋆ *High-angle tracks*: These muon candidates do not leave enough TPC hits to employ TPC PID cuts. Therefore, a ECal-SMRD PID variable, PIDMipEM, was developed in [101] and employed in later analyses to set cuts in order to identify muons. The cut requires that $-100 <$ PIDMipEM < 0 and $1.0 <$ Length/EMEnergy < 2.6, where Length is the length of the track in mm and EMEnergy is the deposit electromagnetic energy in MeV. Additionally, it the track also involves SMRD, the track is always considered as a muon. The MC

distribution of the high-angle ECal muon PID variables in MC can be found in Fig. 5.7.

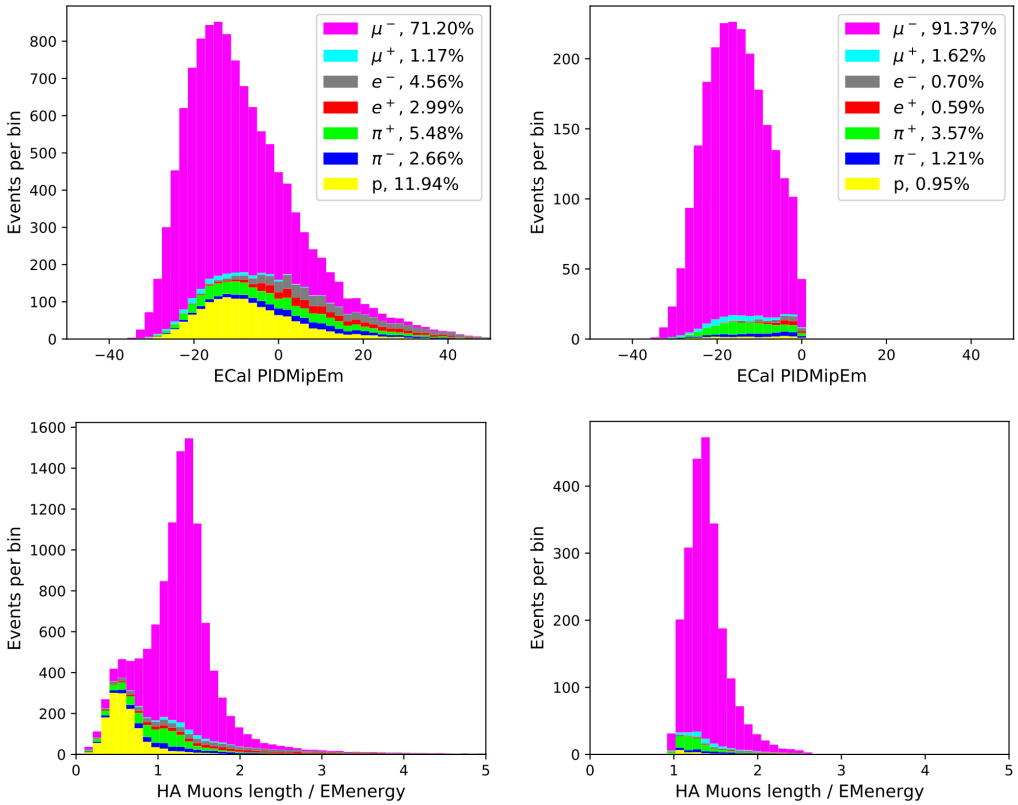

FIGURE 5.7: The distribution of MC ECal objects' muon PID variables. The left column panels are pre-cut, and the right column panels are post-cut. This figure is adapted from [112].

- **Veto cut**

  After applying the muon PID cut, the track with the highest momentum among all possible muon tracks in an event is designated as the muon candidate, or the main track. It is possible for a long track traversing FGD1 to be mis-reconstructed as two separate tracks. For instance, a track originating from the P0D can extend from the P0D through TPC1, FGD1, TPC2, FGD2, and TPC3, but be mis-reconstructed into two tracks: a P0D-FGD1 track and an FGD1-TPC3 track. A schematic illustration of such a track and its erroneous reconstruction is presented in Fig. 5.8.

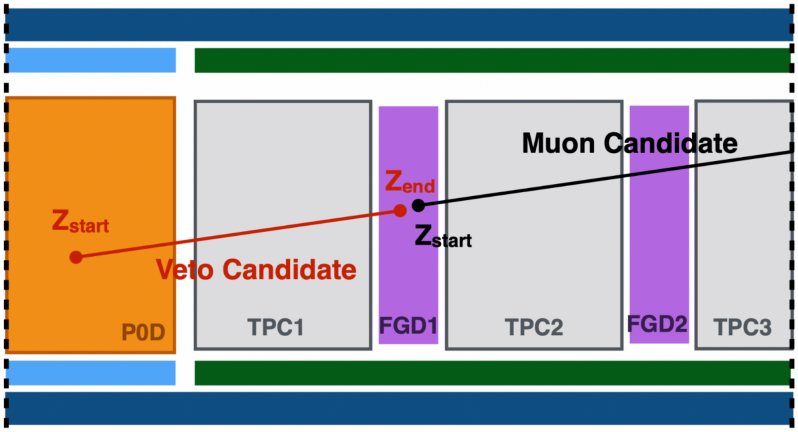

FIGURE 5.8: Schematic drawing of a broken track, which the veto cut is designed to reject. Figure adapted from [54].

To eliminate such tracks, the veto cut loops over all tracks except the muon candidate track and discards the entire event if any of these tracks meet both of the following conditions: $Z^{\mu}_{\text{end}} - Z^{\mu}_{\text{start}} < D$ and $p/p_{\mu} > R$. Here, Z_{start} and p represent the starting z coordinate and momentum of the track under scrutiny, and the same applies to the muon candidate track, as illustrated in Fig. 5.8. The required values D and R vary among different subsamples. Table 5.3 summarises the required values for all muon direction scenarios.

Muon direction	D (mm)	R
High-angle forward	-150	0.9
High-angle backward	-400	0.9
Low-angle forward	-100	0.8
Low-angle forward	-100	0.8

TABLE 5.3: Required veto track parameters in different muon direction scenarios.

5.3.2 Tagging particles

After satisfying all of the cuts mentioned above, an event will be categorised as a ν_{μ} charged-current event and included in the psyche output. The event's category will be determined based on the criteria described in this subsection, which relies on the numbers of three types of particles: pions, protons, and photons. Thus, it is crucial to ascertain the number of each of these particle types present in the event. This subsection provides

an overview of the identification process for these particles and, subsequently, how to determine which sample a selected ν_μ charged-current event belongs to, based on the number of particles of interest.

It is worth emphasising that the criteria introduced in this section serve solely to confirm the presence of particles in the event (referred to as 'tagging') and do not guarantee the accurate reconstruction of the tagged particles' kinematics.

- **TPC Pion PID**

  ND280 TPC pion tagging works differently for neutral pions and charged pions. Charged pions are affected by the magnetic field and can thus be identified using a criterion similar to the one introduced in Sec. 5.3.1, based on a high-level variable. Specifically, a charged TPC track is identified as a charged pion if its likelihood of being a pion, $\mathcal{L}_\pi$, as one hypothesis in $\mathcal{L}_{\mathbf{MIP}}$ defined in Eq. 5.2, satisfies

  $$\mathcal{L}_\pi > 0.3. \tag{5.4}$$

  On the other hand, neutral pions can only be identified in TPCs through their charged decay products. If an electron-positron pair is identified in the ND280 TPCs using the PID variables defined in Sec. 5.3.1, they are most likely the decay products of a primary π^0 from the process $\pi^0 \to \gamma\gamma \to e^+e^-\gamma$, and the event is tagged as a TPC π^0 event.

- **FGD pion PID**

  IsoFGD tracks are defined as tracks that originate and end within the same FGD volume. To identify these tracks as pions, a FGD pull value, $\mathbf{Pull}_i^{FGD}$ was developed. The concept of FGD pulls is similar to that of TPC pulls, which is based on the fact that different types of particles lose energy at different rates in FGD scintillators.

  The formula for $\mathbf{Pull}_i^{\mathrm{FGD}}$ is defined as follows:

  $$\mathbf{Pull}^{\mathrm{FGD}}i = \frac{E_{\mathrm{measured}} - E_i(L)}{\sigma(E_i(L))}, \tag{5.5}$$

  where E_{measured} is the measured energy deposited in the FGD, $E_i(L)$ is the expected energy deposit, which is a function of the length of the FGD track length L, and

$\sigma(E_i(L))$ is the uncertainty on the expectation. For an IsoFGD track to be tagged as a charged pion, the pull value must satisfy the condition $-2 < \mathbf{Pull}_{\pi}^{\mathrm{FGD}} < 2.5$.

- **Michel-electron FGD pion PID**

  Another possible method to identify IsoFGD pions is by identifying Michel electrons. Michel electrons are electrons produced by the decay of a muon, which is a common decay product of pions. ND280 Michel-electron pion tagging works as follows: in an event that produces a pion, the primary pion decays to produce a muon, which in turn decays to produce a single Michel electron. If an electron is detected just outside the beam bunch time window, which typically lasts a few thousand nanoseconds depending on the run [113], it is considered the product of a decaying pion, and the event is tagged as a pion event.

- **Photon PID**

  As previously mentioned, neutral pions primarily decay into a pair of photons [77]. Before 2022, the only viable method to tag neutral pions in ND280 was through the detection of their photon pair decay products using the TPCs.

  To gain a better understanding of the π^0 background, a new ECal photon tagging algorithm was introduced to the ND280 sample selection in 2022 [79]. According to Monte Carlo simulations, most of the photons detected in the ECals are from primary π^0 decays, but not all of them. Primary neutral pion decay accounts for 84% of the ECal photons in the simulations [79]. Other contributing processes include η decays, or the decays of daughter π^0 of primary hadrons, mainly K and Λ.

  The high-level variable EMhip, originally designed in [114] to separate electromagnetically interacting particles such as $e^{\pm}$ from highly-ionsing particles such as protons, is used to perform photon PID in the ECals. The definition of EMhip is complex, utilising the circularity of ECal hit clusters, the deviation of charge deposition left by hits, the ratio of charge deposited in different ECal layers, and dE/dx inside the ECal. The contribution of each type of information was tuned using dedicated Monte Carlo simulations. A full description of EMhip can be found in [114], which was used in the study presented in [79] and this thesis.

  The distribution of EMhip values for particles is shown in Figure 5.9. The plots demonstrate that the variable is effective in rejecting muon and neutron backgrounds,

particularly in the downstream ECal.

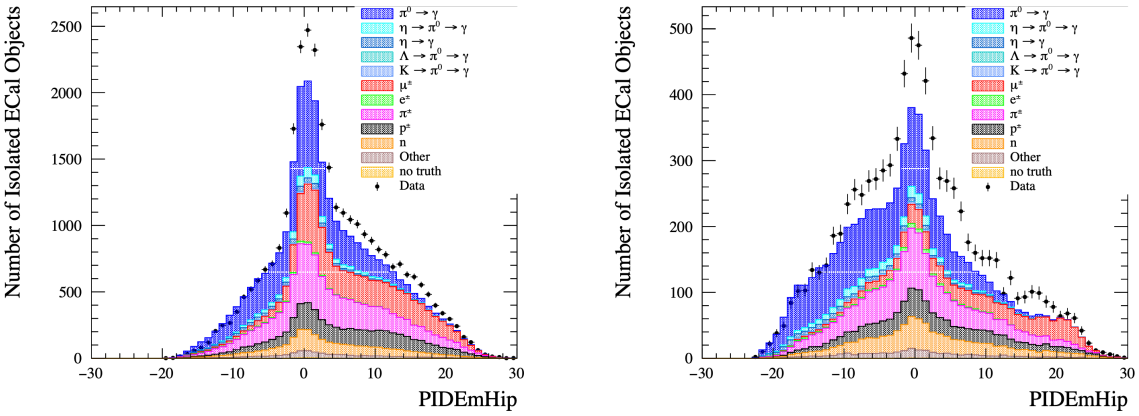

FIGURE 5.9: Distribution of particle EMhip values in a control sample study. Points are data, and the colourful histograms are the MC simulation. Photons from different processes are shown in blue colours, and other particles are shown in different non-blue colours. The cut value on EMhip is set to be < 0 for all ECal modules in order to select photons. The left plot shows particles entering the barrel ECal, and the right plot shows particles entering the downstream ECal. In both plots, a excess in number of data events can be observed, which is believed to be a consequence of more frequent pile-up in data than in MC. This figure is adapted from [109].

- **Proton PID** For positively-charged tracks, those that are not tagged as muons or pions will be considered for proton tagging. For IsoFGD proton candidates, it is required that $\text{Pull}_p^{\text{FGD}} > -4$, where $\text{Pull}_p^{\text{FGD}}$ is the FGD pull value defined in Eq. 5. For those with TPC segments, the requirement is $\mathcal{L}_p > 0.5$, where the $\mathcal{L}_p$ is as defined in Eq. 5.2. The distribution of both variables in Run 2-4 MC simulation is shown in Fig. 5.10. Both results are from [109].

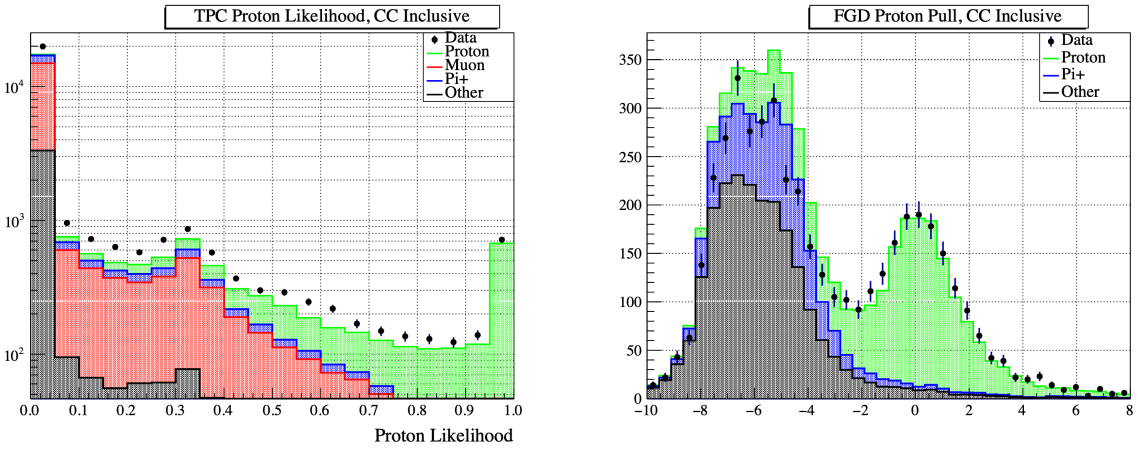

FIGURE 5.10: The distribution of proton PID variables. The left panel shows the isoFGD proton identifying variable, $\text{Pull}_p^{\text{FGD}}$ in a MC control sample, and the right panel shows that of TPC proton identifying variable, $\mathcal{L}_p$. Both results are from [79].

The particle tagging criteria above are applied to all reconstructed objects except the muon candidate. The number of pions, protons and photons are then used to determine which sample an event goes to.

5.3.3 Event categorisation

After completing the process of particle tagging and obtaining the number of tagged protons, pions, and photons, the final step is to determine the appropriate subsample for the event. This section outlines the categorisation criteria utilised in the numuCC4piMultiPiPhotonProton selection.

1. **CCPhoton Low-Angle Forward** : One or more photons in the event, and the muon produced in neutrino charged-current interaction leaves 19 or more TPC hits, and travels forward.

2. **CC1π Low-Angle Forward** : Exactly one charged pion, no photon in the event, and the muon produced in neutrino charged-current interaction leaves 19 or more TPC hits, and travels forward.

3. **CC1π High-Angle Forward** : Exactly one charged pion, no photon in the event, and the muon produced in neutrino charged-current interaction leaves 18 or fewer TPC hits.

4. **CCOther Low-Angle Forward** : Two or more charged pions and no photon in the event, and the muon produced in neutrino charged-current interaction leaves 19 or more TPC hits, and travels forward.

5. **CC0π0p Low-Angle Forward**: No pion, no photon, no proton in the event, and the muon produced in neutrino charged-current interaction travels forward in the z direction, and leaves 19 or more TPC hits.

6. **CC0πNp Low-Angle Forward**: No pion, no photon, one or more protons in the event, and the muon produced in neutrino charged-current interaction travels forward in the beam direction, and leaves 19 or more TPC hits.

7. **CC0π0p Low-Angle Backward**: No pion, no photon, no proton in the event, and the muon produced in neutrino charged-current interaction travels backwards in the beam direction, and leaves 19 or more TPC hits.

8. **CC0πNp Low-Angle Backward**: No pion, no photon, one or more protons in the event, and the muon produced in neutrino charged-current interaction travels backwards in the beam direction, and leaves 19 or more TPC hits.

9. **CC0π0p High-angle**: No pion, no photon, no proton in the event, and the muon produced in neutrino charged-current interaction leaves 18 or fewer TPC hits.

10. **CC0πNp High-angle**: No pion, no photon, one or more protons in the event, and the muon produced in neutrino charged-current interaction leaves 19 or more TPC hits. Unlike CC0π high-angle subsamples, this subsample also requires the muon to travel forward.

A summary of all ten subsamples is provided in Table 5.4. An event may qualify for more than one subsample. For example, an event with a proton, a photon, no pion, and a forward-traveling muon with 80 TPC hits satisfies the criteria for both the CCPhoton and CC0π0p forward subsamples. In such cases, the subsamples are prioritised based on the order given in the list. Therefore, the event mentioned above belongs to the CCPhoton subsample.

It is important to note that this selection does not cover all ν_μ charged-current events. An event that does not qualify for any of the subsamples will be disregarded, such as an event with a photon in the final state and a backward-going muon.

For information on how the direction of the muon is determined, please refer to Chapter 4. [2]

Subsample name	$\gamma + \pi^0$	p^+	$\pi^\pm$	μ^- TPC hits	μ^- direction
CCPhoton Low-Angle forward	> 0	$\times$	$\times$	> 18	Forward
CC1π Low-Angle forward	0	$\times$	1	> 18	Forward
CC1π High-Angle forward	0	$\times$	1	≤ 18	Forward
CCOther Low-Angle forward	0	$\times$	> 1	> 18	Forward
CC0π0p Low-Angle Forward	0	0	0	> 18	Forward
CC0π0p Low-Angle Backward	0	0	0	> 18	Backward
CC0πNp Low-Angle Forward	0	> 0	0	> 18	Forward
CC0πNp Low-Angle Backward	0	> 0	0	> 18	Backward
CC0π0p High-Angle	0	0	0	≤ 18	$\times$
CC0πNp High-Angle	0	> 0	0	≤ 18	$\times$

TABLE 5.4: The summary of which subsample a ν_μ charged-current event goes into in different scenarios, according to the number of different particles in the event, and the direction and TPC hits of the muon candidate. An $\times$ indicates that any value will work.

5.4 Selection results

This section presents the kinematic distributions and subsample composition for the CC4$\pi\gamma p^+$ selection. Specifically, Figures 5.11 to 5.22 illustrate the muon kinematic distributions of neutrino interaction events originating from FGD1 (Fig. 5.13 to 5.12) and FGD2 (Fig. 5.19 to 5.22) subsamples as functions of their reconstructed muon kinematic variables. Each MC histogram is broken down into true event topology, true particle species or true neutrino interaction type.

Overall, the low-angle forward samples exhibit performance that is very similar to the OA2022 results. The low-angle backward samples have muon tracks with sub-500 MeV momentum, and their $\cos\theta$ values measured with respect to the z axis are concentrated around -1. This is not solely becauses of the differential cross-section of neutrino-carbon interaction peaks there; instead, this should be attributed to ND280 detector design and

[2] It's worth noting that while the final set of subsamples consists of only direction-inclusive CC0π0p High-angle and CC0πNp High-angle particles, the program can differentiate between high-angle forward and backward tracks. The high-angle subsamples from both forward and backward directions are merged to increase efficiency and decrease detector systematic uncertainty. In total, there are 12 branches in the selection process, with four of them being CC0π0p high-angle forward, CC0π0p high-angle backward, CC0πNp high-angle forward, and CC0πNp high-angle backward. These four branches are later combined to create the CC0π0p high-angle and CC0πNp high-angle subsamples in the output.

reconstruction algorithm, which works more efficiently when the muon travels at a small angle with respect to the neutrino beam. When the angle is small, the track naturally involves more FGD XY module layer, and more importantly, more layers in the subdetector where the track ends. Also, the TPC reconstruction treats horizontal and vertical clusters in different ways, and the horizontal reconstruction works more efficiently. For more discussion on TPC reconstruction, please refer to [115].

In contrast, the high-angle samples display a double Gaussian distribution in the $\cos\theta$ plot, with one peak near $+0.5$ and another near -0.5. The positive peak arises from the high-angle forward tracks, while the negative peak stems from the high-angle backward tracks. In terms of momentum, most tracks in the high-angle subsamples are below 1 GeV. This two-peak pattern is not physical, but mostly a result of the design of the sample selection, and the in general poor reconstruction efficiency of trakcs that leave ND280 at near 90° angle w.r.t the neutrino beam.

The kinematic distributions of the FGD2 subsample are similar to those of FGD1, as expected.

In conclusion, among all subsamples, while muo forward-going subsamples show good agreement with previous selection results, the event kinematics distribution of the new 4π subsamples is heavily impinged by detector effects. The peak area in the phase spaces are more related to better detector and reconstruction efficiency, instead of large differential cross section. Still, the new subsamples demonstrate good purity and provide enough statistics for oscillation analysis purpose.

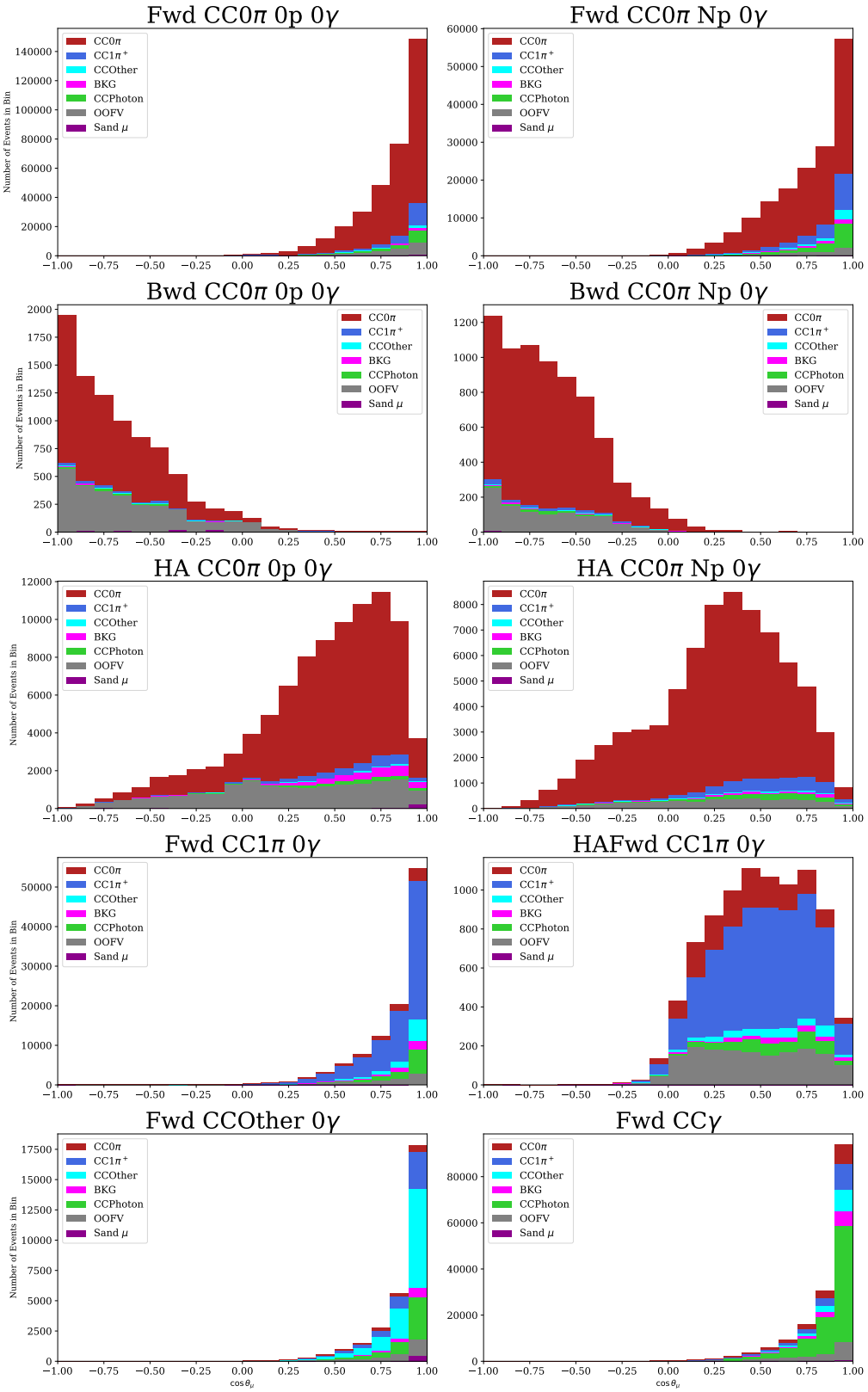

FIGURE 5.11: Distribution of muon $\cos\theta$ in all FGD1 subsamples of the selection using run 2,3,4 and 8 MC. The distribution is break down by topology.

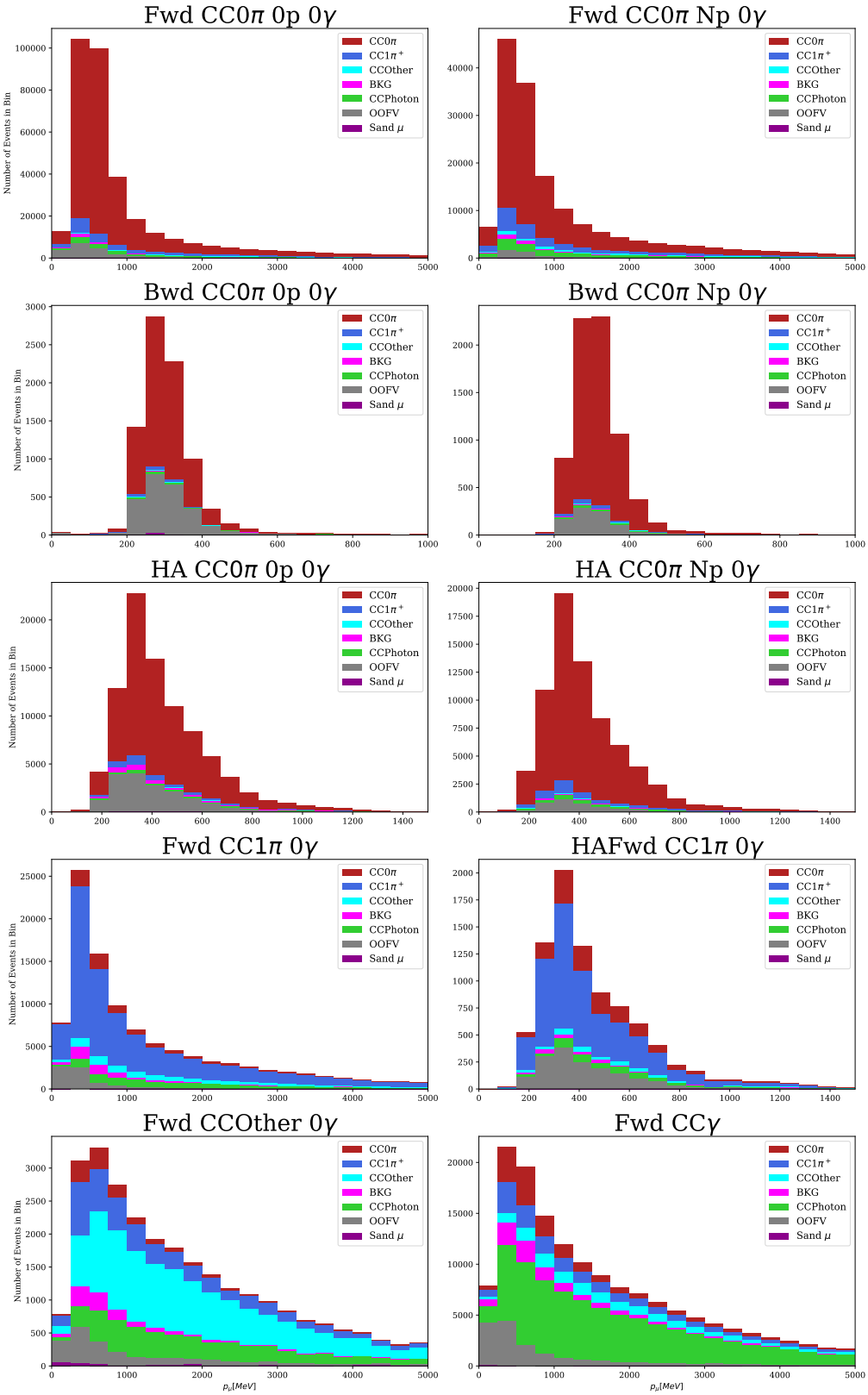

FIGURE 5.12: Distribution of muon momentum in all FGD1 sub-samples of the selection using run 2,3,4 and 8 MC. The distribution is break down by particle type.

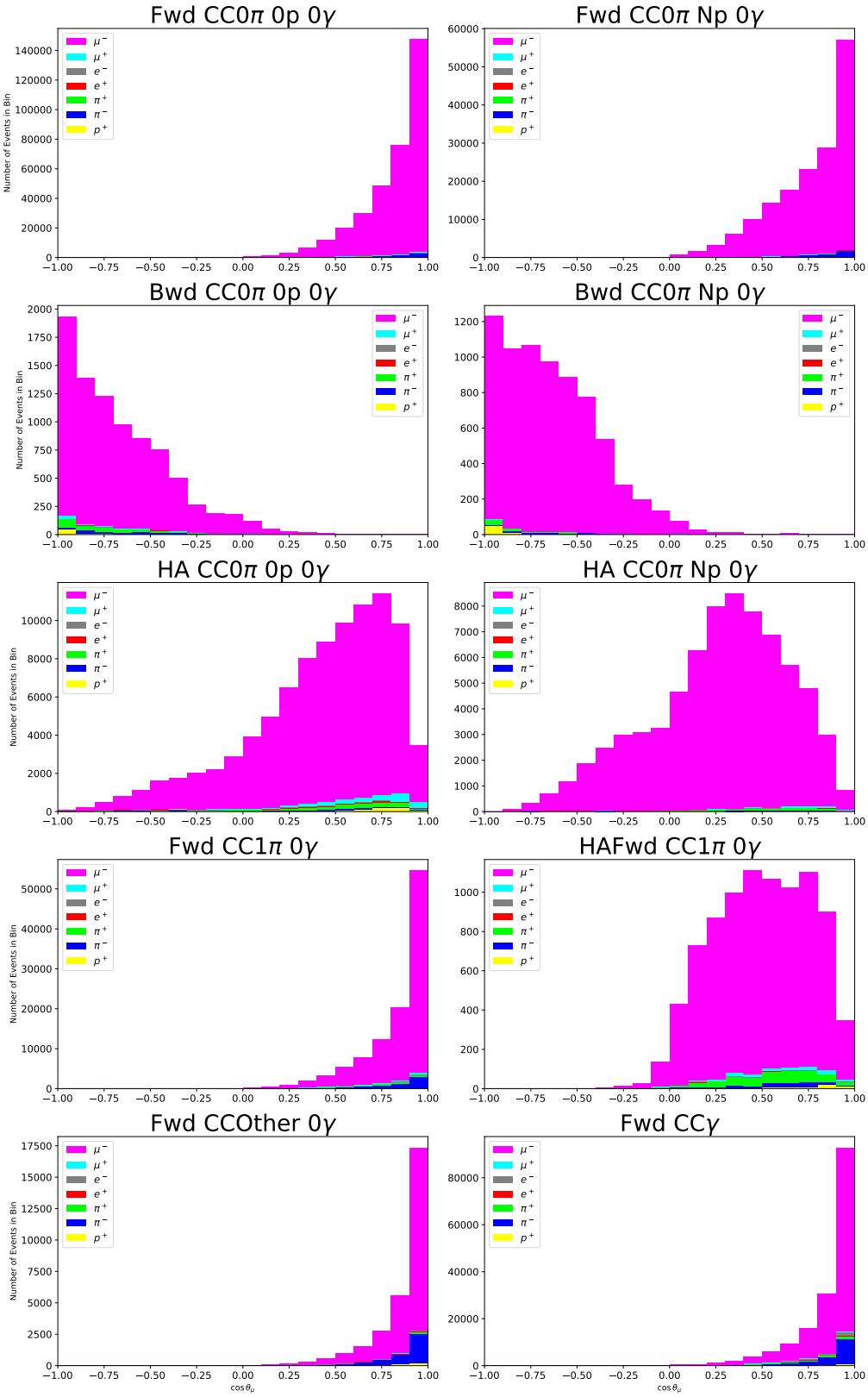

FIGURE 5.13: Distribution of muon $\cos\theta$ in all FGD1 subsamples of the selection using run 2,3,4 and 8 MC. The distribution is break down by particle type.

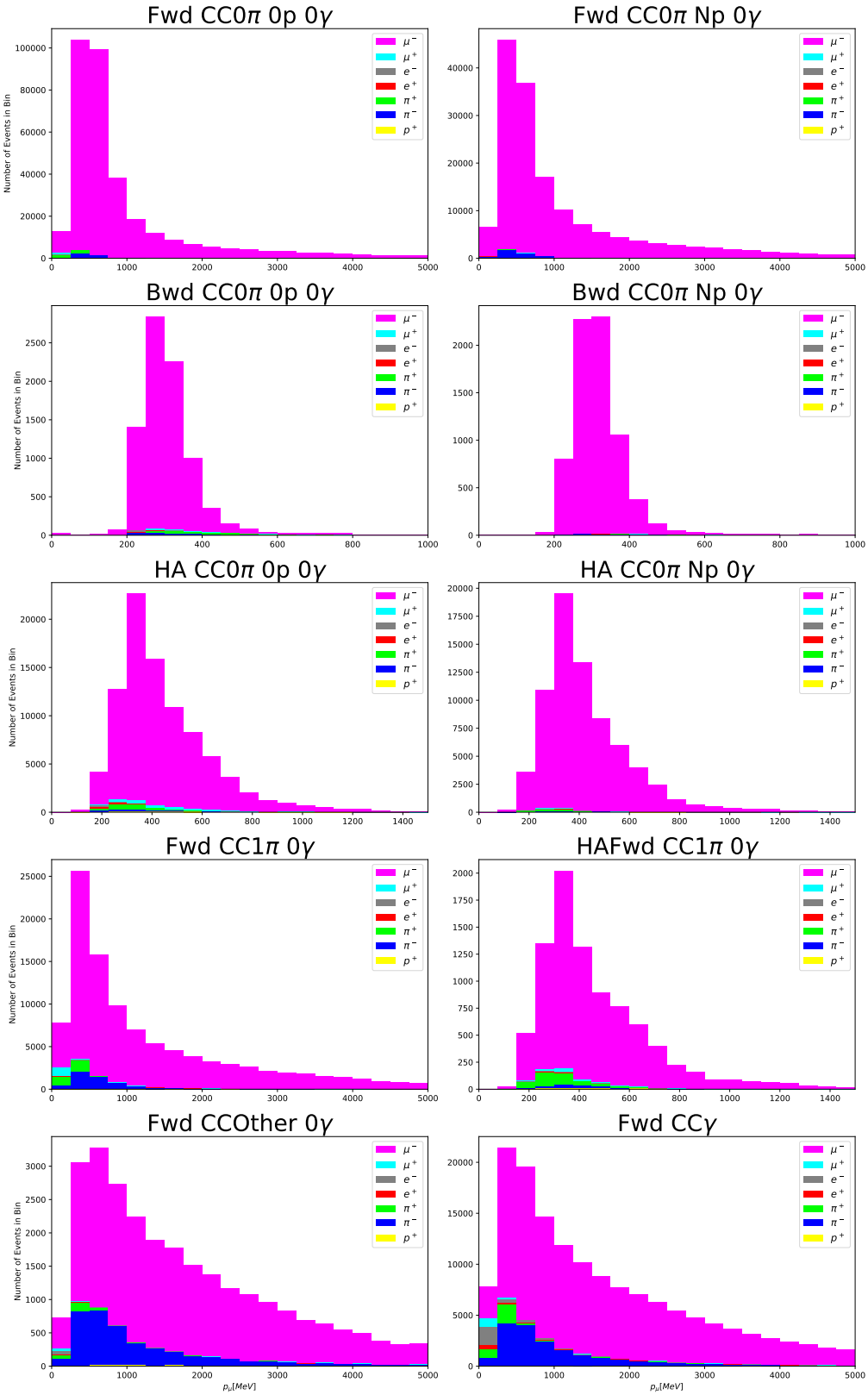

FIGURE 5.14: Distribution of muon momentum in all FGD1 sub-samples of the selection using run 2,3,4 and 8 production 6T MC. The distribution is break down by particle type.

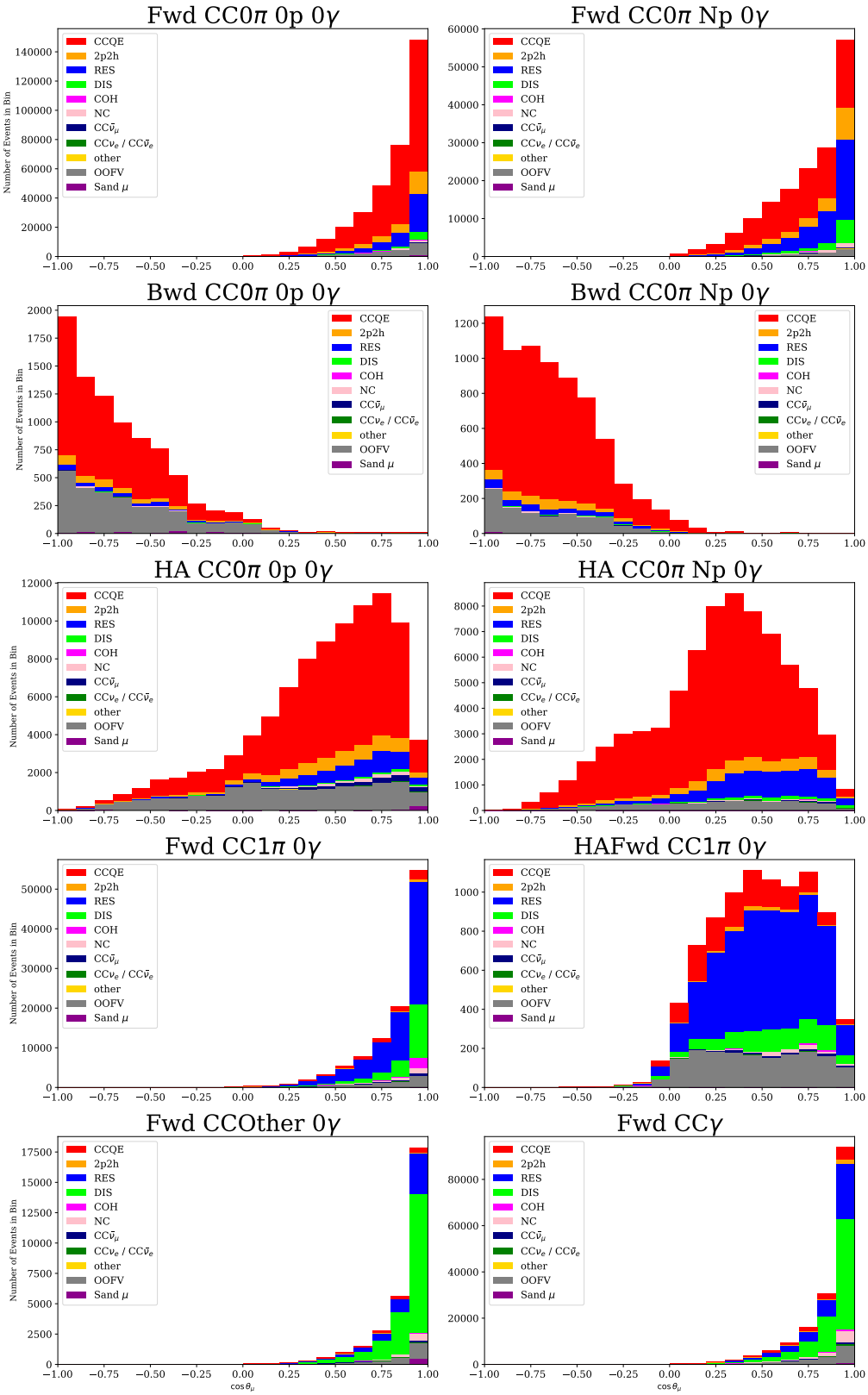

FIGURE 5.15: Distribution of muon $\cos\theta$ in all FGD1 subsamples of the selection using run 2,3,4 and 8 MC. The distribution is break down by neutino interaction type.

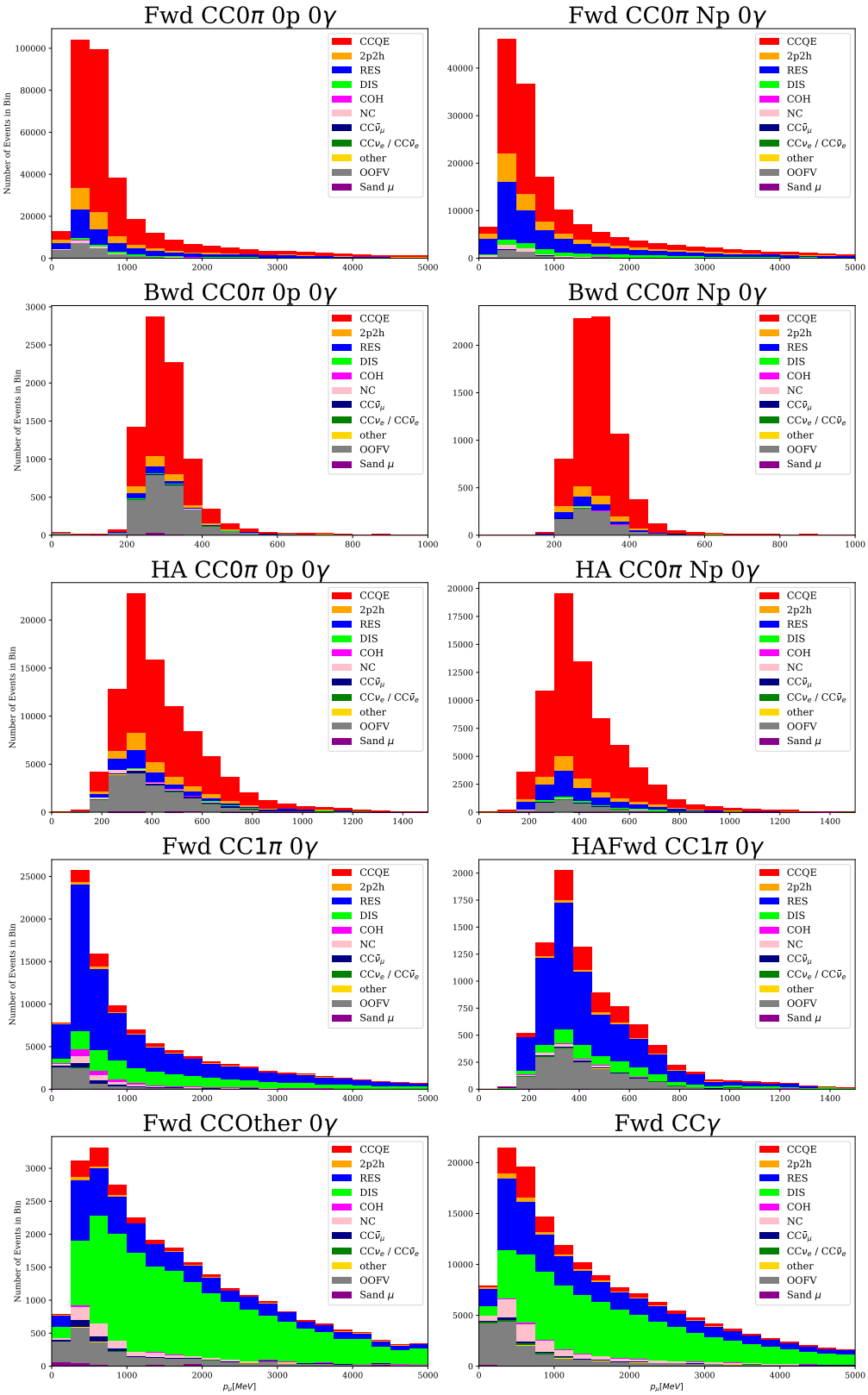

FIGURE 5.16: Distribution of muon momentum in all FGD1 subsamples of the selection using run 2,3,4 and 8 MC. The distribution is break down by neutino interaction type.

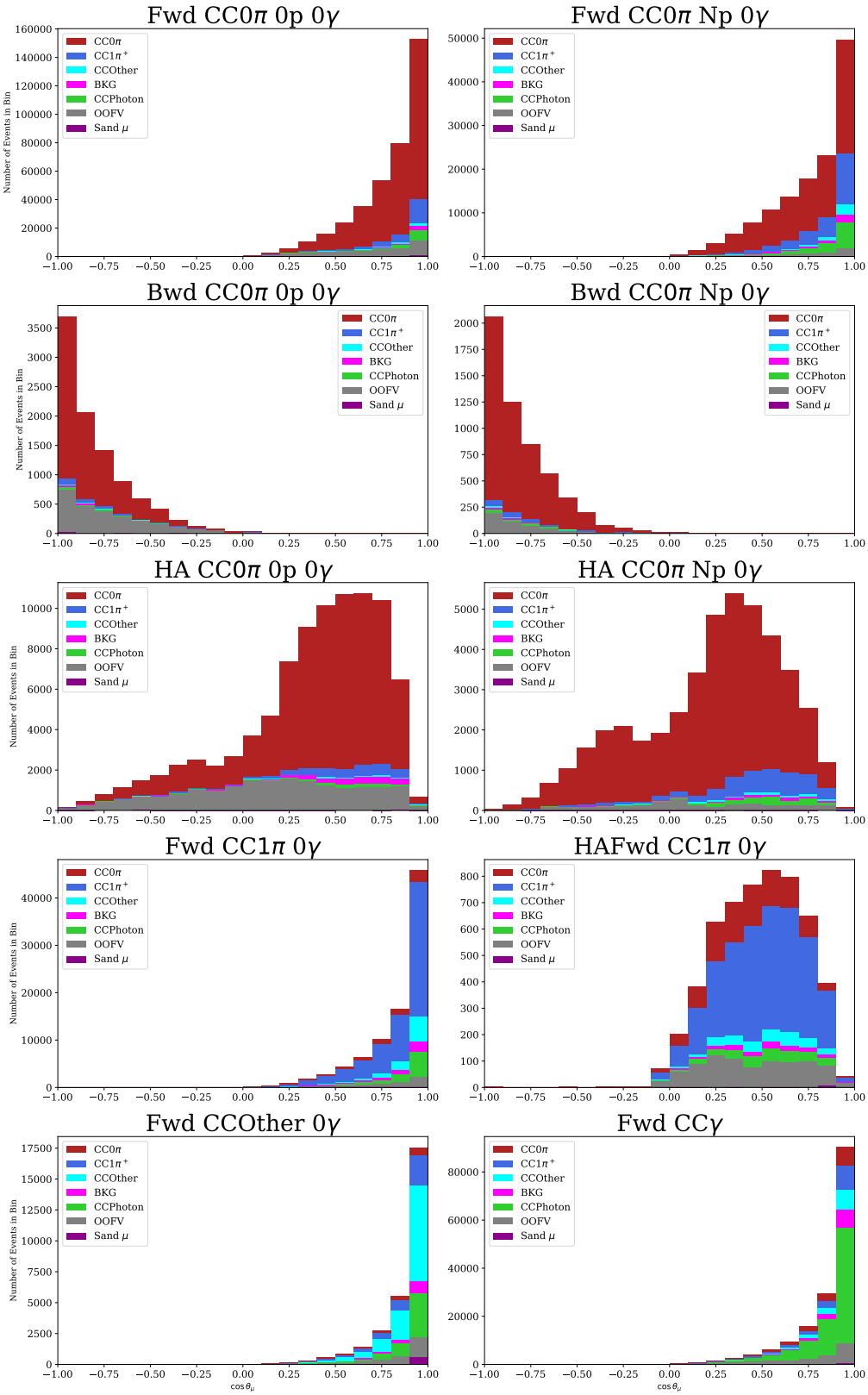

FIGURE 5.17: Distribution of muon $\cos\theta$ in all FGD2 subsamples of the selection using run 2,3,4 and 8 MC. The distribution is break down by event topology.

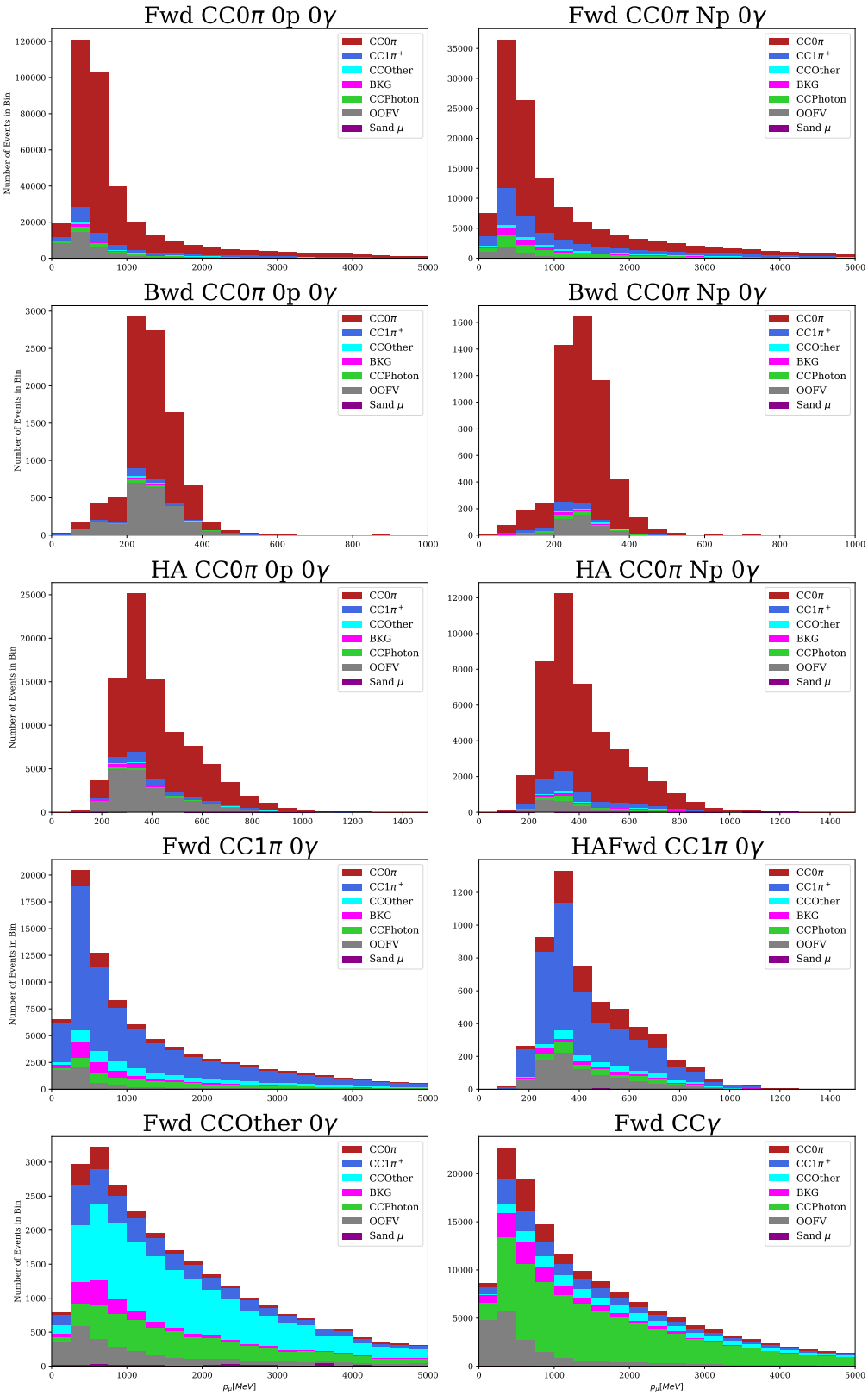

FIGURE 5.18: Distribution of muon momentum in all FGD2 sub-samples of the selection using run 2,3,4 and 8 MC. The distribution is break down by event topology.

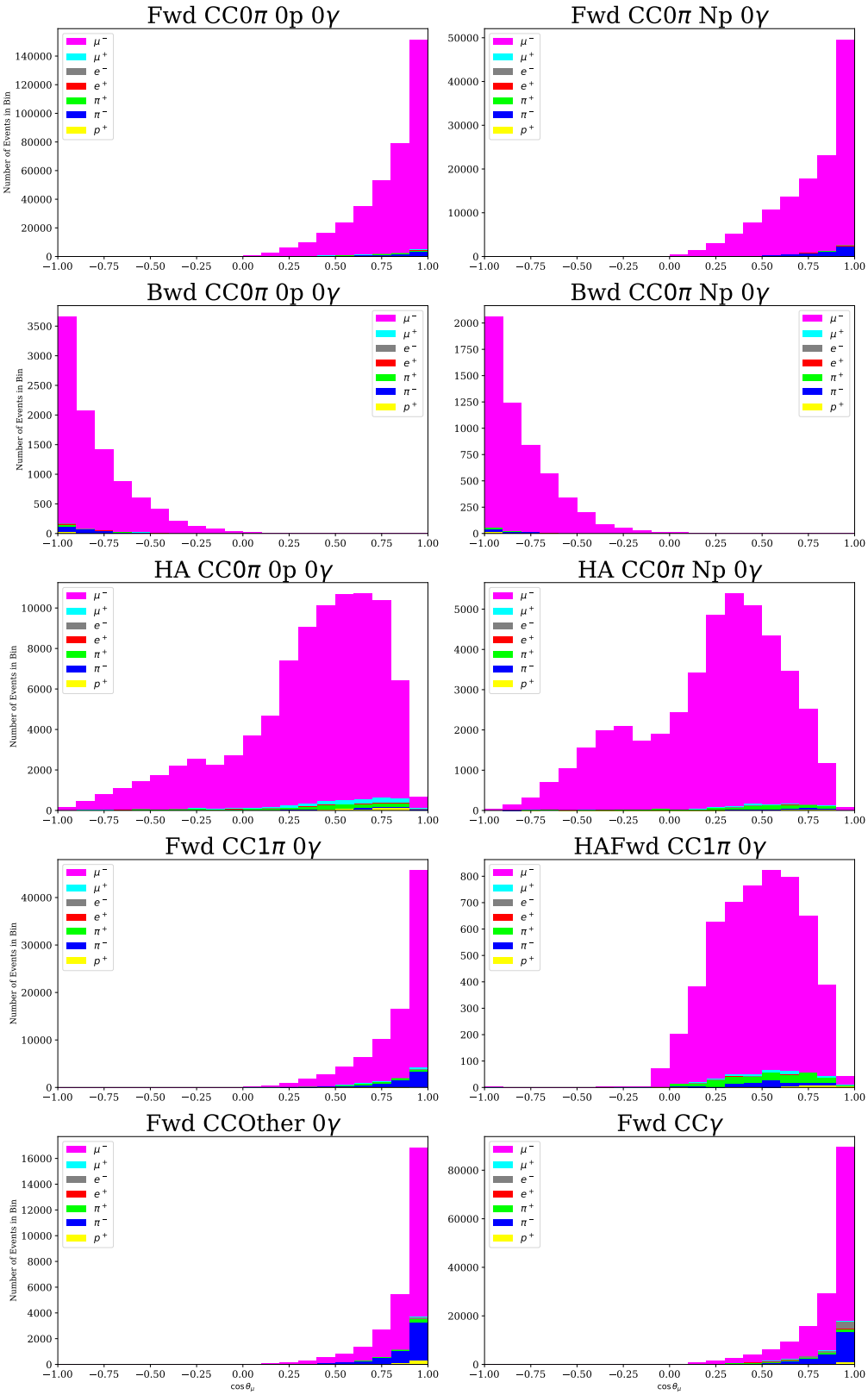

FIGURE 5.19: Distribution of muon $\cos\theta$ in all FGD2 subsamples of the selection using run 2,3,4 and 8 MC. The distribution is break down by particle type.

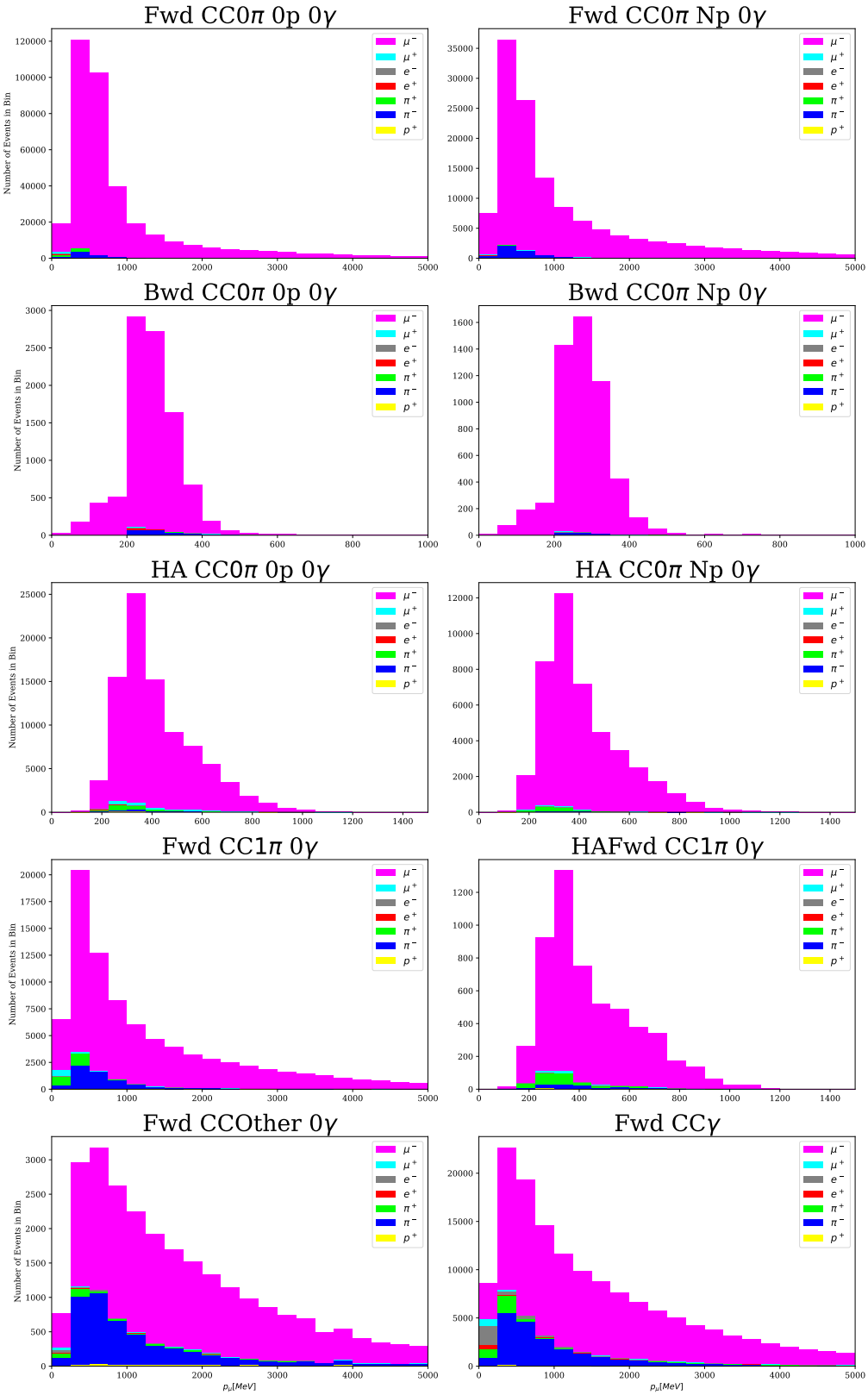

FIGURE 5.20: Distribution of muon momentum in all FGD2 sub-samples of the selection using run 2,3,4 and 8 production 6T MC. The distribution is break down by particle type.

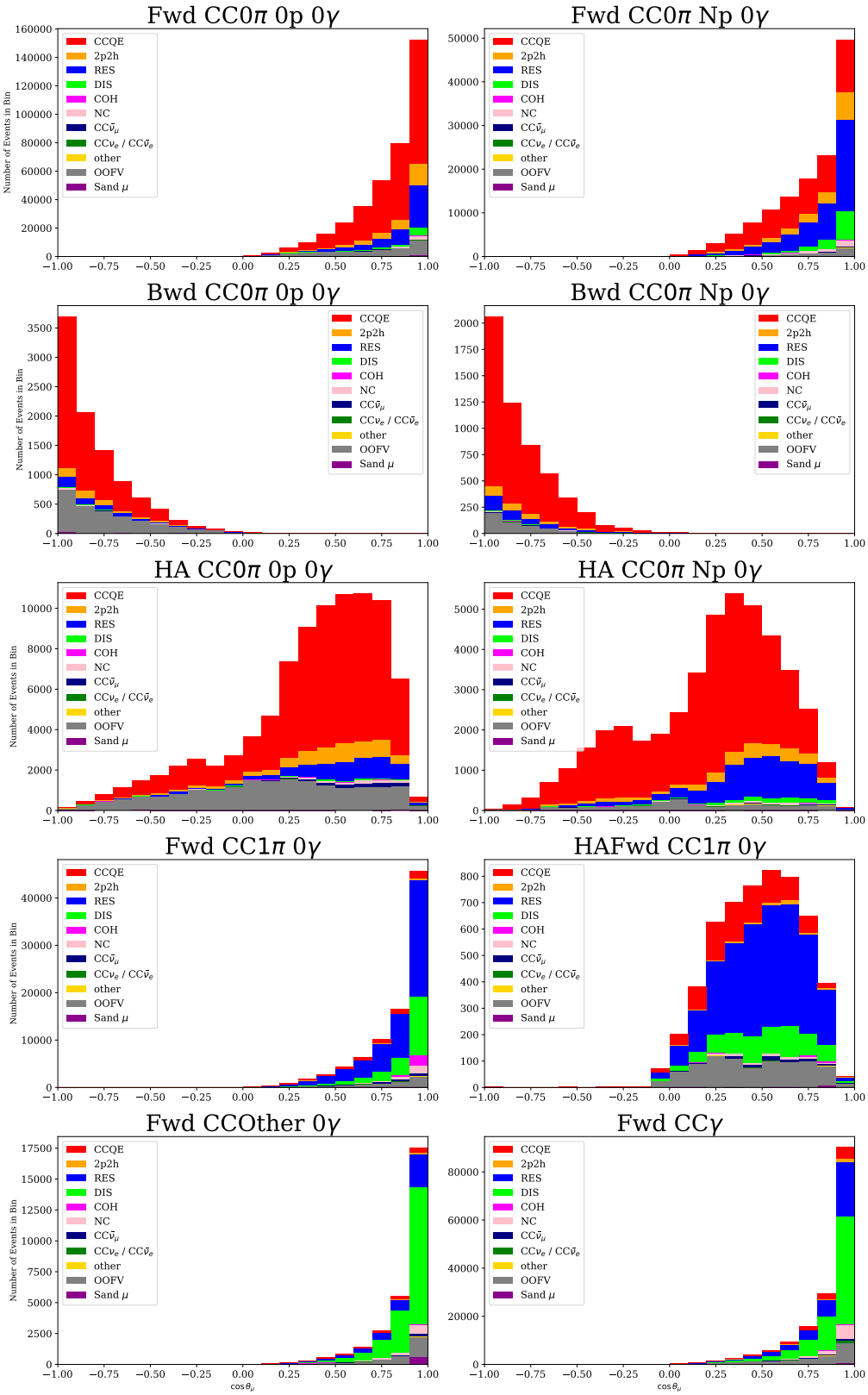

FIGURE 5.21: Distribution of muon $\cos\theta$ in all FGD2 subsamples of the selection using run 2,3,4 and 8 production 6T MC. The distribution is break down by neutrino interaction type.

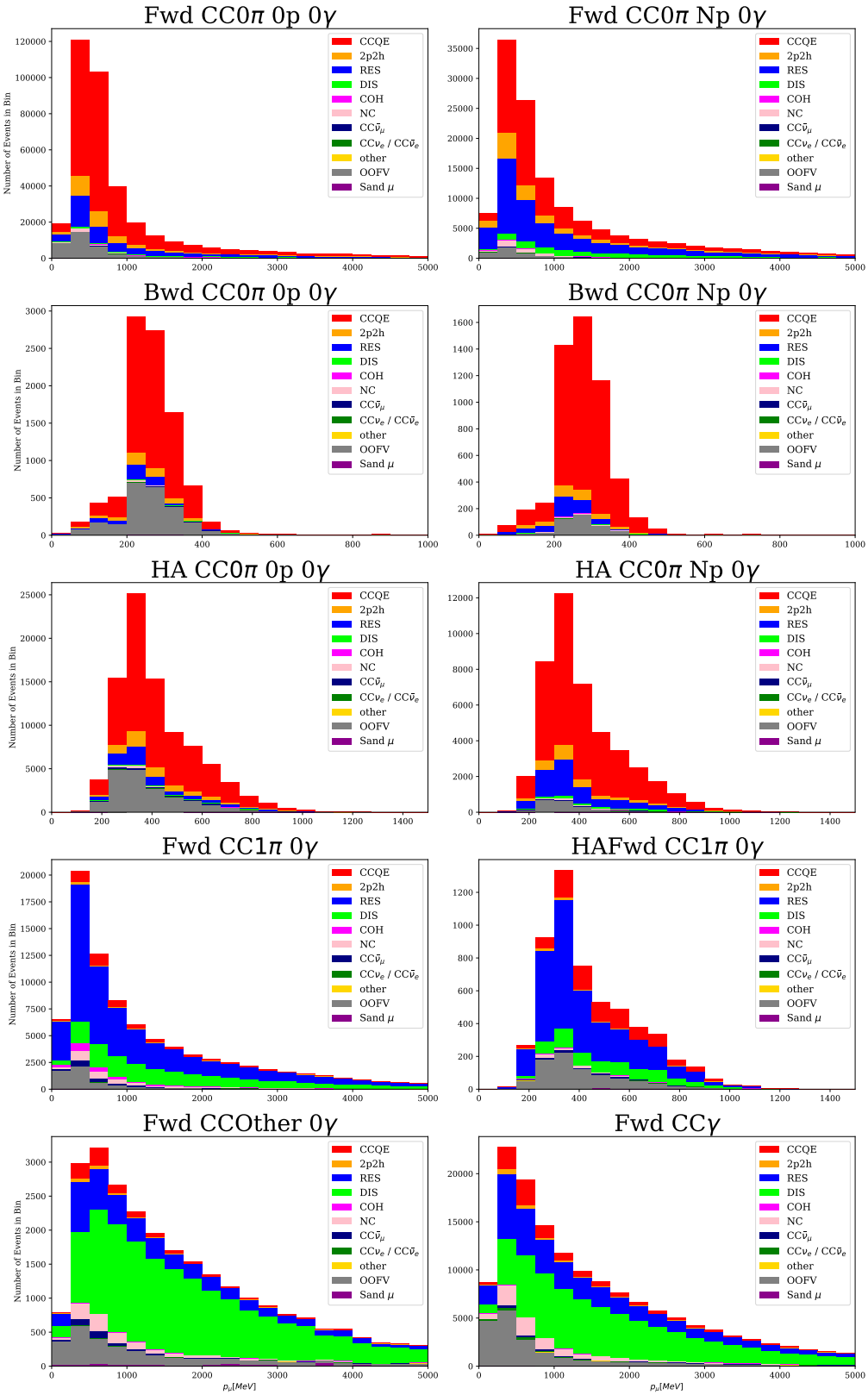

FIGURE 5.22: Distribution of muon momentum in all FGD2 subsamples of the selection using run 2,3,4 and 8 MC. The distribution is break down by neutrino interaction type.

Figures 5.23 and 5.24 display the efficiencies and purities for each topology. Each topology, such as CC0π0p, CCOther, and so on, corresponds to a single line in these plots. It is important to note that when calculating the efficiencies of the CC0π0p and CC0πNp samples, both are normalized to the number of true CC0π events in the MC simulation. This explains why the efficiencies for the high-angle and backward subsamples appear low in the plots and Table 5.5. The binning used here is the same as the tentative binning used for test fit runs, which is more coarse than the uniform binning used in the kinematic plots, for the purpose of smoothing out fluctuations in region with sparse event distribution.

Let's consider the CC0π0p subsample as an example. When calculating its efficiency, the denominator includes not only the CC0π event that goes backward and lacks a reconstructed pion and proton; instead, it includes all charged-current events without a final state pion, regardless of the muon's direction or the number of protons. This can be attributed to two factors. First, the new high-angle samples are defined based on detector responses, specifically the number of TPC hits, making it impossible to define a 'true' high-angle event solely using vertex truth information before any detector response is involved. Second, the combination of the no-proton and has-proton subsamples in the efficiency calculation arises from the fact that the highland code used for this purpose has not been updated accordingly yet as of when this thesis is writen. However, this feature will be implemented before the next summer, ensuring that the CC0π0p and CC0$\pi N p$ samples will have separate true event denominators when calculating efficiency.

Across all subsamples, the low-angle forward subsamples dominate the forward regions, which is consistent with previous findings in [105, 109]. Although the contribution of the new subsamples may not be very visible in the muon momentum plots, it is clearly visible in the $\cos\theta$ plots. There are peaks in the very backward region, and bumps near ± 0.5 due to the high-angle CC0π samples. In both FGDs, the efficiency in the backward region is a lot worse than in the forward region. This is mainly because the backward tracks only comes from ToF flipping using ToF information, which is only available in a small fraction of events. Other reasons include the fact that events with a backward going muon usually involve a large momentum transfer and more particles in the event, making reconstruction more prone to errors. The FGD2 backward samples exhibit better efficiency than FGD1, which may be attributed to the fact that these events come from the FGD1-FGD2 tracks,

while FGD1 backward events are from the FGD1-P0D tracks, and FGD1 has better timing performance than the P0D.

In terms of purities, all new subsamples demonstrate good purity. The CC0π0p backward subsamples have a purity of 0.7, while CC0πNp purity is around 0.6. Once again, the FGD2 subsamples are slightly better than their FGD1 counterparts, thanks to FGD1's advantage over the P0D.

Table 5.5 provides a summary of the efficiencies and purities of all subsamples. The backward subsamples appear with low efficiency due to forementioned reason.

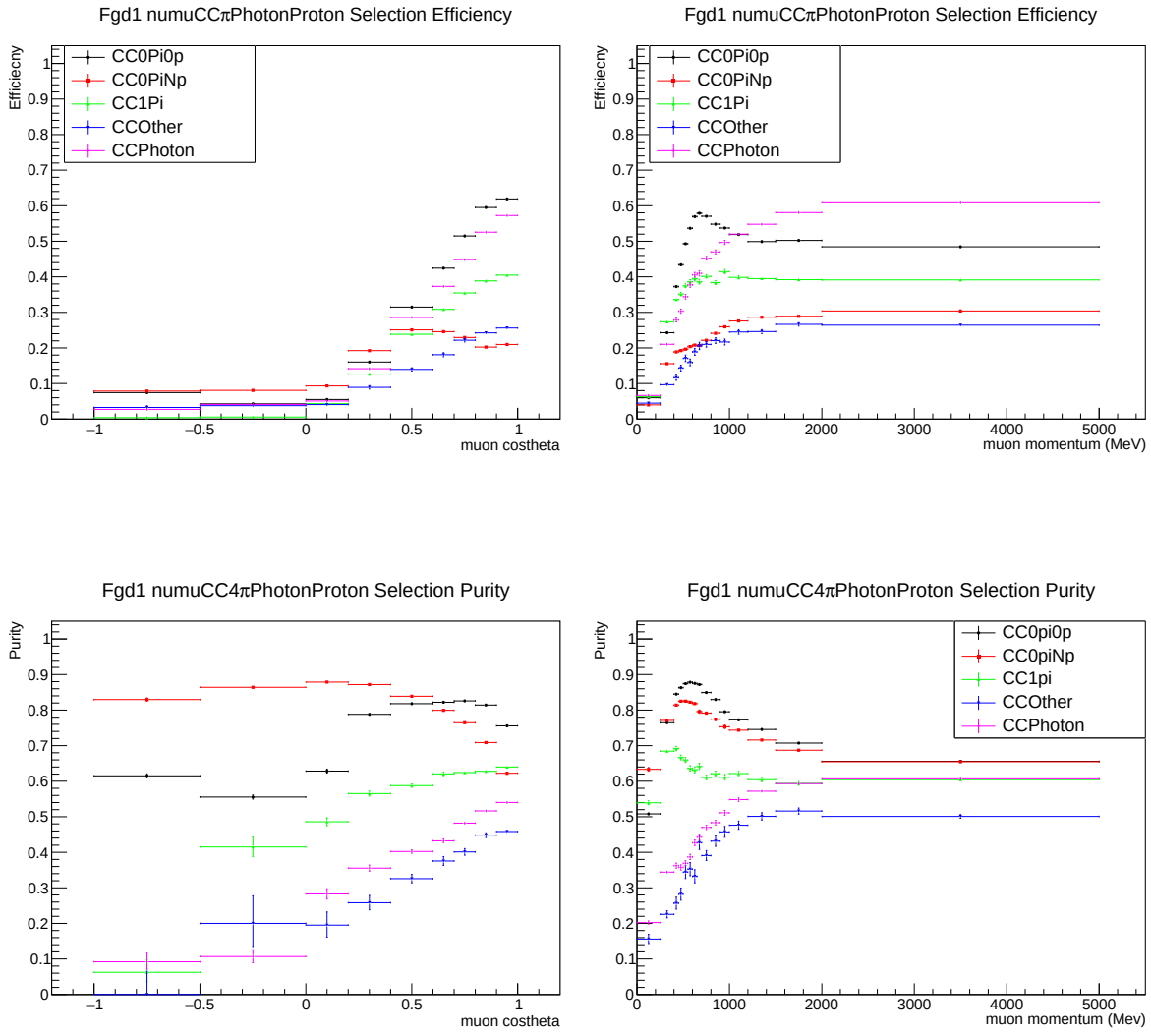

FIGURE 5.23: FGD1 selection efficiencies and purities. Top left: efficiency as a function of muon $\cos\theta$. Top right: efficiency as a function of muon momentum. Bottom left: purity as a function of muon $\cos\theta$. Bottom right: purity as a function of muon momentum.

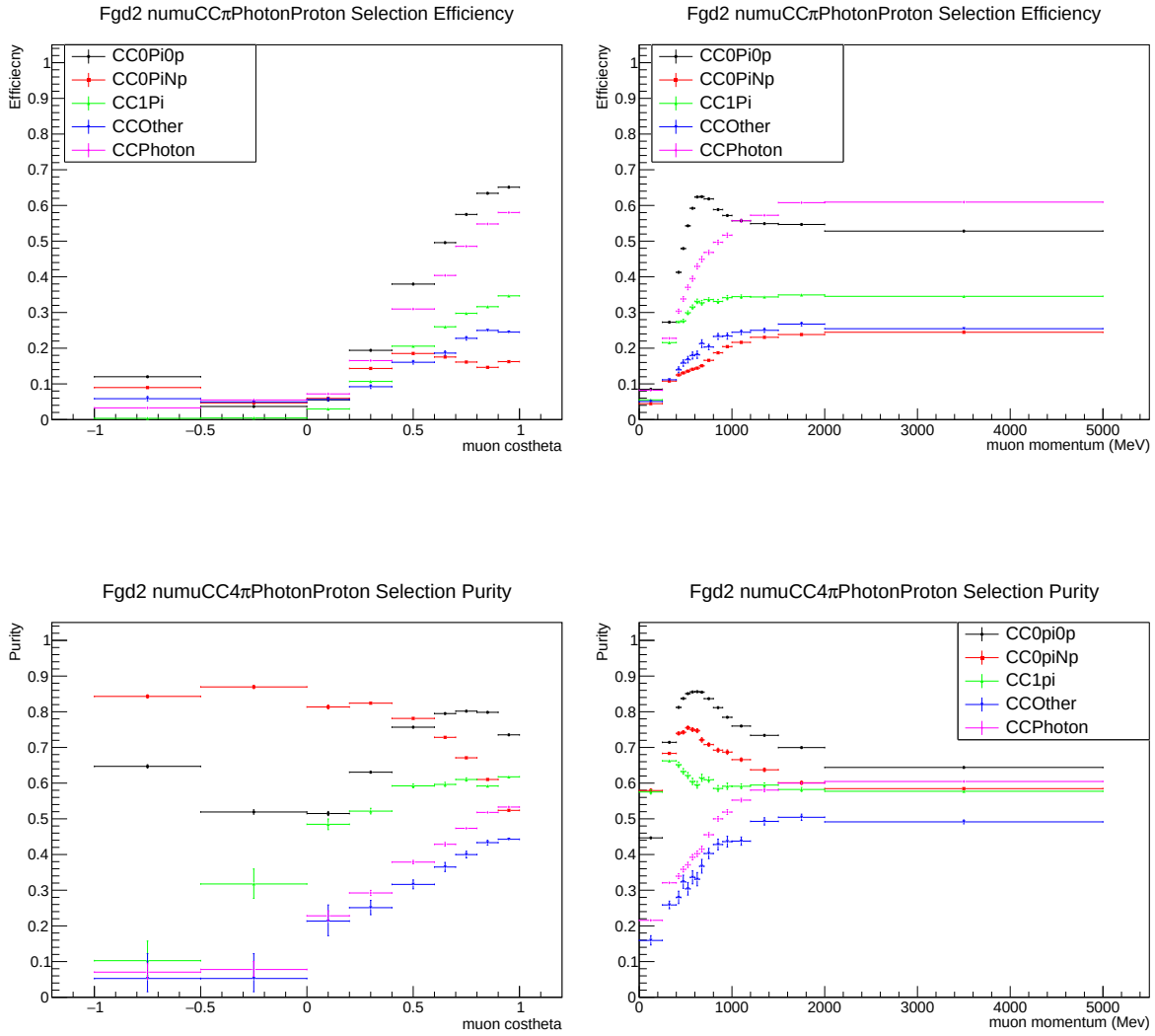

FIGURE 5.24: FGD2 selection efficiencies and purities. Top left: efficiency as a function of muon $\cos\theta$. Top right: efficiency as a function of muon momentum. Bottom left: purity as a function of muon $\cos\theta$. Bottom right: purity as a function of muon momentum.

Sample name	FGD1 efficiency	FGD1 purity	FGD2 efficiency	FGD2 purity
CC0π 0p Fwd	0.32	0.76	0.36	0.79
CC0π Np Fwd	0.14	0.64	0.10	0.73
CC0π 0p Bwd	0.01	0.68	0.01	0.63
CC0π Np Bwd	0.01	0.84	0.01	0.82
CC0π 0p HA	0.04	0.71	0.04	0.71
CC0π Np HA	0.04	0.81	0.03	0.85
CC1π Fwd	0.27	0.61	0.23	0.63
CC1π HA	0.02	0.53	0.01	0.53
CCOther	0.21	0.42	0.20	0.43
CCPhoton	0.44	0.50	0.45	0.51

TABLE 5.5: The efficiencies and purities of all subsamples selected by the CC4$\pi\gamma p^+$ selection.

Chapter 6

Systematic uncertainties of the 4π ND280 sample selection

This chapter focuses on evaluating the impact of detector systematic error on the number of events in each subsample of the ND280 4π selection.

The uncertainties on event numbers are influenced by two sources: statistical error and systematic error. Required to have more than 20 each, the statistical error in the ND280 sample bins can be approximated by a Poisson error which decreases as the total amount of data collected increases. This can be justified using the fact that the probability of a neutrino charged-current event happens and falls into a particular p_μ-$\cos\theta$ bin is very small, usually at the order of a few thousand at maximum; while the overall proton-on-target is over 10^{21}.

On the otherhand, the systematic errors arise due to the limitations of detectors and their models, and such errors do not diminish with the increase in data. Therefore, it is crucial to quantify the degree of imperfection in the MC simulation. T2K employs dedicated control samples to achieve this goal. These control samples are small and intended to demonstrate specific properties of detector response. By comparing the selection results of control samples in data and MC, the physical detector-MC difference is quantified and applied to the MC as a correction. The uncertainty of this correction is treated as a systematic uncertainty.

To propagate known sources of systematic uncertainties to the final samples, T2K employs the highland software. This chapter first details the propagation of different types of systematic uncertainty sources, then provides a comprehensive list. The list mostly

matches the one provided in [109], with the addition of the ToF systematic uncertainty error covered in Chapter 4, the vertex backward migration uncertainty, and the TPC-P0D matching efficiency. These new sources will be elaborated on in this chapter.

6.1 Propagation of systematic uncertainties in Highland2

Highland2, or highland, is the acronym for High Level Analysis at the Near Detector 2. Built upon CERN ROOT, highland was developed to perform physics analysis at a post-reconstruction level [116]. It is capable of reading and writing reconstruction files, applying corrections to files, selecting events and propagating systematic errors. Each systematic error source is modelled and described by a group of parameters.

In terms of evaluating systematic uncertainties, highland uses the toy experiment method. In a single toy experiment, the parameters of a systematic uncertainty source are randomly tossed according to given prior distributions. This will have an effect on all events; either it changes the weight a MC event carries; or it can affect whether an event gets selected or not, i.e. some selected in the nominal parameter setting get disqualified, some the other way around, resulting in a change in the final sample selected. By conducting toy experiments a large number of times, the uncertainty on the systematic model parameters is translated to an error on the number of events selected in each subsample.

Three different types of systematic uncertainty propagation methods are implemented in highland: weight-like, variation, and normalisation. This section will introduce the machinery of these three ways of propagation.

6.1.1 Weight-like

The efficiency of object reconstruction and matching can be different in data and MC, such as the matching efficiency of TPC and P0D objects, or the ECal tracking efficiency. To account for the systematic difference in such efficiencies between data and MC, an efficiency weight is applied to the MC. In each of the efficiency systematics, a control sample selection was designed and applied to MC and data respectively. The overall efficiency (not in a particular bin) evaluated in control samples, $\epsilon^{\mathrm{CS}}_{\mathrm{data}}$ and $\epsilon^{\mathrm{CS}}_{\mathrm{MC}}$, provide a

data-MC ratio:

$$r = \frac{\epsilon^{\mathrm{CS}}_{\mathrm{data}}}{\epsilon^{\mathrm{CS}}_{\mathrm{MC}}} \tag{6.1}$$

It was assumed that this ratio computed from the control sample selection will remain the same in the oscillation analysis selection such as the ND280 4π sample selection. The correction is applied to all MC events as a weight using the value r. Conversely, a weight can also be applied to inefficiencies, given by

$$r_{\mathrm{ieff}} = \frac{1 - \epsilon^{\mathrm{CS}}_{\mathrm{data}}}{1 - \epsilon^{\mathrm{CS}}_{\mathrm{MC}}} \tag{6.2}$$

Such treatment is not perfect; r and r_{ieff} themselves are also subject to error. To propagate the uncertainties brought by the inclusion of these weights, the ratio r is varied in every toy experiment:

$$r' = (1 + \alpha\delta)r \tag{6.3}$$

where δ is the evaluated error of r, α is a normally distributed random variable that varies in each toy experiment.

6.1.2 Normalisation

Certain parameters have an impact on the total number of events that happen at ND280; for example, the mass of FGD1 should be proportional to the total number of events, since it is propotional to the number of target nuclei in ND280.

To propagate the uncertainty on FGD1 mass to the final number of events selected, a weight

$$w_{\mathrm{normalisation}} = 1 + w_{\mathrm{correction}} + \alpha\delta \tag{6.4}$$

is generated in each toy experiment and applied to all events, according to external knowledge and applied to relevant events.

The toy variation method is the same as in weight-like systematic error propagation. Again, $w_{\mathrm{correction}}$ is the computed correction, α is a normally distributed random variable, and δ is the error of $w_{\mathrm{correction}}$. The only difference is that a normalisation weight is applied exactly once to relevant events.

6.1.3 Variation

A more mathematically concrete but computationally demanding way to treat systematic uncertainties is by variation. In the context of ND280 systematic error propagation, two types of sources of systematic uncertainties are propagated using the variation method:

1. The uncertainty is on an underlying physics parameter which affects a reconstructed variable and subsequently whether the event can get selected by the sample selection. For instance, the reconstruction of charged particle momentum linearly depends on the magnetic field strength B. To propagate errors induced by an underlying parameter x in toy events, in each toy event, a new parameter value is thrown as

$$x' = x + \alpha\delta x \tag{6.5}$$

   The error is then propagated onto the reconstructed variable using numerical Gaussian error propagation. The reconstructed variable in each toy, $v_{\mathbf{toy}}$, is varied from its nominal value $v_{\mathbf{nominal}}$ in the following way:

$$v_{\mathbf{toy}} = v_{\mathbf{nominal}} + \alpha\delta v = v_{\mathbf{nominal}} + \alpha\frac{dv}{dx}\delta x \tag{6.6}$$

   and the selection is rerun on the varied variable. Taking particle momentum p and TPC magnetic field strength B, the relation between them is $\frac{\delta B}{B} = \frac{\delta p}{p}$, and the toy experiment momentum variation should be $\delta p = \alpha\frac{p}{B}\delta B$ .Each event is different from its nominal status; some selected events will be disqualified, and some not selected will be picked up in the toy. Thus, the variation of the low-level variable now reflects on the number of selected events. By conducting the toy experiment for a large number of times, the error on the number of events in each subsample caused by the error on x, one example of which is B, can be quantified.

2. Another type of systematic error propagated using the variation method in ND280 analyses is the data-MC discrepancy in more 'raw' (as opposed to reconstructed) information collected by detectors, for instance the ToF value distribution. In such cases, the difference between data and MC distributions are quantified, and corrections are designed accordingly for MC to mitigate such differences. For each correction, the uncertainty on the parameters of such a correction is propagated

using the variation method. To correct a normally distributed variable, a Gaussian correction is applied:

$$x_{\mathrm{MC}} = x_{\mathrm{nominal}} + x_{\mathrm{corr}} \times \mathcal{N}(\mu, \sigma) \tag{6.7}$$

where $\mathcal{N}(\mu, \sigma)$ obeys a Gaussian distribution centered at μ with a standard deviation of σ. x_{corr}, μ and σ all come from control sample studies.

To propagate the uncertainty introduced by such a correction, an additional smearing term is added to the variable:

$$x_{\mathrm{MC}} = x_{\mathrm{nominal}} + \Big(x_{\mathrm{corr}} \times \mathcal{N}(\mu, \sigma)\Big) + \Big(x_{\mathrm{err}} \times \sigma\Big) \tag{6.8}$$

Again, σ is a normally distributed random variable that varies in toy experiments. The distribution of σ, and its coefficient x_{err}, are evaluated for each systematic source using case-by-case methods. [1]

6.2 ND280 detector systematic uncertainties

To estimate the systematic uncertainty on the number of events in each of the two-dimensional bins in the 4π samples, 29 systematic uncertainty sources are considered. Most of them remain the same as in the previous T2K oscillation analyses, while there are three new additions: The first is the ToF resolution systematic error, which describes the uncertainty caused by introducing the ToF track sense flipping, and the intrinsic resolution of the ToF detectors. The second new source of error considered in this thesis is the vertex backward migration, which describes the situation where other particles in the final state get mis-identified as the muon, hence causing the vertex position to be reconstructed away from the real location. Thirdly, the TPC-P0D matching efficiency systematic source is introduced to the oscillation analysis for the first time. The evaluation and parameters of this systematic error remain unchanged from [100]. This section will first cover the newly introduced systematic uncertainties sources, then provide an overview of other

[1] The first correction term is written as $\mathcal{N}(\mu, \sigma)$ instead of σ to emphasise the fact that it is a normal distribution in events, rather than toy experiment. The correction terms to different events are distributed normally; the correction to a particular event remains the same in all toy experiments. In the ND280 software the correction is included in the input file and not handled by the error propagation code.

sources included in this study. Finally, an estimation of the relative error induced by ND280 detector effects will be provided.

6.2.1 Time of flight

As introduced in Chapter 5.1, the most important feature of the 4π sample selection is to include charged-current neutrino events with backward or high-angle going muons. However, since previous T2K oscillation analyses only included events with a forward-going muon, the reconstruction software assumed that all tracks were forward going, that is, travelling from the end closer to the beam source, to the end that is farther from the source. This is not necessarily correct, and to find those backward-going muon tracks, a ToF sense correction is implemented, as covered in Sec. 4. This new treatment inevitably adds new systematic uncertainties to the number of events selected in each sample.

First off, like all other physical quantities measured, the ToF information used to determine the sense of the track has intrinsic errors due to an imperfect detector. Also, a ToF correction is implemented to improve MC-data agreement; here are also errors associated with the parameters in such a correction, which also need to be considered by the systematic uncertainty evaluation process.

To propagate such error, a variation-like systematic is implemented in highland. In each toy experiment, a track's time of flight t_{track} is given by the following equation:

$$t_{\text{track}} = t_{\text{nominal}} + t_{\text{correction}} + \alpha\sigma_{\text{topology, run}} \tag{6.9}$$

where t_{nominal} is the nominal time from reconstruction, $t_{\text{correction}}$ is the correction introduced in Chapter 4, α is a Gaussianly-distributed dimensionless number that varies by event and by track, and $\sigma_{\text{topology, run}}$ is the ToF topology and run specific error [2] .
As described in Sec. 6.1, the scale of the variation (or smearing) associated with a correction, in the ToF case $\sigma_{\text{topology, run}}$, should be the error on the correction parameters. The current implementation of the ToF correction contains five parameters: the detector resolution σ, forward (backward) track bias $\mu_{\pm}$, and the proportion of $+10$ and -10 ns

[2] In some rare cases, a track can simultaneously belong to two different ToF topologies, for instance a track starting from FGD1 can first traverse FGD2, then proceed to the side ECal. Such a track can be considered both a FGD1-ECal track and a FGD1-FGD2 track. For these tracks, separate variations are applied to separate ToFs: a variation α_1 is applied to FGD1-ECal ToF, another variation α_2 applied to FGD1-FGD2 ToF.

shifted tracks, f_1 and f_2. Among all parameters, σ is the most important one because of its large impact on the ToF track distribution. Hence, in this study, only the error on σ is considered. The error on σ was evaluated using a χ^2 interval method: when performing the fit described in Sec. 6.1 to determine the best parameters for the correction, a χ^2 test statistic was used to quantify the resemblance of data and corrected MC. After the best-fit point was found, all other parameters were fixed, and σ alone was varied to construct a 68% confidence interval. For a mathematical explanation of this method, please refer to [117]. After the χ^2 interval was found, the uncertainty used in error propagation is half the length of the interval. In this study, each ToF topology has its own correction parameter, hence a dedicated error is required. FHC run 8 and RHC runs are also treated separately. In the end, there are 3 (FHC, run 8, RHC) $\times$ 22 (number of topologies) = 66 smearing parameters. When scanning the parameter space, the step length for σ is 0.2 ns. To avoid underestimating errors, they were artificially increased to the next integer multiple of 0.5 ns. This is done by requiring that in the ToF distribution of each ToF topology, 68% of the bins are covered by the 1σ systematic error. This ensures that the systematic error can cover the discrepancy between the MC simulation and the data within the statistical error of the data's Poisson distribution. An example can be found in Fig. 6.1. For a comprehensive list of all smearing parameters, please see Table. 6.1. The smearing parameters for run 8 are usually larger than those in other runs, which is understandable because of the poor initial data-MC agreement and consequent stronger correction. The FGD2HAFwd ECal track-like topology has a particularly large error on its correction parameter, which is due to a very large data-MC discrepancy that might be down to an hardware issue.

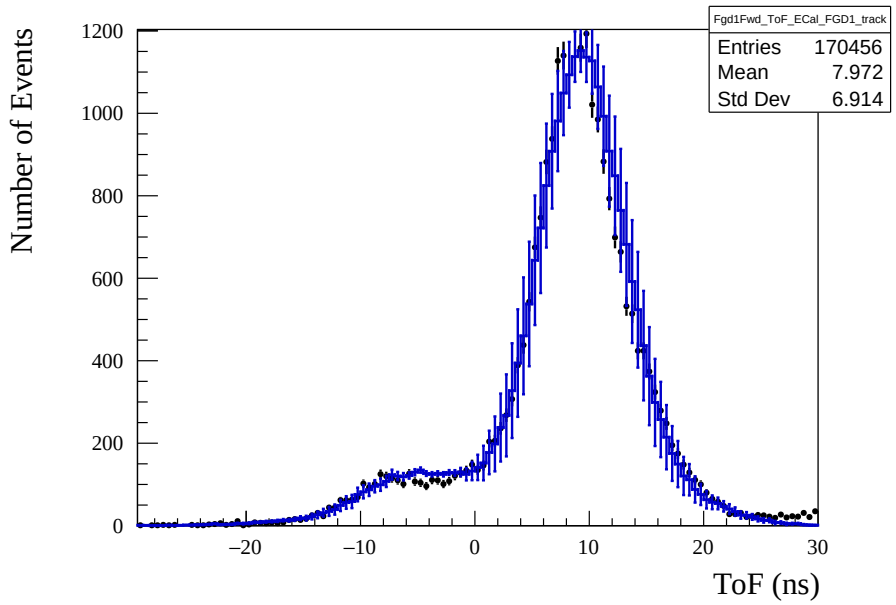

FIGURE 6.1: The systematic error induced by the ToF resolution in tracks belonging to the FGD1 forward ECal track topology, as a function of ToF between FGD1 and barrel ECal, in run8. The black dots are data, and the blue vertical bars are MC 1σ error range. MC and its error are normalised to data using area.

ToF Topology	$\sigma_{\text{FHC run8}}(ns)$	$\sigma_{\text{FHC run2-4}}(ns)$	σ_{RHC}
Fgd1Fwd_ToF_ECal_FGD1_track	0.5	0.5	0.5
Fgd1Fwd_ToF_ECal_FGD1_shower	0.5	0.5	0.5
Fgd1Bwd_ToF_P0D_FGD1_track	0.5	0.5	0.5
Fgd1Bwd_ToF_P0D_FGD1_shower	1.0	0.5	0.5
Fgd1Bwd_ToF_ECal_FGD1_track	1.0	0.5	0.5
Fgd1Bwd_ToF_ECal_FGD1_shower	1.0	0.5	0.5
Fgd1HAFwd_ToF_ECal_FGD1_track	1.0	0.5	0.5
Fgd1HAFwd_ToF_ECal_FGD1_shower	0.5	0.5	0.5
Fgd1HABwd_ToF_ECal_FGD1_track	1.5	0.5	0.5
Fgd1HABwd_ToF_ECal_FGD1_shower	0.5	0.5	0.5
Fgd2Fwd_ToF_ECal_FGD2_track	1.0	0.5	0.5
Fgd2Fwd_ToF_ECal_FGD2_shower	0.5	0.5	0.5
Fgd2Fwd_ToF_DSECal_FGD2_track	0.5	0.5	0.5
Fgd2Fwd_ToF_DSECal_FGD2_shower	0.5	0.5	0.5
Fgd2Bwd_ToF_ECal_FGD2_track	1.0	0.5	0.5
Fgd2Bwd_ToF_ECal_FGD2_shower	1.0	0.5	0.5
Fgd2HAFwd_ToF_ECal_FGD2_track	2.5	0.5	0.5
Fgd2HAFwd_ToF_ECal_FGD2_shower	1.0	0.5	0.5
Fgd2HABwd_ToF_ECal_FGD2_track	1.0	0.5	0.5
Fgd2HABwd_ToF_ECal_FGD2_shower	0.5	0.5	0.5
Fgd1Fwd_ToF_FGD1_FGD2_track	0.5	0.5	0.5
Fgd2Bwd_ToF_FGD2_FGD1_track	1.0	0.5	0.5

TABLE 6.1: Summary of the smearing values, or the error, on the ToF correction parameters, as evaluted by the χ^2 contour method.

The expected error on number of events selected is plotted in Fig. 6.2 and Fig. 6.3. The backward samples are mostly affected by this error, since most of their events come from track flipping.

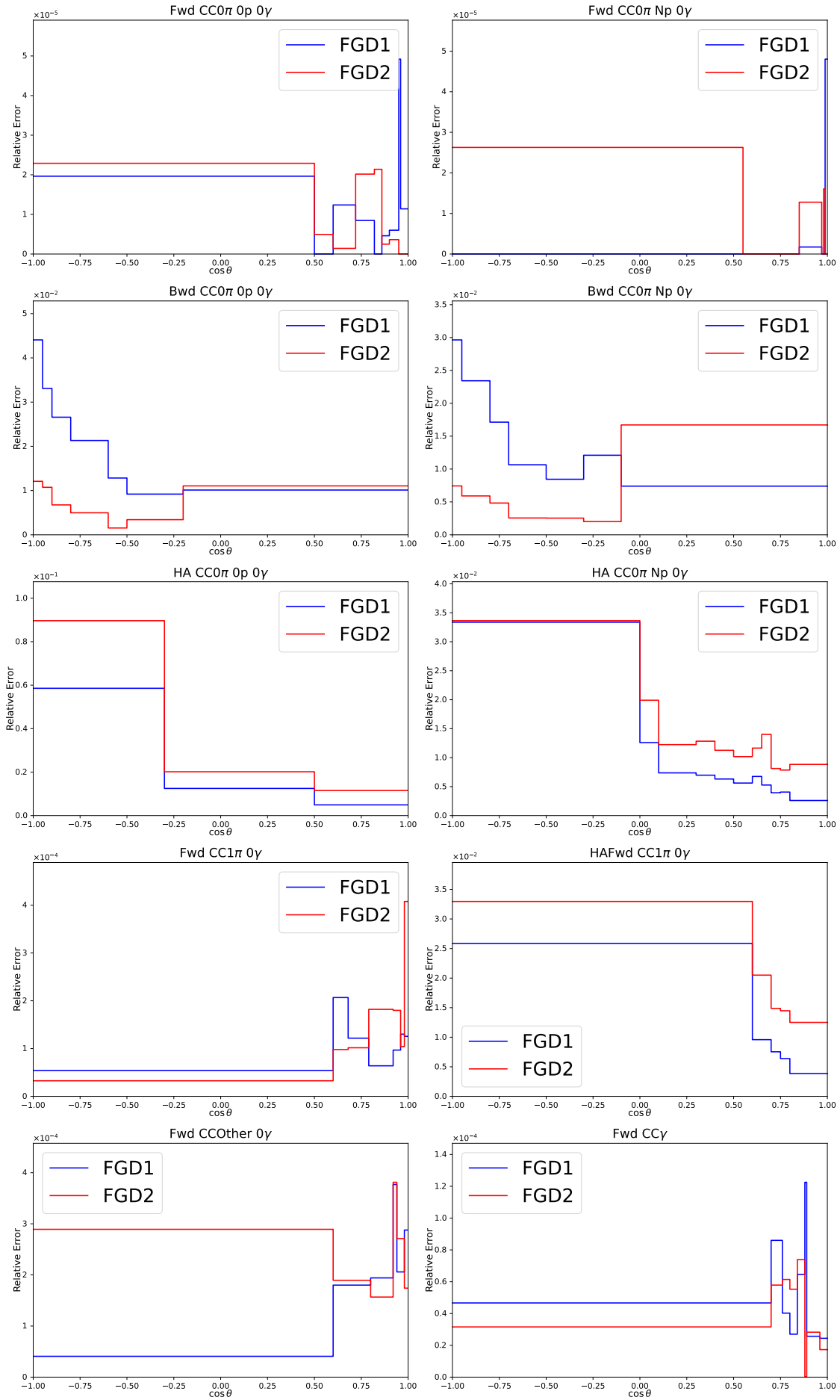

FIGURE 6.2: The relative error in the 4π subsamples caused, by time of flight resolution evaluated using highland2 propagation and parameters described before, as a function of muon $\cos\theta$. The blue solid line stands for events originating in FGD1, and red line for FGD2.

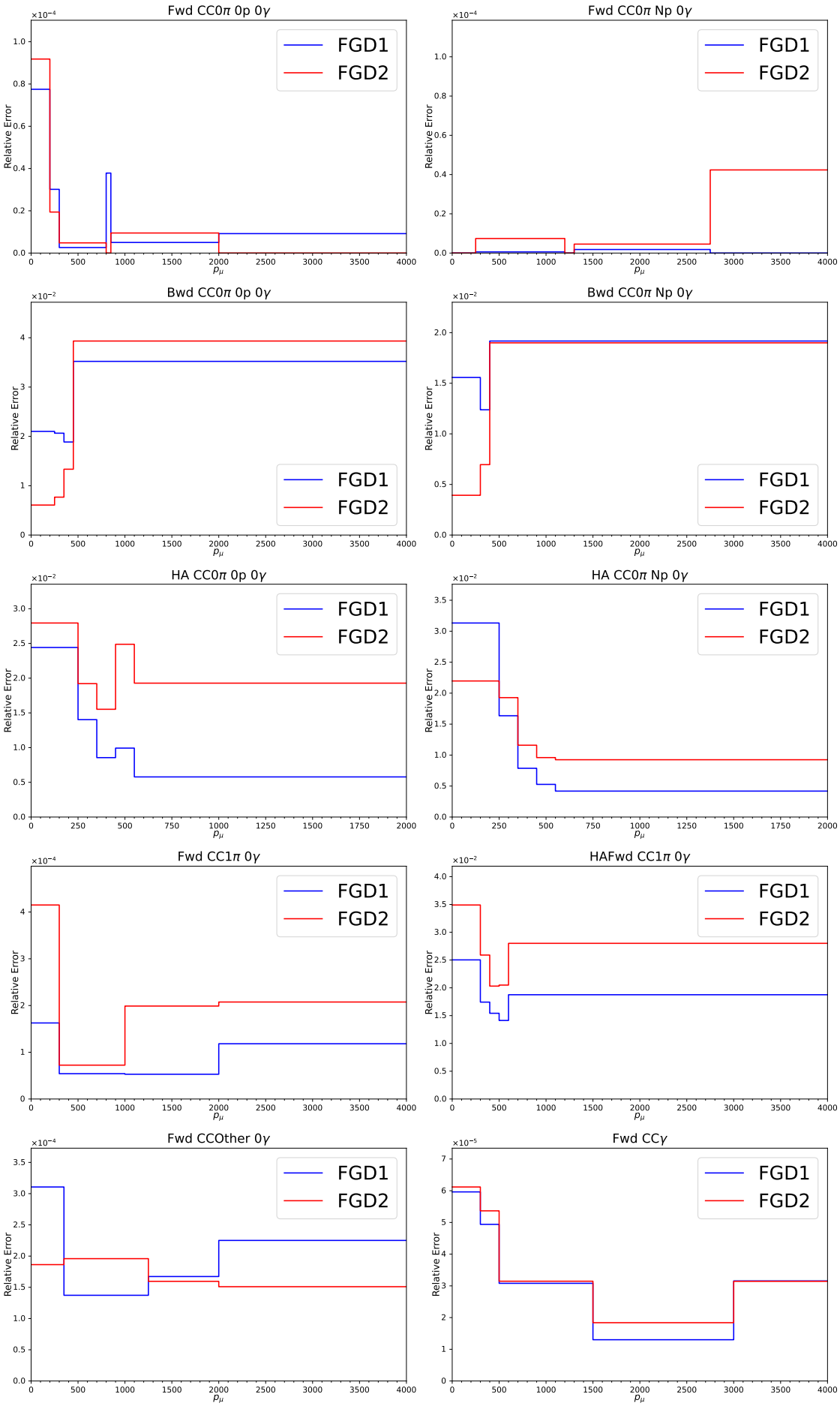

FIGURE 6.3: The relative error caused by time of flight resolution evaluated using highland2 propagation and parameters described before, as a function of muon momentum in MeV. The blue solid line stands for events originating in FGD1, and red line for FGD2.

6.2.2 Momentum bias from vertex backward migration

The term "vertex backward migration" refers to a phenomenon in which, in an event with a high number of tracks, some of the tracks are mistakenly reconstructed as part of the main muon track, leading to an overestimation of its length and a reconstruction of the vertex position farther upstream than its actual location. Since the momentum reconstruction of tracks in FGDs depends on their length, this phenomenon can introduce a bias in the reconstructed momentum of the main track, where the TPC information is not available. Fig. 6.4 provides a schematic drawing of such an effect in FGD2. This effect was first discussed in [100], then included in the cross-section study [54] as a weight systematic affecting muon momentum for FGD1. Following that, studies have been conducted to expand the uncertainty treatment to include FGD2 [118, 119]. This source of systematic uncertainty was, however, never included in an official oscillation analysis sample selection. Since the purpose of this study is to develop a sample selection for the next iteration of the T2K oscillation analysis, it is necessary to include this relevant systematic source and include FGD2 uncertainties as well. This section will provide a compact introduction to this systematic source, its implementation in software, and the re-evalution of the momentum bias for FGD2.

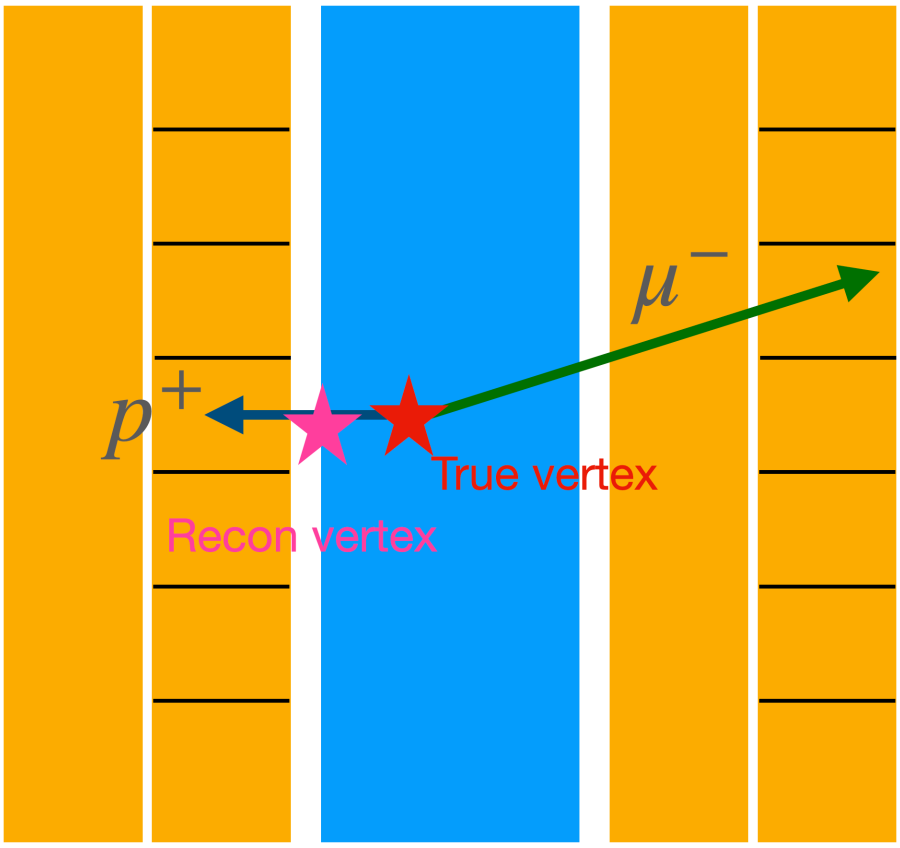

FIGURE 6.4: Drawing of FGD2 vertex backwards migration. A muon and a proton comes out of the vertex: the proton (marked with letter p) stops quickly, while the muon (marked with a letter μ) travels longer before it stops. The blue area in the drawing are the water layers, while X and Y refers to scintillator bar layers with bars laid in the X and Y direction. The red star marks the actual point of interaction, and the magenta star is the reconstructed vertex. As part of the proton track gets confused with the muon track, when the muon travels backwards, the vertex tends to get reconstructed upper-stream than its true location.

The vertex backward migration phenomenon's impact on muon reconstructed momentum comes mainly through its effect on FGD energy loss. In T2K, the FGD energy loss is defined as the energy loss when the muon is traversing the FGD, i.e. the momentum of the global reconstructed muon track minus the energy of the track's TPC segment. Since this effect exists in data and was not considered during the MC simulation, the strategy adopted by [54] is to apply a smearing on the energy loss to the MC energy loss distribution until it resembles data to a good extent, judged by a χ^2 test statistic. For the study described in this thesis, the treatment remains the same. Fig. 6.5 shows examples of the

data vs MC energy loss distribution.

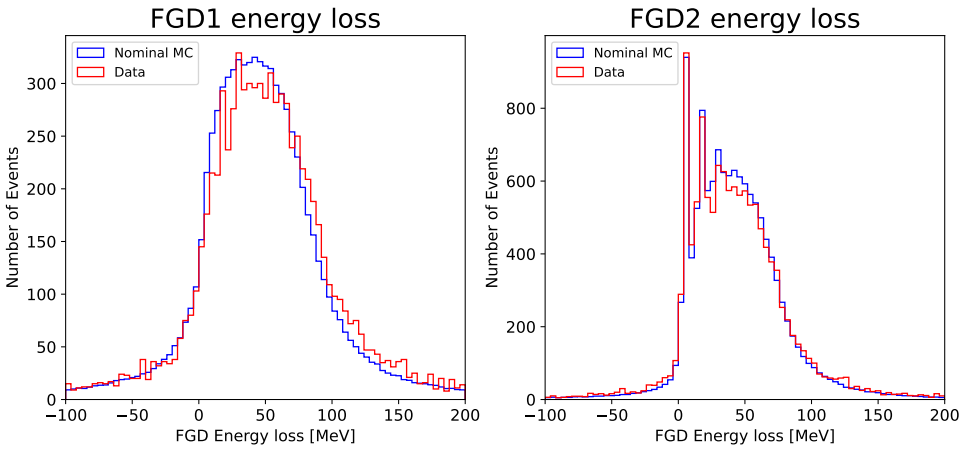

FIGURE 6.5: Data and MC energy loss in FGD1 (left) and FGD2 (right).

To find the uncertainty induced by this smearing, a uniform bias on the energy loss is applied to all MC events, then compared with data to estimate the maximal impact such effect can have. 100 different values have been tested, and the biased MC distribution at each value is compared against the data distribution to compute a χ^2 statistic between them, such that a χ^2-bias value curve can be drawn.

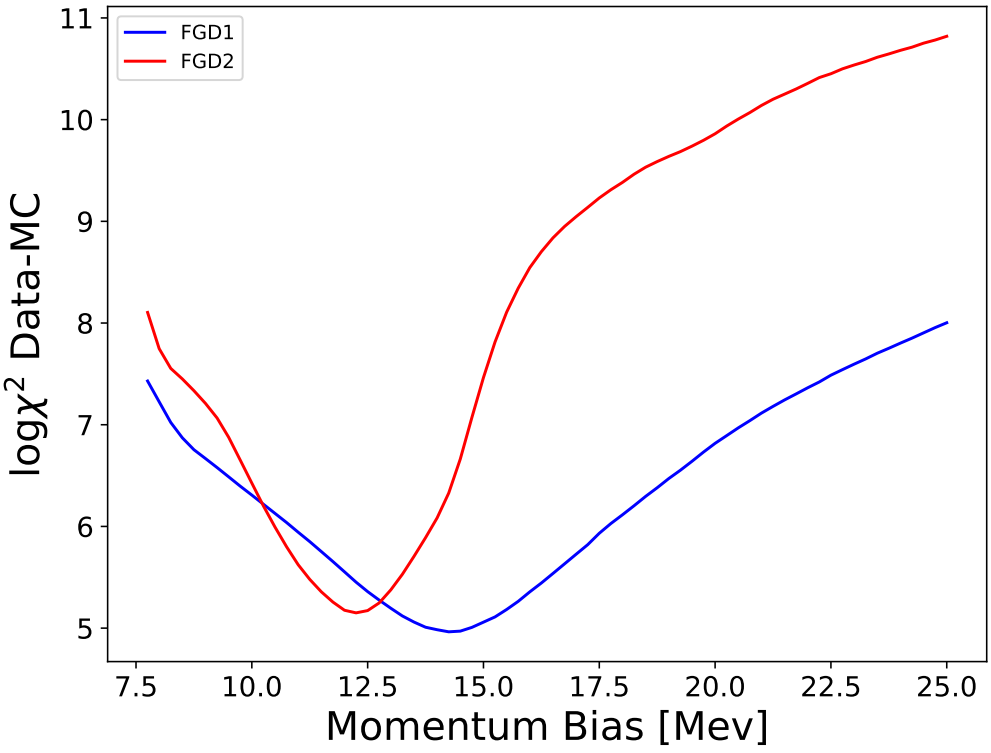

FIGURE 6.6: The biased MC vs data χ^2 distribution as a function of the momentum bias applied.

As shown in Fig. 6.6, a relatively small bias around 12 MeV gives the smallest χ^2 value when fitting MC to data, while for FGD1 the best bias is around 14 MeV. Since this is single parameter inference, the 90% confidence interval edges are set at where where the χ^2 test statistic, as a function of bias, is greater than the minimal χ^2 value by 1, and the uncertainty E on the bias is defined conservatively as the length of the interval. For FGD1, the E estimated using this method is around 7 MeV, while in FGD2, the E value is near 4 MeV. To avoid an underestimate of uncertainty, a 7 MeV uncertainty is also used for FGD2 systematic error propagations in this study. The expected error on the number of events selected is plotted in Fig. 6.7 and Fig. 6.8. The uncertainty is generally small across all 4π subsamples.

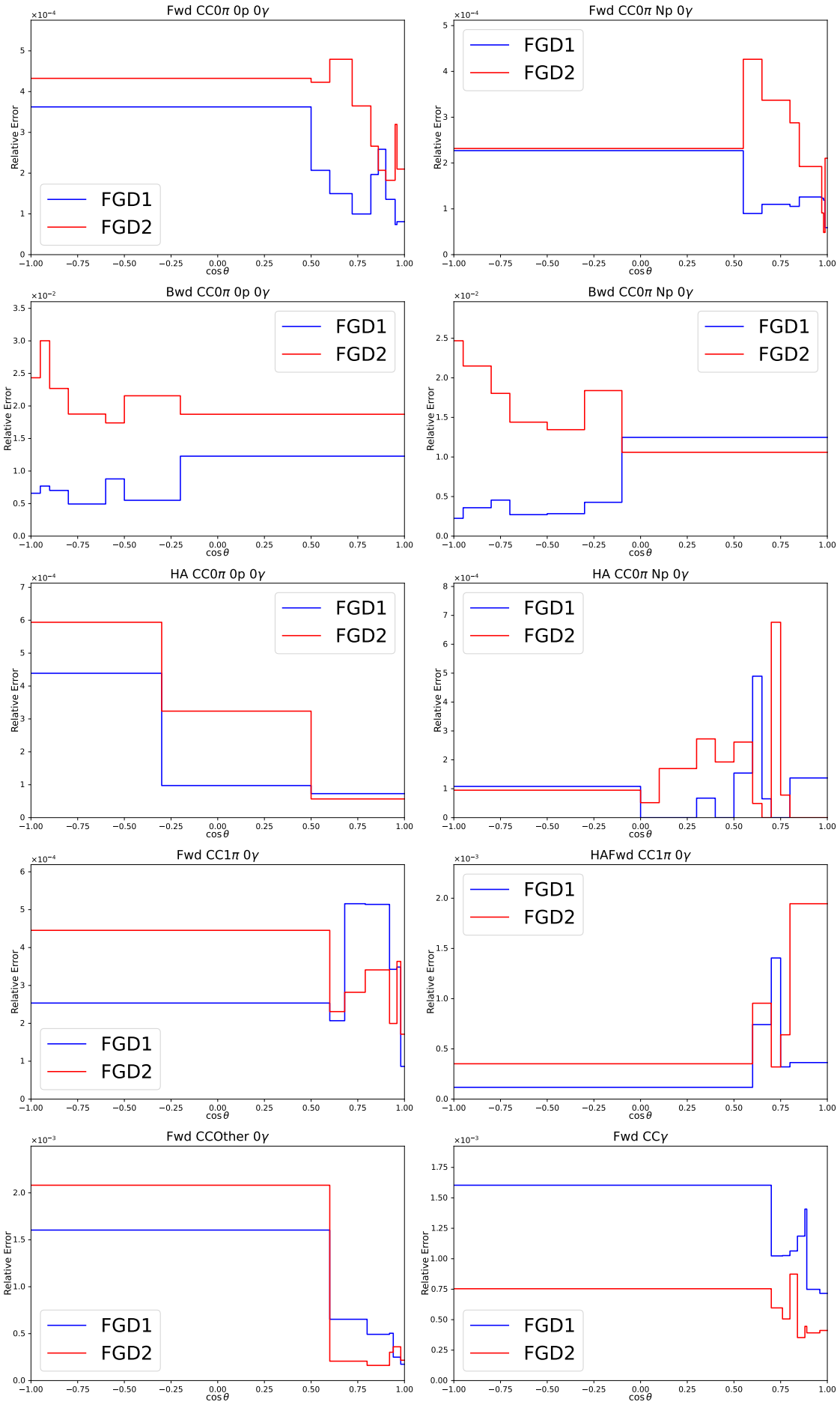

FIGURE 6.7: The relative error caused by momentum bias from vertex migration, evaluated using highland2 propagation and parameters described before, as a function of muon $\cos\theta$. The blue solid line stands for events originating in FGD1, and red line for FGD2.

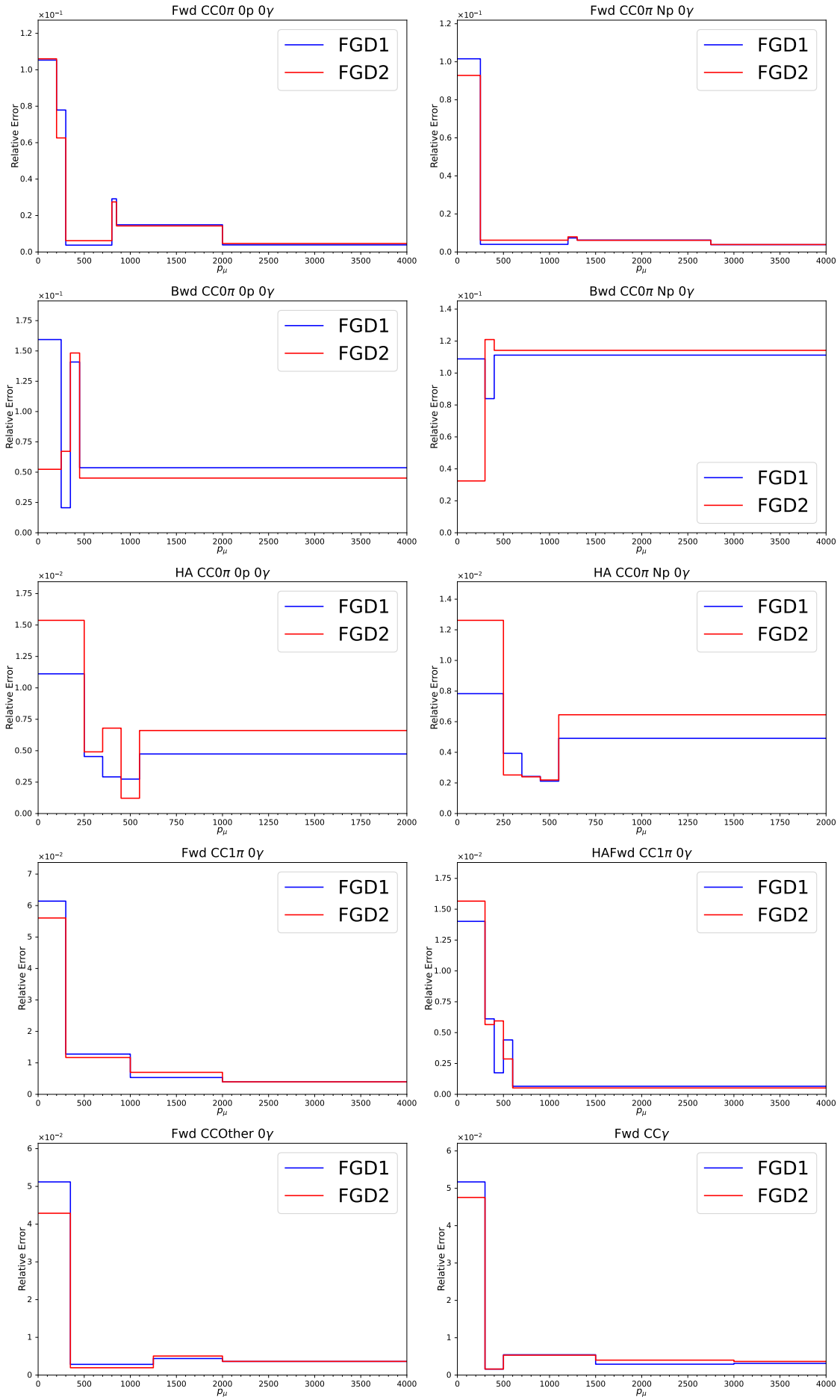

FIGURE 6.8: The relative error caused by momentum bias from vertex migration, evaluated using highland2 propagation and parameters described before, as a function of muon momentum in MeV. The blue solid line stands for events originating in FGD1, and red line for FGD2. The first bins usually see larger uncertainty due to the larger momentum reconstruction error in the low momentum region.

6.2.3 TPC-P0D matching efficiency

The term TPC-P0D matching efficiency refers to the chance that a track crossing both the P0D and FGD1 can be successfully reconstructed as a long track, i.e. the TPC1 segment and P0D segment can be successfully matched to each other. This study was first conducted in [100], and later used in [112] and this analysis without update. A brief introduction to the evaluation is provided here.

Like other matching efficiency systematic errors, the TPC-P0D matching uncertainty is evaluated using a control sample study. The control sample is selected using the following criteria:

- Event trigger is a FGD cosmic ray muon.
- Only one TPC track is in the event, and it has more than 18 TPC clusters.
- Events happen inside the P0D integration windows, $0 < T < 100$ ns or $500 < T < 800$ ns.
- TPC1 starting position is close to the P0D, $z < -755$ mm.

The efficiency is then defined as the number of tracks with a matched P0D segment, over the number of all events in the control sample. Events are binned in muon momentum, and each bin has its own efficiency. The difference in efficiency between control sample data and MC is used in highland weight-like error propagation, and all tracks selected for the backward going samples are subject to this systematic error. The parameters can be found in Table. 6.2.

p_μ (MeV)	ϵ_{data}	ϵ_{MC}
0 -150	0.056 ± 0.009	0.021 ± 0.012
150 -200	0.387 ± 0.018	$0.311^{+0.029}_{-0.032}$
200 -220	$0.880^{+0.026}_{-0.021}$	$0.900^{+0.026}_{-0.026}$
220 -260	$0.944^{+0.018}_{-0.015}$	$0.944^{+0.018}_{-0.015}$
260 -300	$0.991^{+0.006}_{-0.009}$	$0.991^{+0.006}_{-0.009}$
300 -500	$0.960^{+0.006}_{-0.009}$	$0.989^{+0.005}_{-0.009}$
500 -700	$0.974^{+0.009}_{-0.009}$	$0.942^{+0.009}_{-0.009}$
700 -1000	$0.974^{+0.009}_{-0.012}$	$0.978^{+0.009}_{-0.009}$
1000 -1400	$0.991^{+0.006}_{-0.009}$	$0.991^{+0.006}_{-0.009}$
1400 -1000000	$0.971^{+0.006}_{-0.009}$	$0.997^{+0.006}_{-0.009}$

TABLE 6.2: TPC-P0D matching summary of efficiencies and systematic uncertainties. This table is adapted from [100].

The expected error on the number of events selected is plotted in Fig. 6.9. This systematic error is only relevant in backward samples, and is more likely to affect FGD1 than FGD2 as FGD2 is farther from the P0D. The magnitude of relative error induced by this effect is comparable with previous studies [54] and [101].

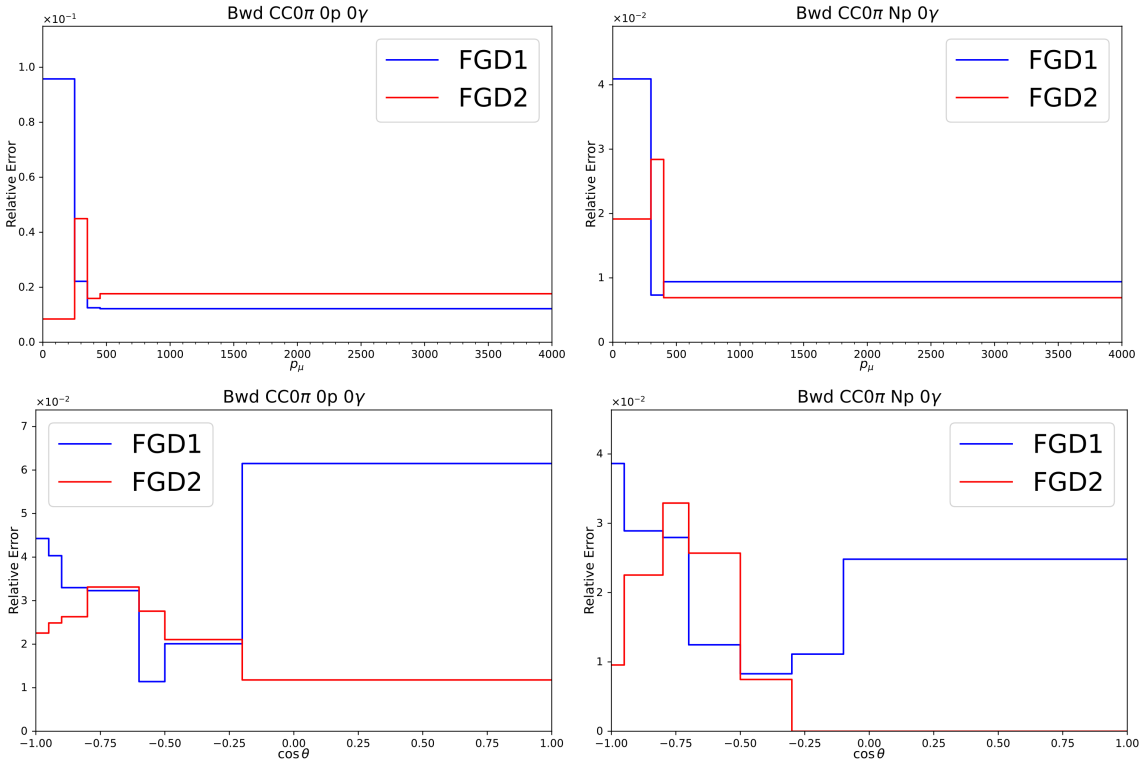

FIGURE 6.9: The relative error caused by TPC-P0D matching efficiency, evaluated using highland2 propagation and parameters described before, as a function of muon momentum in MeV (top) and $\cos\theta$ (bottom). The blue solid line stands for events originating from FGD1, and red line for FGD2.

6.2.4 Summary of ND280 detector systematic uncertainties

This section provides a comprehensive list of sources of other systematic uncertainties considered in this analysis. These systematic errors are already discussed in previous studies, and this thesis does not contain any update or changes to them. Hence, only a list of brief introductions is provided here, alongside with Table **??**. For a more detailed review of them, please refer to [116].

- **TPC cluster efficiency**

  Charged particles get pulled by the Lorentz force when moving in a magnetic field, hence the direction can be used to determine the sign of the charge carried by the particle. Simultaneously, the ionised particles are pulled by the electric field to eventually hit the panel mounted with micromegas readout electronics. While the coordinates of the two directions perpendicular to the electric field are easy to reconstruct based upon the ionised particle hits, the coordinate in the z direction

parallel with the E field can only be determined by the drift time, i.e. the time it takes for the ionisation electron to hit the end board.

As stated in Section 3.3.5, the micromegas boards used to read the TPCs are composed of numerous small pads that serve as their smallest unit. TPC Clusters are created by neighboring pad hits in a column (row) for approximately horizontal (vertical) tracks. A TPC track typically comprises multiple clusters. The probability of successfully clustering TPC pad hits into a cluster can vary between data and MC, as detailed in [116, 120]. The term "TPC clustering efficiency" refers to the ratio between data and MC clustering. The uncertainty on the ratio is propagated in highland as weight-like systematic error, applied to affected TPC objects.

- **TPC magnetic field distortion**

  The magnetic field B inside ND280 is crucial in accurately measuring the momentum and identifying charged particles. Section 3.3 introduces the measurement and modeling of the B field. To account for any mismodeling, two corrections are applied to the MC. The first correction, the main B field correction, is developed using the measured B field map to adjust the position of TPC clusters. The second correction, the empirical correction, is based on the B field distortion measurement obtained using laser-induced photo-electrons. For a detailed description of these corrections, please refer to [116]. The B field distortion systematic uncertainty of highland incorporates the error on these correction parameters in a variation-like manner. [3]

- **TPC tracking efficiency**

  The TPC tracking efficiency describes the chance that a TPC successfully reconstructs tracks from a particle traversing the TPC. Such efficieny is evaluated for each TPC using a number of control samples for MC and data. This includes a through-going cosmic-ray muon control sample to evaluate the TPC pattern recognition algorithm, and a likelihood fit test in the case of two tracks close to each other [116, 121]. The control sample studies reached a conclusion that both the

[3] The distortion of the electric field E is also considered in previous studies. However, more study is currently required to fully evaluate an independent systematic uncertainty from the E field distortion [116]. Also, there exists another TPC momentum systematic error which at least partly covers the error inflicted by the E field error, and introducing another E field systematic will risk double counting. Hence, T2K assumes that the uncertainty of E field distortion has all been absorbed by other higher-level systematic errors e.g. TPC momentum resolution/scale, and hence no stand-alone electric field systematic error is implemented in highland.

pattern recognition algorithm and the likelihood are performing very well, and the track reconstruction efficiency is in general $> 99\%$ in both data and MC. The exact figures of efficiencies are in [116]. The data/MC ratio is propagated in highland as a weight-like systematic error for every TPC track in the event.

- **Charge identification efficiency**

  The ND280 global charge identification relies on the collaboration of ND280 subdetectors. The TPCs provide the main tracking capability for charged particles, and the charge identification of charged particles in TPCs are based on the curvature of the track, i.e. towards which side it bends in the magnetic field. In [122], the probability of a single TPC charge mis-identification and global charge mis-identification were studied, as a function of track kinematics, including momentum, length and number of hits. Each TPC segment is given a relative weight based on these variables to describe the probabilty of its charge being wrongly identified. An efficiency-like weight is propagated in highland with data-MC difference of the parameter as a function of particle momentum, in order to represent the probability of correctly identify the charge using TPC information [122].

- **TPC particle identification**

  The TPC PID algorithm determines the type of the crossing particle. The main information used by the algorithm is the energy loss rate, which is inferred from the mean of ionisation charged collected [123]. Different particles have different energy loss rate dE/dx as given in the Bethe-Bloche formula [124], and the measured energy loss rate is compared with particle hypothesis to compute a pull value:

$$\delta = \frac{(dE/dx)_{\text{measured}} - (dE/dx)^i_{\text{expected}}}{\sigma^i_{\text{exp}}} \tag{6.10}$$

  where $(dE/dx)_{\text{measured}}$ is the measured particle energy loss, $(dE/dx)_{\text{expected}}$ is that of the hypothetical particle, and σ^i_{exp} is the detector's resolution of energy deposit rate, which is a particle-dependent quantity, hence the index. Three hypothetical particles are considered in the TPC PID algorithm: protons, muons and electrons. For more details, please see [123] and [115].

  The source of systematic error in this process is the energy loss rate difference between data and MC. The difference in δ and σ are quantified and used as variation

parameters in highland, where this systematic error source is propagated by the toy-variation method.

- **TPC momentum resolution**

  This systematic error describes the uncertainty on the momentum resolution from TPC and global reconstruction. A study was done in [125], comparing the single TPC and global momentum resolution in data and MC. The smearing factor that makes data and MC similar was determined, and subsequently used as the variation-like systematic uncertainty parameter to propagate in highland.

  To find such parameters, a control sample selection was developed to select long tracks that crossed two TPCs. Such a control sample is used to quantify the TPCs' intrinsic resolution on $1/p_T$, where p_T is the transverse component of the particle momentum, and that of the global reconstruction when multiple TPCs are involved. The difference between data and MC is quantified and extracted as a kinematic-dependent smearing factor to apply to all MC tracks.

- **TPC momentum scale**

  As the measurement of the momentum is dependent on the magnetic field strength B, the error propagation is simple in terms of mathematics:

$$\frac{\delta p}{p} = \frac{\delta B}{B} \tag{6.11}$$

  The uncertainty on the scale of B field inside TPCs is discussed in [126], and this variation systematic in highland takes the error evalutated in [126] and propagates it in a variation-like manner. The relative error on the B field is found to be 0.57% [116].

- **FGD hybrid tracking efficiency**

  As in the TPCs, the efficiency of the FGD track reconstruction is slightly different in data and MC. This is particularly important for short tracks that are fully contained in an FGD (isoFGD tracks), that co-exist with a longer FGD-TPC track [4]

  highland includes a dedicated systematic uncertainty to account for this difference between data and simulation. The term "hybrid" refers to the use of both real data

[4] Without a TPC track, the event cannot be recognised as a charged-current interaction event, making them irrelevant to the oscillation analysis.

and dedicated particle gun simulation to evaluate parameters. For this study, FGD CCQE tracks that traverse neighboring TPCs are selected as a control sample from both data and MC, and their vertex coordinates are saved. Protons and positively-charged pions are simulated near the vertex using a GEANT particle gun, and parameters for their studies were initially evaluated in [127] before being extended to negatively-charged pions in [128].

Subsequently, FGD reconstruction is run to test the probability of successfully reconstructing an isoFGD proton/pion in data and MC as a function of the angle between the isoFGD track and the main muon track. The ratio between data and MC is applied to MC as a weight, and the uncertainty on the ratio is propagated in highland as a weight-like systematic error.

- **FGD particle identification**

  Similarly to the TPC PID, the FGD PID is also based on the energy deposits and the pull values calculated from them. The difference is that while the TPC PID uses dE/dx, FGD PID uses the total energy loss, and the pull is therefore defined as

  $$\text{pull} = \frac{E - E_i(L)}{\sigma^i(L)}$$

  where E is the total measured track energy loss in the FGD, L is the track length measured, E_i and $\sigma^i(L)$ are the expected total energy loss and energy resolution, respectively, with hypothetical particle specie i assumed [127]. Dedicated control samples were selected to build pull value distributions for both MC and data. Both distributions are fit to normal distributions. The differences in the distributions are used as the systematic parameters in the highland variation error propagation.

- **FGD mass**

  In ND280 oscillation analyses, only events produced by neutrino interactions in FGD volumes are considered as signal. The total number of events is therefore proportional to the number of atoms in the FGD and therefore the mass of the FGD. The difference between simulation and truth in FGD matter densities are studied in detail in [116], and the uncertainty on FGD1 mass is evaluated to be 0.6% for FGD1 and 0.4% for FGD2 [129]. Such uncertainty is propagated as a normalisation systematic in highland.

- **ECal tracking efficiency**

  The previous sample selection [105] introduced ECal objects into the oscillation analysis, hence relevant systematic uncertainties must be understood.

  To evaluate this efficiency, a control sample with good quality TPC tracks ending close to the ECals were used, and the efficiency is defined as the number of ECal object candidates successfully reconstructed over the number of all ECal object candidates in the control sample. There are four subsamples in the control sample: shower-like barrel ECal, shower-like downstream ECal, track-like barrel ECal and track-like downstream ECal, and the selection criteria for those samples are delicate and can be found in [109]. Similarly to TPC and FGD tracking efficiency systematic error, efficiencies are evaluated for each subsample in data and MC respectively, and are further binned in the momentum of the track. Then the data/MC ratio is applied to MC as a correction, with the uncertainty on the ratio propagated as a weight-like systematic error in highland.

- **TPC-ECal matching efficiency**

  The TPC-ECal matching efficiency describes the systematic uncertainty in the TPC-ECal object matching, i.e. pairing up a TPC object and an ECal object to form an inter-subdetector ND280 track with a TPC segment and an ECal segment. To quantify such systematic uncertainty, a control sample was developed [130], in which the final cluster of TPC tracks are in the vinicity of ECals ($z > 2665$ mm for downstream ECal, $|x| > 890$ mm or $|y - 55| > 1030$ mm for barrel ECal) so that it is very likely such tracks proceed to the neighbouring ECal. The matching efficiency is then defined as the number of tracks with a reconstructed ECal segment over the number of tracks in the control sample [109]. A full list of efficiencies evaluated can be found in [130]. The difference between data and MC efficiencies is applied to events without any isoECal object to account for cases where an isoECal photon is mistaken as part of a longer track.

- **ECal PID**

  As described in Chapter 5, the ECal PID relies on the EMHip variable, which is designed to discriminate $e^{\pm}$ and γ from more highly-ionising particles like protons. As defined in Sec. 5.2.3, to be considered for the photon selection, an ECal object is required to have EMHip < 0. EMHip is defined using low-level features of the ECal

objects. Dedicated GEANT4 particle gun MC simulations were used to generate the probability density functions of those features for each particle type, and design the EMHip variable. For the definition of those features, and their relation to the EMHip variable, please refer also to [130].

To evaluate the associated systematic uncertainty to this process, electron, muon and proton control samples are selected using TPC PID. The electron control sample selects a pair of oppositely-charged particles starting within 10 cm from each other in the FGD fiducial volume, both identified as electrons by the TPC PID, and at least on of them enters the ECal. The muon control sample comprises the through-going subsample, which requires the track to be confirmed as a muon by TPC PID and also that it enters the ECal; and the cosmic ray muon subsample, which requires a cosmic ray trigger. The proton control sample only requires the track to be proton-like in the TPC PID, and to enter the ECal. For each control sample, a cut is placed on EMHip > 0. The efficiency is then defined as the number of events satisfying this cut, over the number of events in the control sample. As in other efficiency-like systematics, the data/MC ratio is applied to ECal objects with $-0.25 <$ EMHip < 0.35 as a weight correction, and the uncertainty on the ratio is propagated as a weight-like systematic in highland. For the full table of efficiencies and uncertainties on efficiencies, please see [130].

- **ECal pile-up**

  Pile-up occurs in the ECal when tracks from other sources such as cosmic rays coincide with a beam event and get included in the event reconstruction.

  It is also possible that an extra-tracker volume particle gets misidentified as an ECal photon and subsequently changes the topology of the event. Control samples that are used to study such effects require that there is an ECal photon while there is no FGD activity. Each FGD has its own control sample selected separately. The efficiency is then defined to be the number of such events, over the number of all events without any FGD activity [105, 109]. Like other efficiency systematic errors, the data/MC ratio in efficiency is applied to isoECal objects as a correction, and the uncertainty on the ratio is used in the highland weight-like propagation as the parameter.

- **TPC-FGD matching efficiency**

  This systematic uncertainty characterises how well the reconstruction matches FGD tracks to TPC tracks. To evalutate the TPC-ECal matching efficiency, the control sample selection requires the track to cross two TPCs, such that it must have also gone through the sandwiched FGD. The efficiency is defined as the number of events in which the intermediate FGD segment is successfully matched to the track, over the number of all events in the control sample [131]. The efficiency is calculated for data and MC respectively, and the ratio of them is applied to MC as a correction. The uncertainty on the ratio is used as the parameter in highland weight-like propagation. This systematic error is applied to all tracks that have both FGD and TPC segments.

- **Michel electron**

  The term Michel electron in particle physics refers to electrons coming from a parent muon decay. As it takes time for muons to decay, such electrons are usually observed in a later time window than other particles in the event. The efficiency for detecting Michel electrons was studied using the cosmic ray MC and data, as incident triggers by the cosmic ray trigger have a longer time window than beam triggers, long enough to cover the mean lifetime of muons. Events with muon tracks that stop in the FGDs are considered and the selection details can be found in [113]. Among those muon tracks that stop in the FGDs, a delayed cluster of hits is used to identify a Michel electron. As muons are guaranteed to produce an electron when they decay, the tagged Michel electron number over all selected FGD stopping muon events provides an estimate on the Michel electron tagging efficiency of the FGDs. In this case, FGD1 is found to have a higher Michel electron tagging efficiency than FGD2, and data and MC have similar efficiency. The systematic uncertainty applied in highland as a weight-like systematic to all Michel electrons is the difference in data and MC efficiencies.

- **Pion secondary interaction**

  The term pion secondary interaction (pion SI) refers to the interactions the pion undergoes after it leaves the incident nulceus [110]. In T2K, such interactions are initially simulated using GEANT4 in step lengths of 0.1 mm. The simulation result is significantly different from available external data [116], and a weight is calculated and applied to nominal MC using the comparison between GEANT4 MC and data.

The uncertainty propagation uses the uncertainty in the external data for pion interactions. The details of the calculation of weights can be found in [132], and the latest numbers are available in [133].

- **Proton secondary interaction**

  Similar to pions, protons also undergo secondary interactions after exiting the nucleus. This requires modelling, and a systematic uncertainty is introduced to cover the error brought in by the modelling.

  This systematic uncertainty was first developed in [134] using a similar method to that used in pion secondary interaction treatment, and recently updated in [133] in preparation for the proton split of the ND280 CC samples for the previous T2K neutrino oscillation. Just like in pion events, a correction weight is calcuated and applied to nominal MC by comparing GEANT4 simulation and external data. No fundamental difference between simulation and data in the study of this systematic error [134] was observed, hence this uncertainty is propagated in highland as a weight-like systematic to proton events, with a toy weight w of

  $$w = 1 + \sigma \times \alpha_{\text{toy}} \tag{6.12}$$

  where $\sigma = 0.1$ is the systematic error parameter [134], and α_{toy} is the Gaussianly-distributed variation that varies in toys. For the details of the evaluation and numbers, please refers to [134] and [133].

- **Sand muon background**

  In T2K, the term sand muon refers to muon neutrino charged-current interactions that happen outside ND280, i.e. from the sand surrounding the detector pit. The muons produced in such interactions can enter the detector volume to leave tracks that resemble neutrino interactions in FGD. To study such events, dedicated MC simulations are made, and included in whatever selection are made to mimic the contribution from sand events.

  The control sample for this systematic uncertainty requires a track to enter from the upstream wall of the P0D, and is used to evaluate differences in event rates between MC and data. The data-MC difference as evaluated by control samples is applied as

a weight-like error to all selected sand events. For the details of the study, and the exact numbers, please refer to [135].

- **Out-of-fiducial-volume background**

  While sand muon means muon from outside ND280, Out-Of-Fiducial-Volume (OOFV) events refers to neutrino interactions that happen inside ND280 but outside the FGD fiducial volume as defined in Sec. 5.2.3 [5] . Nine potential reconstruction failure modes are discussed in [136]. For those categories where the true vertex is located outside the tracker volume, a flat 20% uncertainty is assigned. Additionally, reconstruction efficiencies are studied for certain OOFV topologies where control samples are available. The data-MC difference is also applied to those OOFV events as a weight; thus, for those OOFV categories with available control samples, two weight-like systematic errors are propagated in highland. The numbers can be found in [136].

- **Event pile-up**

  As with ECal pile-up, the event pile-up occurs for events which coincide with other interactions like cosmic ray or sand muons. Sand muons are the dominant contribution in ND280 pile-ups [116] and are the only type being considered in ND280 error propagation. The rate of such events pile-up has been studied in [110] and [116], and the relavant systematic uncertainty is propagated in highland as a weight-like systematic uncertainty.

The result of all systematic errors propagated together is shown in Fig. 6.10 and Fig. 6.11. For the old samples, as the newly included systematic uncertainties do not contribute much, the overall systematic error is expected to be similar to results in [109]. For the new samples, the error is small enough that they can be used in the oscillation analysis. The backward samples have an overall systematic uncertainty of around 6%, and the high-angle samples 10%. For the systematic error induced by single error sources, please see Appendix C.

[5] To be more precise, OOFV refers to events that happen outside of the fiducial volume, but gets misreconstructed inside the fiducial volume. If it gets reconstructed also outside the FGD fiducial volume, for instance in the ECal, it will not be included in the sample selection, therefore not affecting the oscillation analysis output.

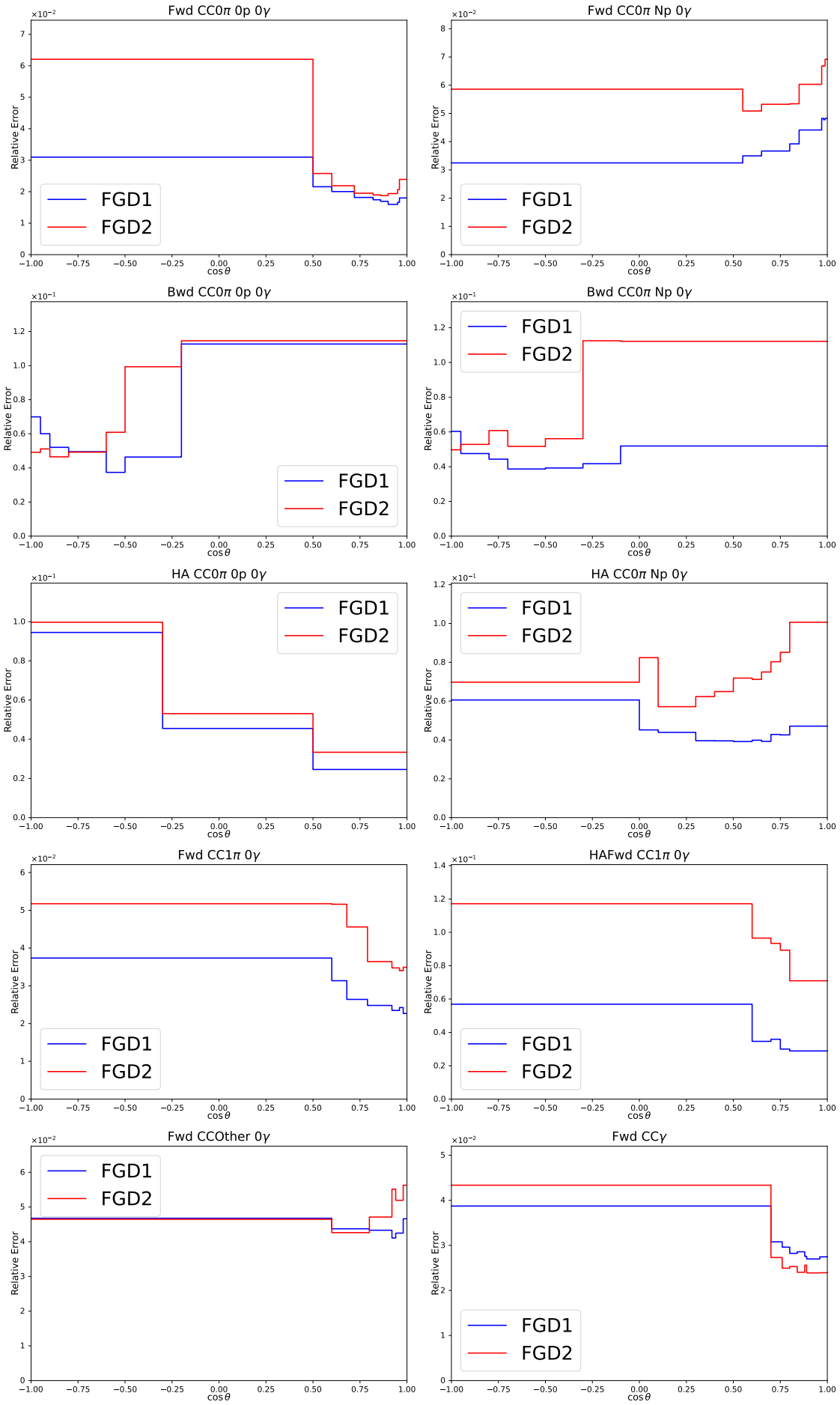

FIGURE 6.10: The relative systematic uncertainty caused by ND280 detector effects, as a function of muon $\cos\theta$. The estimated error tends to be larger in the backward region of the forward samples due to low-statistics.

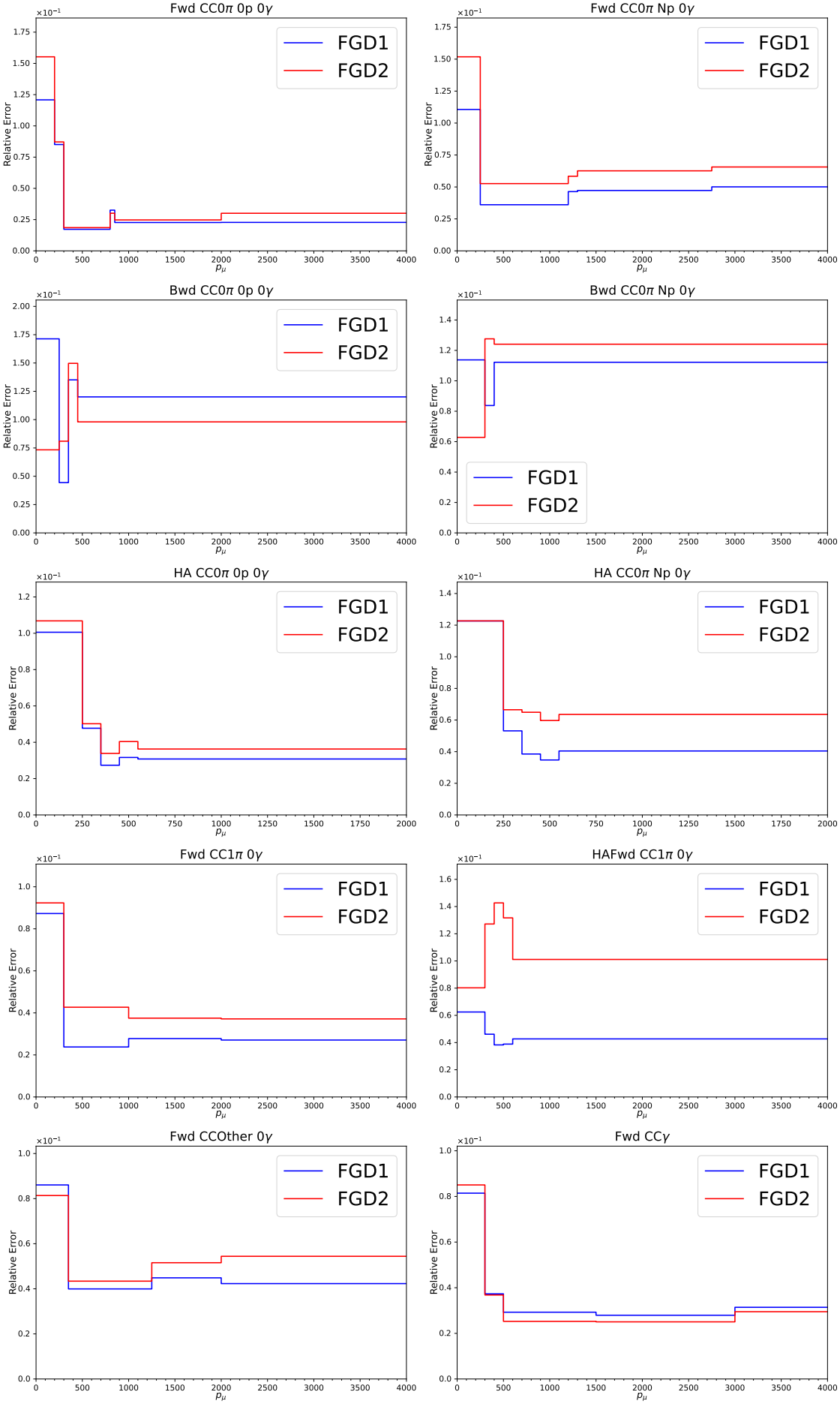

FIGURE 6.11: The relative systematic uncertainty caused by ND280 detector effects, as a function of muon $\cos\theta$. Low momentum region sees large systematic error due to large reconstructed momentum resolution.

Chapter 7

T2K oscillation analysis

This chapter offers an in-depth review of the T2K near detector fitting framework, known as BANFF (Beam And ND280 Flux Extrapolation Task Force), and the integration of the 4π sample selection within it. The discussion begins with an overview of the T2K oscillation analysis framework and an introduction to the software employed in the analysis. Subsequently, the focus shifts to the T2K near detector fit, encompassing a thorough explanation of the process for incorporating new samples. The chapter concludes by evaluating the validation efforts conducted on these newly added samples.

7.1 Neutrino oscillation in the T2K experiment

Chapter 1 previously introduced the T2K experiment and its primary objective of measuring neutrino oscillation parameters. The current neutrino oscillation model consists of six measurable free parameters, as illustrated in Eq. 2.23 and Eq. 2.25: three mixing angles (θ_{13}, θ_{23}, and θ_{12}), a CP-violation phase angle (δ_{CP}), and two mass differences squared (Δm^2_{23} and Δm^2_{31}). The T2K experiment is capable of measurements of θ_{13}, θ_{23}, Δm^2_{23}, and inferring δ_{CP}, as elaborated in the original T2K paper [5]. To accomplish this, T2K compares observations at the SK far detector to the un-oscillated prediction. The primary observable under comparison is the energy distribution of incoming neutrinos reconstructed from charged leptons produced in CC interactions, as detailed in Chapter 2.

The oscillation probability in T2K is dependent on the quantity $\sin^2\left(\frac{1.27\Delta m^2 L}{E}\right)$; hence, the neutrinos' oscillation probability has a sine-like dependence on their energies, as shown

in Fig. 3.3 and described in Eq. 2.23 and Eq. 2.25 as:

$$P(\nu_\mu \to \nu_\mu) \approx 1 - (4c_{13}^4 s_{13}^2 c_{13}^2 + 4s_{13}^2 c_{13}^2) \sin^2 \Phi_{31} \tag{7.1}$$

and

$$\begin{aligned} P(\nu_\mu \to \nu_e) \approx\ & 4c_{13}^2 s_{13}^2 s_{23}^2 \sin \Phi_{31} \\ & + 8c_{13}^2 s_{12} s_{13} s_{23} (c_{12} c_{23} \cos\delta - s_{12} s_{13} s_{23}) \cos \Phi_{32} \sin \Phi_{31} \sin \Phi_{21} \\ & - 8 J_{CP} \sin \Phi_{21} \sin \Phi_{32} \sin \Phi_{32} \\ & + 4s_{12}^2 c_{13}^2 (c_{12}^2 c_{23}^2 + s_{12}^2 s_{23}^2 s_{12}^2 - 2c_{12} c_{23} s_{12} s_{23} s_{13} \cos\delta) \sin^2 \Phi_{21}, \end{aligned} \tag{7.2}$$

where J_{CP} is the Jarlskog invariant [137] defined as

$$J_{CP} = c_{12} c_{13}^2 c_{23} s_{12} s_{13} s_{23} \sin \delta_{CP} \tag{7.3}$$

According to Table 2.2, θ_{13} is smaller than 9° and its cosine value close to 1, meaning that the muon disappearance probability is not very sensitive to changes in θ_{13} at the leading order, because the first derivative of a cosine function is a sine function, and sine functions are close to zero in the vicinity of zero. $\mathrm{Sin}^2(2\theta_{23})$ is not a function of energy; it is believed to be a constant of nature, controlling the depth of the dips in the top plot of Fig. 3.3. The $\sin^2(1.27\Delta m_{32}^2 \frac{E}{L})$ term is where the dependence on E comes from. T2K's off-axis placement is partly in hope of maximising the neutrino flux at 600 MeV, where energy will subsequently maximise the neutrino disappearance probabilty at $L = 295$ km. Therefore, the shape of muon disappearance probability versus neutrino energy provides information on Δm_{32}^2 and θ_{23}. The leading term of the electron neutrino appearance probability in Equation **??** also depends on θ_{23} and Δm_{32}^2, in addition to θ_{13}. The next-to-leading-order term depends on J_{CP}, which is proportional to $\sin \delta_{CP}$. Therefore, fitting the electron neutrino appearance model to data provides information on θ_{23}, θ_{13}, Δm_{32}^2, and δ_{CP}.

To perform such fits, a theoretical model depending on those parameters and a much more delicate prediction than Eq. 2.23 and Eq. 2.25 are pre-requisites. Both muon neutrino disappearance and electron neutrino appearance can only provide constraints on the square of the mass difference between mass eigenstates m_2 and m_3, with the sign of the mass

difference remaining ambiguous. In the case of T2K, the sensitivity to neutrino mass ordering mainly comes from the matter effect term. A a more detailed discussion on that topic is available in [39]. As what's being recorded is neutrino events observations made by complex detectors like ND280 and SK, the model T2K would like should also give predictions directly comparable to that. This invokes not only neutrino oscillation parameters, but also much more knowledge: the incoming neutrino beam flux, described by the flux model; the neutrino-nucleus interaction, described by the cross-section model; and the detector response to neutrino interactions, described by the detector systematic uncertainty model. To improve knowledge in those terms, the ND280 detector was built, and a ND280 model was designed and fit to ND280 measurements. The details of the ND280 models will be given in Sec. 7.3 that follows.

7.2 T2K oscillation analysis framework

The T2K experiment employs a two-phase fit method to set constraints on neutrino oscillation parameters. In the first phase, the ND280 model is fit to the ND280 observation, yielding constraints on both the neutrino-nucleus interaction and the neutrino flux model parameters. In the second phase, these constraints are then applied to the far detector fit, which produces the final constraints on the neutrino oscillation parameters. This section provides an overview of the T2K oscillation analysis framework.

The near detector model that is being fit in the first phase of the oscillation analysis predicts the muon kinematics distribution observed at ND280. As a function of true neutrino energy, this model can be expressed as:

$$N_{\nu_\mu}^{\mathrm{ND280}}(E_\nu) = \Phi_\nu^{\mathrm{ND280}}(E_\nu) \times \epsilon^{\mathrm{ND280}}(E_\nu) \times \sigma^{\mathrm{ND280}}(E_\nu), \tag{7.4}$$

which contains three parts: neutrino beam flux $\Phi_\nu^{\mathrm{ND280}}(E_\nu)$, detector response $\epsilon^{\mathrm{ND280}}(E_\nu)$, and neutrino interaction cross-section $\sigma^{\mathrm{ND280}}(E_\nu)$. As true energy information is never available in practice, the number density as a function of reconstructed neutrino energy is given by a convolution of true energy distribution and reconstruction energy distribution given the true energy:

$$N_{\nu_\mu}^{\mathrm{ND280}}(E_\nu^{\mathrm{rec}}) = N_{\nu_\mu}^{\mathrm{ND280}}(E_\nu) * \rho^{\mathrm{ND280}}(E_\nu^{\mathrm{rec}}|E_\nu), \tag{7.5}$$

The near detector response is not directly related to the event rate at SK, but the flux and cross-section parameters are closely related to their SK counterpart. Thus, fitting the near detector model to data can help to constrain the relevant parameters, including the neutrino-interaction parameters and the flux parameters. Subsequently, this will reduce the systematic uncertainties at SK, and ultimately improve the constraint on neutrino oscillation parameters. This near detector fit is conducted using an internal program named BANFF, which is short for Beam And ND280 Flux extrapolation task Force. This thesis is dedicated to an upgrade to the sample used in the BANFF fit, hence BANFF will be covered in detail in the following Sec. 7.4.

The far detector model should provide the expected distribution as a function of the incident neutrino's energy. For instance, in the case of the ν_μ event rate, the model should provide a function in the form of:

$$N^{\mathrm{SK}}_{\nu_\mu}(E_\nu) = \Phi^{\mathrm{SK}}_{\nu}(E_\nu) \times \epsilon^{\mathrm{SK}}(E_\nu) \times \sigma^{\mathrm{SK}}(E_\nu) \times P_{\nu_\mu \longrightarrow \nu_\mu}(E_\nu | \theta_{13}, \theta_{23}, \Delta m_{23}, \delta_{CP}). \quad (7.6)$$

The equation above describes the observed muon neutrino events at SK as a function of the incoming neutrino energy, denoted by $N^{\mathrm{SK}}_{\nu_\mu}(E_\nu)$. Again, to obtain the reconstructed neutrino energy, the reconstructed energy distribution needs to be included:

$$N^{\mathrm{SK}}_{\nu_\mu}(E^{\mathrm{rec}}_{\nu}) = N^{\mathrm{SK}}_{\nu_\mu}(E_\nu) * \rho^{\mathrm{SK}}(E^{\mathrm{rec}}_{\nu} | E_\nu), \quad (7.7)$$

This quantity is determined by the product of several factors: the expected ν_μ flux from the target station without oscillations $\Phi_\nu(E_\nu)$, the SK reconstruction efficiency $\epsilon^{SK}(E_\nu)$, the far detector target material - ν_μ interaction cross section $\sigma^{SK}(E_\nu)$, and the ν_μ survival probability presented in Fig. 3.3 (top), denoted by $P_{\nu_\mu \longrightarrow \nu_\mu}(E_\nu)$. The last factor is of particular interest as it is the only part of the model that explicitly involves neutrino oscillation parameters. By using the model described in Eq. 7.6 and varying the values of θ_{13}, θ_{23}, Δm^2_{23}, and δ_{CP}, it is possible to find the best fit values for $N^{\mathrm{SK}}_{\nu_\mu}(E_\nu)$ and construct confidence intervals for the varied parameters.

Two frequentist fitting frameworks, VaLOR [138] and PTheta [139], are used by T2K to perform this far detector fit. Although they are very different in terms of code implementation, the most important physical difference is the way that they bin far detector data. Both fitting frameworks bin event kinematics in two dimensions, and they both

use the reconstructed lepton's angle with respect to the neutrino beam direction θ as one dimension. In terms of the other variable, VaLOR uses the reconstructed neutrino energy E_ν^{rec}, while PTheta can use either E_ν or the incident charged lepton momentum p.

Both far detector fit marginalises all nuisance parameters i.e. parameters that are not in Eq. 7.2 and Eq. 7.1 and only varies the oscillation parameters. Then the fit recomputes the expected neutrino event distribution based on the varied oscillation parameters, and compares with data, to construct post-fit confidence intervals (frequentist) or credible intervals (Bayesian). A flow chart showing the entire T2K process using the frequentist approach is presented in Fig. 7.1.

On top of the frequentist analysis streams, T2K uses a Markov Chain Monte Carlo-based, Bayesian fitting framework known as ToF [140] for cross-check purposes. In contrast to VaLOR or PTheta, ToF simultaneously fits near and far detector data and only bins the far detector events in a single variable, the reconstructed neutrino energy E_ν^{rec}.

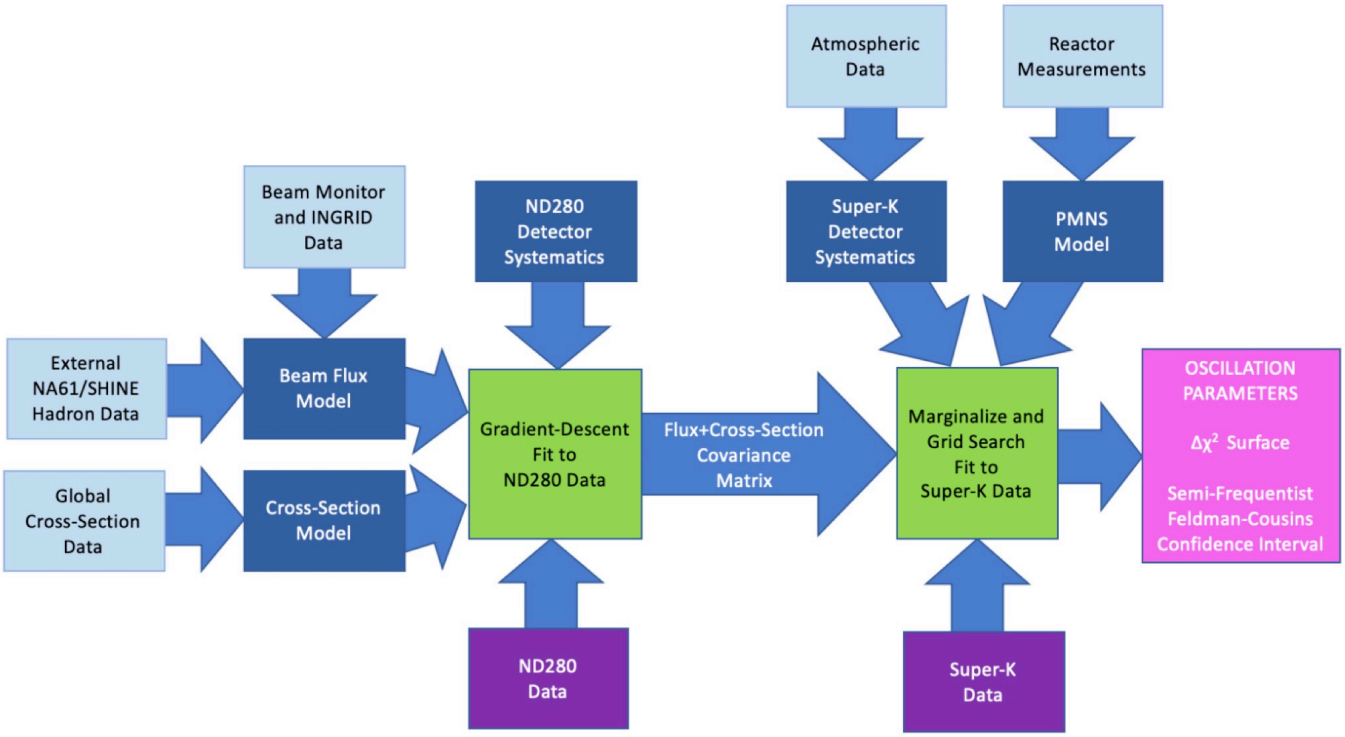

FIGURE 7.1: This flowchart depicts the T2K oscillation frequentist analysis procedure, which consists of a near detector fit and a distinct far detector fit. The light blue boxes indicate external data, the purple boxes are the T2K measurements, the dark blue boxes are models used in the T2K oscillation analysis, and the two green boxes are the two fits conducted during the frequentist stream of analysis. The final pink box is the final output constraint on the neutrino oscillation parameter. An arrow indicates an input.

7.3 Near detector model

The near detector model is multifaceted, comprising three key components: the flux model, which characterises the neutrino flux entering ND280; the cross-section model, which describes how neutrinos interact with target atoms; and the ND280 detector systematic uncertainty model, which quantifies the impact of detector uncertainties on the final selected sample. Subsequently, this section will thoroughly discuss each component and every parameter within the ND280 model in sequence.

Prior to delving into the models, it is essential to introduce the two categories of parameter implementation in BANFF. The parameters of the near detector model can be classified into two groups based on their influence on the physics model. The first group

consists of normalisation parameters, which alter the overall number of anticipated events from the data. These parameters are applied as weights to relevant events, making their implementation in the fitter relatively straightforward. Conversely, the second group comprises shape parameters, which do not impact the total number of events but modify the distribution of events in relevant physical properties, such as neutrino energy or momentum transfer. Implementing these parameters in the event generator is typically more challenging, and is usually done on a parameter-by-parameter basis.

7.3.1 Flux model

The T2K neutrino flux is simulated using a series of MC simulation tools. This process begins with the proton beam colliding with the carbon rod in the target station, which is simulated using FLUKA version 2011.2x [141, 142, 143]. In T2K terminology, this collision is known as the primary interaction, and it generates a large number of charged particles that exit the target volume and are focused by the horn system. To simulate this process, JNUBEAM is utilised, which is a GEANT-based package [144] that models the products of the primary interaction as they propagate and decay in the horn's magnetic field and the secondary beam line. A flowchart of the flux prediction process in T2K is presented in Fig. 7.2.

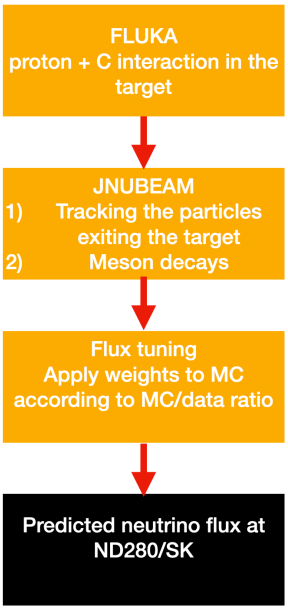

FIGURE 7.2: A flow chart showing the process of T2K flux simulation.

To address any discrepancy between the data and the MC simulation, T2K applies a "tuning" to its flux MC simulation based on the results of *ex situ* measurements. This involves assigning a weight to the simulated neutrino flux based on the comparison between the MC and external data from the NA61/SHINE experiment [82, 141, 142, 145]. Earlier analyses used NA61/SHINE measurements from a thin target [146], but since 2020, the thin target measurements have been updated with measurements from a T2K replica target for an apples-to-apples comparison [147]. In the T2K replica target tuning, a weight $W^{\alpha}_{p,\theta,z}$ is assigned to each simulated neutrino according to the differential ratio between experimental measurements and model expectations:

$$W^{\alpha}_{p,\theta,z} = \left[\frac{dn^{\alpha}_{\text{replica}}}{dp}\right]_{\text{NA61}} \Bigg/ \left[\frac{dn^{\alpha}_{\text{replica}}}{dp}\right]_{\text{FLUKA}} \tag{7.8}$$

where

$$\frac{dn^{\alpha}_{\text{replica}}}{dp} = Y^{\alpha}(p,\theta,z) = \frac{1}{N_{\text{POT}}} \frac{N^{\alpha}_{i,j,k} C_{i,j,k}}{\Delta p_{i,j,k}} \tag{7.9}$$

and Y is the yield of a particle of certain specie α, with a particular momentum p, transverse angle θ, and track length z. The distribution of events of species α in a three-dimensional space is a differential distribution, and its analytical form can only be obtained via QCD computation to a limited precision. In practice, $N^{\alpha}_{i,j,k}$, the total number of measured events in a bin (p,θ,z) with index i,j,k, is used. $C_{i,j,k}$ is a correction applied to MC to account for known issues, and $\Delta p_{i,j,k}$ is the 3D volume of the bin $p_{i,j,k}$ [82, 141, 142].

When assessing flux uncertainties, numerous sources are considered, as detailed in [82, 142]. These sources encompass uncertainties in hadron interactions, which pertain to the proton-target interaction and subsequent hadronic processes, as well as uncertainties in the proton beam profile, T2K neutrino beam direction, horn current strength, horn positions, horn field distortion, and T2K target displacement. For a comprehensive examination of flux uncertainty sources, please consult [141, 142, 148].

The overall flux uncertainty is minimal around the 600 MeV region, which coincides with the peak of the T2K neutrino beam energy distribution [82]. The total flux uncertainty across neutrino energy bins at ND280 and Super-Kamiokande is depicted in Fig. 7.3 and Fig. 7.4, respectively. Generally, in both FHC and RHC modes, the flux uncertainty is approximately 5% near the 600 MeV peak of the neutrino energy distribution.

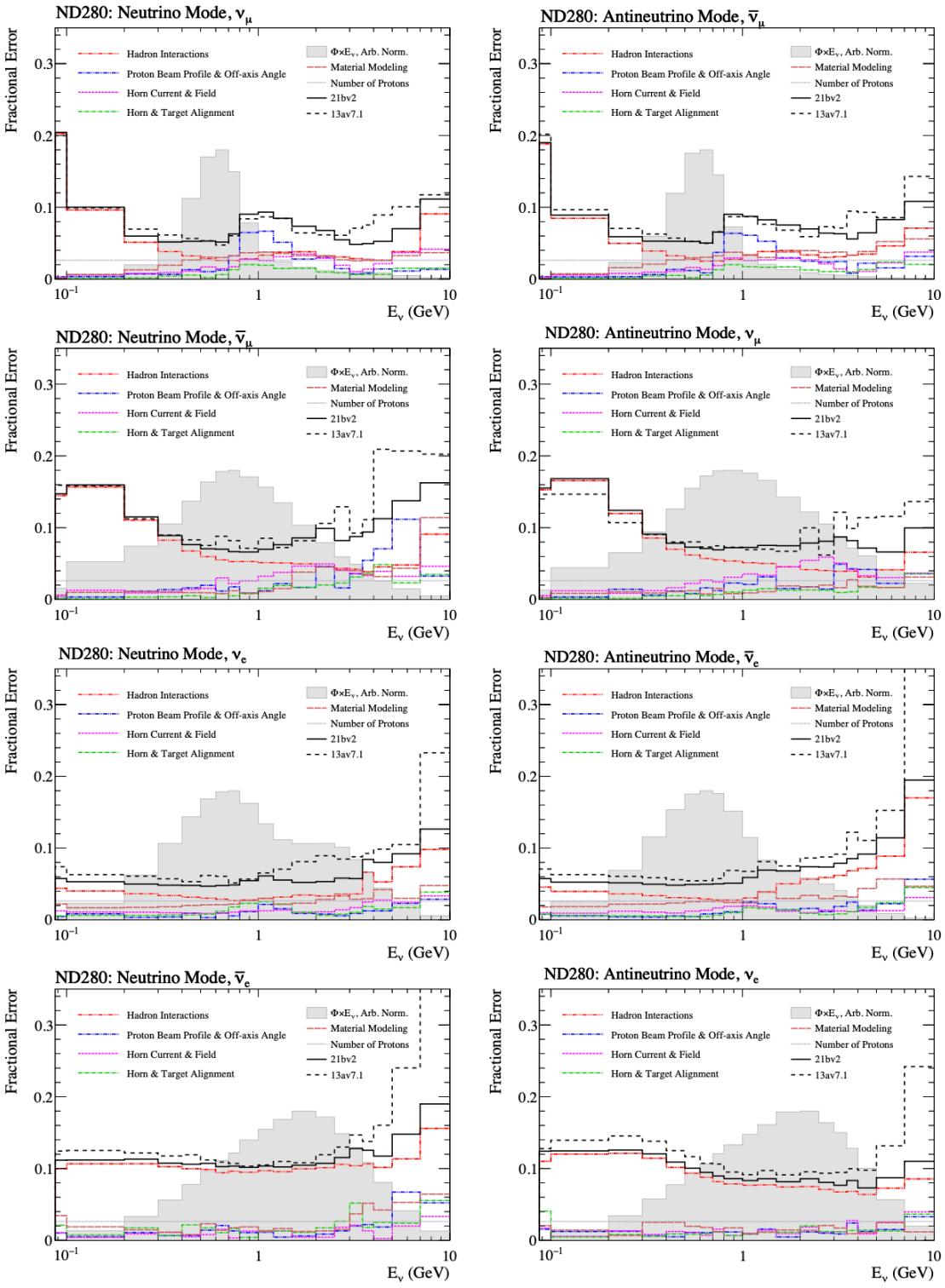

FIGURE 7.3: Total ND280 flux uncertainty versus true neutrino energy, in all beam modes. FHC is on the left, and RHC is on the right, for each neutrino component in the beam. The shaded region shows the predicted T2K flux profile for each neutrino type. The red line is the hadronic uncertainties combined, blue line is the proton beam profile uncertainty, pink is horn uncertainty, green is target alignment uncertainty, the dark red line is the material modelling uncertainty and the gray line is the proton number uncertainty. The solid black line is all sources of uncertainties combined, and the dashed black line represents the previous version of flux uncertainty release. This figure is adapted from [82].

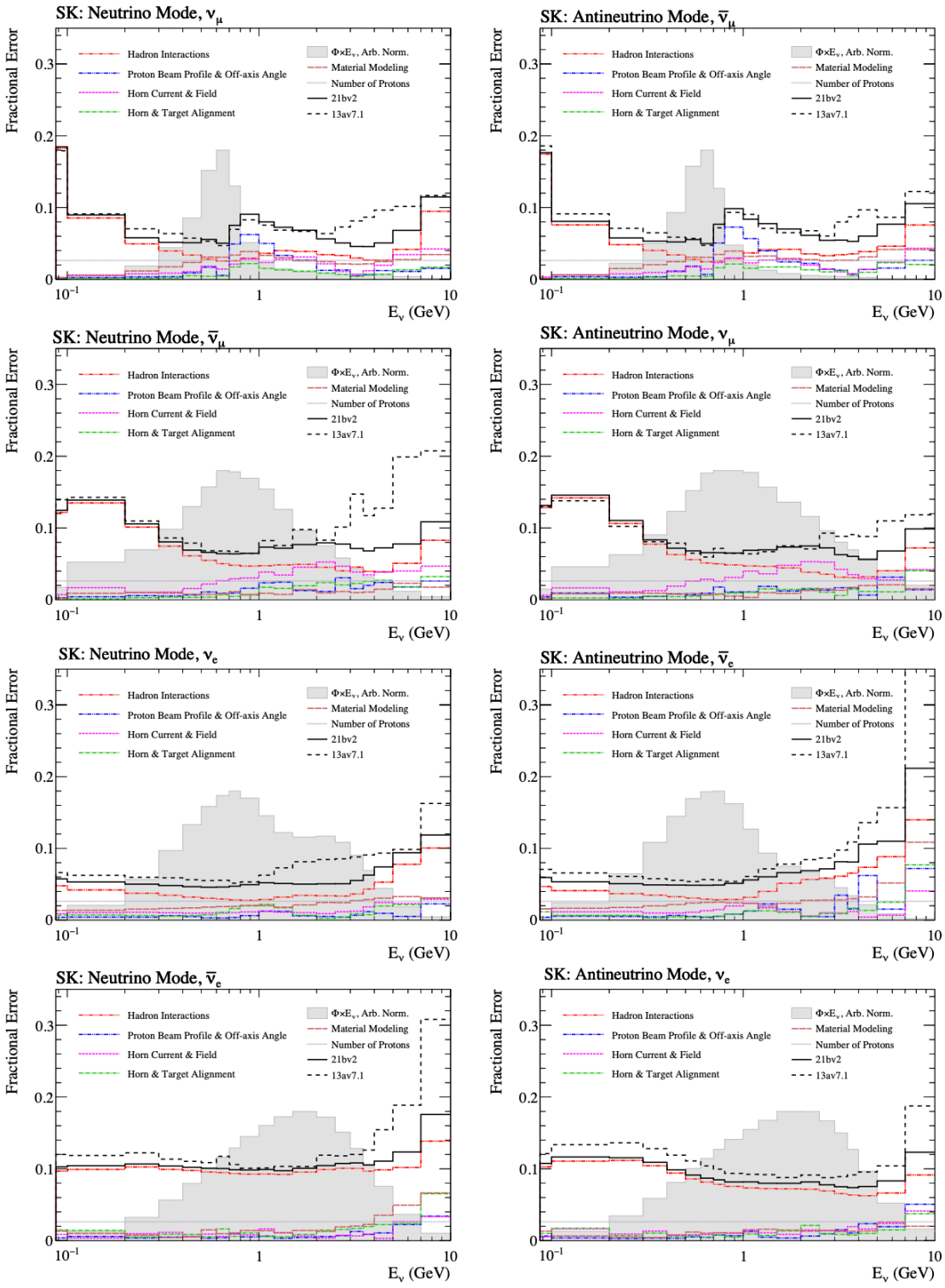

FIGURE 7.4: Total SK flux uncertainty versus true neutrino energy, in all beam modes. FHC is on the left, and RHC is on the right, for each neutrino component in the beam. The shaded region shows the predicted T2K flux profile for each neutrino type. The red line is the hadronic uncertainties combined, blue line is the proton beam profile uncertainty, pink is horn uncertainty, green is target alignment uncertainty, the dark red line is the material modelling uncertainty and the gray line is the proton number uncertainty. The solid black line is all sources of uncertainties combined, and the dashed black line represents the previous version of flux uncertainty release. This figure is adapted from [82].

The flux MC simulation outlined above provides a preliminary estimate of the neutrino flux, but it is computationally demanding due to the complexity of its QCD simulation and the use of multiple layers of software. In the near detector fit, it is impractical to fit the underlying parameters in these hadronic interaction generators, and a simplified version is used.

As of the time this thesis was written, the uncertainties on the flux prediction are parameterised in BANFF using simple normalisation parameters for each neutrino energy bin. In other words, neutrinos in the MC simulation are binned in energy, and neutrinos belonging to different bins have different flux weights, which will be fitted by the near detector fit. The current binning edges in neutrino energy (GeV) are:

- **FHC**: ν_μ 0, 0.4, 0.5, 0.6, 0.7, 1, 1.5 2.5, 3.5, 5, 7, 30
- **FHC**: $\bar{\nu}_\mu$ 0, 0.7, 1, 1.5, 2.5, 30
- **FHC**: ν_e 0, 0.5, 0.7, 0.8, 1.5, 2.5, 4, 30
- **FHC**: $\bar{\nu}_e$ 0, 2.5, 30
- **RHC**: $\bar{\nu}_\mu$ 0, 0.4, 0.5, 0.6, 0.7, 1, 1.5 2.5, 3.5, 5, 7, 30
- **RHC**: ν_μ 0, 0.7, 1, 1.5, 2.5, 30
- **RHC**: $\bar{\nu}_e$ 0, 0.5, 0.7, 0.8, 1.5, 2.5, 4, 30
- **RHC**: ν_e 0, 2.5, 30

The list above contains 50 flux bins, which together with the independent treatment of SK and ND280 flux parameters make a total of 100 bins. The prior uncertainties and correlations are incorporated into a 100×100 covariance matrix V, which is an input to BANFF. The diagonal elements, $V_{ii} = \sigma_i^2$, represent the uncertainties squared in each bin, while the non-diagonal elements $V_{ij} = \rho_{ij}\sigma_i\sigma_j$ capture the correlation between parameters i and j, in which ρ is the correlation between parameter i and j. For details on how to compute this matrix, please refer to [142] and [82]. BANFF fits all 100 parameters to determine new best-fit values, accompanied by a covariance matrix. These updated best-fit values, along with the covariance matrix, serve as inputs for the far detector fit.

7.3.2 Cross-section model

The next model fitted in BANFF is the neutrino-nucleus interaction model, which describes how likely a particular neutrino-nucleus interaction is to happen, and the differential distribution of its final-state products. The cross section is modelled separately for each interaction mode. For the interactions considered in this study, please see Sec. 2.4 and [39]. This section will provide an overview of the neutrino interaction models, and their parameters implemented in the BANFF fit. All the prior values and prior uncertainty distribution remain the same as in [149] and [105] unless specified otherwise.

7.3.2.1 CCQE interaction model

The CCQE neutrino-nucleon interaction model implemented in T2K event generator is Llewellyn Smith [150], and the nucleon motion inside the nucleus is modelled using the Benhar Spectral Function model (SF) [151], which is an upgrade from the previously-used relativistic Fermi gas model [152] in terms of systematic uncertainties. The CCQE neutrino-nucleon interaction differential cross section as a function of momentum transfer, Q^2, is given in [150] as:

$$\frac{d\sigma}{dQ^2}\frac{G_F^2 M^2 \cos^2\theta_C}{8\pi E_\nu^2} = \left[A(Q^2) \pm \frac{s-u}{M^2}B(Q^2) + \frac{(s-u)^2}{M^4}C(Q^2)\right], \tag{7.10}$$

where G_F is the Fermi constant for weak interactions, M is the mass of the nucleon, $\cos\theta_C$ is the Cabibbo angle $\theta_C = 13.02°$ [77], E_ν is the energy of the neutrino, s and u are the Mandelstam variables of two-particle final states, as defined in [10]. $s - u = 4ME_\nu - Q^2 - m^2$, and m is the mass of the lepton being produced. A, B and C are combinations of form factors to be determined experimentallyand depend only on Q^2. This subsection will provide an overview of the parameters in the SF model implemented and fitted in BANFF. For a summary of parameters and their prior values, please see Table. 7.1.

- $M_{\mathbf{QE}}^A$

  One of the key parameters in the neutrino interaction model is the axial mass in quasi-elastic neutrino interaction, or $M_{\mathbf{QE}}^A$. This parameter plays a central role in the axial vector form factors outlined in Eq. 7.10, which are described by the Llwellyn

Smith formalism [150]. Specifically, in Eq. 7.10,

$$B(Q^2) = \frac{Q^2}{M^2} \frac{g_A^2}{(1 + \frac{Q^2}{(M_{\mathrm{A}}^{\mathrm{QE}})^2})^2} (F_1^2(Q^2) + F_2^2(Q^2)), \tag{7.11}$$

where g_A is a dimensionless normalisation parameter of value 1.2670 ± 0.0035, F_1 and F_2 are other form factors depending only on the momentum transfer Q^2. The prior value of $M_{\mathbf{QE}}^A$ is 1.03 GeV, and a stringent 60 MeV prior error has been set based on bubble chamber experiment data [153, 154, 155]. For a more detailed description of how this parameter is implemented in the ND model, please refer to [156].

- **Q^2 dependence alteration**

  For different neutrino-nucleus momentum transfer squared in neutrino interactions, Q^2, a normalisation weight is introduced, binned in true Q^2, with bins of 0.25-0.5 GeV, 0.5 GeV-1.0 GeV, and greater than 1.0 GeV, refered to as Q^2 norm 5, 6, and 7 in the fitter. The weights are introduced to control the event rate of such interactions; a large weight indicate a bigger interaction probability in the energy bin. These three normalisation parameters are introduced to match MINERνA data, as the experimental measurement is significantly smaller than model prediction [111, 157, 158].

- **Shell model parameters**

  Another important group of parameters being fitted in BANFF is the shell modification parameters. According to the spectral function model, a nucleon is not fixed in its nucleus; instead, it carries some momentum, which has an impact on the neucleon's interaction with neutrinos. The distribution can be described by a 2D distribution with probability density function $P(\vec{p}, E)$, which is measured experimentally and corrected by theoretical computation [58, 149]. To introduce more freedom to the shape of $P(\vec{p}, E)$, the T2K ND model introduced the shell occupancy normalisation parameters, or the Mean Field (MF) normalisation parameters. A weight is assigned to each nuclear shell in order to tune the probability that the neutrino interacts with a nucleon in this shell via a CCQE interaction. For carbon there are two such parameters (S and P shell) to tune the energy distribution, and for oxygen there are three (S, $P_{1/2}$ and $P_{3/2}$). Similarly, there are also splined MF shape parameters to tune the shape of the missing momentum distribution in each

shell: two for carbon and three for oxygen [149]. Additionally, there are two parameters, one for oxygen and the other for carbon, to account for short-range correlated nucleons [58, 149]. The neutrino interaction model has twelve parameters in total to increase the flexibility of the shell model.

- **Pauli blocking**

  Both nucleons, protons and neutrons, are fermions, thus two identical nucleons are not allowed to occupy the exact same quantum state. In the ground state of the nucleus, all the nucleons are in their lowest possible energy state, and the momentum of the nucleons with highest momentum is referred to as the Fermi momentum, p_F. As a result, the incoming neutrino must carry enough energy to excite the struck nucleon to a higher energy level whose energy eigenvalue is greater than the Fermi energy determined by the Pauli exclusion principle. This puts a lower limit on the neutrino energy and suppresses the neutrino interaction cross section in general. This effect is known as Pauli blocking [57]. In the neutrino interaction model, cross sections of neutrinos of energy below a certain value are set to zero, and this value is a parameter being fitted in BANFF. Four such parameters are implemented as dimensionless shape parameters for different interaction participants, $\nu - C, \bar{\nu} - C, \nu - O$ and $\bar{\nu} - O$ [79, 149]. The prior values are set at 0, which corresponds to the nominal $p_f = 209$ MeV. Their uncertainty parameter is set to 1, which corresponds to 30 MeV.

- **Binding energy**

  Nucleons within a nucleus are bound together in a quantum mechanical bound state by the strong force carried by gluons. However, as a nucleon is a quantum very-many-body state, the exact solutions are not achievable via QCD calculations. The binding energy of a nucleus refers to the amount of energy required to remove a nucleon from it, and plays a direct role in the relationship between muon and neutrino energies. Hence, the binding energies are implemented as parameters in BANFF to control such effects.

  By varying this parameter, the simulated momentum of the muon can be affected. Specifically, as binding energy increases, the momentum of the muon decreases, because the amount of energy required for a nucleon to break free from the nucleus

increases. This can potentially cause the event to shift from one lepton kinematic bin to another. However, such a shift can create issues with the MIGRAD algorithm utilised in the ROOT MINUIT2 library [105] due to the discontinuous changes in the likelihood function.

To mitigate this, the current neutrino interaction model employs a reweighting strategy, where the weight of an event changes in response to variations in the binding energy. The change in weight is determined by the ratio of the current binding energy to the nominal binding energy. For more information about this implementation, refer to [159].

- **Optical potential**

  In the current NEUT neutrino interaction event generator using the spectral function model, the final-state interactions are not considered when computing the cross section [149, 156, 158]. The optical potential correction is introduced to cover the impact of final-state interactions on the CCQE cross section in the spectral function model. These corrections reweight events according to their energy and kinematics using results from previous and external studies. There are again four parameters to tune such a correction, two for carbon and two for oxygen [149].

Parameter name	Type	Prior value	Prior uncertainty
$M_{\mathbf{QE}}^{A}$	Shape	1.03 (GeV)	0.06 (GeV)
Q^2 norm 5	Normalisation	1	11%
Q^2 norm 6	Normalisation	1	11%
Q^2 norm 7	Normalisation	1	40%
P shell MF norm C	Normalisation	0	20%
S shell MF norm C	Normalisation	0	45%
SRC norm C	Normalisation	1	200%
P shell MF p_{miss} shape C	Shape	0	100%
S shell MF p_{miss} shape C	Shape	0	100%
P 1/2 shell MF norm O	Normalisation	0	20%
P 3/2 shell MF norm O	Normalisation	0	45%
S shell MF norm O	Normalisation	0	75%
SRC norm O	Normalisation	1	200%
P 1/2 shell MF p_{miss} shape O	Shape	0	100%
P 3/2 shell MF p_{miss} shape O	Shape	0	100%
S shell MF p_{miss} shape O	Shape	0	100%
Pauli Blocking C ν	Shape	0 (209 MeV)	1 (30 MeV)
Pauli Blocking C $\bar{\nu}$	Shape	0 (209 MeV)	1 (30 MeV)
Pauli Blocking O ν	Shape	0 (209 MeV)	1 (30 MeV)
Pauli Blocking O $\bar{\nu}$	Shape	0 (209 MeV)	1 (30 MeV)
E_b C ν	Binding energy	0 (2 MeV)	100% (6 MeV)
E_b C $\bar{\nu}$	Binding energy	0	100% (6 MeV)
E_b O ν	Binding energy	0 (4 MeV)	100% (6 MeV)
E_b O $\bar{\nu}$	Binding energy	0 MeV	100% (6 MeV)
E_b C α	Binding energy	0	100% (41.6 MeV)
Optical potential C	Shape	0 (No correction)	Uniform (0-1)
Optical potential O	Shape	0 (No correction)	Uniform (0-1)

TABLE 7.1: The summary of all CCQE parameters implemented and fitted in the BANFF fit. The unit of $M_{\mathbf{QE}}^{A}$ is GeV. For all other parameters, the value outside the parenthesis is the number used in the fit, and the in between is its physical meaning. Those do not have a parenthesis are shape-controlling or normalisation parameters. In other words, they control the scale or the shape of distributions, and do not carry any direct physical meaning. All parameters remain the same as [79, 109]. For more information on setting prior values and errors, please refer to [149, 158].

7.3.2.2 Two particle two hole model

The Two-Particle-Two-Hole (2p2h) interaction refers to interactions in which the neutrino interacts with a pair of bound nucleons instead of a single nucleon. In NEUT, such processes are implemented using the Valencia model (or Nieves model) described in [160]. The following parameters regarding 2p2h interactions are fitted in BANFF:

- **Normalisation parameters**

  There are three 2p2h normalisation parameters, one for neutrino interactions, another for antineutrino interactions, and another for the carbon to oxygen interaction rate ratio. As their name suggests, these parameters control the overall event rate of 2p2h interactions.

- **Shape parameters**

  There are four parameters in the 2p2h implementation that vary the energy and momentum transfer distributions. There are parameters for carbon and oxygen, two-neutron pairs and neutron-proton pairs, making a total of four such parameters. Additionally, there is a PNNN shape parameter for the antineutrinos, which can interact on two-protons and neutron-proton pairs. In the end, there are five such 2p2h shape parameters.

It is worth mentioning that there are another four parameters in the model describing the 2p2h event rate's dependence on the neutrino energy, for high and low energy 2p2h interactions with neutrinos and antineutrinos respectively. Currently BANFF does not fit these parameters, only MaCh3 does [149, 159]. This is because that the near detector sample does not have much constraining power over those parameters. For a summary of 2p2h parameters being fitted in BANFF, please see Table. 7.2.

Parameter name	Type	Prior value	Prior uncertainty
2p2h norm ν	Normalisation	1	100%
2p2h norm $\bar{\nu}$	Normalisation	1	100%
2p2h norm C/O ratio	Normalisation	1	20%
PNNN shape	Shape	0	33%
2p2h shape C np	Shape	0	100%
2p2h shape C nn	Shape	0	100%
2p2h shape O np	Shape	0	100%
2p2h shape O nn	Shape	0	100%

TABLE 7.2: The summary of all 2p2h parameters implemented and fitted in the BANFF fit in OA2022.

7.3.2.3 Single pion production

In the NEUT generator, the CC resonant Single-Pion Production (SPP) model is implemented using the Rein-Sehgal model [161]. This subsection will cover all parameters implemented in BANFF of this model.

- **Axial mass and form factor**

  Similarly to the CCQE interaction, the differential cross section of neutrino single pion production events also includes form factors and an axial mass [161, 162, 163, 164]. Two parameters are included in the fit to scale the single pion production axial mass and the form factors.

- **Isospin-half background**

  The Rein-Sehgal model describes the single-pion production process, in which the nucleon is first excited to the resonance state, and subsequently decays to a single pion and a nucleon. However, this is not the only channel via which a neutrino CC interaction can produce a single pion, as the non-resonant state of nucleons can also produce pions [165]. The single-pion events from such interactions are considered as background to the CC resonant single-pion production. Thus, another two parameters are included in BANFF to account for the non-resonant isospin-half pion production, one scales the spin-half events relative to the spin-one events, another scales the spin-half background with low pion momentum.

- **Resonant binding energy**

  The resonant binding energy parameters are included to tune the impact of binding energy in neutrino resonant interactions. There are four separate parameters for neutrinos and antineutrinos, interacting on carbon and oxygen nuclei respectively. The neutrino and antineutrino parameters are implemented separately as the incident nucleon is different.

- **Resonant decay**

  In the decay of nucleon resonant states in the Rein and Sehgal model, there are two methods to compute $W(\theta, \phi)$, the angular distribution of the final-state pion and the nucleon. The first singles out the decay of the resonant state and considers its decay in its center-of-mass frame, where the pion and the nucleon are ejected back-to-back isotropically. The second method takes also the $N \to \Delta$ transition process into consideration [149], in which process the πN final state is produced through the excitation of an initial-state nucleon, producing an intermediate resonance that shortly decays. A parameter is included in BANFF to tune the ratio between the two methods.

- **CC coherent**

  The term CC coherent interaction refers to an interaction such that the neutrino interacts with the nucleus and produces a charged lepton and a pion with opposite charge, leaving the nucleus in the same state as pre-interaction. The model of such interactions fitted in BANFF was developed by Rein and Sehgal in 1983 [166]. The event rate of simulated CC coherent processes is controlled by two normalisation parameters, for carbon and oxygen separately.

- **π^0 normalisation**

  Two normalisation parameters are applied to tune the event rate of resonant interactions that result in the production of a single π^0. There are separate parameters for neutrino and antineutrino interactions.

A summary of SPP parameters implemented in BANFF is given in Table. 7.3.

Parameter name	Type	Prior value	Prior uncertainty
CA5	Shape	1.06	0.1
M_A^{RES} GeV	Shape	0.91 GeV	0.1 GeV
ISO BKG Low p	Shape	1.3	1.3
ISO BKG	Shape	1.21	0.27
RES E_b C ν	Shape	25 MeV	25 MeV
RES E_b O ν	Shape	25 MeV	25 MeV
RES E_b C $\bar{\nu}$	Shape	25 MeV	25 MeV
RES E_b O $\bar{\nu}$	Shape	25 MeV	25 MeV
Resonant Δ decay	Shape	1	1
CC Coherent C	Normalisation	1	0.3
CC Coherent O	Normalisation	1	0.3
SPP π^0 norm ν	Normalisation	1	0.3
SPP π^0 norm $\bar{\nu}$	Normalisation	1	0.3

TABLE 7.3: The summary of all single-pion production parameters implemented and fitted in the BANFF fit in [109].

7.3.2.4 Multi-pion and deep inelastic interactions

As described in Sec. 2, Deep Inelastic Scattering (DIS) interactions refers to the situation in which the neutrino energy is high enough to break the quark bound state and interact with component quarks inside a nucleon. Currently, the computation of neutrino multi-pion and deep inelastic interaction cross sections uses the GRV98 [167] parton distribution functions, with Bodek-Yang modifications [168, 169]. In the NEUT generator implementation, for hadronic states with invariant mass 1.3 GeV $< W <$ 2.0 GeV, a custom multi-pion model is used. For interactions with $W >$ 2.0 GeV, the final-state hadronisation is simulated using PYTHIA [170]. Various parameters for such interactions have been introduced into BANFF to allow for freedom in the model.

- **Bodek-Yang correction parameters**

  As mentioned, the deep inelastic interaction model in NEUT has a Bodek-Yang correction applied. A shape parameter is implemented in BANFF to control the effect of this correction. Another two normalisation parameters are implemented to

control the overall number of CC deep inelastic events, with a separate parameter for neutrinos and antineutrinos.

- **Multi-pion multiplicity parameters**

  Two shape multi-pion production parameters are fitted in BANFF. The first one accounts for the difference between multi-pion multiplicity models, the AGKY model [171] and the one used in NEUT. The second one tunes the shape of the cross section in terms of total invariant mass W and number of pions N_π.

- **Multi-pion Bodek-Yang vector and axial parameters**

  New corrections to the BY model in the low Q^2 region were published in 2010 [172], and the model is different from what was originally implemented in NEUT. Two parameters are included to account for the differences between the two models.

- **CC Multi-pion normalisation**

  The overall event rate of CC multi-pion interactions is modelled and controlled by two normalisation parameters: one for neutrinos, the other for anti-neutrinos.

- **CC Misc**

  The charged-current miscellaneous parameter accounts for higher-multiplicity (i.e. more tracks in the final state) events that do not fall into the deep-inelastic or multi-pion category. Usually, this means the production of non-pion hadrons, including kaons and eta. It is a shape parameter that controls the distribution of such events.

A summary of multi-pion and deep inelastic scattering parameters implemented in the T2K near detector fit is given in Table. 7.4.

Parameter name	Type	Prior value	Prior uncertainty
Multiπ BY Vector	Shape	0	100%
Multiπ BY Axial	Shape	0	100%
Multiπ multiplicity total cross section	Shape	0	100%
Multiπ multiplicity shape	Shape	0	100%
CC BY DIS	Shape	0	100%
CC DIS norm ν	Normalisation	1	3.5%
CC DIS norm $\bar{\nu}$	Normalisation	1	6.5%
CC MISC	Shape	1	100%

TABLE 7.4: The summary of all multi-pion and deep inelastic parameters implemented and fitted in the BANFF fit in [109].

7.3.2.5 Final-state interaction parameters

The term Final-State Interaction (FSI) refers to interactions between the particles produced in a neutrino-nucleon interaction and other nucleons in the same nucleus [173, 174]. Pions are heavily affected by FSI, and because such interactions impact the pion multiplicity of events, it is important for T2K to model such interactions and constrain relevant systematic uncertainties. In the T2K MC simulation, the low-momentum pion FSI are modelled using the Salcedo model [175], while the high-momentum pion FSI are instead modelled using the model described in [176].

In the BANFF fit implementation, for each type of FSI, quasi-elastic, charge exchange, pion absorption and pion production, a parameter is included to vary the probability for a given type of interaction to happen. Quasi-elastic and charge exchange interactions have an additional parameter for high-energy incidents. An extra nucleon FSI parameter is also included to control the probability of nucleon final-state interactions. In the end, there are seven FSI parameters in the BANFF fit. A summary of FSI parameters fitted in BANFF is provided in Table. 7.5.

Parameter name	Type	Prior value	Prior uncertainty
FEFQE	Shape	1.069	31.3%
FEFQEH	Shape	1.824	85.9%
FEFINEL	Shape	1.002	110.1%
FEFABS	Shape	1.404	43.2%
FEFCX	Shape	0.697	30.5%
FEFCXH	Shape	1.8	28.8%
Nucleon FSI	Shape	0	30.0%

TABLE 7.5: The summary of all final-state interaction parameters implemented and fitted in the BANFF fit in OA2022. Each parameter scales its corresponding pion or nucleon interaction probability, and hence is naturally dimensionless.

7.3.2.6 Other parameters

There are a few other parameters that do not belong to any of the genres previously mentioned. They will be discussed in this subsection.

- **Neutral current parameters**

  Four normalisation parameters are implemented in BANFF to control the event rate of neutral current interactions. This includes one parameter to control NC coherent interactions, where the same neutrino is also among the final state products; another parameter scales the event rate of NC events that emits a single photon; two parameters controlling the event rates of all other NC processes, one for ND280, another for SK.

- **Electron neutrino**

  Although in the standard model, all charged leptons couple identically to QED photons, the heavier mass of μ and τ can only be produced in a limited phase space. Two parameters are implemented in BANFF to model these differences, one controls the difference caused by lepton masses in the phase space of the initial neutrino-nucleus interaction, the other controls the mass difference's impact on the radiative correction applied to the interaction in the simulation process. Both are implemented as normalisation parameters. Another two parameters are implemented for neutrino

and antineutrino. The priors of electron neutrino parameters are summarised in Table. 7.6

- **Coulomb corrections**

  The simulation of neutrino interactions and production of charged leptons considers only the relevant weak interaction process. However, as the charged lepton carries charge, once it is ejected from the nucleus, it is then affected by the nucleus via the Coulomb force. This effect is parameterised as

$$|V_C| = \frac{E_0}{\langle r^2 \rangle^{1/2}} \times \mathbf{Z}$$

  where $E_0 = 1.27 \pm 0.10$ MeV·fm, $\langle r^2 \rangle^{1/2} = 2.47$ fm and $\mathbf{Z}$ is the atomic number of the incident nucleus, per measurements in [177].

  To account for this effect, a posterior correction is applied to muon interactions. Given that ν and $\bar{\nu}$ interactions create charged leptons of opposite sign, and the Coulomb forces subsequently work in opposite directions, there are separate parameters to control corrections for neutrino and anti-neutrino interactions.

The priors of the Coulomb correction parameters are summarised in Table. 7.6

Parameter name	Type	Prior value	Prior uncertainty
NC coherent	Normalisation	1	30%
NC 1γ	Normalisation	1	100%
NC other ND280	Normalisation	1	30%
NC other SK	Normalisation	1	30%
ν_e/ν_μ	Normalisation	1	2.82343%
$\bar{\nu}_e/\bar{\nu}_\mu$	Normalisation	1	2.82343%
Coulomb correction ν	Normalisation	1 (2.6 MeV for C, 3.3 MeV for O)	2.002%5
Coulomb correction $\bar{\nu}$	Normalisation	1 (-3.6 MeV for C, -4.3 MeV for O)	1.00499%

TABLE 7.6: The summary of the electron neutrino and Columb correction parameters implemented and fitted in the BANFF fit in [149].

7.3.3 Detector model

The ND280 detector systematic errors are also implemented in the BANFF fit. A long list of systematic uncertainty sources has been introduced in Chapter 6, each has its own model and parameters. The ideal way to include the effect of detector parameters would be to vary the parameters of systematic sources and rebuild the MC histograms. However, this is beyond what current computing hardware can manage, and a simplified treatment was adopted by BANFF. BANFF parameterises the effect of detector errors as normalisation parameters for each bin. To do this, a covariance matrix was made using 500 toy MC experiments in psyche, where the ND280 detector error source parameters are varied. The toy experiments are then used to extract the systematic errors in bins, and the correlation between bins.

The BANFF sample binning currently contains 5416 bins. Should all of them have associated normalisation weight being varied in BANFF, the time the fit takes to converge will be too long. BANFF reduces the number of parameters by applying the same weight to neighbouring bins that have similar total uncertainty. Currently, if the difference of relative error of neighbouring bins is smaller than 5%, those two bins will be merged. After the merge, there are 750 detector bin normalisation parameters in the fit, which is a big increase from the 592 of the previous non-4π sample [109], i.e. before this work. Such parameters are usually referred to as observable normalisation ('ObsNorm') parameters in other T2K documents [79, 159, 173].

7.4 T2K near detector BANFF fit

This section presents an in-depth explanation of the T2K near detector fitter, BANFF, and its role in fitting the ND280 Monte Carlo (MC) simulation to experimental data to minimise uncertainties in flux and neutrino interaction parameters. BANFF arranges detector observations into two-dimensional binned samples, specifically binning the events selected for each of the samples discussed in Sec. 5 according to their p_μ and $\cos\theta_\mu$ values.

For all MC events included in the samples, their responses to parameter variations are pre-calculated and stored within "spline" files. The event weight, or the change in the event's probability, is first evaluated at some given knots, then extrapolated using a polynomial function and saved as a ROOT TSpline class for each event and each parameter

[109, 159, 178]. As BANFF adjusts these parameters, it constructs a new MC prediction based on the current parameter values using the spline files. The prediction is then compared to the data, and the similarity is assessed through a $\Delta\chi^2$ test statistic derived from a likelihood function.

The fitting process itself is carried out using the ROOT MINUIT2 library [179]. This section provides an overview of the likelihood definition for 2D binned samples and the subsequent minimization using the MINUIT2 algorithm.

7.4.1 Reweighting and splines

The most rigid way to compute how the variation of a shape parameter changes the subsample is to change the parameter in the MC generator and re-run the whole MC simulation and selection, which is too computationally demanding. Alternatively, T2K computes the impact of varying a parameter beforehand and save them as spline files. For each event and each parameter, the spline generation code calculates the event's new weight at $\pm3\sigma, \pm2\sigma, \pm1\sigma$ and the nominal value of the parameter of interst while fixing all other parameters to their nominal values using NEUT, and extrapolates the event weight's response to the parameter using a third-order polynomial. This is done for all selected MC events, and all shape parameters. For more details on how reweighting works, please refer to [159]. The third-order polynomials are stored in a CERN ROOT TSpline3 class, and are the most important input to the BANFF fit. BANFF assumes that all parameters are mutually independent when close to their nominal value. It then evaluates the polynomial functions of each parameter at the current value of the parameter, to obtain a weight from each parameter. Then all of the weights of the parameters are multiplied together to produce the final weight of the MC event. The 2D ($\cos\theta$-p_μ) kinematic histograms of each subsample at the current parameter setting is then rebuilt with all events' weights considered.

7.4.2 Likelihood definition

The selection criteria outlined in Sec. 5 yield ten subsamples for each FGD, with each subsample containing a number of events. A selected ND280 event consists of one or more tracks, characterised by various low- or high-level features such as the number of

hits in the TPC, starting and ending positions, track length, or reconstructed momentum transfer between the incoming neutrino and incident nucleon. All these features provide some physics information, and depend on both the neutrino interaction event, and the properties of ND280.

However, it is not feasible for the fitter to simultaneously consider all this information. In the T2K near detector fit, only two features are taken into account: the magnitude of the momentum of the charged-current muon track, $|\vec{p_\mu}|$, commonly referred to as p_μ; and the angle between the muon track and the neutrino beam axis, $\cos\theta_\mu$.

The ND280 FHC 4π selection comprises 20 subsamples, with ten in each FGD. An additional 12 RHC subsamples are used in the ND fit, resulting in a total of 32 subsamples. Within each subsample, events are binned according to their p_μ and $\cos\theta_\mu$ values to create 2D histograms. The binning edges are manually designed for each subsample to balance fineness, efficiency, purity, and relative error. In the current configuration, there are a total of 750 bins across all samples. Thus, the ND280 observation is represented by a rank-3 tensor: [1]

$$N^{\alpha}_{i,j}, \tag{7.12}$$

where $\alpha = 1, 2, 3...32$ is the subsample index, i is the momentum bin index, and j is the $\cos\theta$ bin index. This tensor has 750 degrees of freedom in total, each corresponding to an observable bin. The ND fitter flattens this tensor and uses a single index i, for all bins. This thesis will follow this indexing convention, and the ND fit input will be described as a flattened one-dimensional vector:

$$N_i, i = 0, 1, 2...749 \tag{7.13}$$

In instances where the likelihood of obtaining a true outcome, p_ω, from a Boolean experiment (i.e., a result that can only be true or false) is small, and the experiment is conducted a significantly large number of times, X, the binomial distribution for the occurrence of the outcome k times, can be effectively approximated by the Poisson distribution.

In the T2K experiment, the outcome of neutrino interactions within a single bunch of protons can be characterised in two distinct ways: either the event is assigned to the N_i

[1] By the most rigid mathematical standard this is not a tensor, as the dimensionality of i,j changes as α changes.

bin (true result), or it is not (false result). Given that the probability of an event being of a specific type, and having an incident muon with the appropriate momentum and $\cos\theta$ value is low, the true outcome is considerably less likely to occur than the false outcome. This justifies the use of the Poisson approximation.

Consequently, the probability of observing k events in bin i, represented by N_i, can be described using a Poisson distribution:

$$P(N_i = k) = \frac{\lambda^k \exp(-\lambda)}{k!}, \tag{7.14}$$

where $\lambda = X \times p_\omega^i$ is the expected number of appearances after all N tests, and p_ω^i is the probability of a proton bunch fired at the target producing an CC event that falls in to observable bin index i.

Assuming that the number of events in each bin is mutually independent, the overall likelihood of the experiment can be calculated as the product of all 750 mutually independent events, i.e. the observed number of events in bin i being N_i. In other words, the likelihood of observing a result of N_i in each bin is the product of the likelihoods of all the bins.

$$\mathcal{L} = \prod_i \frac{\lambda_i^{N_i} \exp(-\lambda_i)}{N_i!} \tag{7.15}$$

where λ_i is the expected number of events in the ith bin, which is a quantity the T2K near detector model predicts using MC simulation. The model used for Monte Carlo simulation depends on various parameters, including flux parameters, neutrino-nuclei interaction parameters and detector parameters. Annotating all these parameters using a single vector $\vec{\theta}$ in the model, Eq. 7.15 can be rewritten as a penalty term:

$$\mathcal{L}_{ND280}(\vec{\theta}) = \prod_i \frac{\lambda_i^{N_i} \exp(-\lambda_i)}{N_i!}. \tag{7.16}$$

It can be simplified by dividing it using the likelihood evaluated at the nominal parameter values, which is independent of $\vec{\theta}$ when $N_i = \lambda_i$:

$$\mathcal{L}_{ND280}(\vec{\theta}) = \prod_i \left[\frac{\lambda_i^{N_i} \exp(-\lambda_i)}{N_i!} \times \left(\frac{N_i^{N_i} \exp(-N_i)}{N_i!} \right)^{-1} \right]. \tag{7.17}$$

The dividing term takes this form as the definition of nominal parameter values is the

set of parameters that makes prediction match observation, i.e. $N_i = \lambda_i$ for every i. This works for uncorrelated parameters with definite prior knowledge. In reality, each parameter has its own prior distribution from theory and other experiments, and the parameters are inter-correlated. To take those into account, the distribution terms must also be multiplied with a penalty term. All prior distributions of parameters are assumed to be Gaussian and hence can be written as

$$\pi(\vec{\theta}) = \frac{1}{(2\pi)^{n/2}|V_\theta|^{\frac{1}{2}}} \exp\left(\frac{1}{2}\Delta\vec{\theta}(V_\theta)^{-1}\Delta\vec{\theta}^T\right). \tag{7.18}$$

In Eq. 7.18, V_θ is the correlation matrix of all parameters that make up the θ vector, $\Delta\vec{\theta}$ represents the parameters' deviation from their nominal value, and n is the number of parameters. It is reasonable to assume that the flux, cross section and detector parameters only physically correlate in their own group [2], and the large covariance matrix is three-block diagonal with the three blocks being flux, detector and cross section. Thus, the prior can be written as

$$\pi(\vec{\theta}) = \pi(\vec{x})\pi(\vec{b})\pi(\vec{d}) \tag{7.19}$$

where $\vec{x}, \vec{b}$ and $\vec{d}$ are the multivariate normal distributions of cross section, flux and detector parameters, respectively. The likelihood function then becomes

$$\mathcal{L}_{ND280}(\vec{\theta}) = \frac{\pi(\vec{x})\pi(\vec{b})\pi(\vec{d})}{\pi(\vec{x}_{nom})\pi(\vec{b}_{nom})\pi(\vec{d}_{nom})} \times \prod_i \left[\frac{\lambda_i^{N_i}\exp(-\lambda_i)}{N_i!} \times \left(\frac{N_i^{N_i}\exp(-N_i)}{N_i!}\right)^{-1}\right]. \tag{7.20}$$

where $\pi(\vec{x}_{nom})$, $\pi(\vec{b}_{nom})$ and $\pi(\vec{d}_{nom})$ are the prior distribution functions evaluated at the nominal parameter value. This is in principle the full likelihood function constructed using BANFF samples. Still, this form is rather complicated and not efficient when used in the actual fit, and steps are taken to speed up the process.

The first part of Eq. 7.20 diminishes as the parameter variation from nominal expectation grows, and is referred to as the penalty term. All the sample contributions are in the second part, the production obtained by multiplying bin contribution from index 1 to N. The second part is therefore called the sample term. After the cancellation of terms,

[2] Anti-correlations between flux and cross-section parameters have been found in previous T2K analysis. In practice, the fitter is allowed to explore correlation between different groups of parameters, and a single large correlation matrix is used as input to the fitters.

the sample term becomes:

$$\mathcal{L}^{\mathrm{S}}_{\mathrm{ND280}}(\vec{\theta}) = \prod_i \left(\frac{\lambda_i}{N_i}\right)^{N_i} \times \exp(-\lambda_i + N_i). \tag{7.21}$$

Although the right hand side of the equation does not explicitly contain model parameters $\vec{\theta}$, the expected number of events in bin i still depends on $\vec{\theta}$, and consequently the product. Taking the logarithm of Eq. 7.21, the product becomes a sum, and the full expression transforms into

$$\ln \mathcal{L}^{\mathrm{S}}_{\mathrm{ND280}}(\vec{\theta}) = \sum_i N_i(\ln \lambda_i - \ln N_i) - \lambda_i + N_i. \tag{7.22}$$

Multiplying the expression with an additional factor of -2 produces the uncorrelated, no prior likelihood-based quantity:

$$(\Delta\chi^2{}_{\mathrm{ND280}})^{\mathrm{S}}(\vec{\theta}) = 2\sum_i(\lambda_i - N_i + N_i \ln \frac{N_i}{\lambda_i}) \tag{7.23}$$

Adding back the penalty term, the full ND280 likelihood of observing N_i, when the model parameters take the values set in $\vec{\theta}$, becomes

$$\Delta\chi^2{}_{\mathrm{ND280}}(\vec{\theta}) = 2\Sigma_i(\lambda_i - N_i + N_i \ln \frac{N_i}{\lambda_i}) - \Delta\vec{\theta}_a (V_\theta)^{-1}_{ab} \Delta\vec{\theta}^T_b. \tag{7.24}$$

Note that Einstein's summing convention is used to emphasise the matrix multiplication. This statistic, $\Delta\chi^2{}_{\mathrm{ND280}}(\vec{\theta})$, is what the BANFF fit minimises. The first part, $2\Sigma_i(\lambda_i - N_i + N_i \ln \frac{N_i}{\lambda_i})$ is determined by the MC prediction at the current value of the parameter and is usually referred to as the sample contribution. The second part is the penalty term; with it included, the farther a parameter is from its prior value, the larger its contribution to the penalty term becomes.

7.4.3 Minimisation using MINUIT

BANFF uses the ROOT MINUIT library [179] to conduct the minimisation of $\Delta\chi^2_{\mathrm{ND280}}$. To compute the post-fit probability density function of each fitted parameter, BANFF assumes that $\Delta\chi^2_{\mathrm{ND280}}$ can be approximated well enough by quadratic functions in the $\Delta\chi^2$ in the vicinity of the global minimum that is found. The multi-variate Taylor expansion

of $\Delta\chi^2$ to the first order is

$$\Delta\chi^2_{\text{ND280}} = \sum_i \sum_j \frac{\partial^2 \Delta\chi^2(\vec{\theta})}{\partial_i \partial_j}(\theta_i - \theta_i^{min})(\theta_j - \theta_j^{min} + \mathcal{O}(\delta\chi^3)) \tag{7.25}$$

and this is what MINUIT finds using the HESSE algorithm. There is no linear term since near the minimum the first order derivatives are 0. The first part, $\frac{\partial^2 \Delta\chi^2(\vec{\theta})}{\partial_i \partial_j}$ is the Hessian matrix, the inverse matrix of which is the fitted parameters covariance matrix at the best fit point [179]

$$\pi_{post}(\vec{\theta}) = C \exp(-\frac{1}{2}\Delta\chi^2_{min}\vec{\theta}) \tag{7.26}$$

where C is some normalisation constant. In practice, BANFF integrates out all nuisance parameters in $\pi_{post}(\vec{\theta})$ to obtain $\pi_{post}(\vec{f})$, which is only dependent on parameters of interest to the far detector fit i.e. cross-section parameters and flux parameters.

7.5 Validation of the BANFF fit

In addition to the data fitting process that generates post-fit central values, constraints, and covariance for far detector fits, numerous validation techniques are employed to ensure that the BANFF fit functions as intended and to identify potential problems in the likelihood function that may disrupt the fitting process. These validation methods encompass event-rate studies, likelihood scans, Asimov fits, bias studies, and fake-data studies.

As of early 2023, at the time of this thesis composition, likelihood scans and Asimov fits i.e. fit to nominal MC instead of data, have been performed to validate the BANFF fit with the latest samples. This section will offer a comprehensive examination of these two validation methods and present their respective results. The remaining validation techniques, which await to be conducted in future studies, will be briefly introduced in this section.

7.5.1 Likelihood scan

To test a parameter's impact on the likelihood, the first validation for the fitter is the likelihood scan. As the ROOT MINUIT2 MIGRAD algorithm can easily be broken by discontinuities in the functions being fitted [179], it is important to detect kinks in the likelihood function. The idea of this validation is to fix all but one parameter of interest

to their nominal values, then vary the parameter of interest to watch how the likelihood responds to the variation. For each parameter, the likelihood function is evaluated at 50 equally-spaced points from -3σ to $+3\sigma$. In most cases, the farther the parameter gets from its nominal value, the less likely the event is to happen, and the test statistic grows. Hence, a bowl shaped curve is drawn using the likelihood at those 50 dots, with the bottom of the bowl sitting on the nominal value. Such curves not only help detect roughness in the likelihood function, but also provide information on how much constraining power the current samples have on this particular parameter. A steeper bowl means the likelihood function is more sensitivite to the change of this parameter, hence a stronger constraint can be expected. On the other hand, should the likelihood function not be dependent on the parameter ($\frac{\partial \chi^2}{\partial x} = 0$), the plot is a flat line. Fig. 7.5 shows the likelihood for the MAQE parameter. Using the newly introduced 4π sample, the likelihood function is more sensitive now to the variation of the M_{QE}^A parameter, suggesting a potentially better constraint on M_{QE}^A.

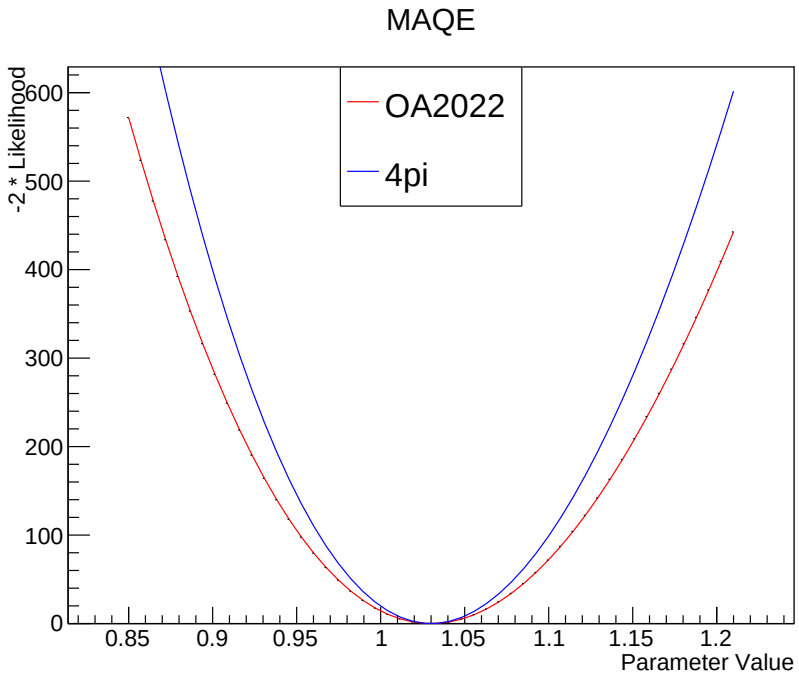

FIGURE 7.5: The likelihood scan output of the M_{QE}^A parameter with the 4π sample (blue solid line) and OA2022 samples (red solid line).

Likelihood scans also show that the inclusion of the new samples, while including more data into the T2K oscillation analysis, does decrease the likelihood function's sensitivity to

some parameters. As displayed in Fig. 7.6, the inclusion of 4π samples made the likelihood function less sensitive to the variation of the quasi-elastic low-energy final-state interaction parameter, FEFQE. The exact reason for each parameter is yet to be understood; in general this tends to happen to parameters which the new high-angle or backward CC0π samples are not directly related to, for instance the pion FSI dials controlling the final state interaction probability of pions, or the multi-π parameters, which affects the events with high multiplicity. This can partly explained by the fact that new ToF flip correction also has an impact on those samples i.e. the sense correction of pions and protons could change the topology an event belongs to.

Another feature of the FEFQE parameter scan plot in Fig. 7.6 is that the likelihood output is not symmetric about the nominal value. This is common in FSI parameters and Pauli blocking parameters, because of the physical implementation of such parameters in the model [79, 149, 158]. Although this is not what was assumed in the design of BANFF, this does not break the fit, and hence is accepted as a physical fact. Among all 70 cross-section parameters being fitted in the BANFF fit, 54 are improved by the inclusion of 4π subsamples, while 16 suffer a decrease in sensitivity.

For the likelihood scan outputs of all cross-section parameters, please see Appendix B.

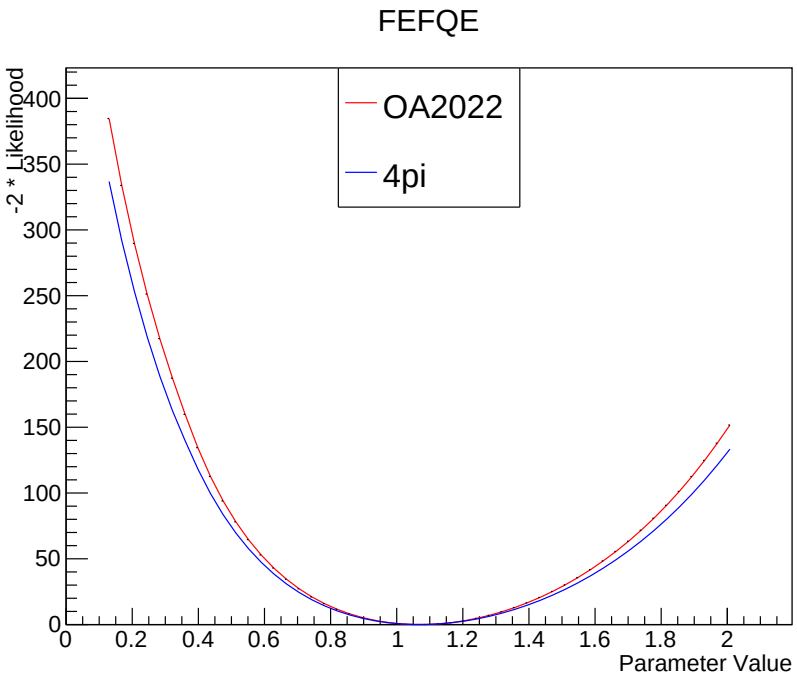

FIGURE 7.6: The likelihood scan output of the FEFQE parameter with the 4π sample (blue solid line) and OA2022 samples (red solid line).

7.5.2 Asimov fits

Another important validation of the fitter is the Asimov fit. The term Asimov fit refers to a fit to the nominal MC predictions rather than the actual data collected. The data is collected from the physical world and the actual mechanism behind the physical process remains hidden. A fit to data provides a set of parameter values that best describes the real world in the setting of the model, given the data. On the other hand, the MC simulation is generated by the sample model as implemented in the fitter, with each of the model parameters set to its nominal value. A fit to the MC prediction can give an upper limit on how much the data fit can reduce systematic uncertainties on model parameters [3] .

Like likelihood scans, running Asimov fits also helps to identify problems in the likelihood function. It is possible that the fitter falls into a group of local minima due to degenerate parameter responses. This problem could stop the fit from converging and

[3]The MC prediction of number of events in each sample bin is usually non-integer, while this quantity in data is integer definite. The Asimov fit is different from the data fit in this sense.

producing usable post-fit priors and uncertainties for the far detector fit. Since the likelihood function is the same in an Asimov fit and a data fit, it is likely that the Asimov fit runs into the same convergence problem as the data fit. Should the Asimov fit fail to converge, the fit log can help identify the parameter that caused the issue [4] .

It is expected that an Asimov fit returns all parameters being varied to their nominal prior values, where the fit begins, with a reduced uncertainty. Fig. 7.7a - 7.9b show the Asimov fit outputs produced using the 4π samples, as compared with the OA2022 samples in [109] and [105]. In all those plots, the top row of plots shows the constraints of the 4π samples compared to the constraints of OA2022 samples. Values smaller than 1 indicate an improvement, while values greater than 1 indicate a setback. The second row displays the differences between 4π and OA2022 postfit central values. In Asimov fits, the values are expected to converge back to the prefit central value regardless of the sample, thus the differences should be zero in all cases. As expected, all the differences are exactly zero in the results. The bottom panels show the postfit constraints on the ND model parameters. The bars indicate the 1σ confidence interval per the fitting result, hence the shorter a bar is, the stronger the constraint it represents. Like in the likelihood scans, the blue bars represent the OA2022 constraints, and the red bars represent the 4π samples. The 4π sample provides improvements in most CCQE and 2p2h parameters, while setbacks can be seen in FSI and DIS parameters. An observation is that this draw back tends to happen in parameters to which the new samples do not wield much power to constrain, for instance DIS parameters. When more irrelevant events are included in the fit, the likelihood becomes relatively less sensitive to the change of such parameters, and consequently the constraining power the fit has over those parameter decreases. For the FSI parameters, the constraint significantly worsens, which could be a hint of poor detector reconstruction in the muon backward events.

[4] Another common problem that occurs to the fit is when the post-fit value of a parameter is very close to its physical boundary. This will stop the Hessian algorithm from computing the partial derivative matrix numerically, and subsequently stops a valid correlation matrix from being produced. To avoid this problem, some parameters are 'mirrored' near their physical boundary, i.e. let the unphysical value give the same value as the physical value symmetric about the boundary. For example, the physical lower limit of the optical potential carbon parameter is 0, but the postfit prior value is very close to 0, and a value of -0.1 gives the same output as 0.1. For a more detailed description of the parameter mirroring, please refer to [79, 109].

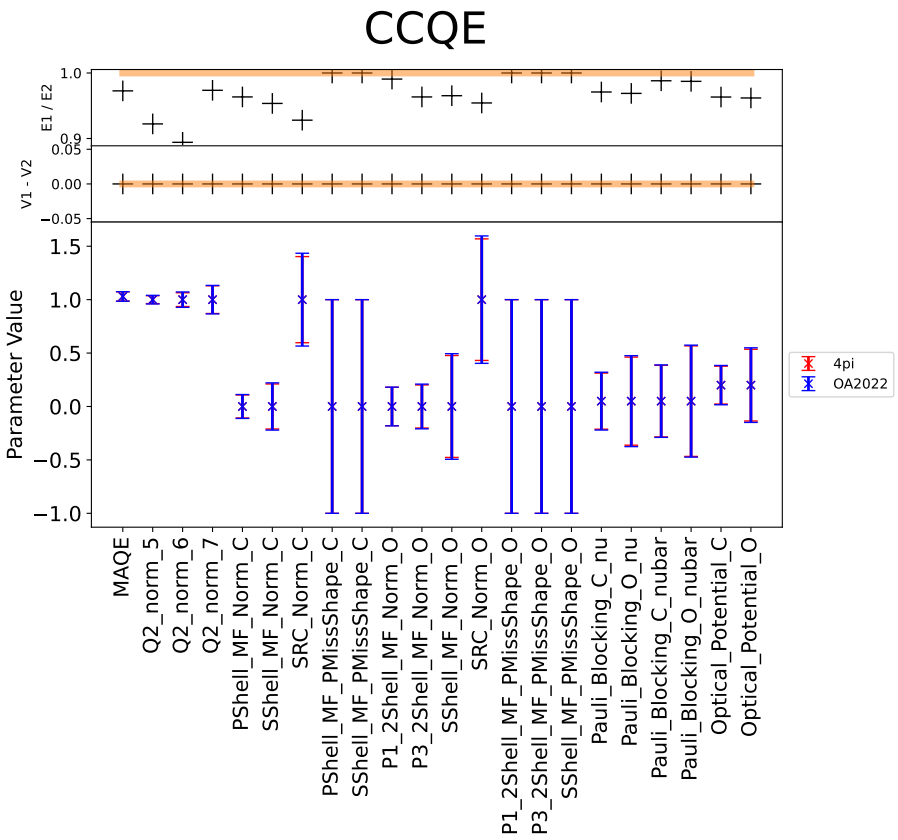

(A) CCQE parameters

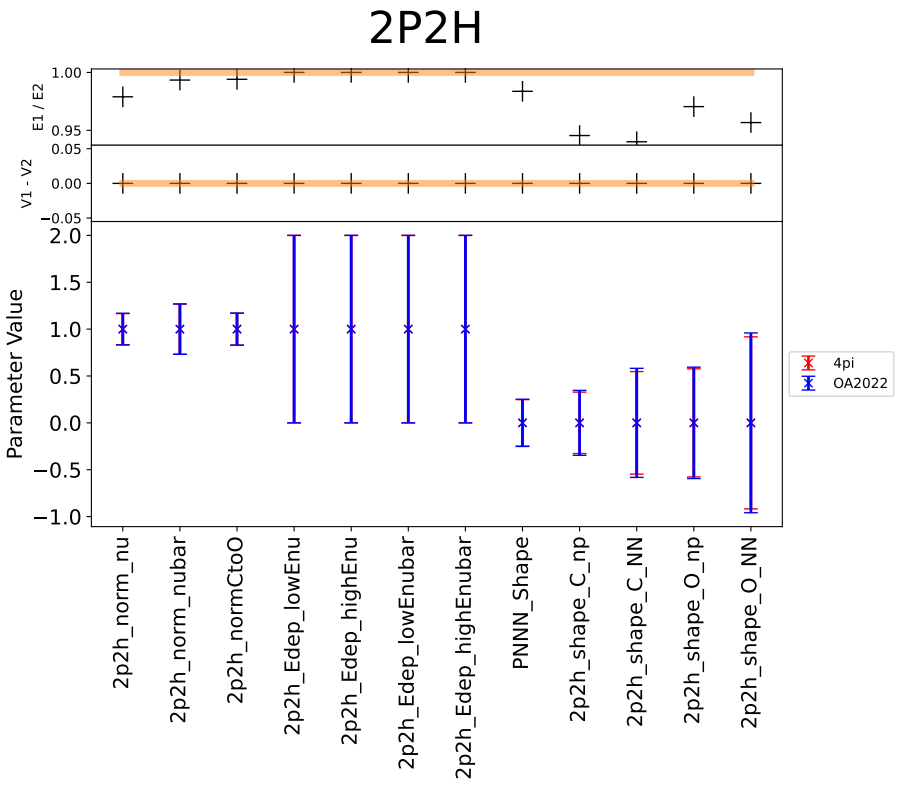

(B) 2p2h parameters

FIGURE 7.7: Quasi-elastic and two particle two hole parameters' post fit priors and errors (red), as compared with prefit and OA2022 samples (blue). The top panel is the ratio of post-fit error between 4π and OA2022 samples; a smaller than 1 value indicates improvement. The middle panel is the difference between post-fit central values. In an Asimov fit, it expected that this is zero across all parameters. The bottom panel shows the actual postfit central value and errors.

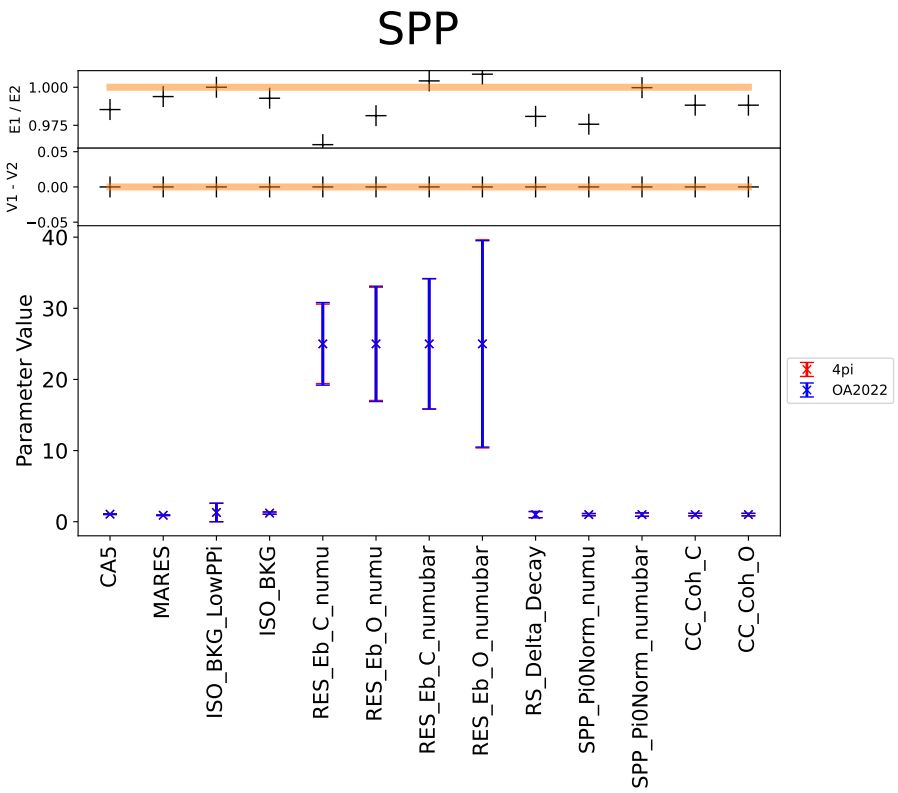

(A) Single pion production parameters

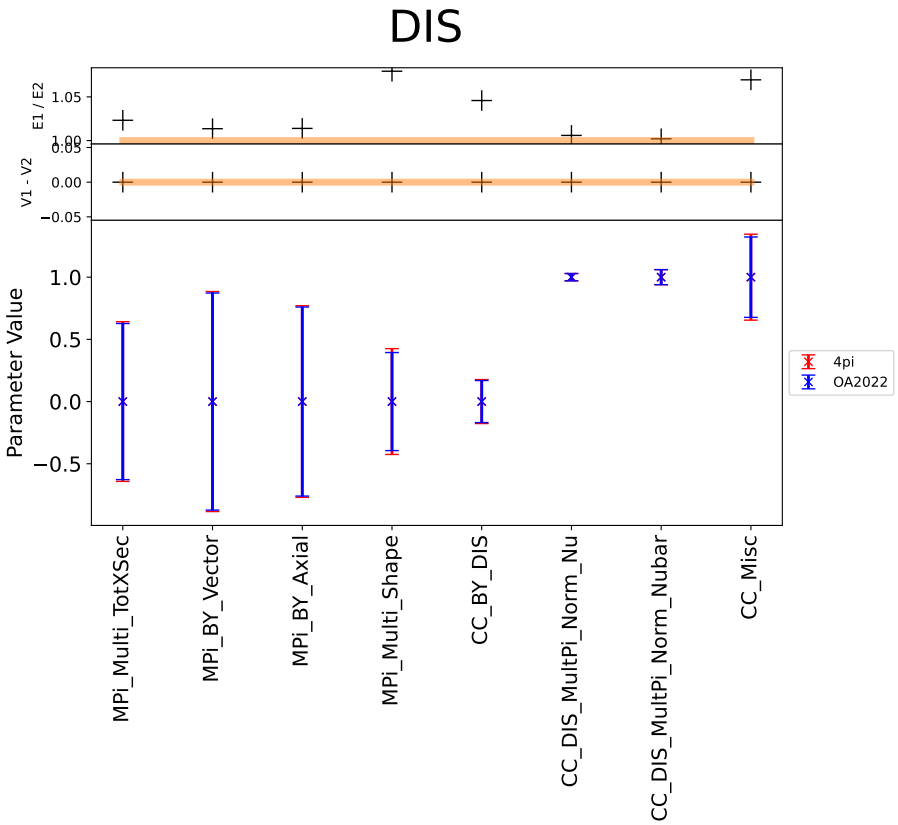

(B) Deep-inelastic scattering parameters

FIGURE 7.8: Single pion production and deep-inelastic parameter post fit priors and errors (red), as compared with prefit and OA2022 samples (blue). The top panel is the ratio of post-fit error between 4π and OA2022 samples; a smaller than 1 value indicates improvement. The middle panel is the difference between post-fit central values. In an Asimov fit, it expected that this is zero across all parameters. The bottom panel shows the actual postfit central value and errors.

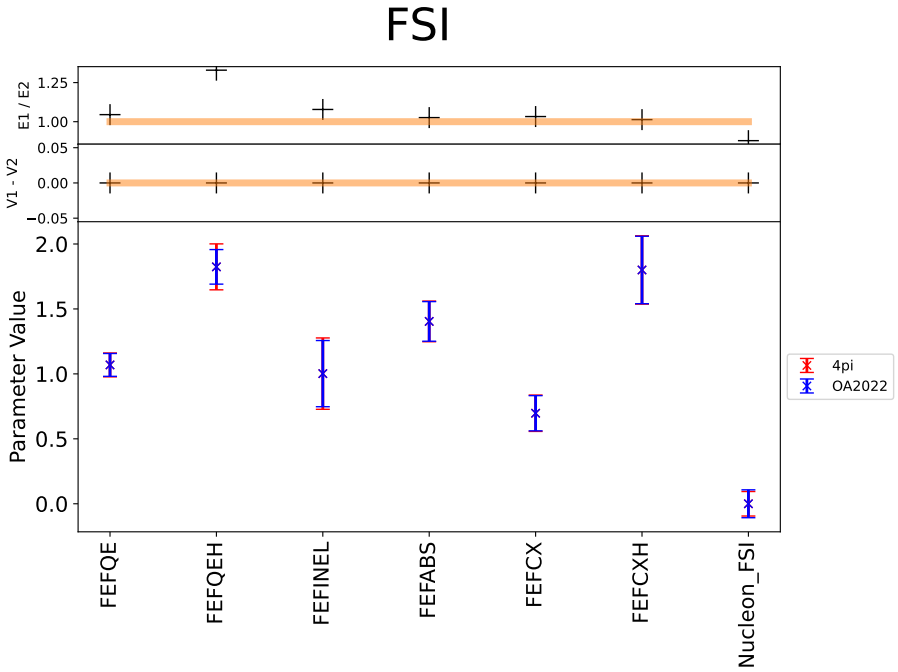

(A) FSI parameters

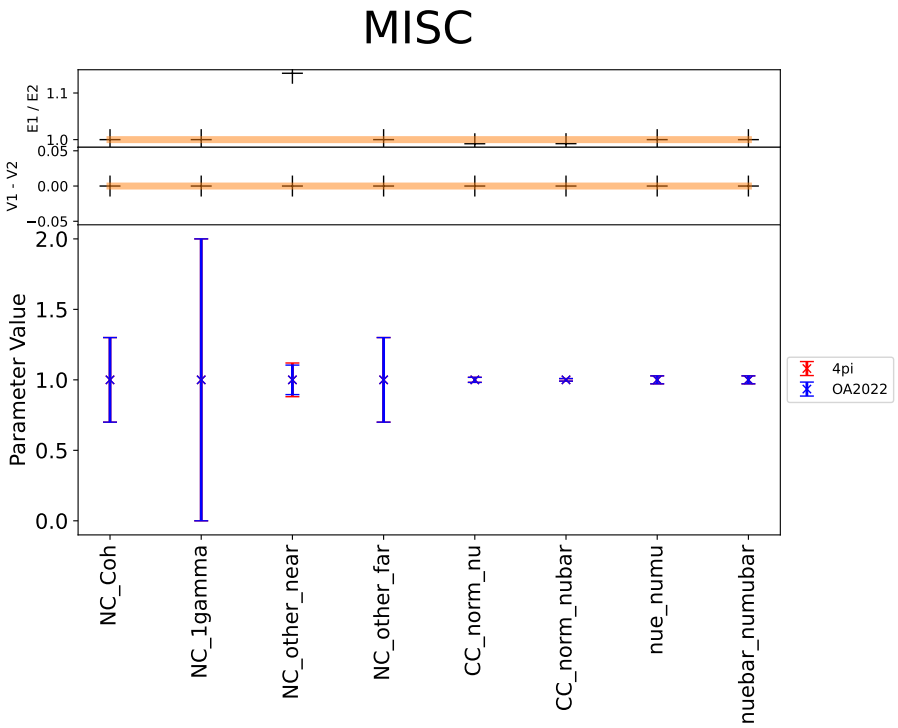

(B) MISC

FIGURE 7.9: Final state interaction and miscellaneous parameters' post fit priors and errors (red), as compared with prefit and OA2022 samples (blue). The top panel is the ratio of post-fit error between 4π and OA2022 samples; a smaller than 1 value indicates improvement. The middle panel is the difference between post-fit central values. In an Asimov fit, it expected that this is zero across all parameters. The bottom panel shows the actual postfit central value and errors.

7.5.3 Other validations

On top of likelihood scans and Asimov fits, there are also other ways to validate the fitters, including event rate studies, pull studies, and fake-data studies. As of when this thesis is written, these studies are not complete yet with the 4π samples. Hence, here only a brief introduction on how they work is provided. For a more detailed description, please see [109, 159].

- **Event rate studies**

  The easiest validation possible for the BANFF fit is to compare the model prediction to data, after the 2D binned sample has been constructed using the method introduced in Sec. 7.4.2. This is useful when compared with other fitters, like ToF, to make sure the reweighting and sample construction process is working normally. Computing the event rate prediction in certain variations of particular parameters also helps identify problems with reweighting or unphysical parameter response.

- **Pull studies**

  To test the fitter's ability to explore the desired parameter space, the pull study validation throws parameters based on their prior uncertainties and covariance in a number of toy experiments [178]. The thrown values will be the new prior values of parameters in this toy experiment. Toy MCs are then built using reweighting, and statistical variation is applied on a bin-by-bin basis. The 'data' to which this toy experiment fits MC is the nominal prediction with a statistical variation applied in each bin, and a set of post-fit values of parameters are found accordingly. The pull of a particular parameter in the model is then defined as

$$\text{pull} = \frac{p_{\text{fit}} - p_{\text{throw}}}{\sigma_{\text{fit}}} \tag{7.27}$$

  where p_{fit} is the fitted value of the parameter, p_{throw} is the true value, in this case the nominal MC values, and σ_{fit} is the post-fit error given by the toy fit [5] . After

[5] To include the prior constraint, the pull value definition is then updated to:

$$\text{pull} = \frac{p_{\text{fit}} - p_{\text{thrown}}}{\sqrt{\sigma_c^2 - \sigma_{\text{fit}}^2}}$$

where σ_c is the prefit constraint. This, however, is causing computational problems when the number of parameters in the fit becomes very large and the parameters are strongly correlated. Current BANFF implementation does not include the prior constraint term in the denominator.

2000 toy fits are performed, the distribution of pull values of a given parameter is expected to be distributed normally, and centered at zero. Deviation of the central value of the Gaussian distribution from zero indicates a bias in the fit [109, 178].

- **P-value study** Another toy experiment-based study performed after the data fit to validate the ND model is the p-value calculation. The p-value in this case is defined as the probability of making an observation more extreme than the data [109, 178]. In other words, given the model and parameters, the p-value is a measure of how extreme a case the real-world observation is. If the model is a Gaussian distribution centered at 0 with a variance of 1, then an observation of 3 is very unlikely, with a p-value of 0.0027, rendering the model and parameters questionable. A model p-value greater than 0.05 is commonly regarded as compatible with real world data.

  To construct such a value, a number of toy experiments are conducted. Each has a set of parameters thrown. As in the pull studies, the parameter values are randomly thrown using their central values, uncertainties, and correlations [6] . The MC predictions are then reweighted accordingly, and a Poisson fluctuation is applied bin-wise to become the 'data' in this toy experiment. The nominal (not reweighted) MC is then fitted to the varied 'data'. Each fit should return a minimal $\Delta\chi^2$, which is then compared to the $\Delta\chi^2$ found in the real data fit, $\Delta\chi^2_{\text{data}}$. The p-value is then defined as the percentile of $\Delta\chi^2_{\text{data}}$ in the distribution of $\Delta\chi^2$ found in the toy experiments.

[6] By using the post-fit parameter central values, uncertainties and correlations, the p-value study can also put the post-fit model to the test. Such a study is called a post-fit p-value test, and is covered in detail in [159].

Chapter 8

Conclusion and outlook

The T2K experiment measures neutrino oscillation parameters using a long-baseline neutrino beam. Mesons produced from a proton beam directed at a carbon target decay into neutrinos, which are measured at the near detector (ND280) and the far detector (SK) placed at a 2.5° angle away from the proton beam direction. The difference in neutrino-flavour measurements between the two sites is used to infer the oscillation parameters. To reduce systematic uncertainties, T2K fits the near detector model to near detector data and calculates correlations between model parameters. These constraints are then used as priors for the far detector fit, which produces the final constraint on neutrino oscillation parameters by fitting the SK detector observation to its data.

For the first time, the angular acceptance of the near detector sample selection employed in oscillation analysis has been expanded to encompass a complete 4π solid angle. This is achieved through introducing new subsamples produced by selecting events with muons that go backwards or at a high angle with respect to the neutrino beam direction. The new subsamples have over 50% efficiency; backward samples have 20% purity in the very backward region, while the high-angle samples have more than 50% purity around $\cos\theta = 0.5$ and 15 % purity around $\cos\theta = -0.5$. As the sample selection at the SK far detector inherently covers a 4π solid angle, this enhancement significantly improves the comparability between the near and far detector data. Typically, these events with a high-angle or backward-going final-state muon involve large momentum transfers Q^2 , and therefore contribute to a more comprehensive understanding of neutrino-nucleus interactions. This will benefit not only T2K, but also other neutrino experiments around the world.

Time-of-Flight (ToF) information was used to identify backward tracks in the selection of new subsamples. However, run 8 data had bad ToF data due to hardware issues, resulting in a much larger data-MC discrepancy compared to other runs. To mitigate this issue, a hardware-inspired correction was developed that significantly reduced the data-MC discrepancy and allowed backward samples to be used in oscillation analyses. The resulting systematic uncertainty induced by this new correction was also studied and found to be at an acceptable level.

As T2K collects more data, the statistical uncertainty decreases, and the importance of understanding the detector systematic error increases. An overview of the expected relative systematic error of the new subsamples are provided. Three systematic error sources that are new to oscillation analyses, the ToF, momentum from vertex backward migration and TPC-P0D matching efficiency, are reviewed in detail. Those new systematic uncertaities have been carefully evaluated, and studies found that the ToF error is the dominant systematic error source in the new samples. Still, after including the new errors, the overall systematic error of the number of events in each sample bin is small and can be used in an oscillation anaylsis.

An overview of the T2K near detector fit is presented, including the near detector model, parameters in the model, the minimisation of the likelihood statistic from detector observations, and how the correlation between parameters is found. As of when this thesis is written, fitting to data is still being run, and the output is awaited. Some other validations of the 4π sample's usage in the fitter has been done, including the likelihood scans and Asimov fits. Likelihood scan outputs show improved constraints on CCQE and some FSI parameters, but reduced constraints on FSI parameters are also observed. Overall, 54 parameters are improved by the new subsamples, while 16 suffer a reduced sensitivity, as the likelihood scan study found. Asimov fit outputs returns similar indications, and the reason to such indication is yet to be understood. This, in turn, ultimately will lead to an increased sensitivity to neutrino oscillation parameters.

The plans for the 4π samples in the near future is first to use them in both data fit using existing ND280 data. The data fits will produce post-fit central values, uncertainties and correlations of near detector model parameters, which will pass on to the far detector fit and produce the neutrino oscillation parameter constraints in year 2024. In the mean

time, further validations will also be performed. The MaCh3 fit will also use the same 4π samples as its input.

On top of the 4π sample selection, many upgrades have been planned for the T2K near detector. The first part is the near detector upgrade. To further reduce the near detector systematic uncertainties through a native 4π sample selection, a lower hadron momentum threshold, neutron kinematics and more statistics, T2K plans to replace the P0D with three new subdetector modules: the Super FGD (SFGD), two horizontal TPCs, and six dedicated time-of-flight detectors. The SFGD will be built by stacking 2,000,000 scintillator cubes, each of $1 \times 1 \times 1$ cm^3 in dimension with three orthogonal WLS fibres running through in all three dimensions. This allows the SFGD to provide better spatial resolution for the neutrino-interaction vertices and isoFGD hadrons, and also provides an additional two tonnes of target mass. The author of this thesis joined the effort of construction of the SFGD in Feburary 2023. He was involved in the installation of optical fibres and the quality control of the installation. Two TPCs will be installed over and under the SFGD to assist the tracking of particles that leave the SFGD at a large angle. Six scintillator-based ToF detector panels will be installed surrounding the SFGD and the horizontal TPC. The ToF detector will provide an excellent ToF resolution of 0.13 ns and rejection of inward background events. Together, the near detector upgrade will eventually reduce the systematic uncertainties on near detector model parameters.

The treatment of detector systematic error parameters in the near detector model currently differs from that of other parameters. While the response of samples to the variation of other parameters is simulated using spline files, detector parameters are not directly varied. Instead, the information is encapsulated in a covariance matrix, whose rows and columns each represents the overall detector systematic error in a single bin. To ensure consistency in handling all parameters, an update to the ND fit involves treating detector systematic error parameters similarly to cross-section parameters, specifically by utilising splines. The objective is to convert the fundamental real detector parameters, such as the FGD masses or the uncertainty of the magnetic field, into spline representations instead of relying on errors associated with the number of events in each bin. This enhancement will enable the T2K experiment to implement finer binning without increasing the number of parameters in the fit, which proves highly beneficial in the context of the forthcoming ND280 upgrade. By allowing greater flexibility in the design of near detector samples, this

update can contribute to a reduced systematic uncertainty for the ND model parameters, ultimately leading to improved sensitivity to neutrino oscillation parameters.

In the realm of software, a cutting-edge near-detector fitter, GUNDAM, is nearing completion and undergoing validation against BANFF using previous samples. Designed to execute the same fitting process, GUNDAM supports GPU-acceleration and is significantly faster than BANFF. Given current tests, GUNDAM outpaces BANFF by approximately an order of magnitude, as BANFF relies solely on CPUs. An Asimov fit, which typically takes around four days to converge using BANFF, can be reduced to mere hours by employing GUNDAM as a replacement. This accelerated process facilitates fitting a more detailed ND model or performing additional fine tunings and tests on the fit. Given that the update to the 4π sample has expanded the number of subsamples from 22 to 32, GUNDAM's increased speed will prove particularly advantageous.

In summary, the 4π near-detector sample has been meticulously developed and tested within the near detector fit, resulting in numerous enhancements. Together with other updates, such as hardware upgrades, new treatment methods, and the advanced fitter software, the future of near detector fitting promises to explore neutrino physics with unprecedented precision, and opens a portal to studies that were impossible before.

Bibliography

[1] G. Aad et al. Observation of a new particle in the search for the standard model higgs boson with the ATLAS detector at the LHC. *Physics Letters B*, 716(1):1–29, 2012.

[2] S. Chatrchyan et al. Observation of a new boson at a mass of 125 GeV with the CMS experiment at the LHC. *Physics Letters B*, 716(1):30–61, 2012.

[3] Andrei D Sakharov. Violation of cp invariance, c asymmetry, and baryon asymmetry of the universe. *Soviet Physics Uspekhi*, 34(5):392, 1991.

[4] Antonio Riotto. Baryogenesis and leptogenesis. *Journal of Physics: Conference Series*, 335(1):012008, 2011.

[5] K. Abe et al. The T2K Experiment. *Nucl. Instrum. Meth. A*, 659:106–135, 2011.

[6] Sheldon L. Glashow. Partial-symmetries of weak interactions. *Nuclear Physics*, 22(4):579–588, 1961.

[7] Steven Weinberg. A model of leptons. *Phys. Rev. Lett.*, 19:1264–1266, 1967.

[8] Abdus Salam. Weak and Electromagnetic Interactions. *Conf. Proc. C*, 680519:367–377, 1968.

[9] Matthew D. Schwartz. *Quantum Field Theory and the Standard Model*. Cambridge University Press, 2014.

[10] Michael E. Peskin and Daniel V. Schroeder. *An Introduction to quantum field theory*. Addison-Wesley, Reading, USA, 1995.

[11] Felix Buot, Gibson Maglasang, and Allan Roy Elnar. Unification of mixed hilbert-space representations in condensed matter physics and quantum field theory. 2022.

[12] Steven Weinberg. A Model of Leptons. *PRL*, 19(21):1264–1266, 1967.

[13] A. Salam. Magnetic monopole and two photon theories of C -violation. *Physics Letters*, 22(5):683–684, 1966.

[14] S. Abe et al. Precision Measurement of Neutrino Oscillation Parameters with KamLAND. *Phys. Rev. Lett.*, 100:221803, 2008.

[15] J Chadwick. Intensitätsverteilung im magnetischen Spectrum der β-Strahlen von radium B + C. *Verhandl. Dtsc. Phys. Ges.*, 16:383, 1914.

[16] W. Pauli. Dear radioactive ladies and gentlemen. *Phys. Today*, 31N9:27, 1978.

[17] E. Fermi. Versuch einer Theorie der β-Strahlen. I. *Zeitschrift fur Physik*, 88(3-4):161–177, 1934.

[18] C. L. Cowan, F. Reines, F. B. Harrison, H. W. Kruse, and A. D. McGuire. Detection of the free neutrino: A Confirmation. *Science*, 124:103–104, 1956.

[19] G. Danby, J-M. Gaillard, K. Goulianos, L. M. Lederman, N. Mistry, M. Schwartz, and J. Steinberger. Observation of high-energy neutrino reactions and the existence of two kinds of neutrinos. *Phys. Rev. Lett.*, 9:36–44, 1962.

[20] K. Kodama et al. Observation of tau neutrino interactions. *Physics Letters B*, 504(3):218–224, 2001.

[21] Raymond Davis, Don S. Harmer, and Kenneth C. Hoffman. Search for neutrinos from the sun. *Phys. Rev. Lett.*, 20:1205–1209, 1968.

[22] JN Abdurashitov, Sage Collaboration, et al. Measurement of the solar neutrino capture rate by the russian-american gallium solar neutrino experiment during one half of the 22-year cycle of solar activity. *arXiv preprint astro-ph/0204245*, 2002.

[23] Kohji S Hirata, Takaaki Kajita, T Kifune, K Kihara, Masayuki Nakahata, K Nakamura, S Ohara, Y Oyama, N Sato, M Takita, et al. Observation of b 8 solar neutrinos in the kamiokande-ii detector. *Physical Review Letters*, 63(1):16, 1989.

[24] Ayse Bat, Emrah Tiras, Vincent Fischer, and Mirac Kamislioglu. Low energy neutrino detection with a compact water-based liquid scintillator detector. *The European Physical Journal C*, 82(8):1–11, 2022.

[25] Bruno Pontecorvo. Mesonium and antimesonium. *Zhur. Eksptl'. i Teoret. Fiz.*, 33, 1957.

[26] B Pontecorvo. Neutrino experiments and the question of leptonic-charge conservation. *Old and New Problems in Elementary Particles*, page 251, 2012.

[27] Ziro Maki, Masami Nakagawa, and Shoichi Sakata. Remarks on the unified model of elementary particles. *Prog. Theor. Phys.*, 28:870–880, 1962.

[28] Sidney Coleman. *Lectures of Sidney Coleman on Quantum Field Theory.* WSP, Hackensack, 2018.

[29] Steven Weinberg. A New Light Boson? *Phys. Rev. Lett.*, 40:223–226, 1978.

[30] P. W. Anderson. Plasmons, gauge invariance, and mass. *Phys. Rev.*, 130:439–442, 1963.

[31] Julian Schwinger. Gauge invariance and mass. *Phys. Rev.*, 125:397–398, 1962.

[32] F. Englert and R. Brout. Broken symmetry and the mass of gauge vector mesons. *Phys. Rev. Lett.*, 13:321–323, 1964.

[33] Peter W. Higgs. Broken symmetries and the masses of gauge bosons. *Phys. Rev. Lett.*, 13:508–509, 1964.

[34] G. S. Guralnik, C. R. Hagen, and T. W. B. Kibble. Global conservation laws and massless particles. *Phys. Rev. Lett.*, 13:585–587, 1964.

[35] David J Griffiths. *Introduction to elementary particles; 2nd rev. version.* Physics textbook. Wiley, New York, NY, 2008.

[36] Particle Data Group. Review of Particle Physics. *Progress of Theoretical and Experimental Physics*, 2020(8), 2020. 083C01.

[37] S. Schael et al. Precision electroweak measurements on the Z resonance. *Phys. Rept.*, 427:257–454, 2006.

[38] B. Pontecorvo. Neutrino Experiments and the Problem of Conservation of Leptonic Charge. *Zh. Eksp. Teor. Fiz.*, 53:1717–1725, 1967.

[39] C. Riccio. Mesure du flux et de la section efficace des antineutrinos dans le d etecteur proche de lexp erience t2k. 2018.

[40] Ivan Esteban, M. C. Gonzalez-Garcia, Michele Maltoni, Thomas Schwetz, and Albert Zhou. The fate of hints: updated global analysis of three-flavor neutrino oscillations. *JHEP*, 09:178, 2020.

[41] L. Wolfenstein. Neutrino oscillations in matter. *Phys. Rev. D*, 17:2369–2374, 1978.

[42] S. P. Mikheev and A. Yu. Smirnov. Neutrino Oscillations in an Inhomogeneous Medium: Adiabatic Regime. *Sov. Phys. JETP*, 65:230–236, 1987.

[43] Yoshinari Hayato. A neutrino interaction simulation program library NEUT. *Acta Phys. Polon. B*, 40:2477–2489, 2009.

[44] Costas Andreopoulos, Christopher Barry, Steve Dytman, Hugh Gallagher, Tomasz Golan, Robert Hatcher, Gabriel Perdue, and Julia Yarba. The GENIE Neutrino Monte Carlo Generator: Physics and User Manual. 2015.

[45] Nakajima Y. et al. Measurement of inclusive charged current interactions on carbon in a few-gev neutrino beam. *Phys. Rev. D*, 83:012005, 2011.

[46] Q. Wu et al. A Precise measurement of the muon neutrino-nucleon inclusive charged current cross-section off an isoscalar target in the energy range $2.5 < \mathrm{E(nu)} < 40$-GeV by NOMAD. *Phys. Lett. B*, 660:19–25, 2008.

[47] Abe K. et al. Measurement of the inclusive ν_μ charged current cross section on carbon in the near detector of the t2k experiment. *Phys. Rev. D*, 87:092003, 2013.

[48] Abe K. et al. Measurement of the inclusive ν_μ charged current cross section on iron and hydrocarbon in the t2k on-axis neutrino beam. *Phys. Rev. D*, 90:052010, 2014.

[49] Devan J. et al. Measurements of the inclusive neutrino and antineutrino charged current cross sections in minerva using the low-ν flux method. *Phys. Rev. D*, 94:112007, 2016.

[50] V Lyubushkin et al. A Study of quasi-elastic muon neutrino and antineutrino scattering in the NOMAD experiment. *Eur. Phys. J. C*, 63:355–381, 2009.

[51] Aguilar-Arevalo A. A. et al. First measurement of the muon neutrino charged current quasielastic double differential cross section. *Phys. Rev. D*, 81:092005, 2010.

[52] Fiorentini G. A. et al. Measurement of muon neutrino quasielastic scattering on a hydrocarbon target at $E_\nu \sim 3.5$ GeV. *Phys. Rev. Lett.*, 111:022502, 2013.

[53] Abe K. et al. Measurement of the ν_μ charged current quasielastic cross section on carbon with the t2k on-axis neutrino beam. *Phys. Rev. D*, 91:112002, 2015.

[54] A. Garcia. Study of the ν_ν interactions via charged-current in the t2k near detector. 2017.

[55] Mark Thomson. *Modern particle physics*. Cambridge University Press, New York, 2013.

[56] M. Glück, E. Reya, and A. Vogt. Dynamical parton distributions revisited. *Eur. Phys. J. C*, 5:461–470, 1998.

[57] Luke Pickering. Examining nuclear effects in neutrino interactions with transverse kinematic imbalance. *JPS Conf. Proc.*, 12:010032, 2016.

[58] O. Benhar, A. Fabrocini, S. Fantoni, and I. Sick. Spectral function of finite nuclei and scattering of GeV electrons. *Nucl. Phys. A*, 579:493–517, 1994.

[59] S. Bilenky. Neutrinos: Majorana or Dirac? 2020.

[60] J. Schechter and J. W. F. Valle. Neutrinoless double-beta decay in su(2)×u(1) theories. *Phys. Rev. D*, 25:2951–2954, 1982.

[61] A. Gando et al. Search for Majorana Neutrinos near the Inverted Mass Hierarchy Region with KamLAND-Zen. *Phys. Rev. Lett.*, 117(8):082503, 2016. [Addendum: Phys.Rev.Lett. 117, 109903 (2016)].

[62] Agostini M. et al. First results from GERDA Phase II. In *Journal of Physics Conference Series*, volume 888 of *Journal of Physics Conference Series*, page 012030, 2017.

[63] H. V. Klapdor-Kleingrothaus, I. V. Krivosheina, A. Dietz, and O. Chkvorets. Search for neutrinoless double beta decay with enriched Ge-76 in Gran Sasso 1990-2003. *Phys. Lett. B*, 586:198–212, 2004.

[64] I. Nutini et al. Latest Results from the CUORE Experiment. 2022.

[65] Alavi-Harati A. et al. Observation of direct cp violation in $k_{s,l} \to \pi\pi$ decays. *Phys. Rev. Lett.*, 83:22–27, 1999.

[66] Aubert B. et al. Observation of *CP* violation in the b^0 meson system. *Phys. Rev. Lett.*, 87:091801, 2001.

[67] Aaij R. et al. Observation of *cp* violation in charm decays. *Phys. Rev. Lett.*, 122:211803, 2019.

[68] J. H. Christenson, J. W. Cronin, V. L. Fitch, and R. Turlay. Evidence for the 2π decay of the k_2^0 meson. *Phys. Rev. Lett.*, 13:138–140, 1964.

[69] K. Abe et al. Constraint on the matter–antimatter symmetry-violating phase in neutrino oscillations. *Nature*, 580(7803):339–344, 2020. [Erratum: Nature 583, E16 (2020)].

[70] G. Barbiellini et al. NEUTRINO COUNTING. In *LEP Physics Workshop*, 1989.

[71] Basudeb Dasgupta and Joachim Kopp. Sterile neutrinos. *Physics Reports*, 928:1–63, 2021. Sterile neutrinos.

[72] A. Aguilar-Arevalo et al. Evidence for neutrino oscillations from the observation of $\bar{\nu}_e$ appearance in a $\bar{\nu}_\mu$ beam. *Phys. Rev. D*, 64:112007, 2001.

[73] A. A. Aguilar-Arevalo et al. Significant Excess of ElectronLike Events in the MiniBooNE Short-Baseline Neutrino Experiment. *Phys. Rev. Lett.*, 121(22):221801, 2018.

[74] K. Abe et al. Search for light sterile neutrinos with the T2K far detector Super-Kamiokande at a baseline of 295 km. *Phys. Rev. D*, 99(7):071103, 2019.

[75] M. et al Tanabashi. Review of particle physics. *Phys. Rev. D*, 98:030001, 2018.

[76] Marcus Beck. The KATRIN Experiment. *J. Phys. Conf. Ser.*, 203:012097, 2010.

[77] R. L. Workman and Others. Review of Particle Physics. *PTEP*, 2022:083C01, 2022.

[78] K. Matsuoka et al. Design and performance of the muon monitor for the t2k neutrino oscillation experiment. *Nuclear Instruments and Methods in Physics Research Section A: Accelerators, Spectrometers, Detectors and Associated Equipment*, 624(3):591–600, 2010.

[79] T.A. Doyle. T2k status and plans, 2022.

[80] L. Berns et al. T2K Internal Technical Note 401, Flux Prediction and Uncertainty with NA61/SHINE 2010 Replica Target Mesaurements. 2021.

[81] Laura Zambelli, A. Fiorentini, and T. Vladisavljevic. Towards T2K neutrino flux predictions using the replica target measurements by NA61/SHINE. In *27th International Conference on Neutrino Physics and Astrophysics*, volume 888, page 012067, London, United Kingdom, 2016.

[82] T2K Collaboration. Flux prediction and uncertainty with na61/shine 2010 replica target measurements. 2022.

[83] K. Abe et al. Measurements of the t2k neutrino beam properties using the INGRID on-axis near detector. *Nuclear Instruments and Methods in Physics Research Section A: Accelerators, Spectrometers, Detectors and Associated Equipment*, 694:211–223, 2012.

[84] T2K Collaboration. T2k internal technical note 61, measurement and correction of magnetic field distortions in the time projection chambers. 2012.

[85] Y. Fukuda et al. The Super-Kamiokande detector. *Nucl. Instrum. Meth. A*, 501:418–462, 2003.

[86] S. Assylbekov et al. The T2K ND280 Off-Axis Pi-Zero Detector. *Nucl. Instrum. Meth. A*, 686:48–63, 2012.

[87] P. A. Amaudruz et al. The T2K Fine-Grained Detectors. *Nucl. Instrum. Meth. A*, 696:1–31, 2012.

[88] N. Abgrall et al. Time Projection Chambers for the T2K Near Detectors. *Nucl. Instrum. Meth. A*, 637:25–46, 2011.

[89] S. Assylbekov et al. The T2K ND280 Off-Axis Pi-Zero Detector. *Nucl. Instrum. Meth. A*, 686:48–63, 2012.

[90] D. Allan et al. The Electromagnetic Calorimeter for the T2K Near Detector ND280. *JINST*, 8:P10019, 2013.

[91] S. Aoki et al. The T2K Side Muon Range Detector (SMRD). *Nucl. Instrum. Meth. A*, 698:135–146, 2013.

[92] T. Ovsiannikova et al. The new experiment wagasci for water to hydrocarbon neutrino cross section measurement using the j-parc beam. *Journal of Physics: Conference Series*, 675:012030, 2016.

[93] M. Antonova et al. Baby MIND: A Magnetized Segmented Neutrino Detector for the WAGASCI Experiment. *JINST*, 12(07):C07028, 2017.

[94] A. Ajmi et al. Baby MIND detector first physics run. In *Prospects in Neutrino Physics*, 2020.

[95] M. Jiang et al. Atmospheric Neutrino Oscillation Analysis with Improved Event Reconstruction in Super-Kamiokande IV. *PTEP*, 2019(5):053F01, 2019.

[96] A. Takenaka et al. Search for proton decay via $p \to e^+\pi^0$ and $p \to \mu^+\pi^0$ with an enlarged fiducial volume in Super-Kamiokande I-IV. *Phys. Rev. D*, 102(11):112011, 2020.

[97] T. Totani, K. Sato, H. E. Dalhed, and J. R. Wilson. Future detection of supernova neutrino burst and explosion mechanism. *Astrophys. J.*, 496:216–225, 1998.

[98] George M. Hale and Marvin R. Querry. Optical constants of water in the 200-nm to 200-μm wavelength region. *Appl. Opt.*, 12(3):555–563, 1973.

[99] T2K Collaboration. T2k internal technical note 400, nd280 scm timeslip systematic evaluation. 2020.

[100] T2K Collaboration. T2k technical report 245 ν_ν cc event selections in the nd280 tracker using run 2+3+4 data. 2016.

[101] D. Vargas. Cross section measurement of the muon neutrino charged current single positive pion interaction on hydrocarbon using the t2k near detector with 4π solid angle acceptance. 2021.

[102] CERN. Fraction fitter in CERN ROOT. 2009.

[103] Kurt Jacobs. *Stochastic Processes for Physicists: Understanding Noisy Systems*. Cambridge University Press, 2010.

[104] Charles R. Harris et al. Array programming with NumPy. *Nature*, 585(7825):357–362, 2020.

[105] T2K Collaboration. T2k internal technical note 421, nd280 fhc samples with photon and proton information for the 2021 oscillation analysis. 2022.

[106] T2K Collaboration. Super-kamiokande data quality, mc, and systematics 2 in run 10. 2020.

[107] S. Agostinelli et al. GEANT4: A simulation toolkit. *Nucl. Instrum. Meth.*, A506:250–303, 2003.

[108] R. Brun and F. Rademakers. ROOT: An object oriented data analysis framework. *Nucl. Instrum. Meth. A*, 389:81–86, 1997.

[109] T. Tristan. Development of new off-axis near detector samples for the t2k oscillation analysis. 2022.

[110] T2K Collaboration. T2k internal technical note 152, cc multiple pion nu-mu event selections in the nd280 tracker using run 1+2+3+4 data. 2013.

[111] K. Abe et al. Simultaneous measurement of the muon neutrino charged-current cross section on oxygen and carbon without pions in the final state at T2K. *Phys. Rev. D*, 101(11):112004, 2020.

[112] T2K Collaboration. T2k internal technical note 390, ν_ν cc multi pion selections at nd280 tracker with using run 2,3,4 and 8 of production 6t. 2019.

[113] T2K Collaboration. T2k internal technical note 104, michel electron tagging in fgds. 2012.

[114] T2K Collaboration. T2k technical report 111 second generation particle id with the nd280 tracker ecals tracker. 2016.

[115] T2K Collaboration. T2k internal technical note 221, tpc-pid status and performances with production 6. 2010.

[116] T2K Collaboration. T2k technical report 212 ν_ν cc event selections in the nd280 tracker using run 2+3+4 data. 2015.

[117] E. Wall. The minimum chi-square method. 2001.

[118] T2K Collaboration. T2k internal technical note 272, a study to assign a systematic uncertainty to the backward vertex migrations in fgd2. 2015.

[119] T2K Collaboration. T2k internal technical note 368, tbackward migration uncertainty in fgd2. 2018.

[120] T2K Collaboration. T2k internal technical note 234, nd280 tpc cluster efficiency. 2017.

[121] T2K Collaboration. T2k internal technical note 163, nd280 tpc track-finding efficiency. 2016.

[122] T2K Collaboration. T2k internal technical note 229, nd280 global charge identification systematic error. 2016.

[123] T2K Collaboration. T2k internal technical note 001, particle identification with tt2k tpc. 2010.

[124] John Douglas Cockcroft. Experimental nuclear physics. *Nature*, 175:53–54, 1955.

[125] T2K Collaboration. T2k internal technical note 222, study of momentum resolution and scale using tracks that cross multiple tpcs. 2014.

[126] T2K Collaboration. T2k internal technical note 081, b-field calibration and systematic errors. 2011.

[127] T2K Collaboration. T2k internal technical note 223, particle identification with the fine grained detectors. 2012.

[128] T2K Collaboration. T2k internal technical note 410, isorecon hybrid efficiency for fhc and rhc using production 6t. 2022.

[129] T2K Collaboration. T2k internal technical note 122, fgd mass calculation compared to as built. 2012.

[130] T2K Collaboration. T2k internal technical note 279, study of the tracker ecal systematics. 2016.

[131] T2K Collaboration. T2k internal technical note 75, nd280 tpc tracking efficiency. 2012.

[132] T2K Collaboration. T2k internal technical note 125, determination of pion secondary interaction systematics for the nd280 numu analysis. 2012.

[133] T2K Collaboration. T2k internal technical note 407, fhc muon neutrino charged current multiple pion samples in the nd280 tracker for the 2020 oscillation analysis inputs: Run 2+3+4+8 with p6t neut d mc. 2021.

[134] T2K Collaboration. T2k internal technical note 216, cc-0pi multi-topology selection and systematics in fgd1. 2014.

[135] T2K Collaboration. T2k technical report 077 the simulations of the beam neutrinos interactions outside the nd280 detector. 2011.

[136] T2K Collaboration. T2k internal technical note 098, systematics on out-of-fiducial-volume backgrounds in the nd280 tracker. 2015.

[137] C. Jarlskog. Commutator of the Quark Mass Matrices in the Standard Electroweak Model and a Measure of Maximal CP Nonconservation. *Phys. Rev. Lett.*, 55:1039, 1985.

[138] T2K Collaboration. T2k internal technical note 394, t2k neutrino and anti-neutrino 3-flavour joint analysis of run 1-10 (1.4938»$10^{21}\nu$ pot + 1.6346»$10^{21}\bar{\nu}$ pot) data sets. 2022.

[139] T2K Collaboration. T2k internal technical note 397, five sample joint oscillation analysis with t2k run110 data. 2021.

[140] T2K Collaboration. T2k internal technical note 393, measuring pmns parameters in a joint nd280-sk analysis using mcmc. 2021.

[141] T2K Collaboration. Neutrino flux prediction. 2013.

[142] T. Vladisavljevic. Predicting the t2k neutrino flux and measuring oscillation parameters. 2019.

[143] Alfredo Ferrari, Paola R. Sala, Alberto Fasso, and Johannes Ranft. FLUKA: A multi-particle transport code (Program version 2005). 2005.

[144] René Brun, F. Bruyant, Federico Carminati, Simone Giani, M. Maire, A. McPherson, G. Patrick, and L. Urban. GEANT Detector Description and Simulation Tool. 1994.

[145] N Abgrall et al. "na61/shine facility at the cern sps: beams and detector system". *Journal of Instrumentation*, 9(06):P06005, 2014.

[146] N. Abgrall et al. Measurements of $\pi^{\pm}$, $K^{\pm}$, K^0_S , Λ and proton production in proton–carbon interactions at 31 GeV/c with the NA61/SHINE spectrometer at the CERN SPS. *Eur. Phys. J. C*, 76(2):84, 2016.

[147] N. Abgrall et al. Measurements of $\pi^{\pm}$, $K^{\pm}$ and proton double differential yields from the surface of the T2K replica target for incoming 31 GeV/c protons with the NA61/SHINE spectrometer at the CERN SPS. *Eur. Phys. J. C*, 79(2):100, 2019.

[148] N. Abgrall et al. Flux Prediction and Uncertainties for the 2012a Oscillation Analysis. 2013.

[149] T2K Collaboration. Niwg model recommendations for oa 2021. 2021.

[150] C.H. Llewellyn Smith. Neutrino reactions at accelerator energies. *Physics Reports*, 3(5):261–379, 1972.

[151] O. Benhar, A. Fabrocini, and S. Fantoni. The Nucleon Spectral Function in Nuclear Matter. *Nucl. Phys. A*, 505:267–299, 1989.

[152] R. A. Smith and E. J. Moniz. NEUTRINO REACTIONS ON NUCLEAR TARGETS. *Nucl. Phys. B*, 43:605, 1972. [Erratum: Nucl.Phys.B 101, 547 (1975)].

[153] Veronique Bernard, Latifa Elouadrhiri, and Ulf-G. Meissner. Axial structure of the nucleon: Topical Review. *J. Phys. G*, 28:R1–R35, 2002.

[154] S. J. Barish, J. Campbell, G. Charlton, Y. Cho, M. Derrick, R. Engelmann, L. G. Hyman, D. Jankowski, A. Mann, B. Musgrave, P. Schreiner, P. F. Schultz, R. Singer, M. Szczekowski, T. Wangler, H. Yuta, V. E. Barnes, D. D. Carmony, A. F. Garfinkel, and G. M. Radecky. Study of neutrino interactions in hydrogen and deuterium: Description of the experiment and study of the reaction $\nu + d \to \mu^- + p + p_s$. *Phys. Rev. D*, 16:3103–3121, 1977.

[155] W. A. Mann, U. Mehtani, B. Musgrave, Y. Oren, P. A. Schreiner, R. Singer, H. Yuta, R. Ammar, S. Barish, Y. Cho, M. Derrick, R. Engelmann, and L. G. Hyman. Study of the reaction $\nu + n \to \mu^- + p$. *Phys. Rev. Lett.*, 31:844–847, 1973.

[156] T2K Collaboration. Implementation of the niwg cross section parametrization. 2013.

[157] L. Aliaga et al. Design, Calibration, and Performance of the MINERvA Detector. *Nucl. Instrum. Meth. A*, 743:130–159, 2014.

[158] T2K Collaboration. Niwg model and uncertainties for 2019-2020 oscillation analysis - version 5. 2019.

[159] J. Walsh. Constraining the t2k neutrino oscillation parameter results using data from the off-axis near detector, nd280 2k. 2021.

[160] R. Gran, J. Nieves, F. Sanchez, and M. J. Vicente Vacas. Neutrino-nucleus quasi-elastic and 2p2h interactions up to 10 GeV. *Phys. Rev. D*, 88(11):113007, 2013.

[161] Dieter Rein and Lalit M. Sehgal. Neutrino Excitation of Baryon Resonances and Single Pion Production. *Annals Phys.*, 133:79–153, 1981.

[162] Krzysztof M. Graczyk and Jan T. Sobczyk. Form Factors in the Quark Resonance Model. *Phys. Rev. D*, 77:053001, 2008. [Erratum: Phys.Rev.D 79, 079903 (2009)].

[163] K. Abe et al. First T2K measurement of transverse kinematic imbalance in the muon-neutrino charged-current single-π^+ production channel containing at least one proton. *Phys. Rev. D*, 103(11):112009, 2021.

[164] Jan T. Sobczyk, Jaroslaw A. Nowak, and Krzysztof M. Graczyk. WroNG - Wroclaw Neutrino Generator of events for single pion production. *Nucl. Phys. B Proc. Suppl.*, 139:266–271, 2005.

[165] Krzysztof M. Graczyk. Resonance contribution to single pion production in neutrino-nucleon scattering. In *27th International Workshop on Nuclear Theory*, 2008.

[166] Dieter Rein and Lalit M. Sehgal. Coherent pi0 Production in Neutrino Reactions. *Nucl. Phys. B*, 223:29–44, 1983.

[167] M. Glück, E. Reya, and A. Vogt. Dynamical parton distributions revisited. *Eur. Phys. J. C*, 5:461–470, 1998.

[168] A. Bodek and U. K. Yang. Modeling neutrino and electron scattering cross-sections in the few GeV region with effective LO PDFs. *AIP Conf. Proc.*, 670(1):110–117, 2003.

[169] Arie Bodek and Un-ki Yang. A Unified model for inelastic e - N and nu - N cross-sections at all Q**2. *AIP Conf. Proc.*, 792(1):257–260, 2005.

[170] Christian Bierlich et al. A comprehensive guide to the physics and usage of PYTHIA 8.3. 2022.

[171] T. Yang, C. Andreopoulos, H. Gallagher, and P. Kehayias. A hadronization model for the MINOS experiment. *AIP Conf. Proc.*, 967(1):269–275, 2007.

[172] Arie Bodek and Un-ki Yang. Axial and Vector Structure Functions for Electron- and Neutrino- Nucleon Scattering Cross Sections at all Q^2 using Effective Leading order Parton Distribution Functions. 2010.

[173] L. Munteanu. Vers la mesure de la violation de la symétrie cp dans les oscillations de neutrinos avec lexpérience t2k. 2022.

[174] Sowjanya Gollapinni. Neutrino Cross section Future. In *Prospects in Neutrino Physics*, 2016.

[175] L. L. Salcedo, E. Oset, M. J. Vicente-Vacas, and C. Garcia-Recio. Computer Simulation of Inclusive Pion Nuclear Reactions. *Nucl. Phys. A*, 484:557–592, 1988.

[176] K. Nakamura et al. Review of particle physics. *J. Phys. G*, 37:075021, 2010.

[177] P. Gueye et al. Coulomb distortion measurements by comparing electron and positron quasielastic scattering off C-12 and Pb-208. *Phys. Rev. C*, 60:044308, 1999.

[178] T2K Collaboration. T2k internal technical note 106, constraining the flux and cross section models with data from the nd280 detector for the 2012a oscillation analysis. 2012.

[179] F. James. Minuit reference manual. 2000.

Appendix A

ND280 coordinate system

The ND280 coordinate system's origin is the geometric center of the magnet system, which is inside TPC1 in the vicinity of FGD1. The direction is defined as below: the z axis is the beam axis, and a greater z coordinate corresponds to a more downstream location; the x direction is the up and down; and the y direction left and right. The detector placement is symmetric about the x axis, while their is a 55 mm shift in the y direction to provide drainage in case of water leak. A cross-section view of ND280 with coordinates is shown in Fig. A.1.

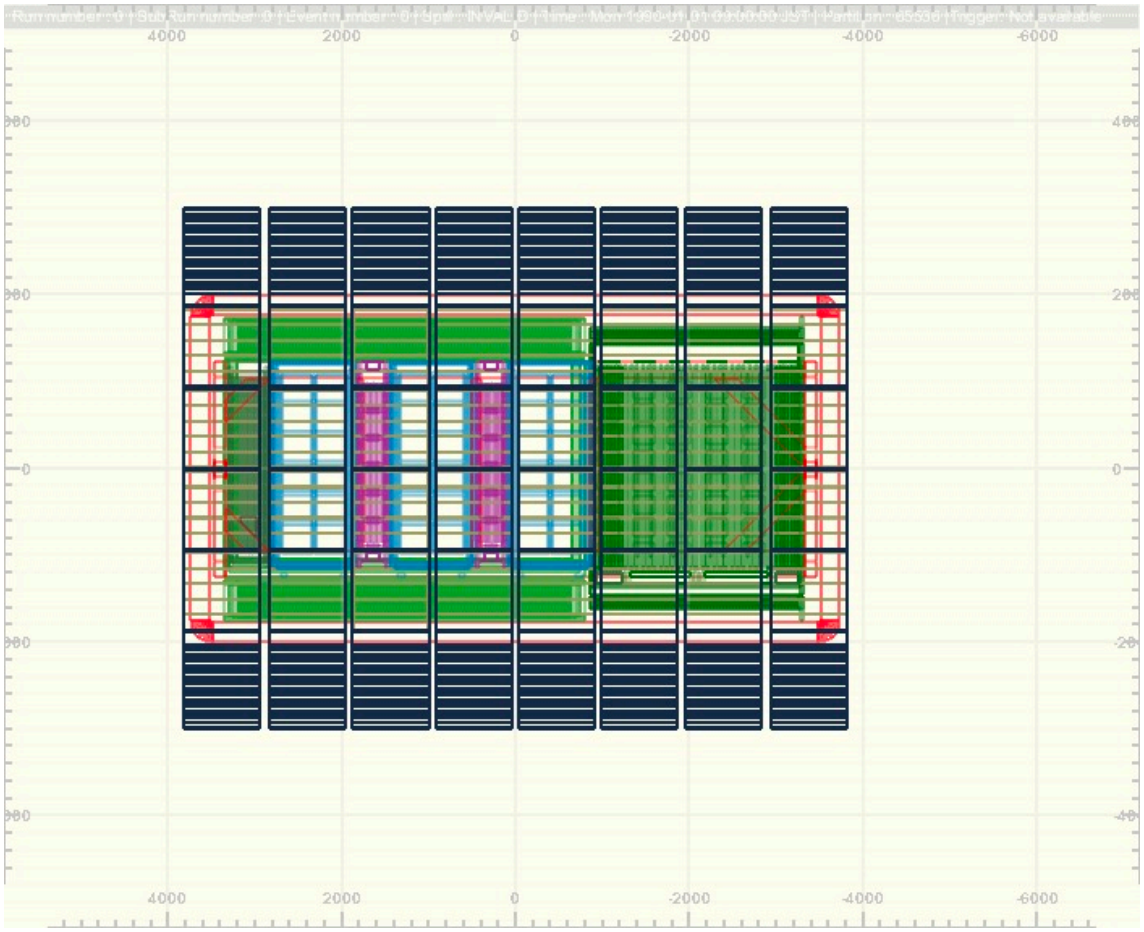

FIGURE A.1: Cross-section view of ND280 with coordinates.

Appendix B

Likelihood scan outputs

This section presents the likilihood scan outputs of all parameters varied in the likilihood scan studies.

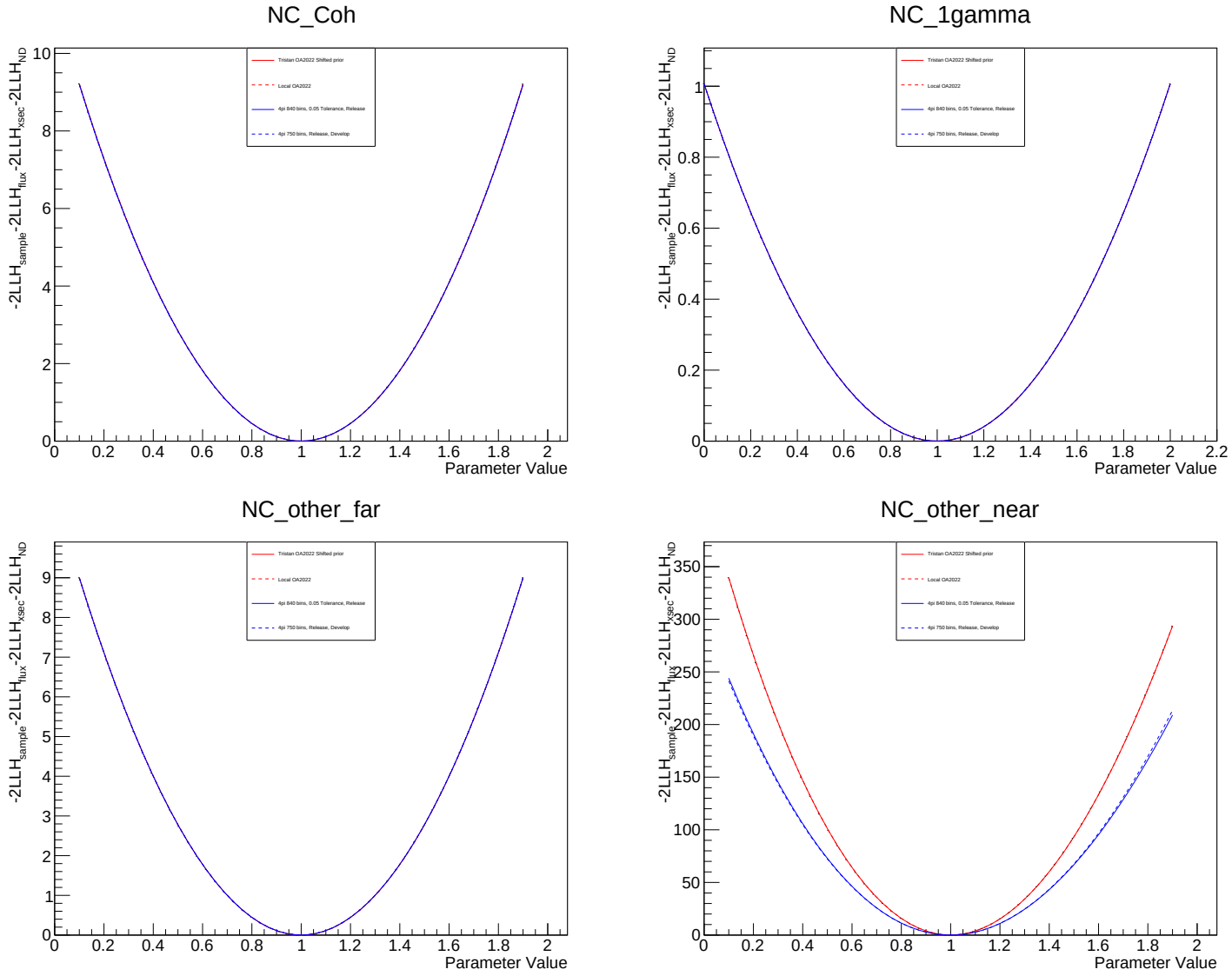

FIGURE B.1: Neutral current interaction parameters' LLH scan outputs.

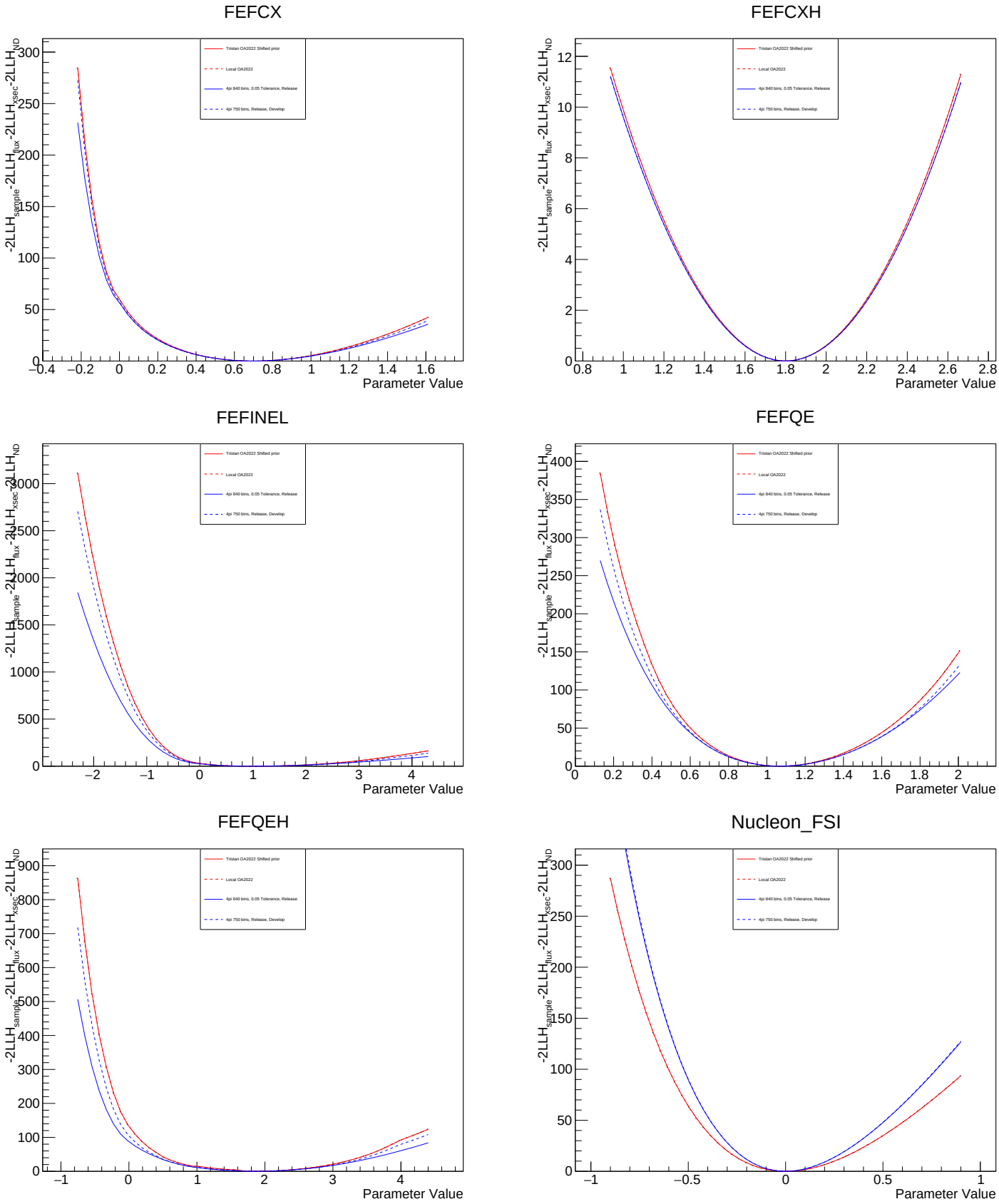

FIGURE B.2: FSI parameters' LLH scan outputs.

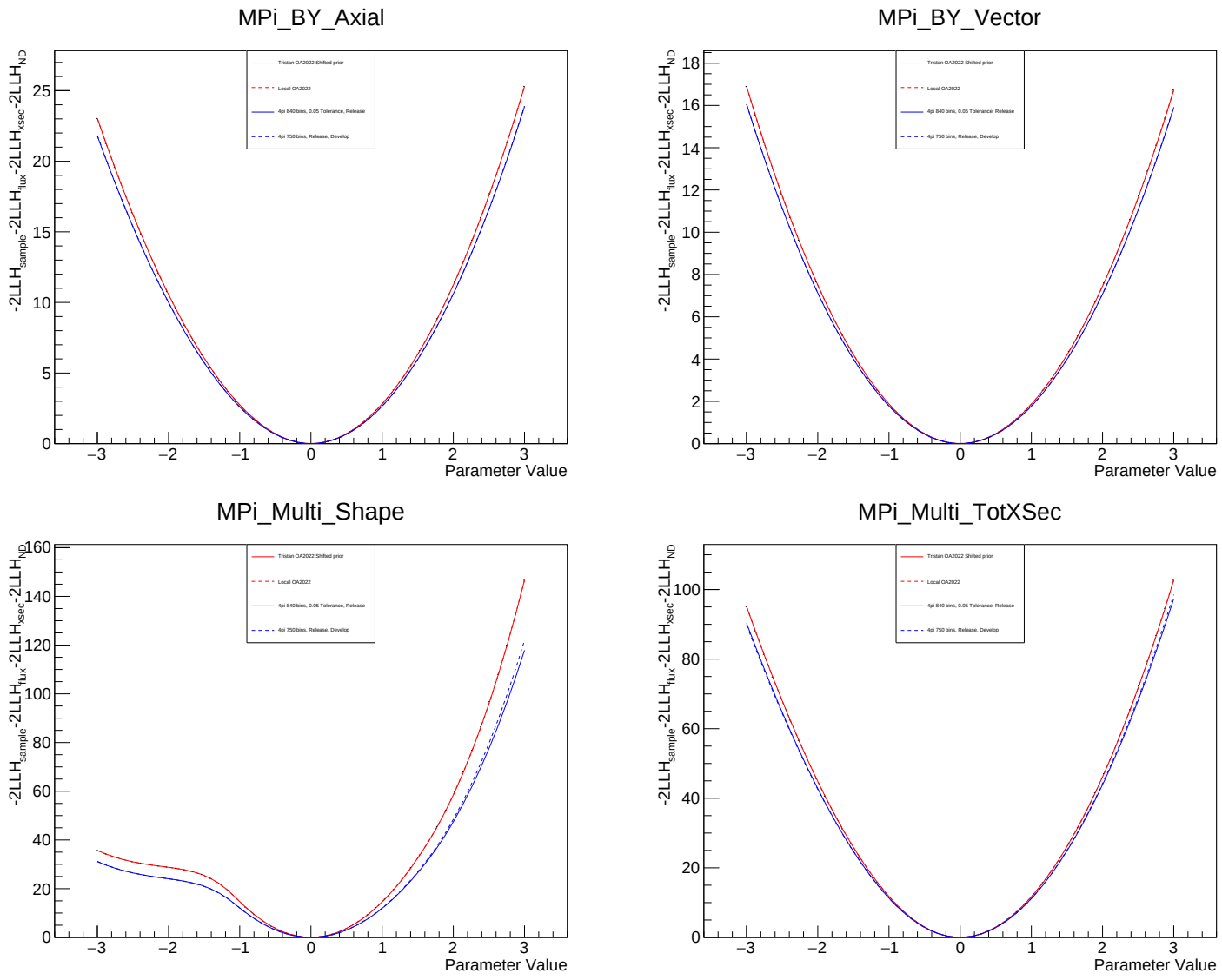

FIGURE B.3: Multi pion production parameters' LLH scan results.

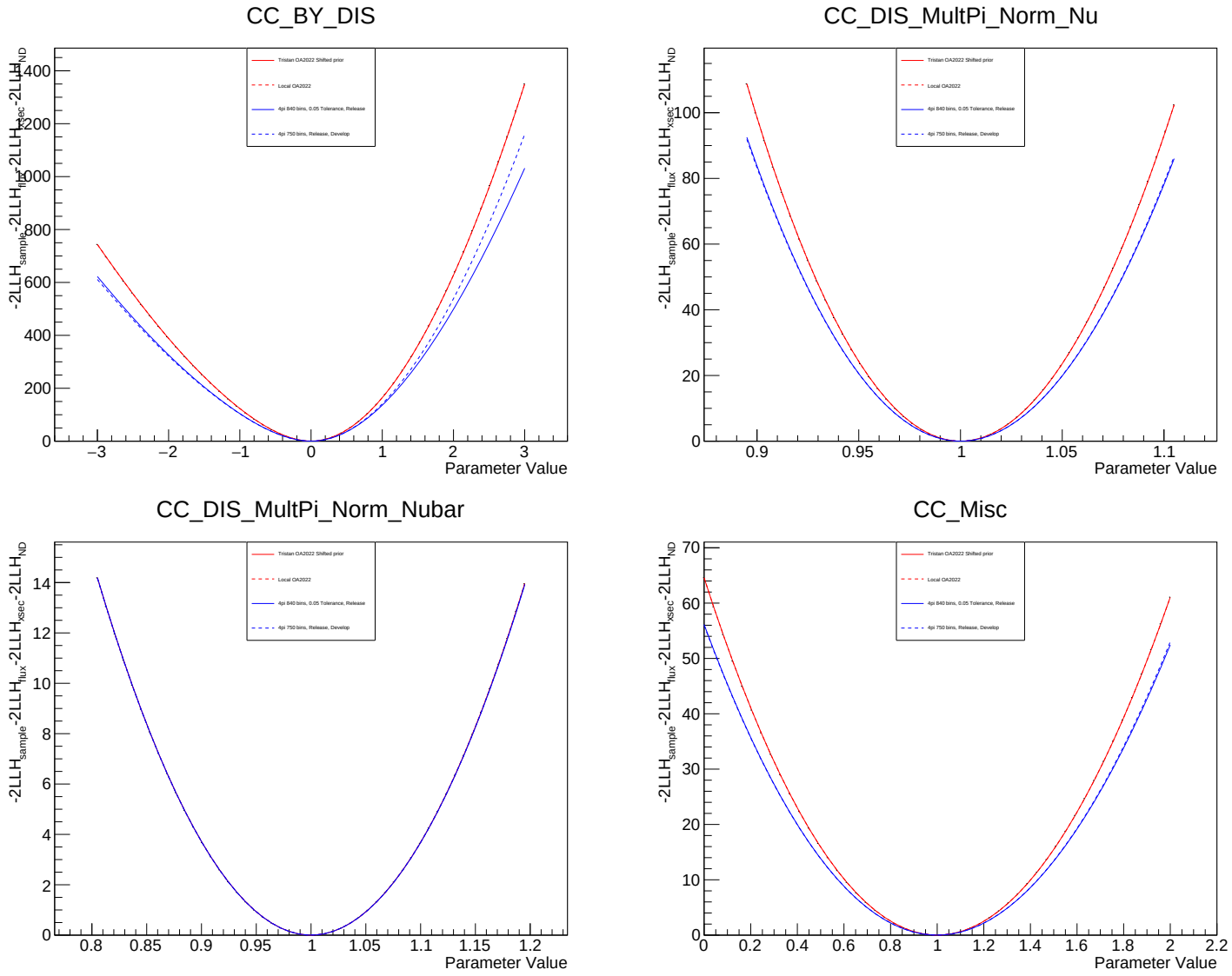

FIGURE B.4: Deep-inelastic scattering parameters' scan results.

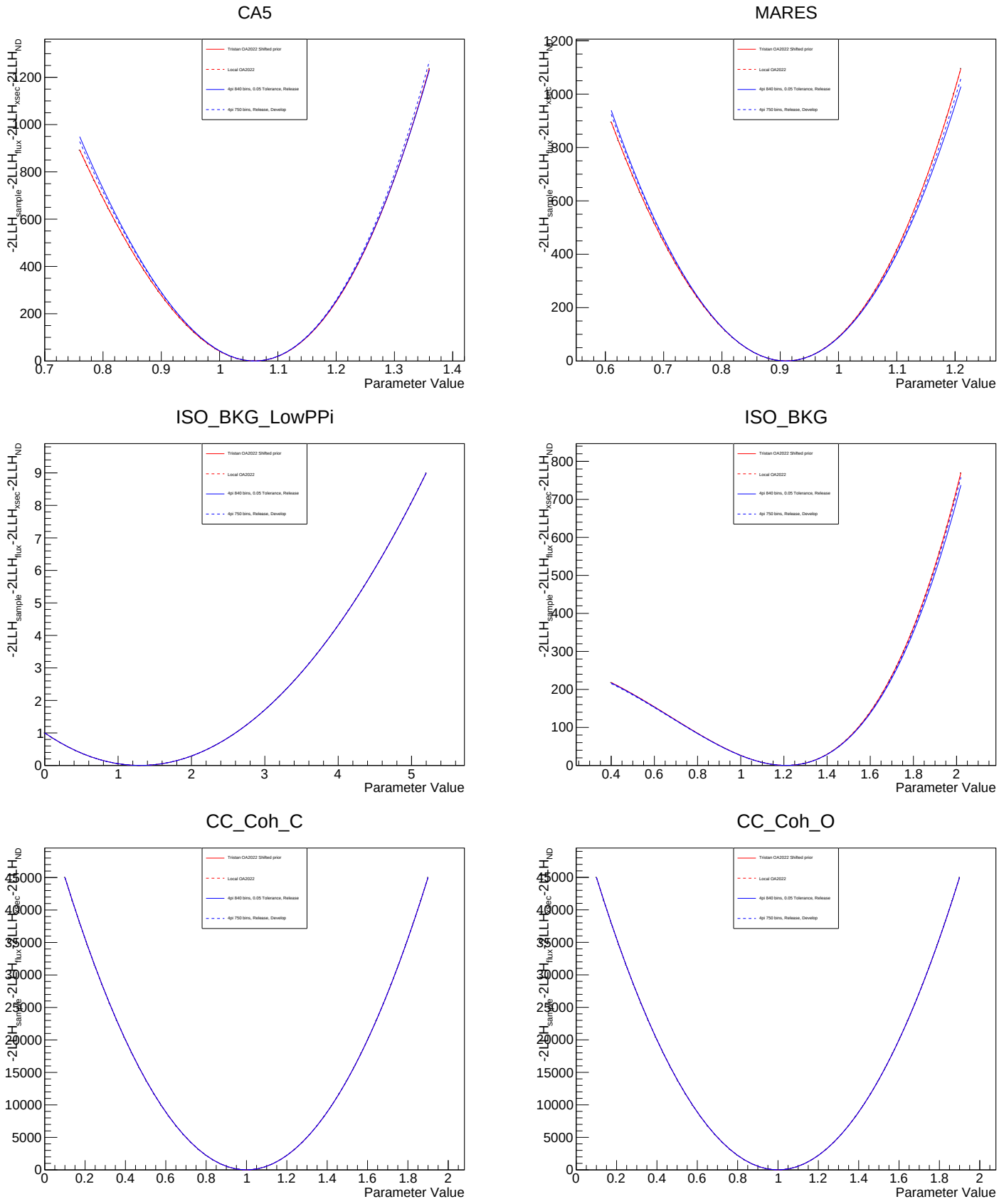

FIGURE B.5: Single pion production parameters' LLH scan outputs (1).

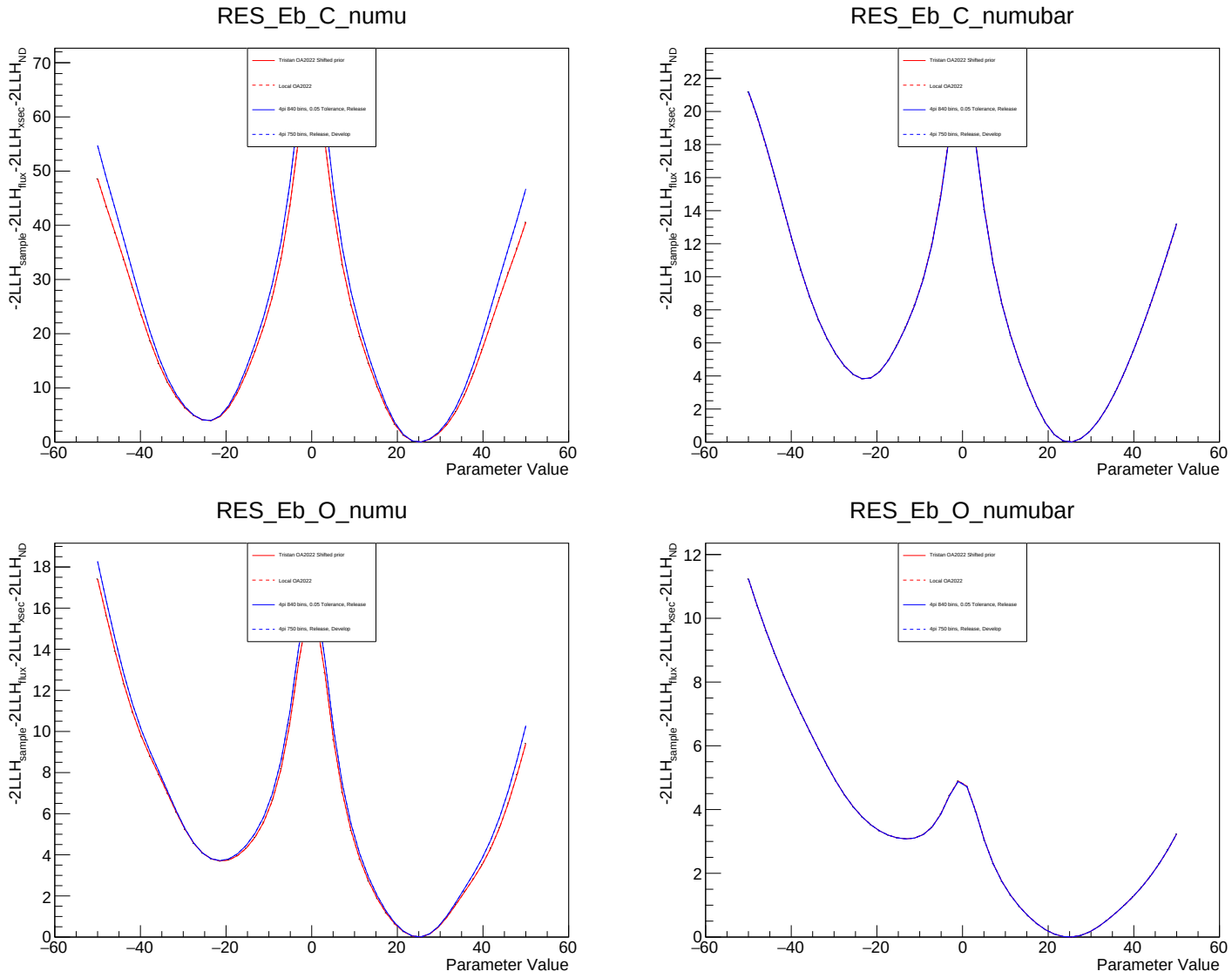

FIGURE B.6: Res EB parameters' LLH scan outputs.

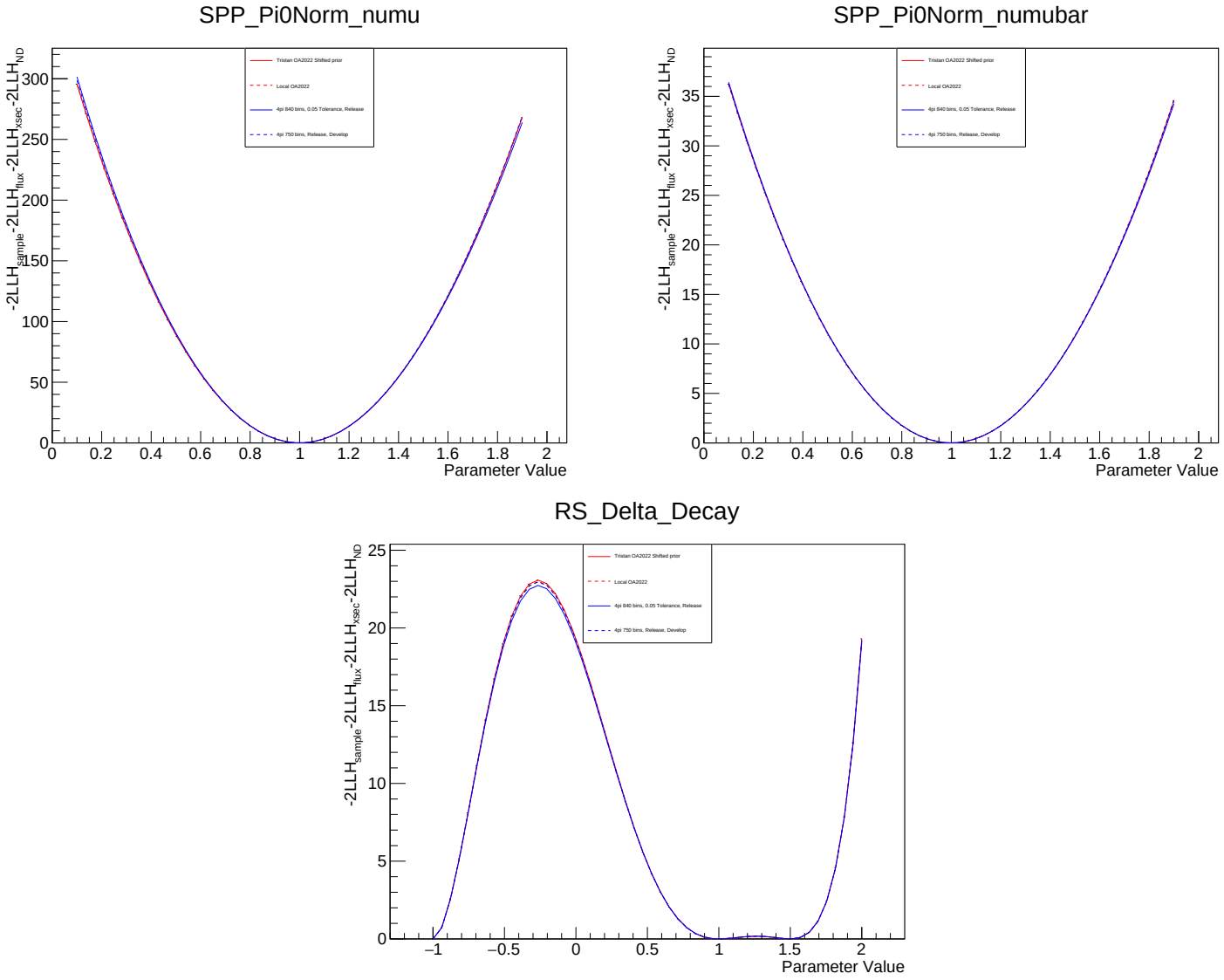

FIGURE B.7: Single pion production parameters' LLH scan outputs (2).

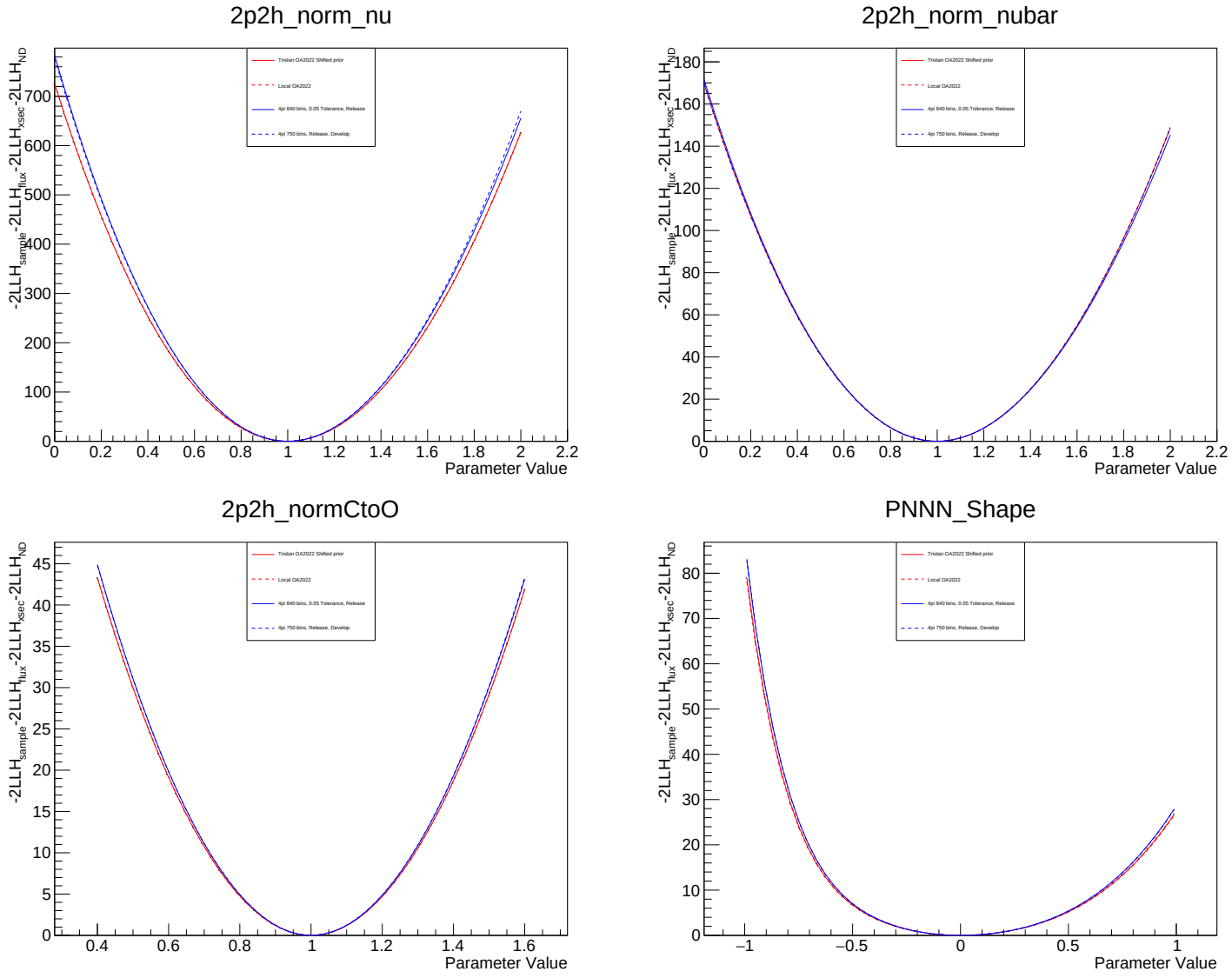

FIGURE B.8: 2p2h parameters' LLH scan outputs (1).

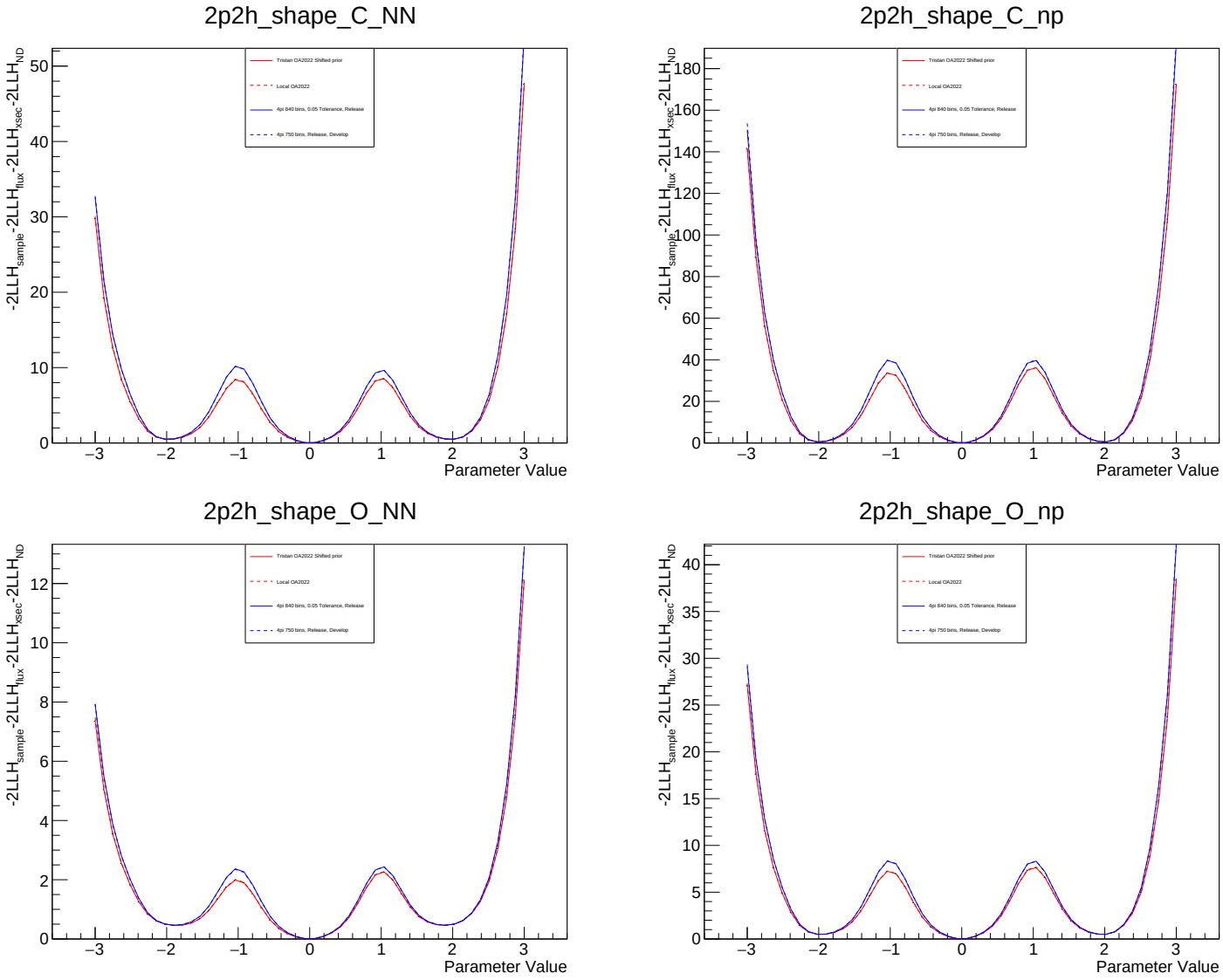

FIGURE B.9: 2p2h parameters' LLH scan outputs (2).

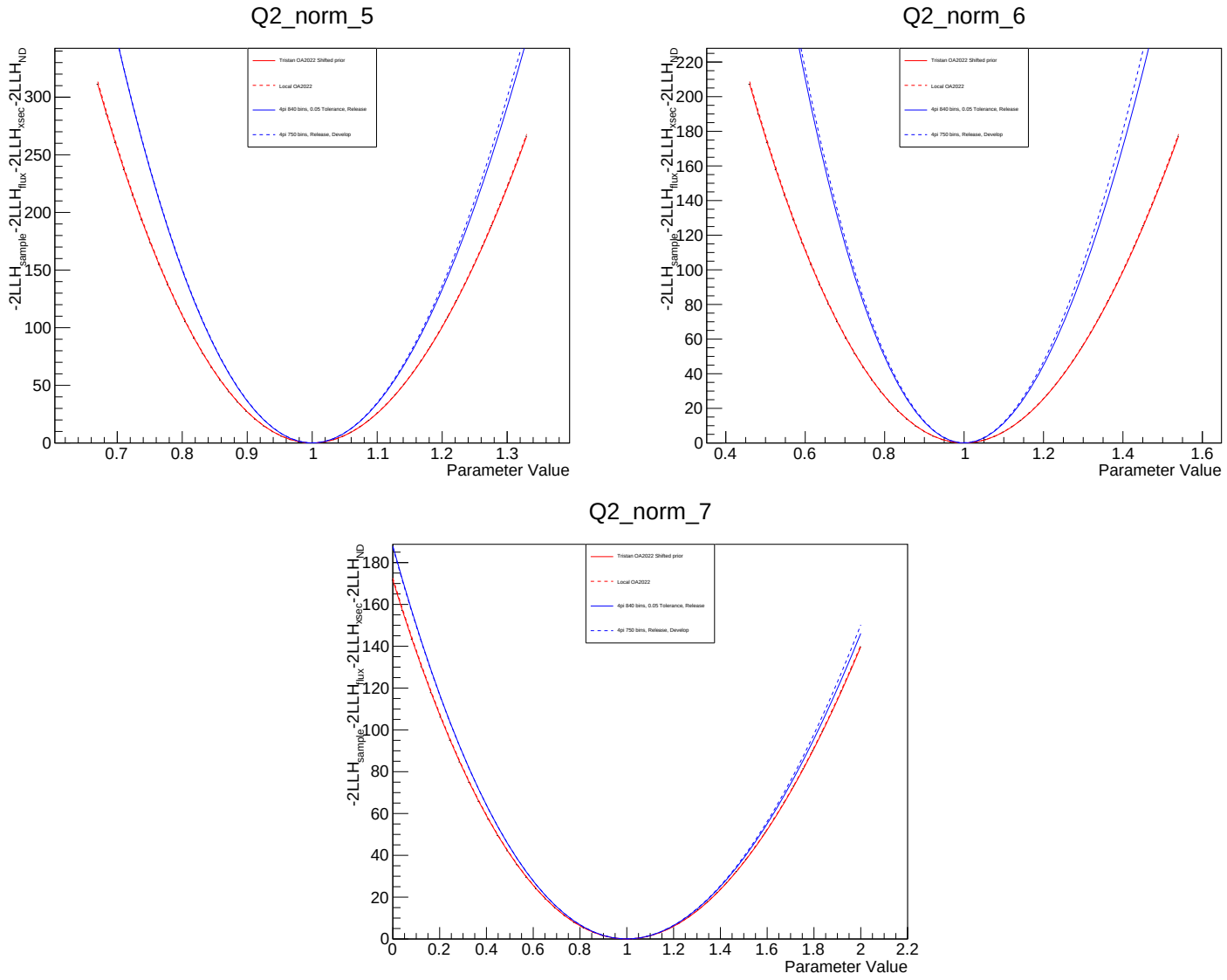

FIGURE B.10: CCQE Q2 parameters' LLH scan outputs.

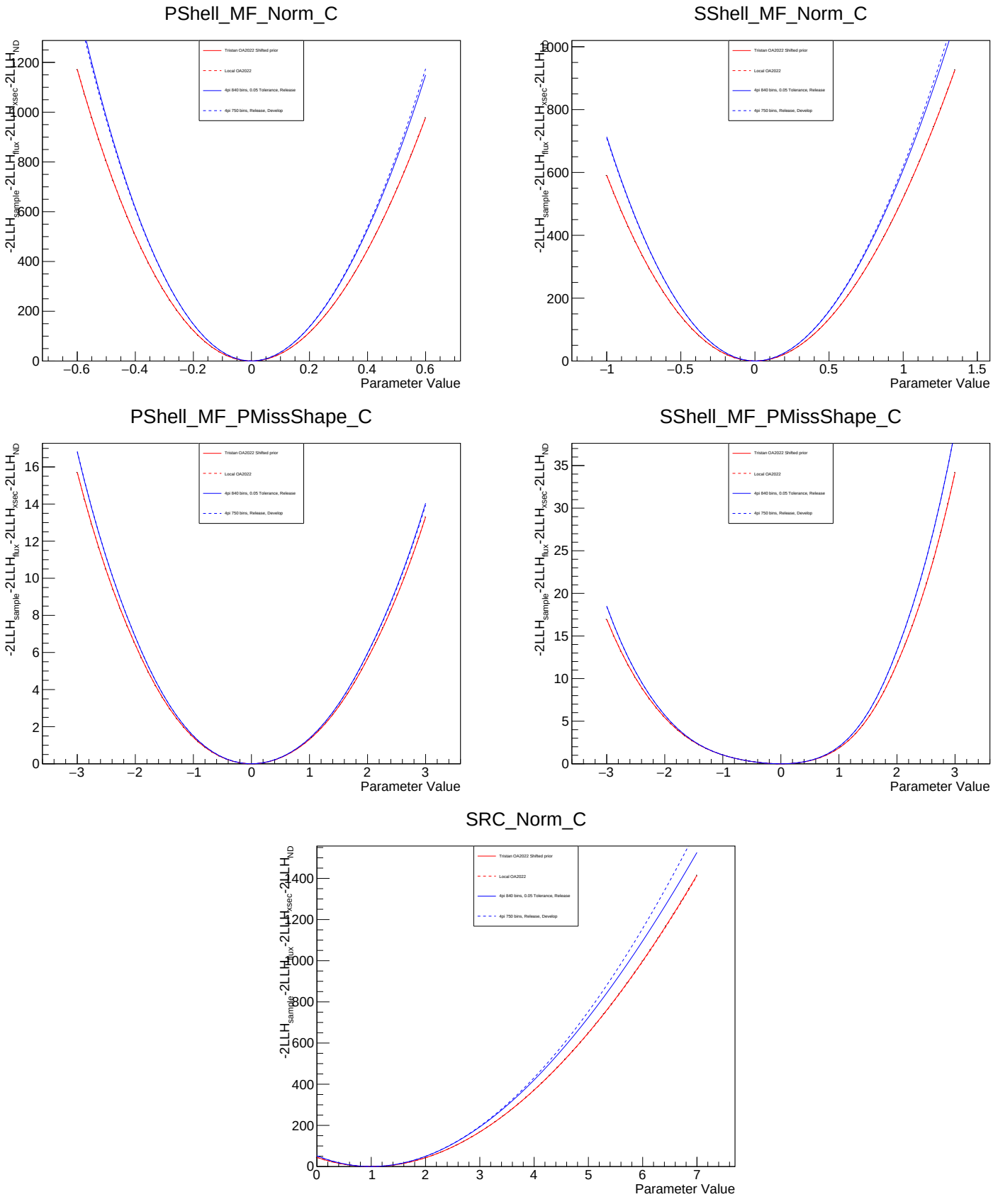

FIGURE B.11: CCQE carbon parameters' LLH scan outputs.

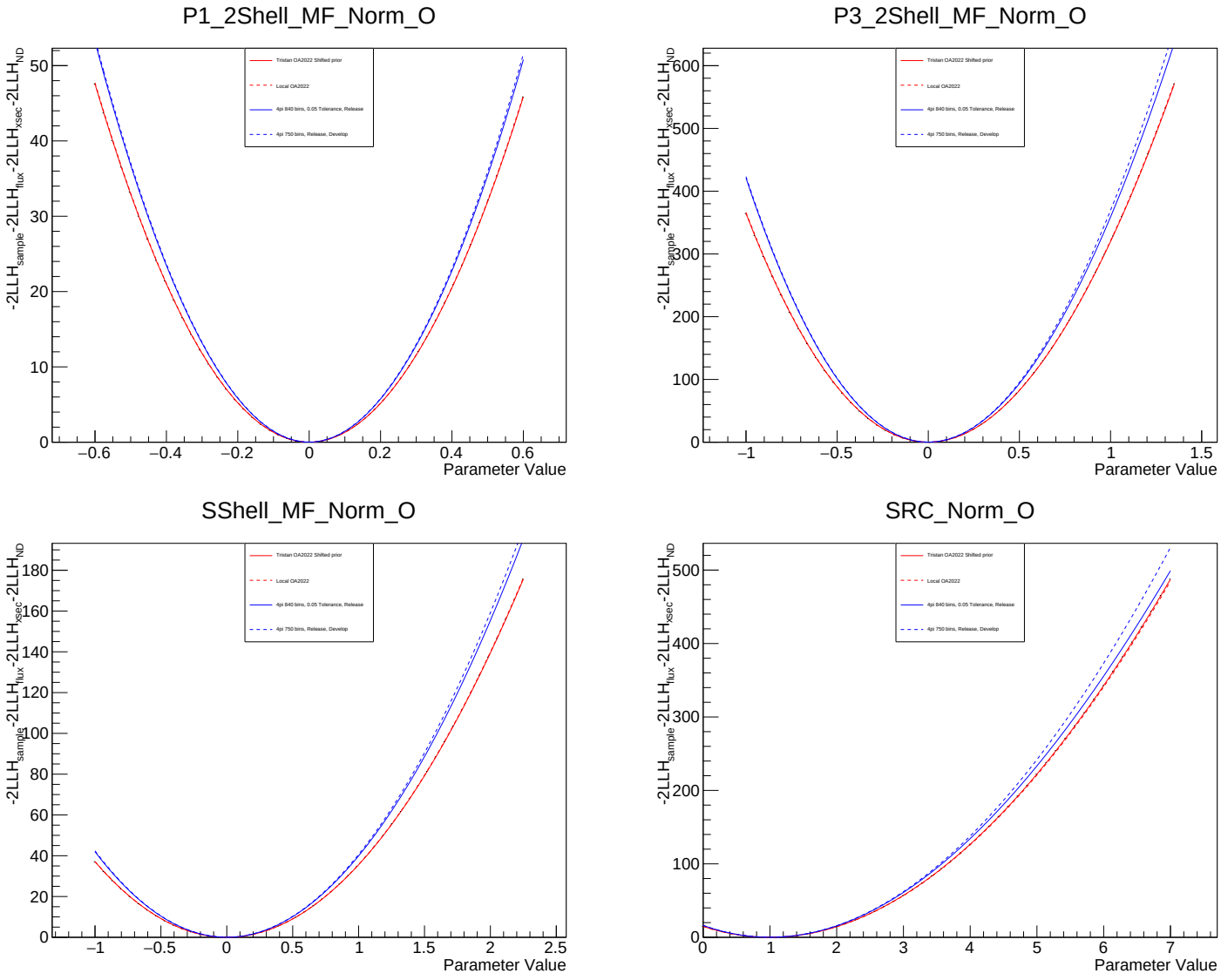

FIGURE B.12: CCQE Oxygen parameters' LLH scan outputs (1).

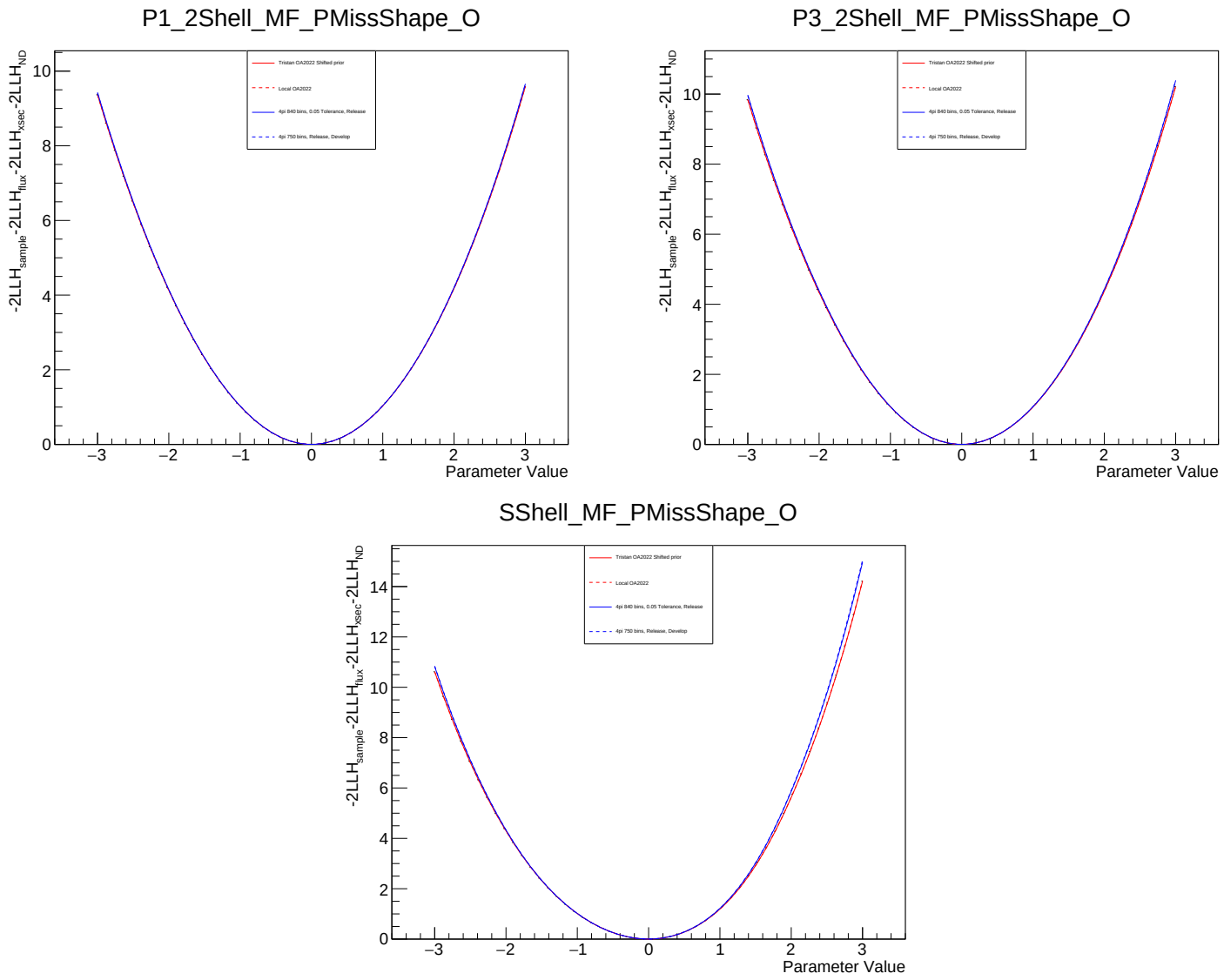

FIGURE B.13: CCQE Oxygen parameters' LLH scan outputs (2).

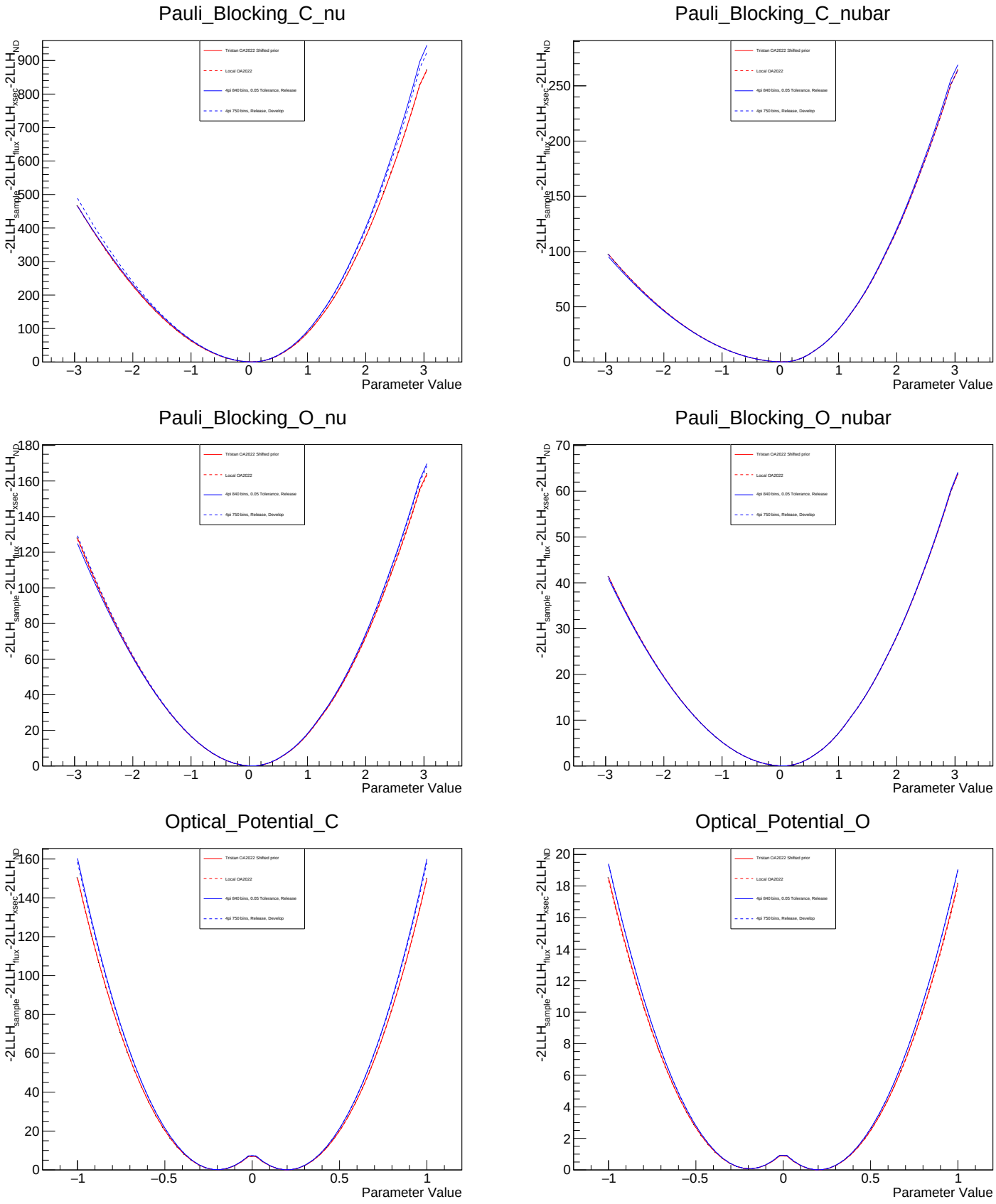

FIGURE B.14: Pauli blocking and optical potential parameters' LLH scan outputs.

Appendix C

Individual systematic errors

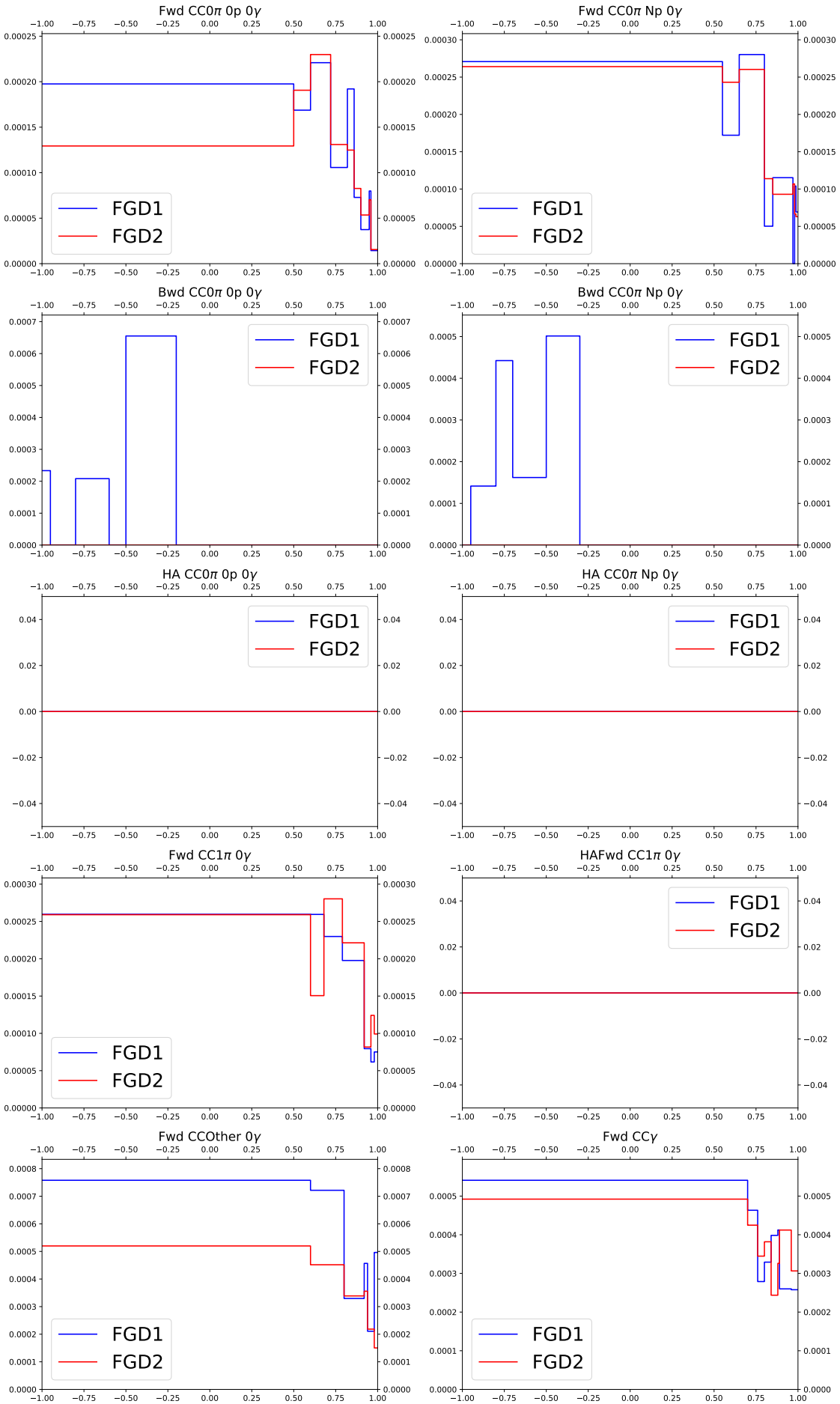

FIGURE C.1: The relative error caused by TPC clustering efficiency, evaluated using highland2 propagation and parameters described before, as a function of muon $\cos\theta$ in different samples. The blue solid line stands for FGD1, and red line for FGD2.

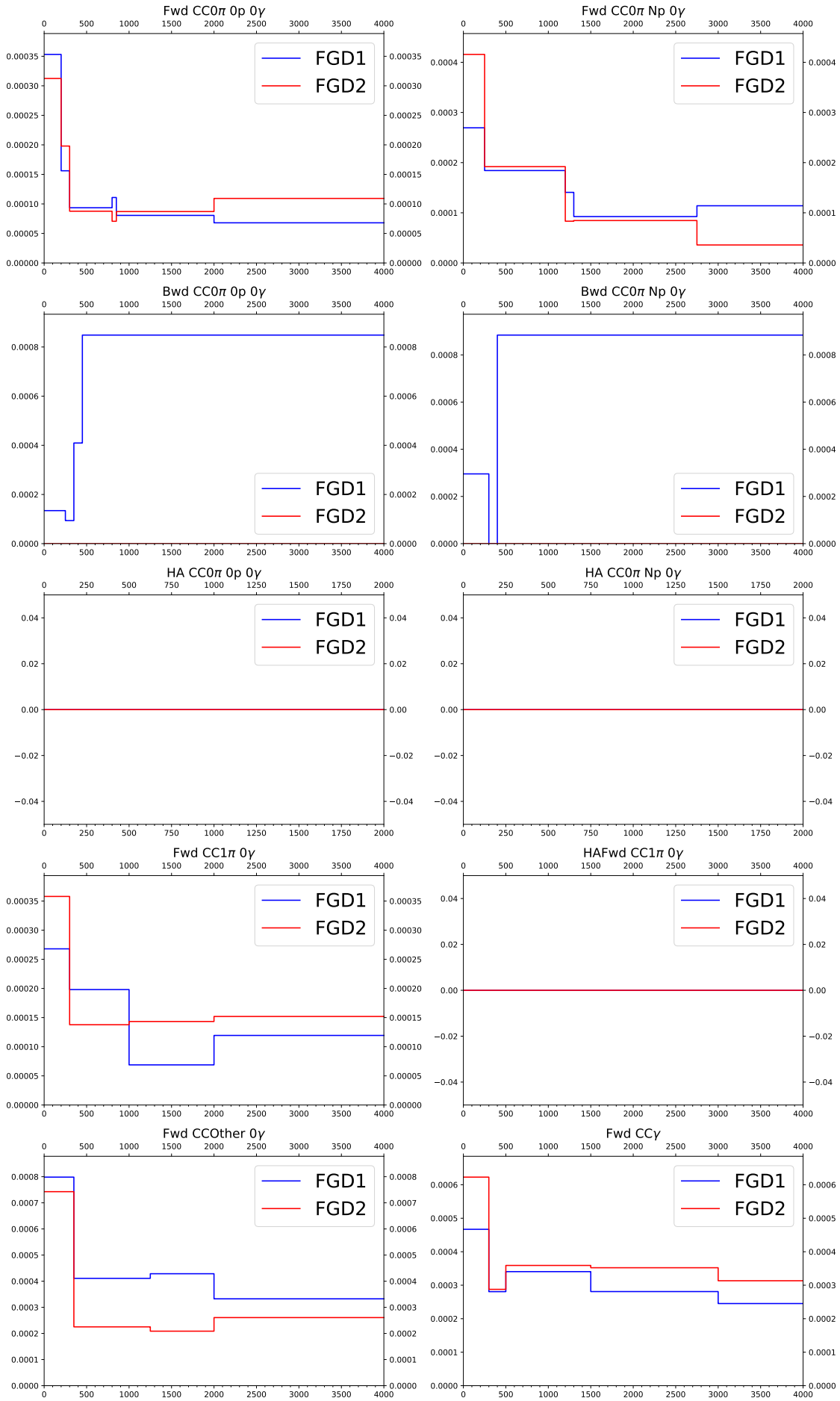

FIGURE C.2: The relative error caused by TPC clustering efficiency, evaluated using highland2 propagation and parameters described before, as a function of muon $\cos\theta$ in different samples. The blue solid line stands for FGD1, and red line for FGD2.

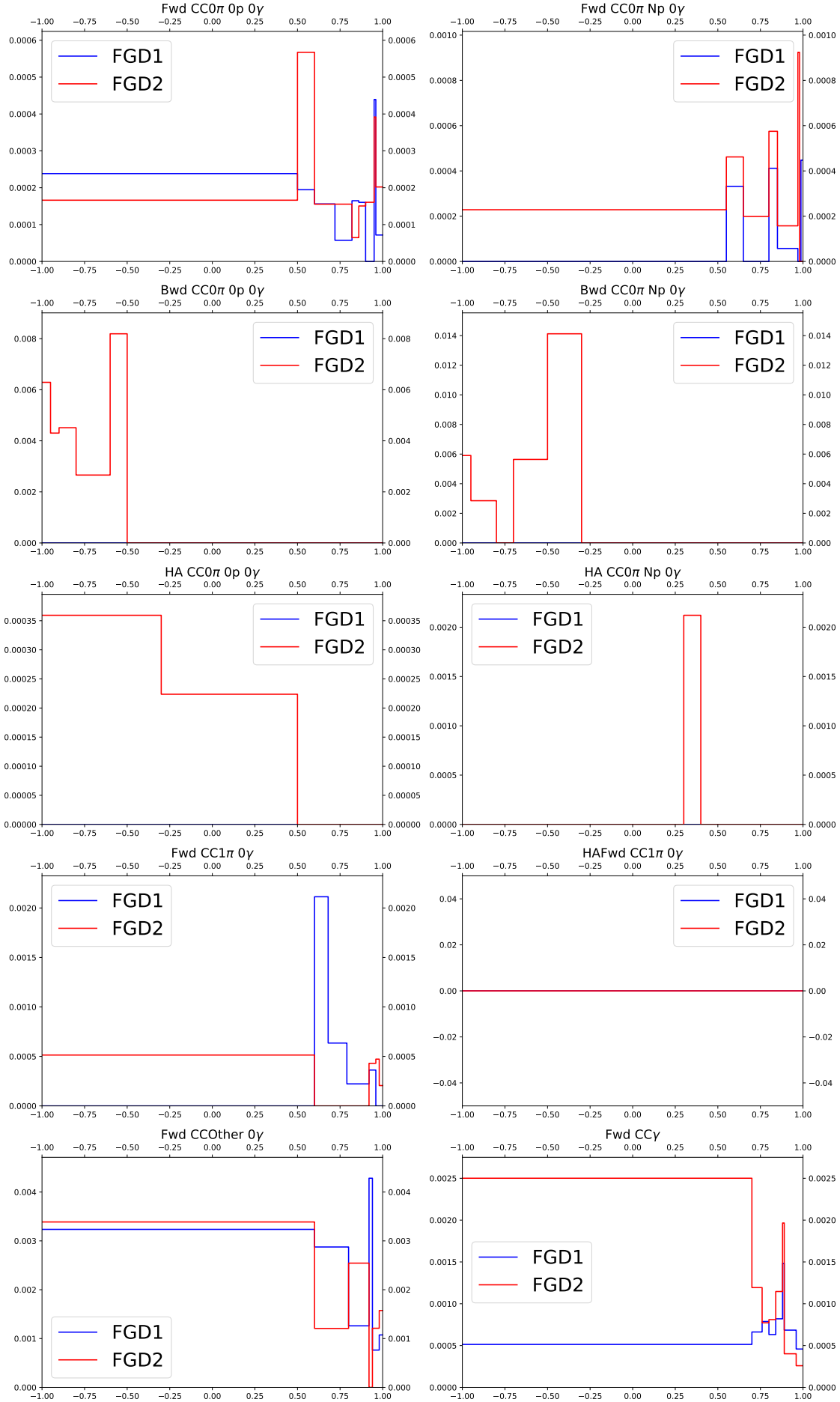

FIGURE C.3: The relative error caused by B field distortion, evaluated using highland2 propagation and parameters described before, as a function of muon $\cos\theta$ in different samples. The blue solid line stands for FGD1, and red line for FGD2.

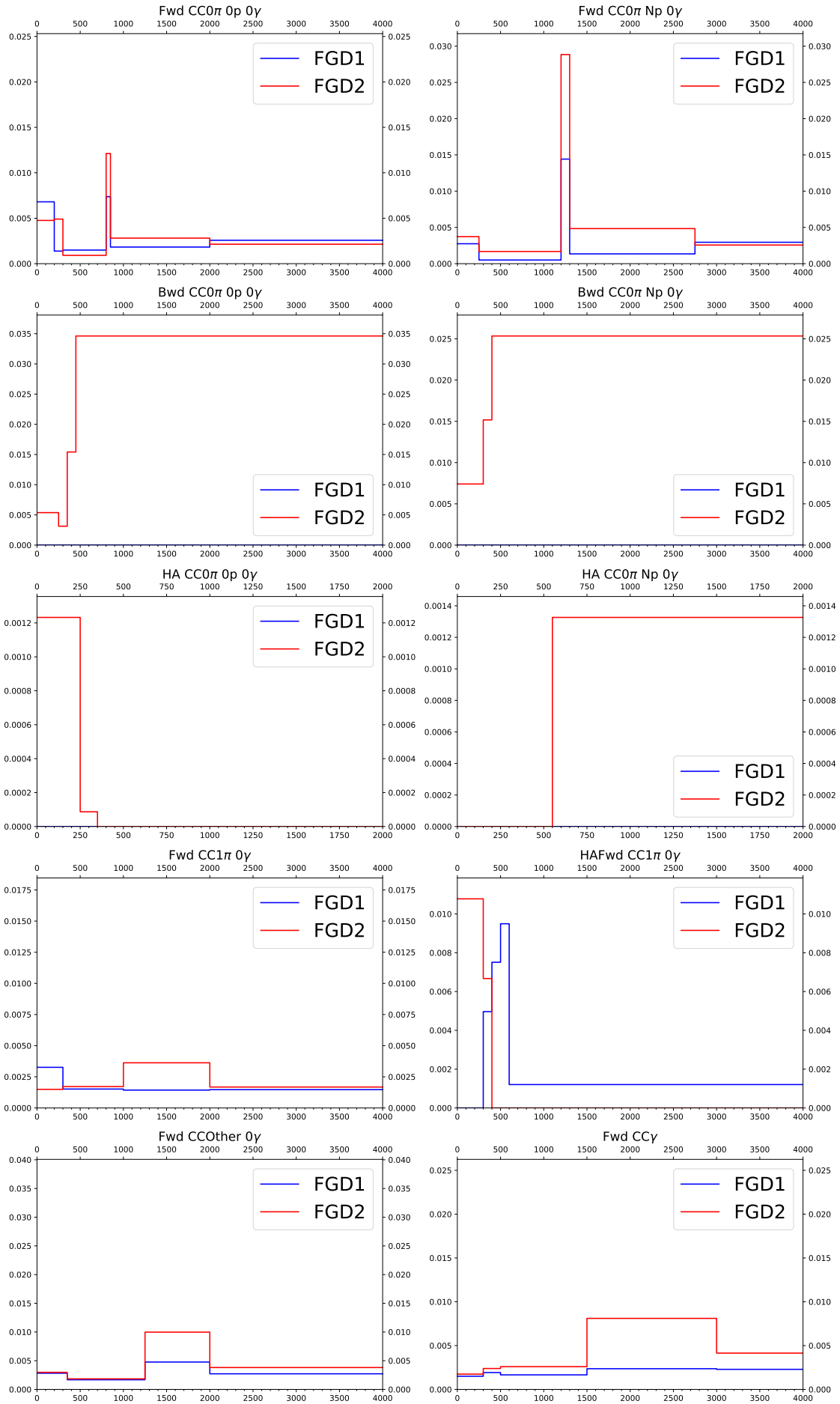

FIGURE C.4: The relative error caused by B field distortion, evaluated using highland2 propagation and parameters described before, as a function of muon $\cos\theta$ in different samples. The blue solid line stands for FGD1, and red line for FGD2.

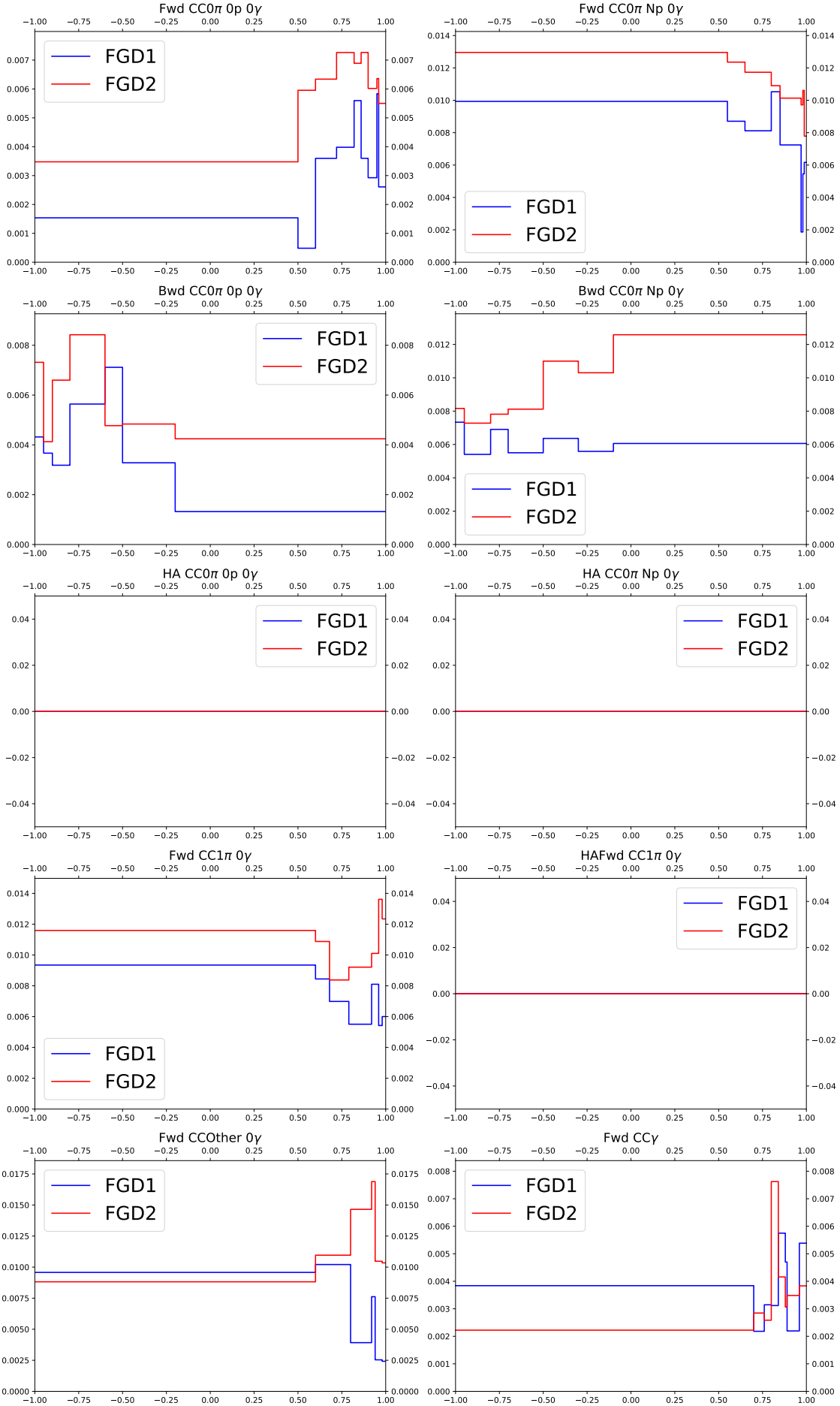

FIGURE C.5: The relative error caused by TPC tracking efficiency, evaluated using highland2 propagation and parameters described before, as a function of muon $\cos\theta$ in different samples. The blue solid line stands for FGD1, and red line for FGD2.

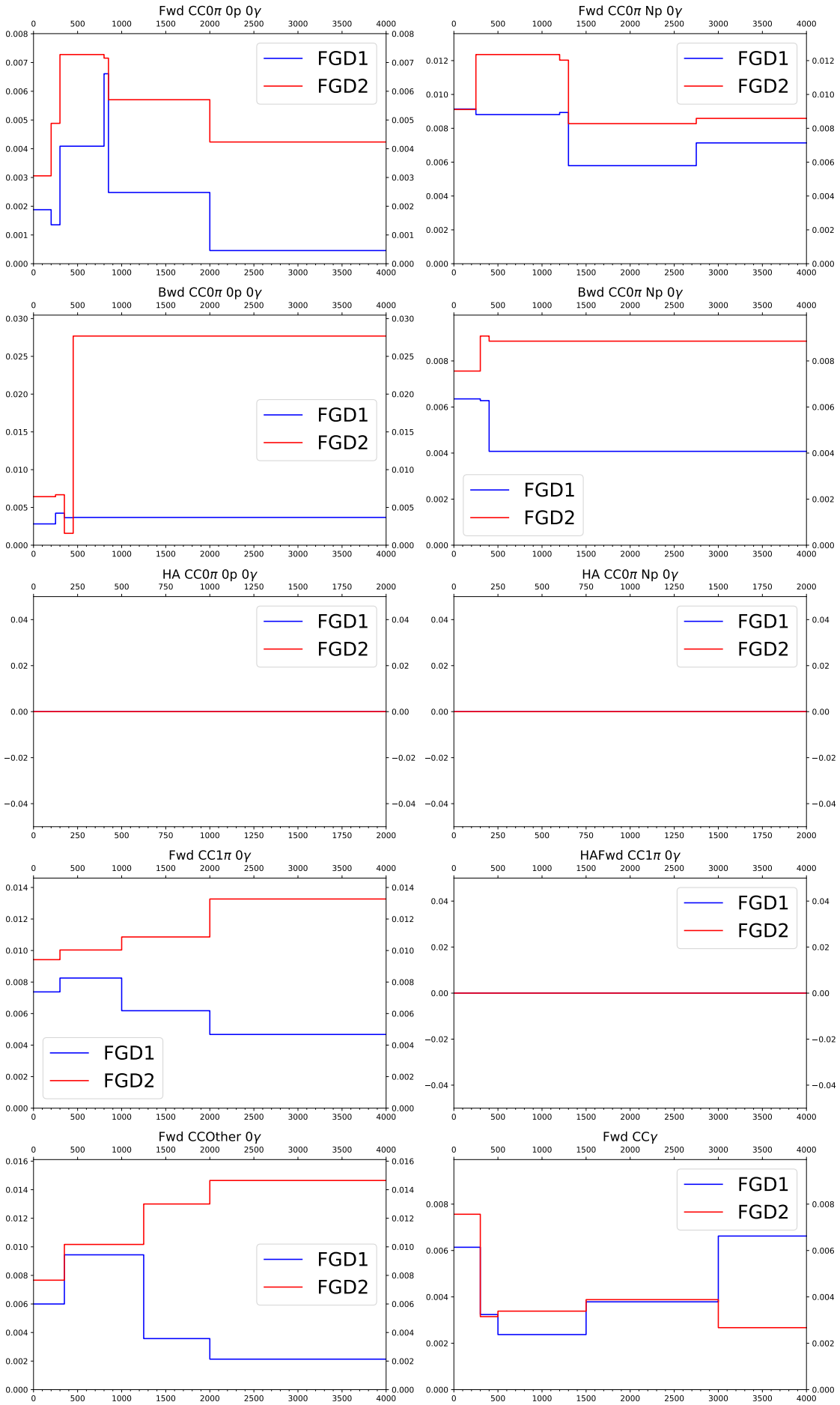

FIGURE C.6: The relative error caused by TPC tracking efficiency, evaluated using highland2 propagation and parameters described before, as a function of muon $\cos\theta$ in different samples. The blue solid line stands for FGD1, and red line for FGD2.

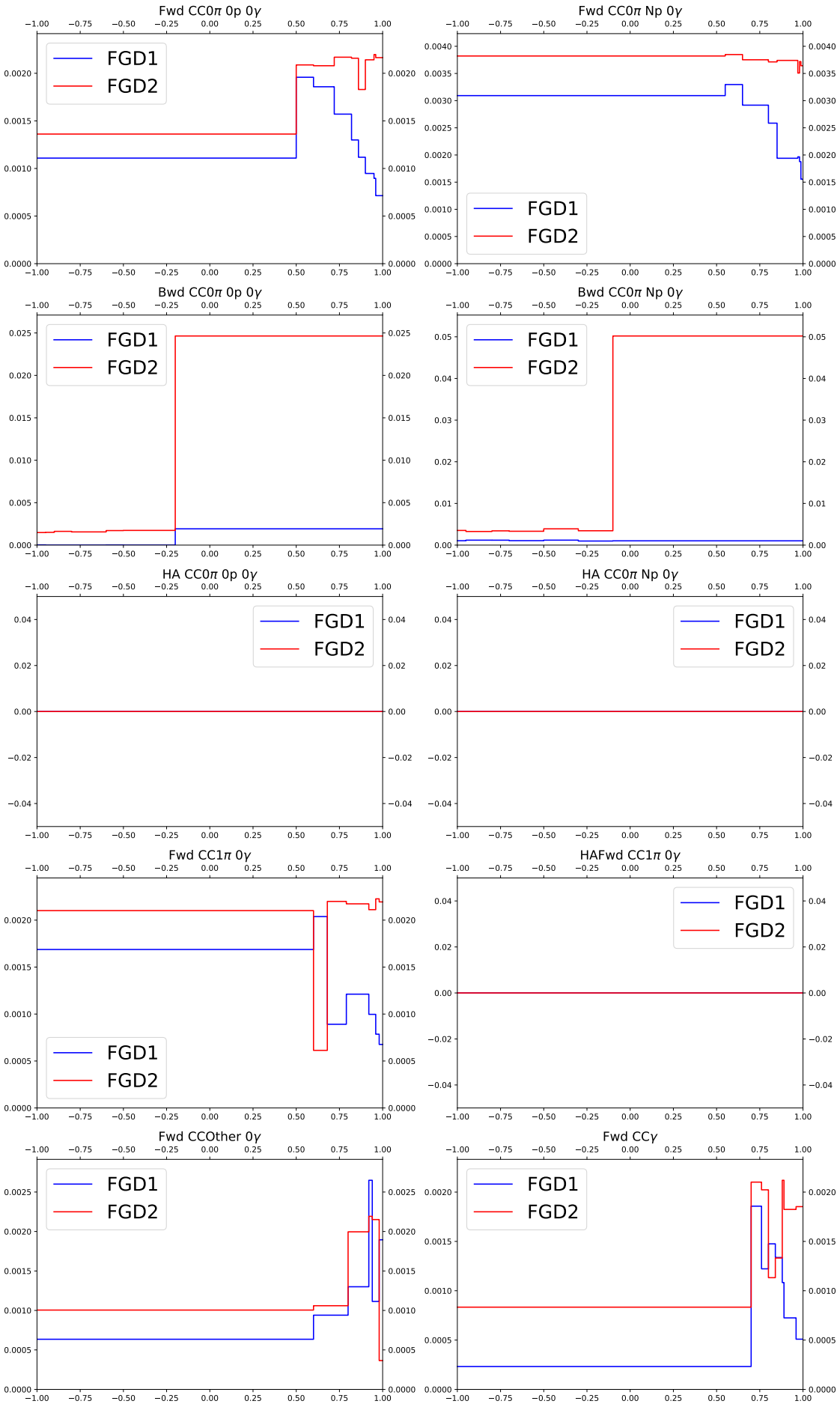

FIGURE C.7: The relative error caused by charge identification efficiency, evaluated using highland2 propagation and parameters described before, as a function of muon $\cos\theta$ in different samples. The blue solid line stands for FGD1, and red line for FGD2.

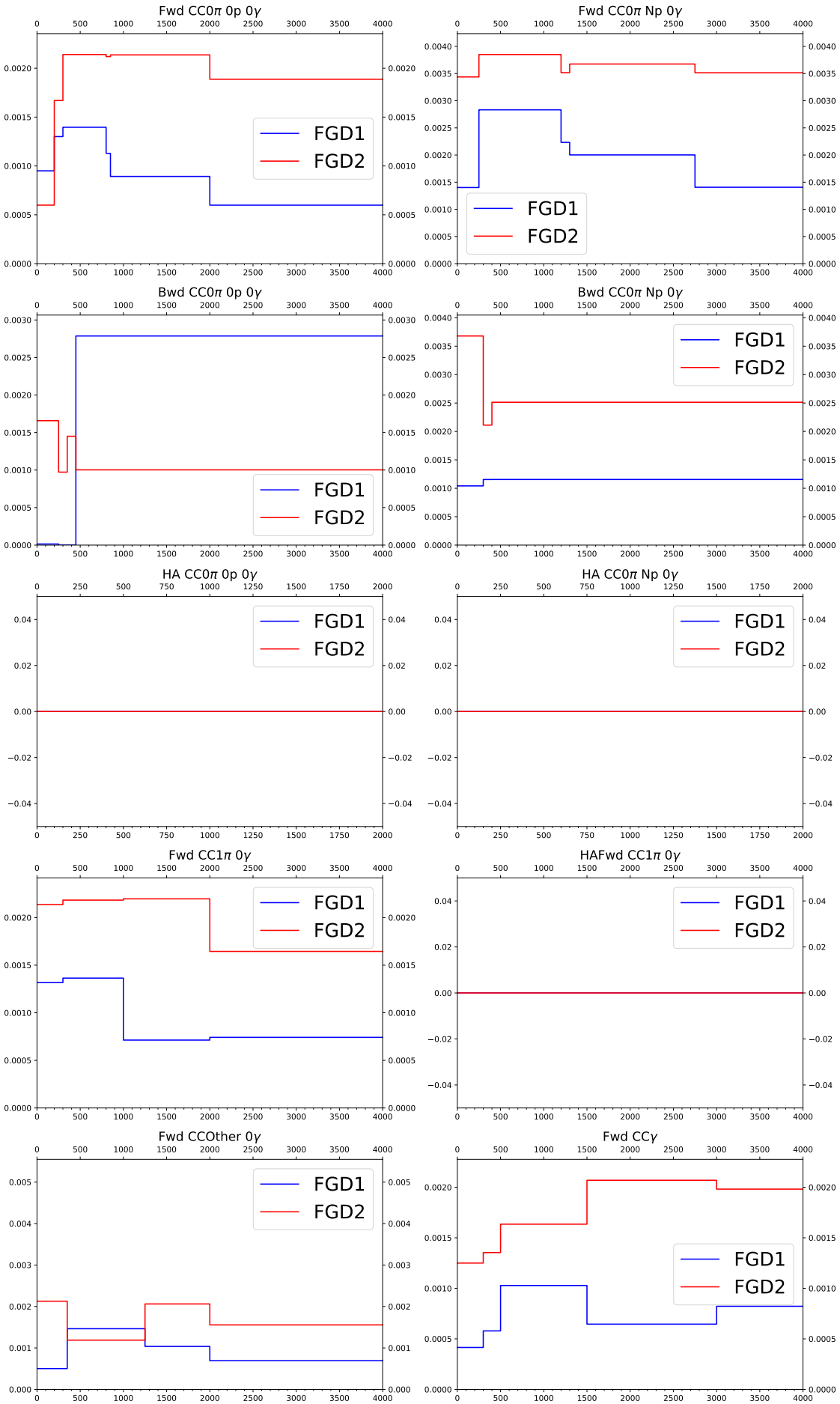

FIGURE C.8: The relative error caused by charge identification efficiency, evaluated using highland2 propagation and parameters described before, as a function of muon $\cos\theta$ in different samples. The blue solid line stands for FGD1, and red line for FGD2.

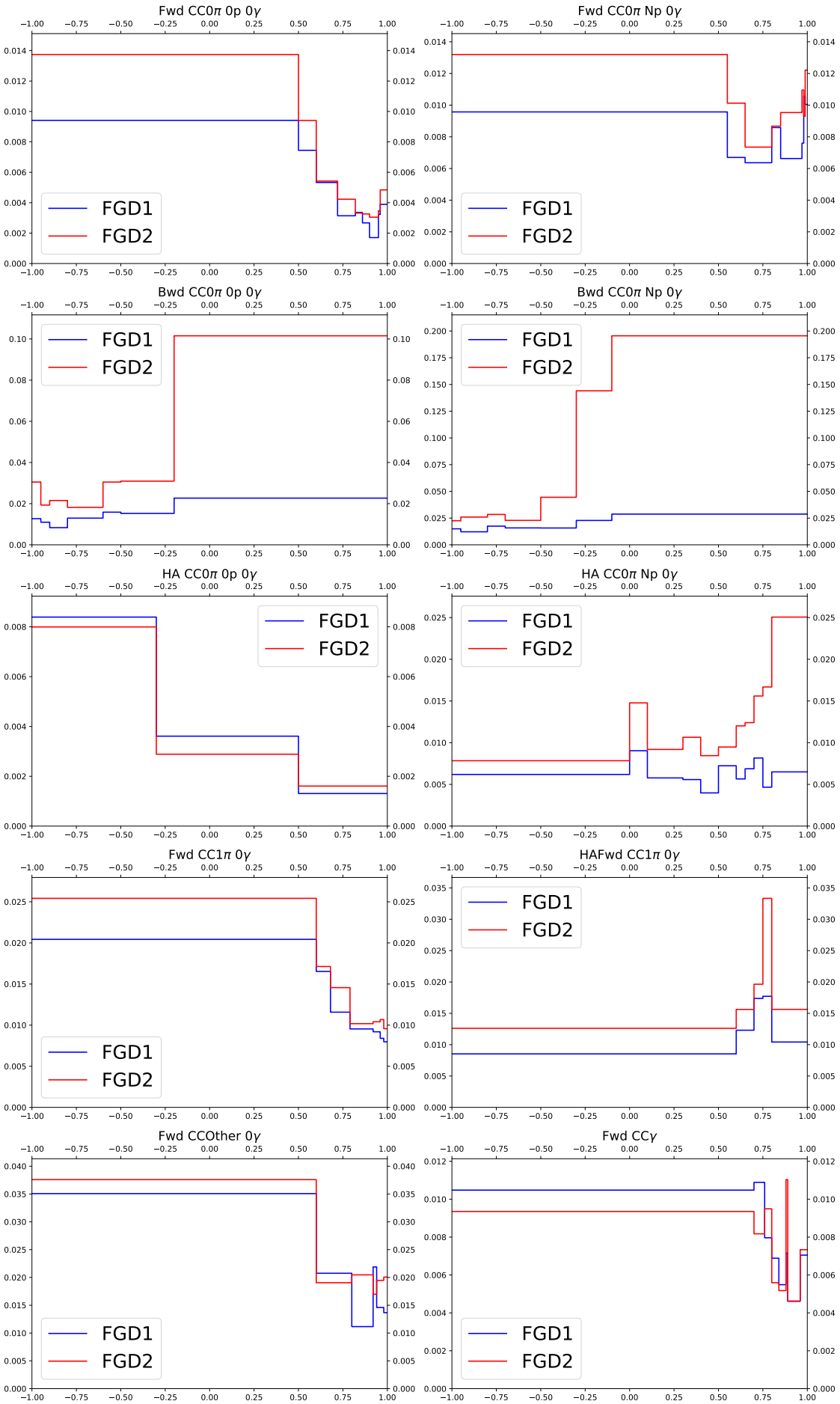

FIGURE C.9: The relative error caused by TPC PID, evaluated using highland2 propagation and parameters described before, as a function of muon $\cos\theta$ in different samples. The blue solid line stands for FGD1, and red line for FGD2.

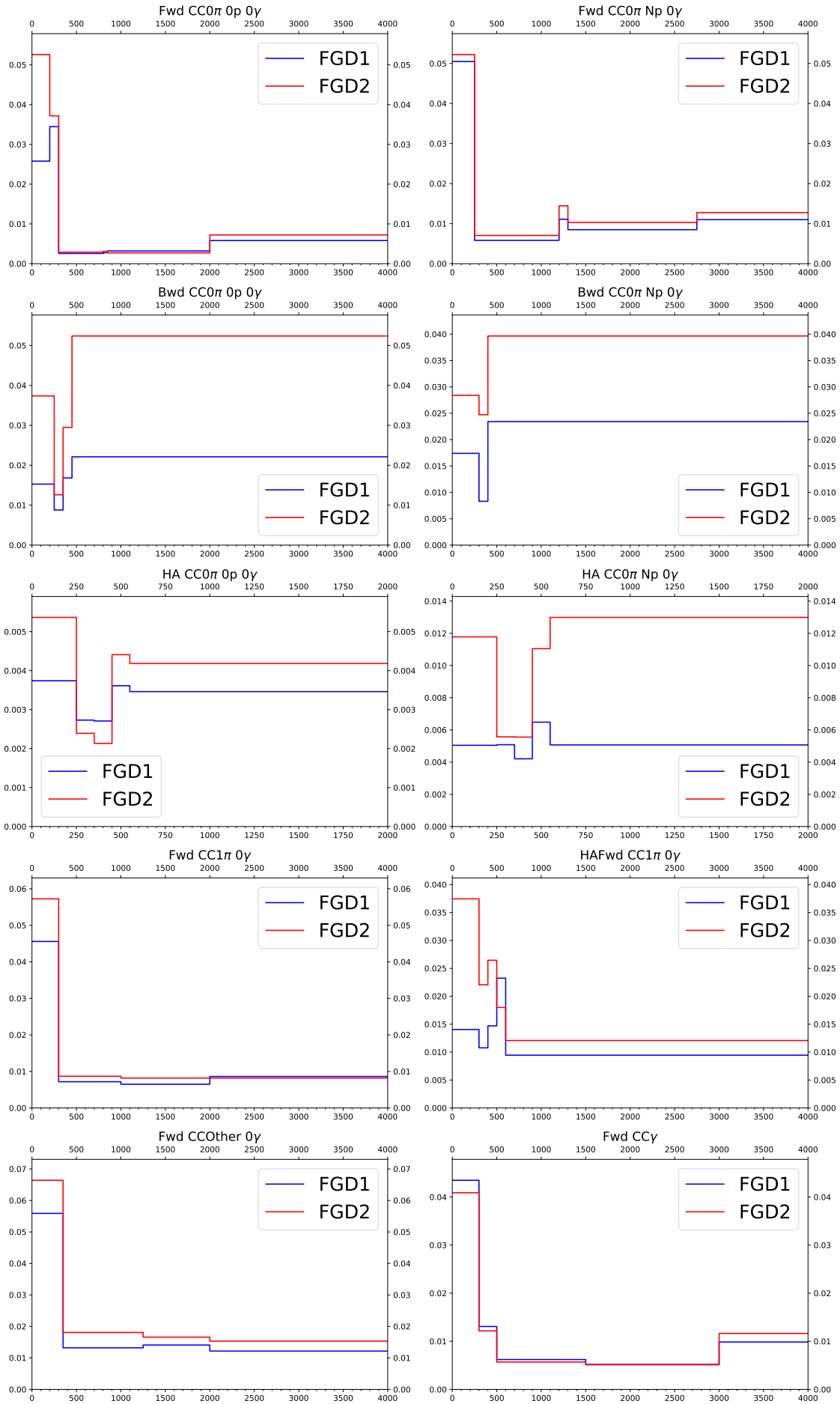

FIGURE C.10: The relative error caused by TPC PID, evaluated using highland2 propagation and parameters described before, as a function of muon $\cos\theta$ in different samples. The blue solid line stands for FGD1, and red line for FGD2.

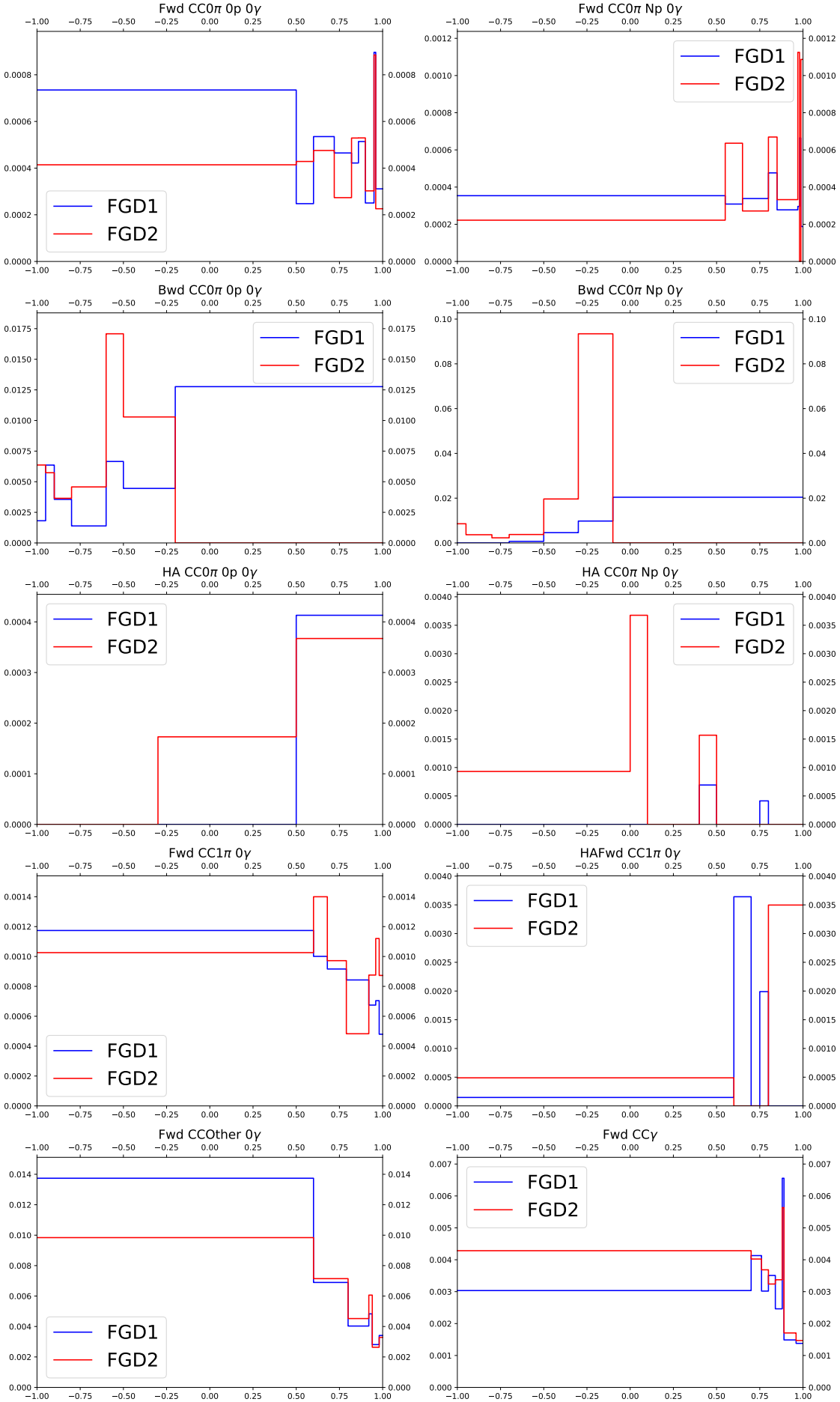

FIGURE C.11: The relative error caused by momentum resolution, evaluated using highland2 propagation and parameters described before, as a function of muon $\cos\theta$ in different samples. The blue solid line stands for FGD1, and red line for FGD2.

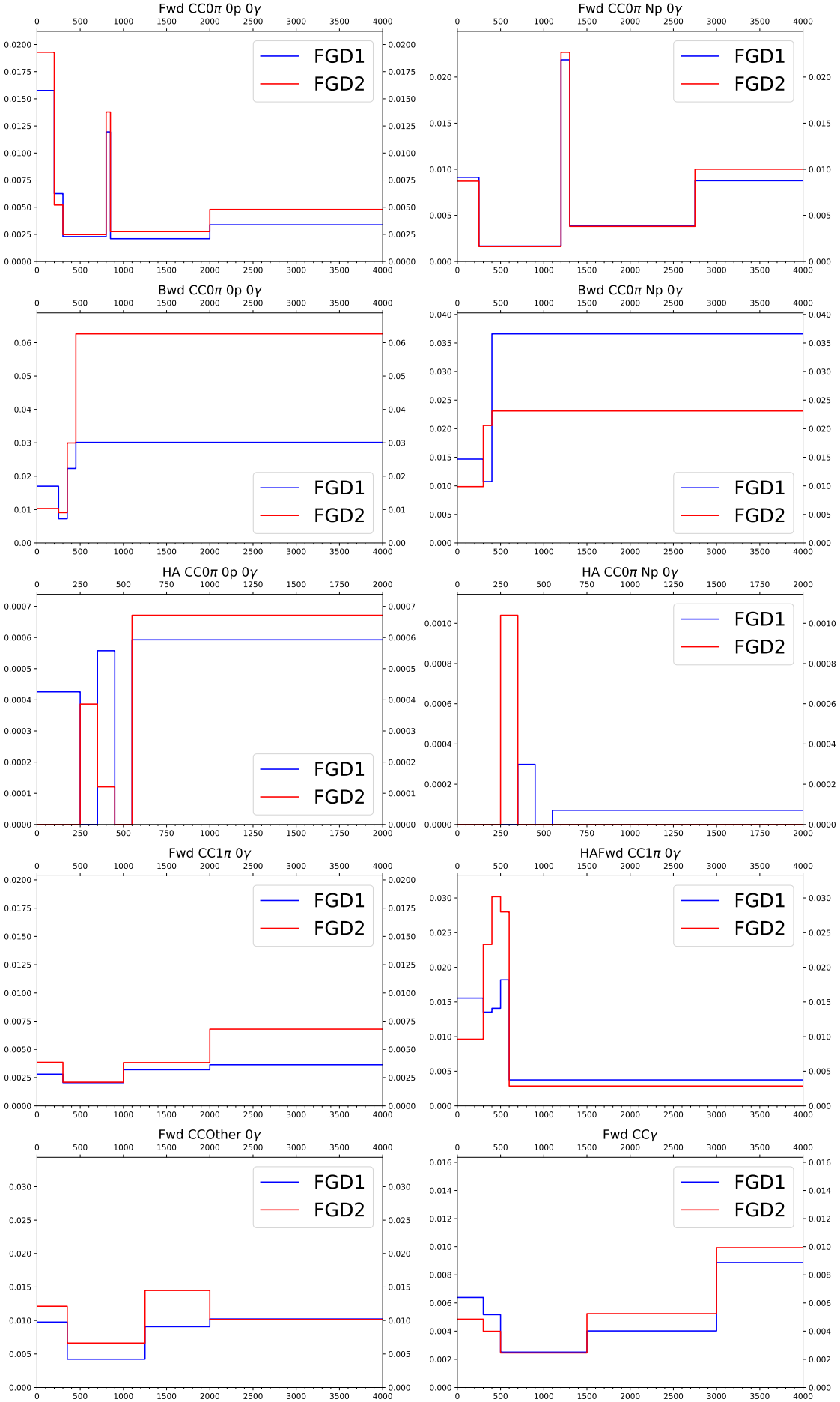

FIGURE C.12: The relative error caused by momentum resolution, evaluated using highland2 propagation and parameters described before, as a function of muon $\cos\theta$ in different samples. The blue solid line stands for FGD1, and red line for FGD2.

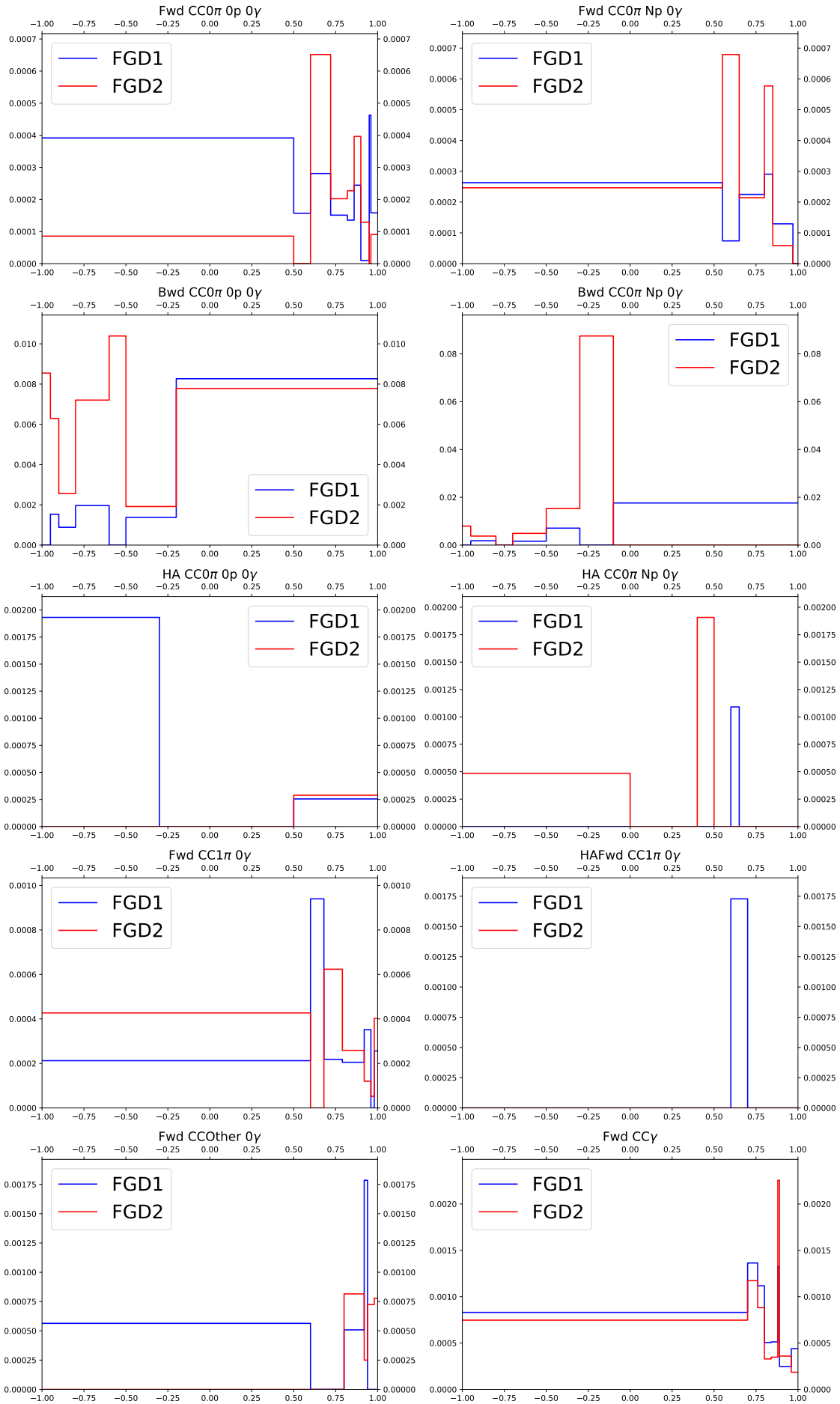

FIGURE C.13: The relative error caused by momentum scale, evaluated using highland2 propagation and parameters described before, as a function of muon $\cos\theta$ in different samples. The blue solid line stands for FGD1, and red line for FGD2.

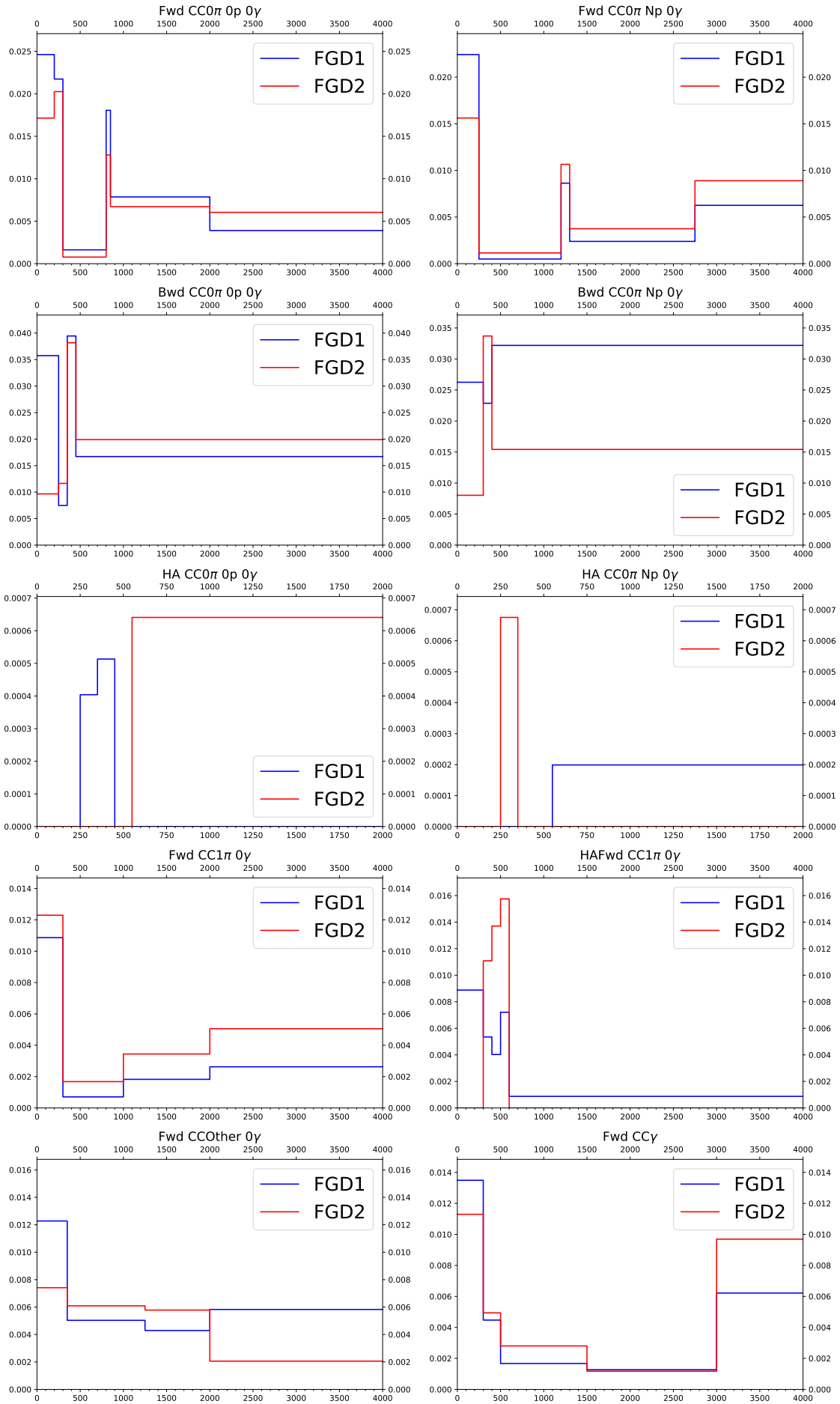

FIGURE C.14: The relative error caused by momentum scale, evaluated using highland2 propagation and parameters described before, as a function of muon $\cos\theta$ in different samples. The blue solid line stands for FGD1, and red line for FGD2.

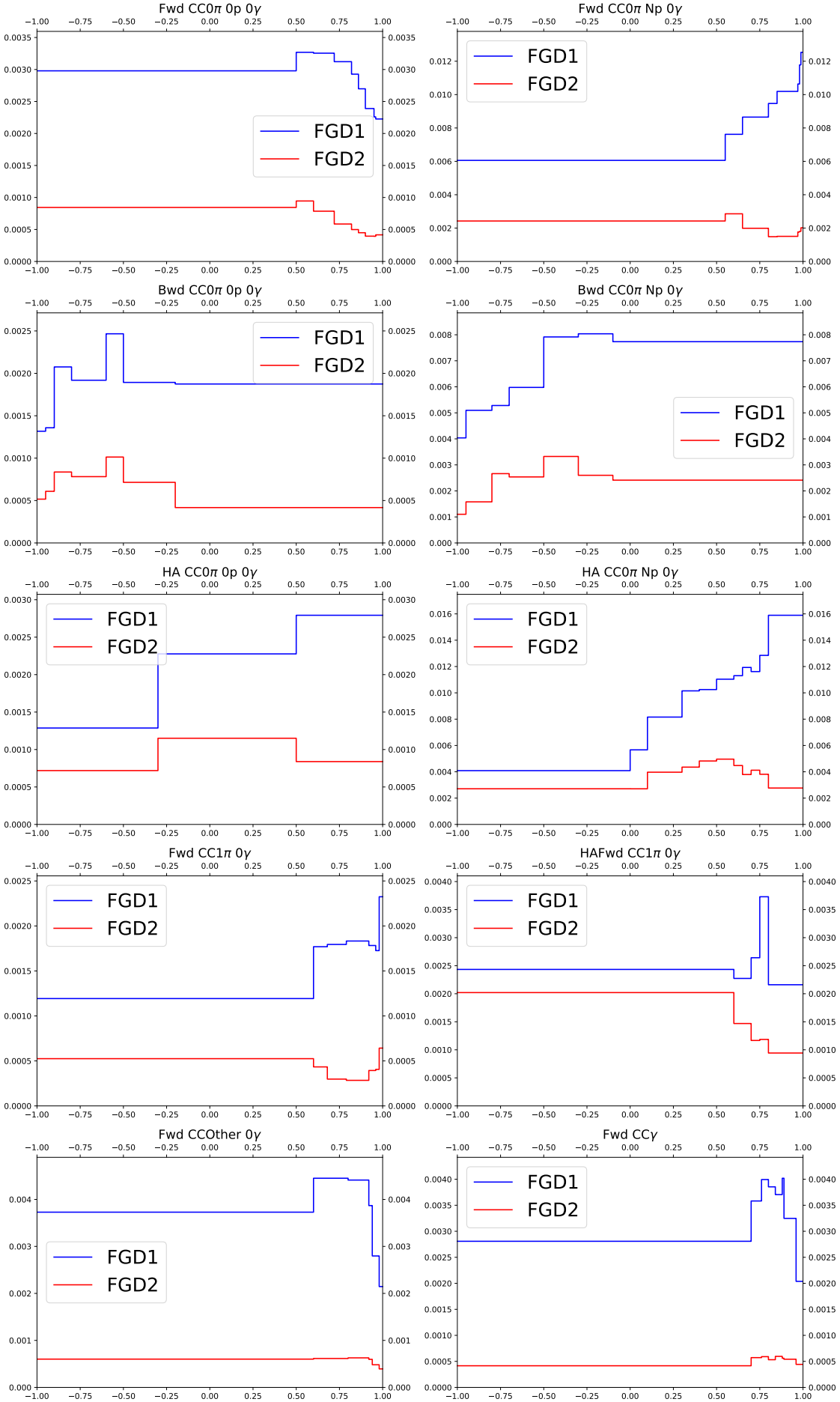

FIGURE C.15: The relative error caused by FGD hybrid tracking, evaluated using highland2 propagation and parameters described before, as a function of muon $\cos\theta$ in different samples. The blue solid line stands for FGD1, and red line for FGD2.

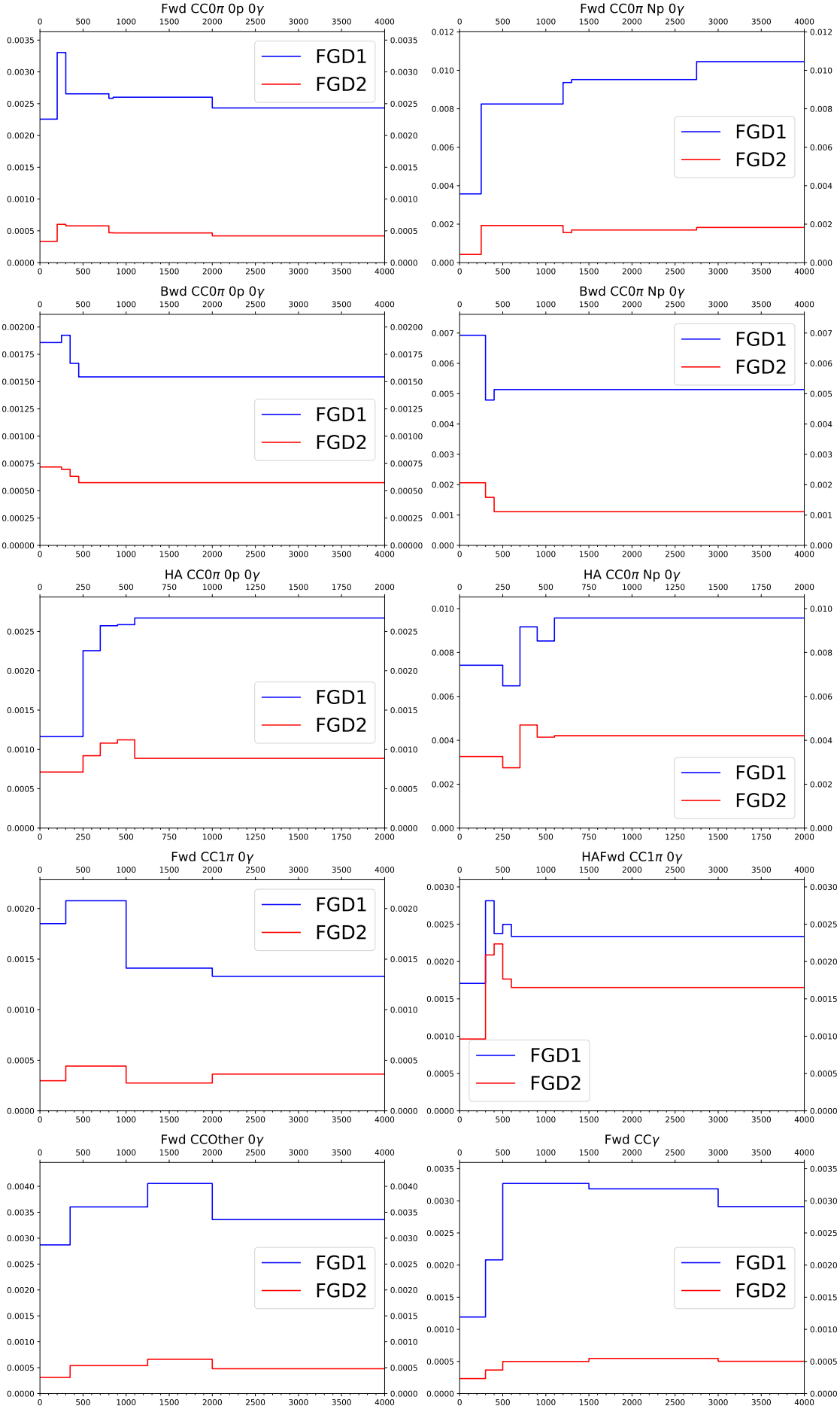

FIGURE C.16: The relative error caused by FGD hybrid tracking, evaluated using highland2 propagation and parameters described before, as a function of muon $\cos\theta$ in different samples. The blue solid line stands for FGD1, and red line for FGD2.

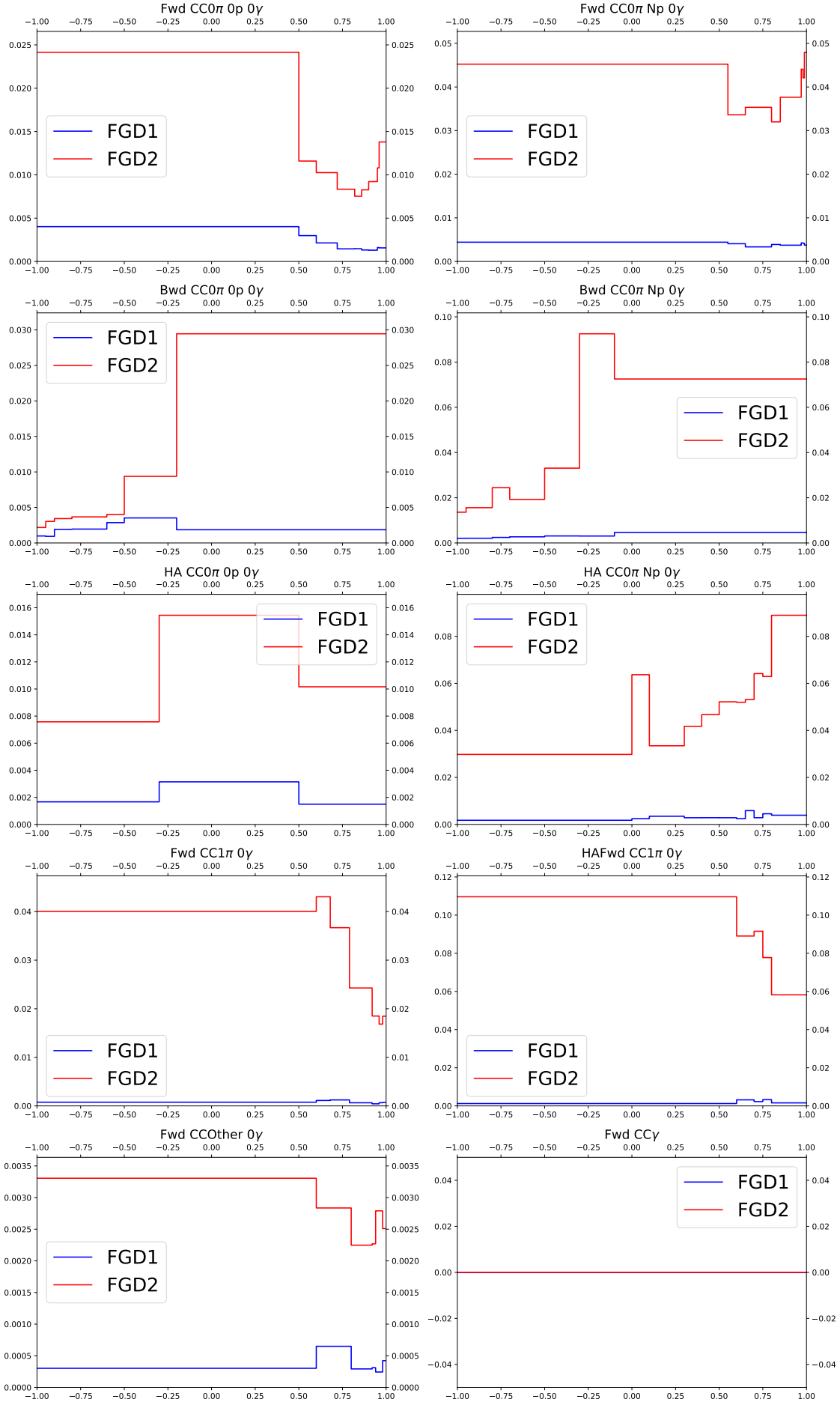

FIGURE C.17: The relative error caused by FGD PID, evaluated using highland2 propagation and parameters described before, as a function of muon $\cos\theta$ in different samples. The blue solid line stands for FGD1, and red line for FGD2.

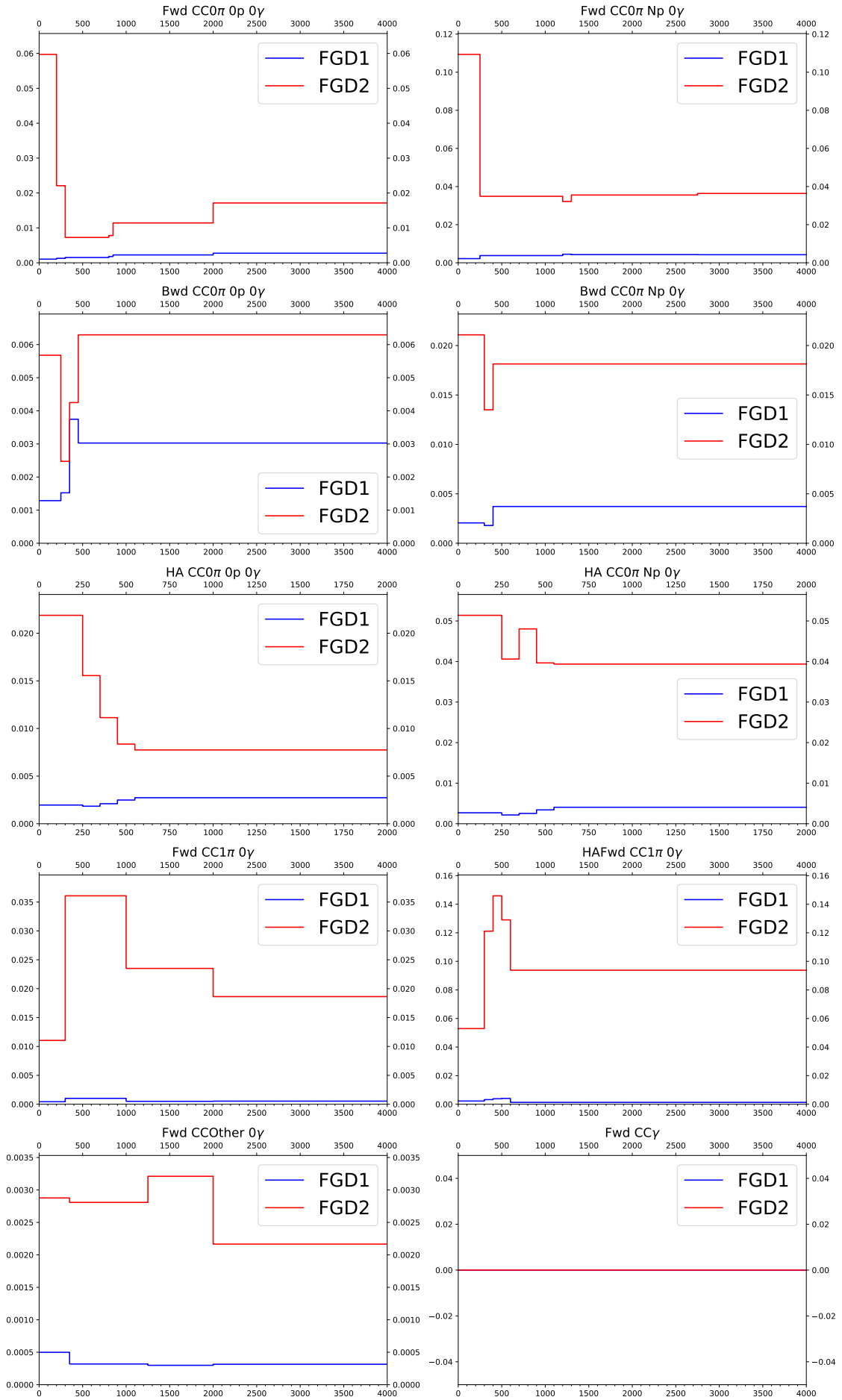

FIGURE C.18: The relative error caused by FGD PID, evaluated using highland2 propagation and parameters described before, as a function of muon $\cos\theta$ in different samples. The blue solid line stands for FGD1, and red line for FGD2.

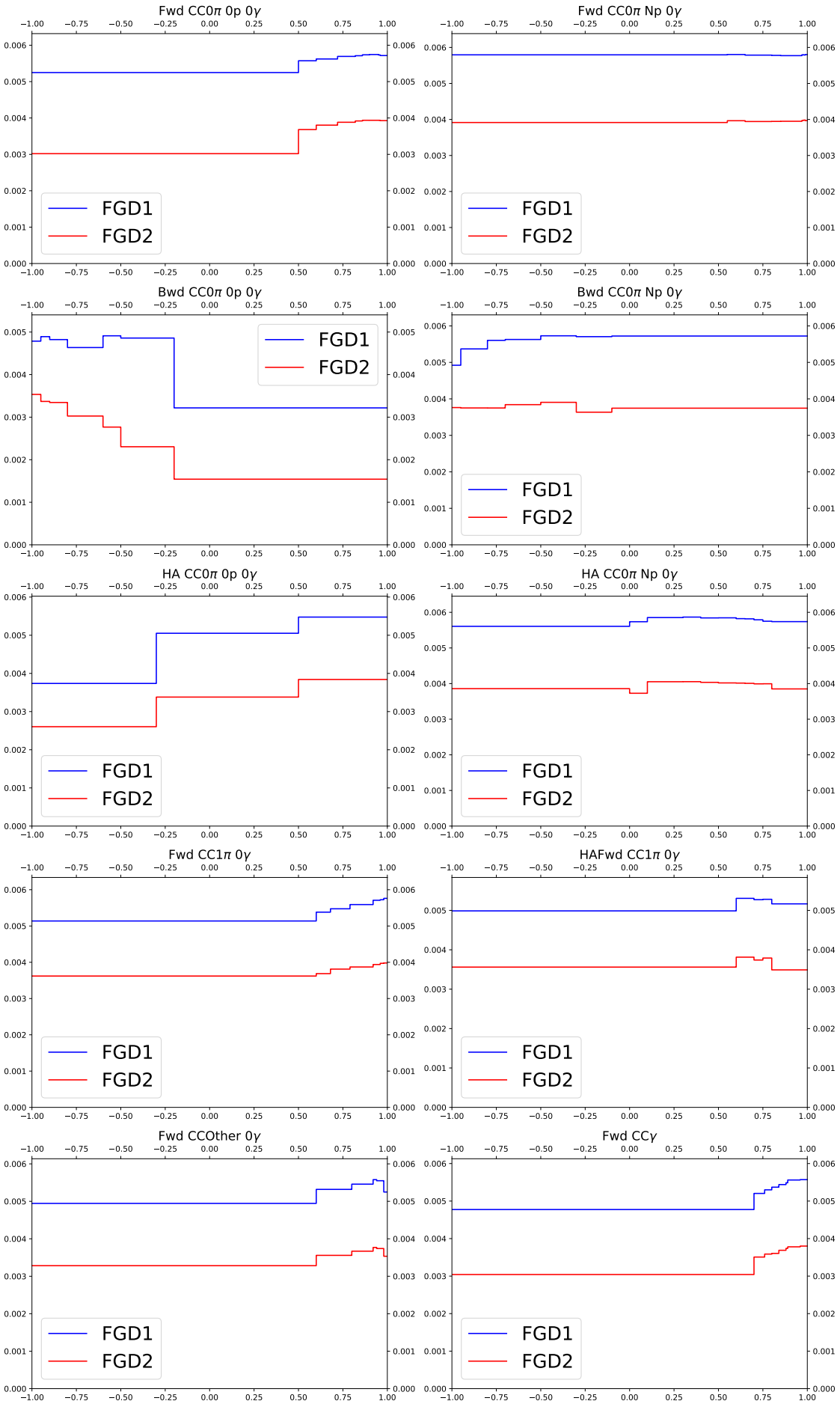

FIGURE C.19: The relative error caused by FGD mass, evaluated using highland2 propagation and parameters described before, as a function of muon $\cos\theta$ in different samples. The blue solid line stands for FGD1, and red line for FGD2.

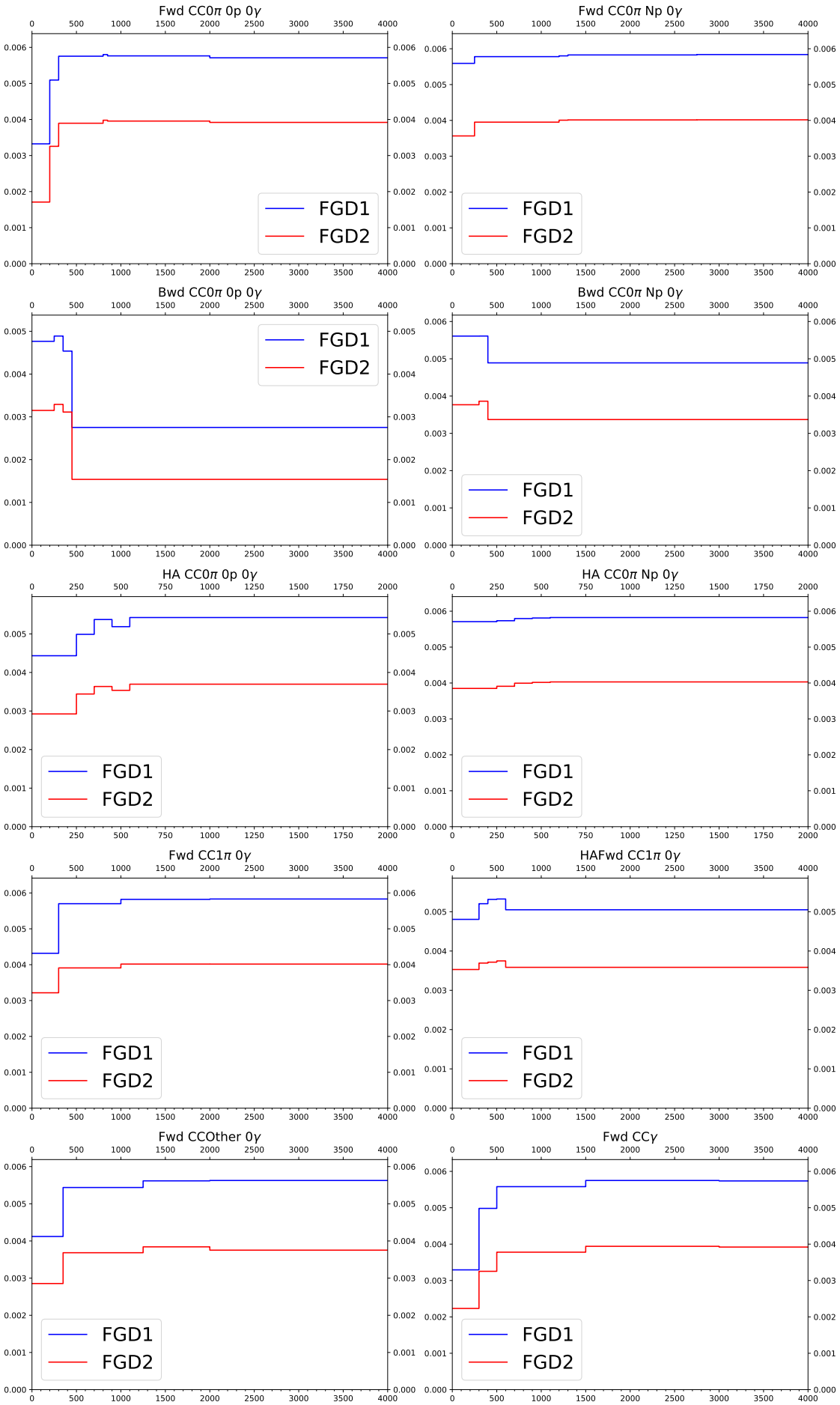

FIGURE C.20: The relative error caused by FGD mass, evaluated using highland2 propagation and parameters described before, as a function of muon $\cos\theta$ in different samples. The blue solid line stands for FGD1, and red line for FGD2.

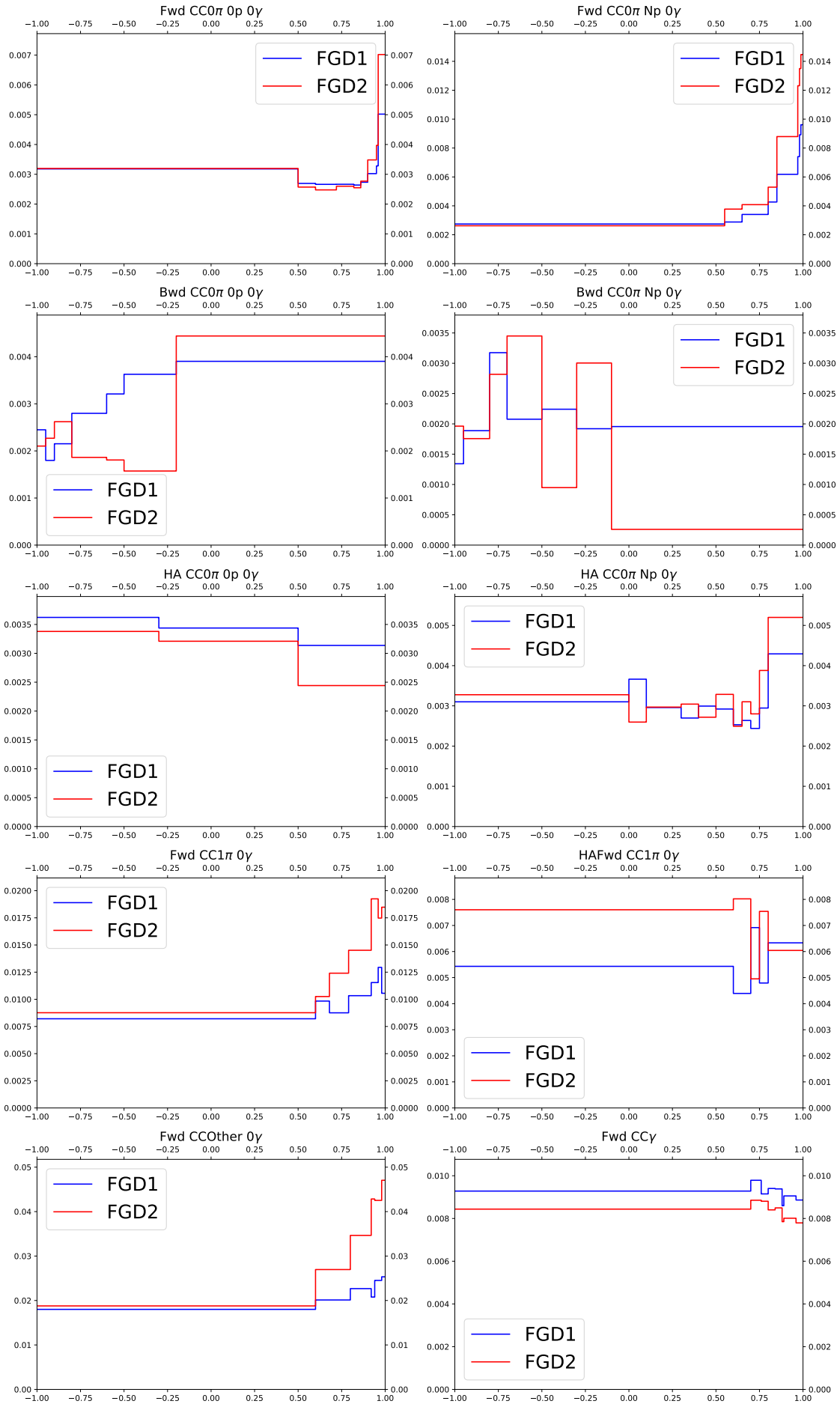

FIGURE C.21: The relative error caused by ECal tracking efficiency, evaluated using highland2 propagation and parameters described before, as a function of muon $\cos\theta$ in different samples. The blue solid line stands for FGD1, and red line for FGD2.

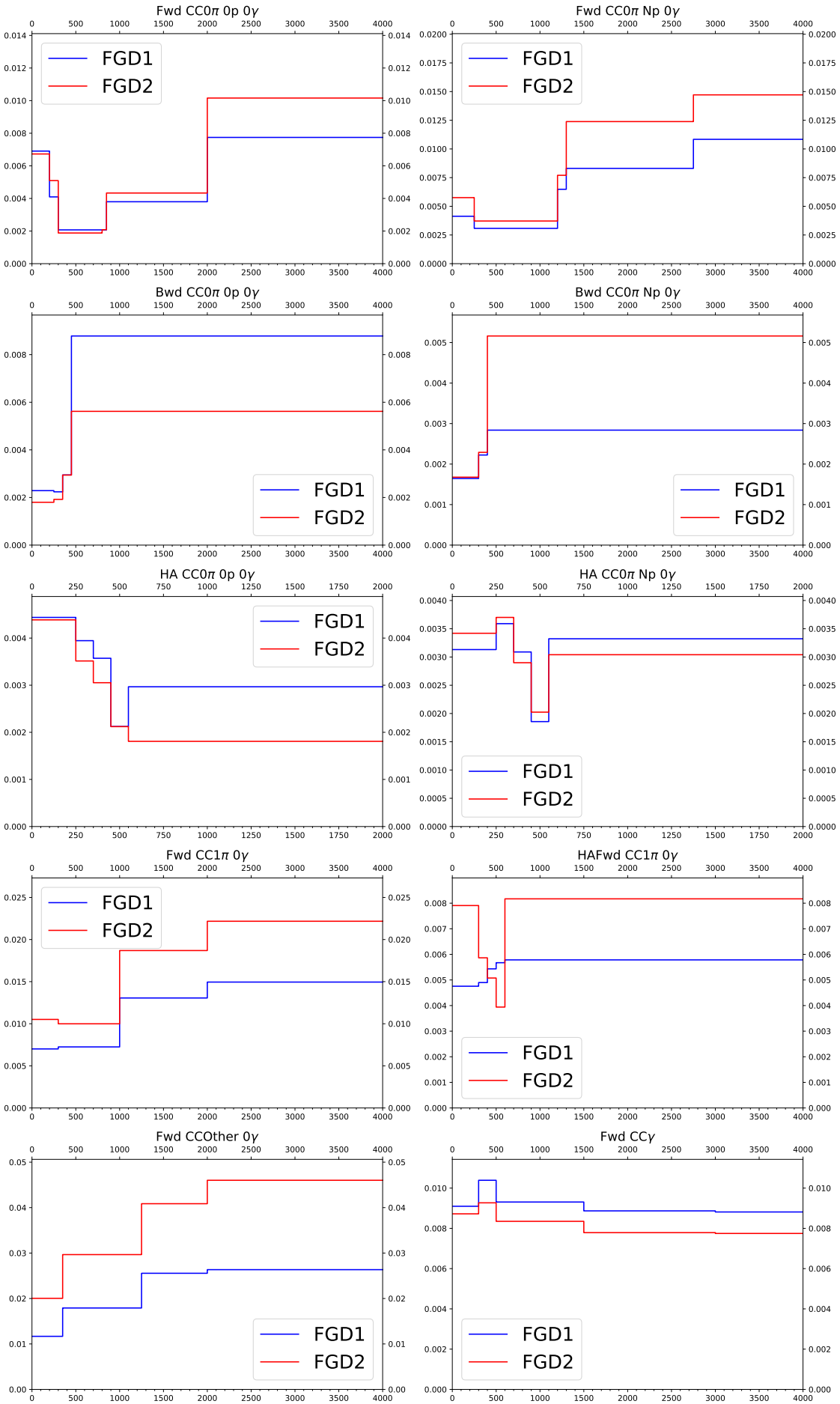

FIGURE C.22: The relative error caused by ECal tracking efficiency, evaluated using highland2 propagation and parameters described before, as a function of muon $\cos\theta$ in different samples. The blue solid line stands for FGD1, and red line for FGD2.

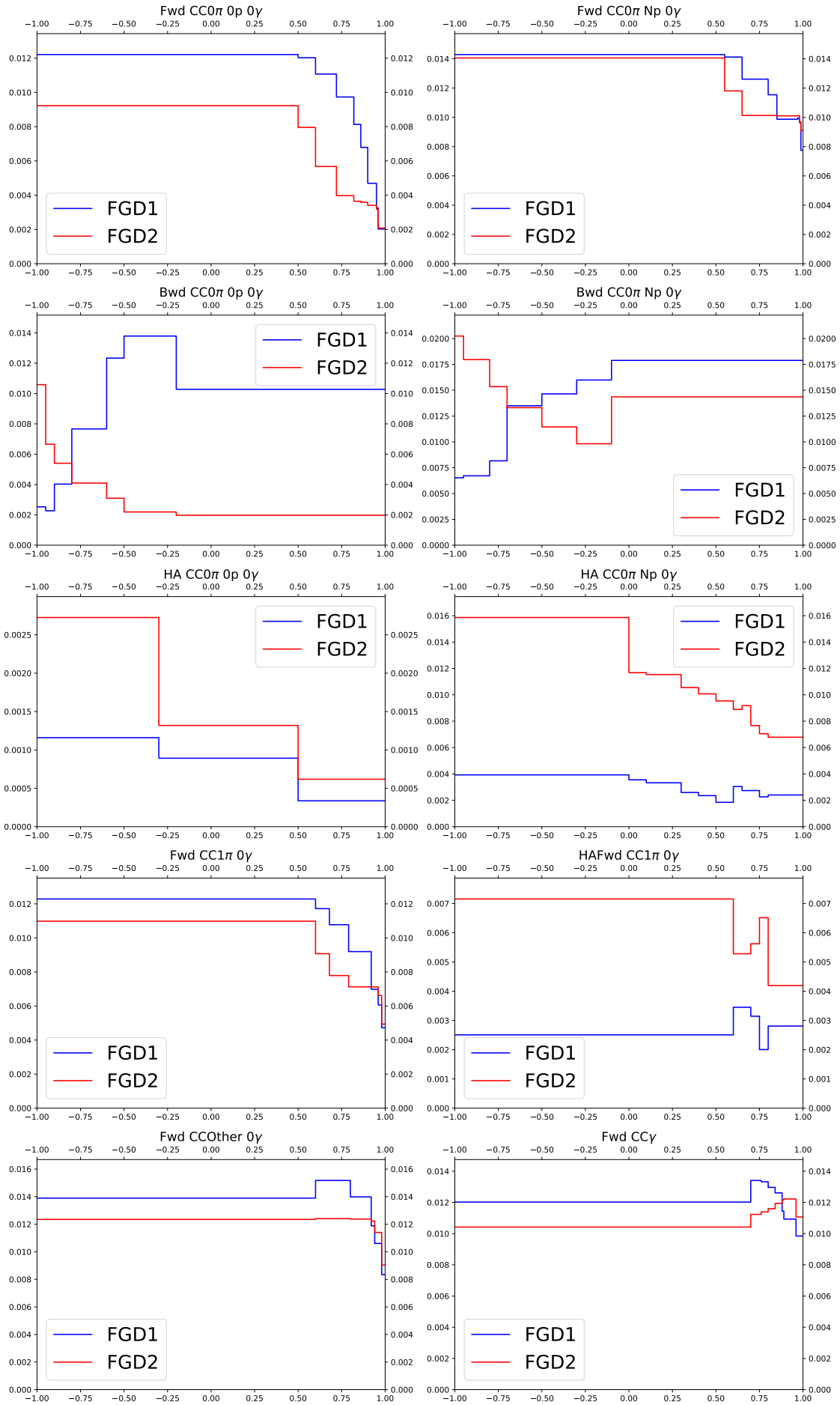

FIGURE C.23: The relative error caused by TPC-ECal matching efficiency, evaluated using highland2 propagation and parameters described before, as a function of muon $\cos\theta$ in different samples. The blue solid line stands for FGD1, and red line for FGD2.

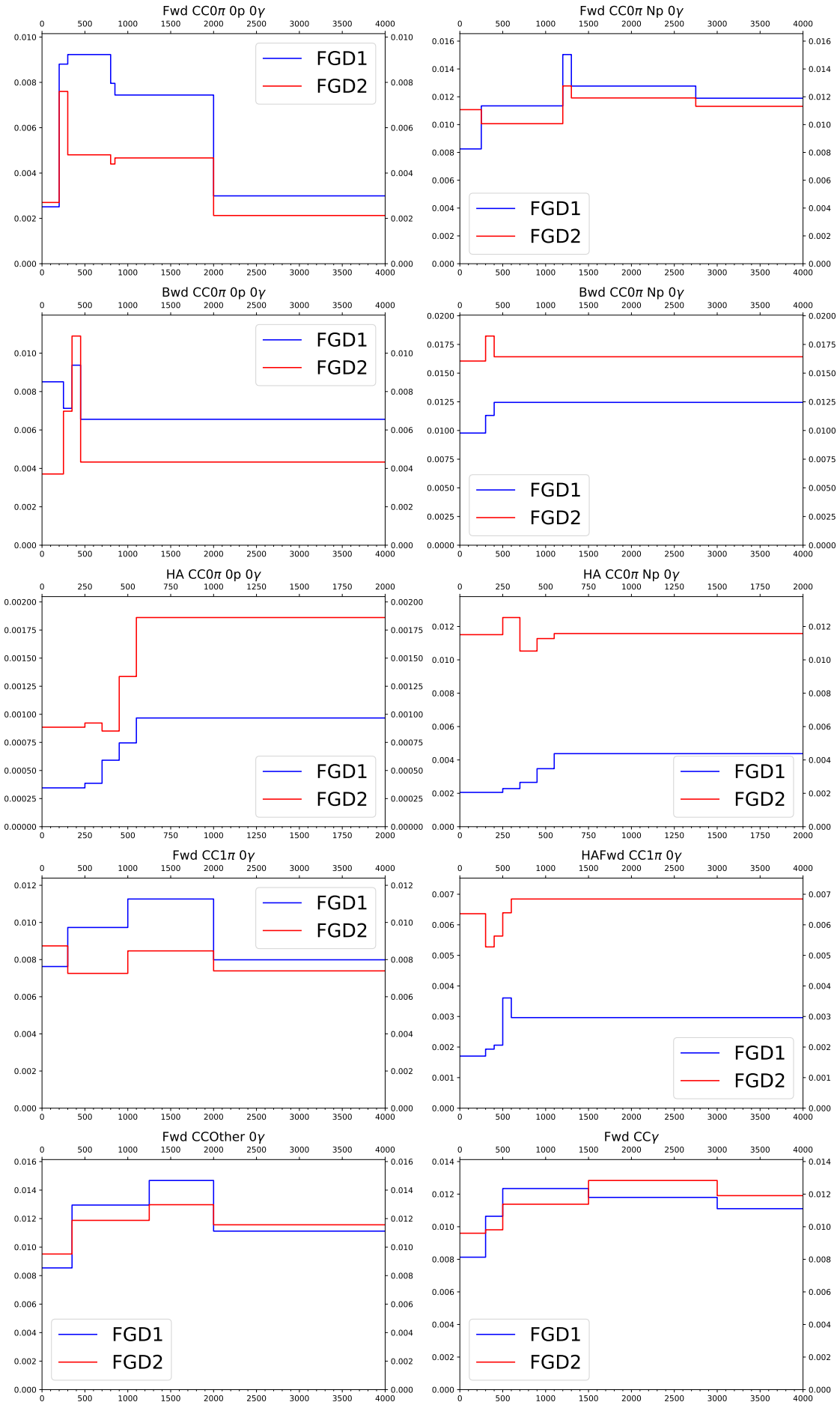

FIGURE C.24: The relative error caused by TPC-ECal matching efficiency, evaluated using highland2 propagation and parameters described before, as a function of muon $\cos\theta$ in different samples. The blue solid line stands for FGD1, and red line for FGD2.

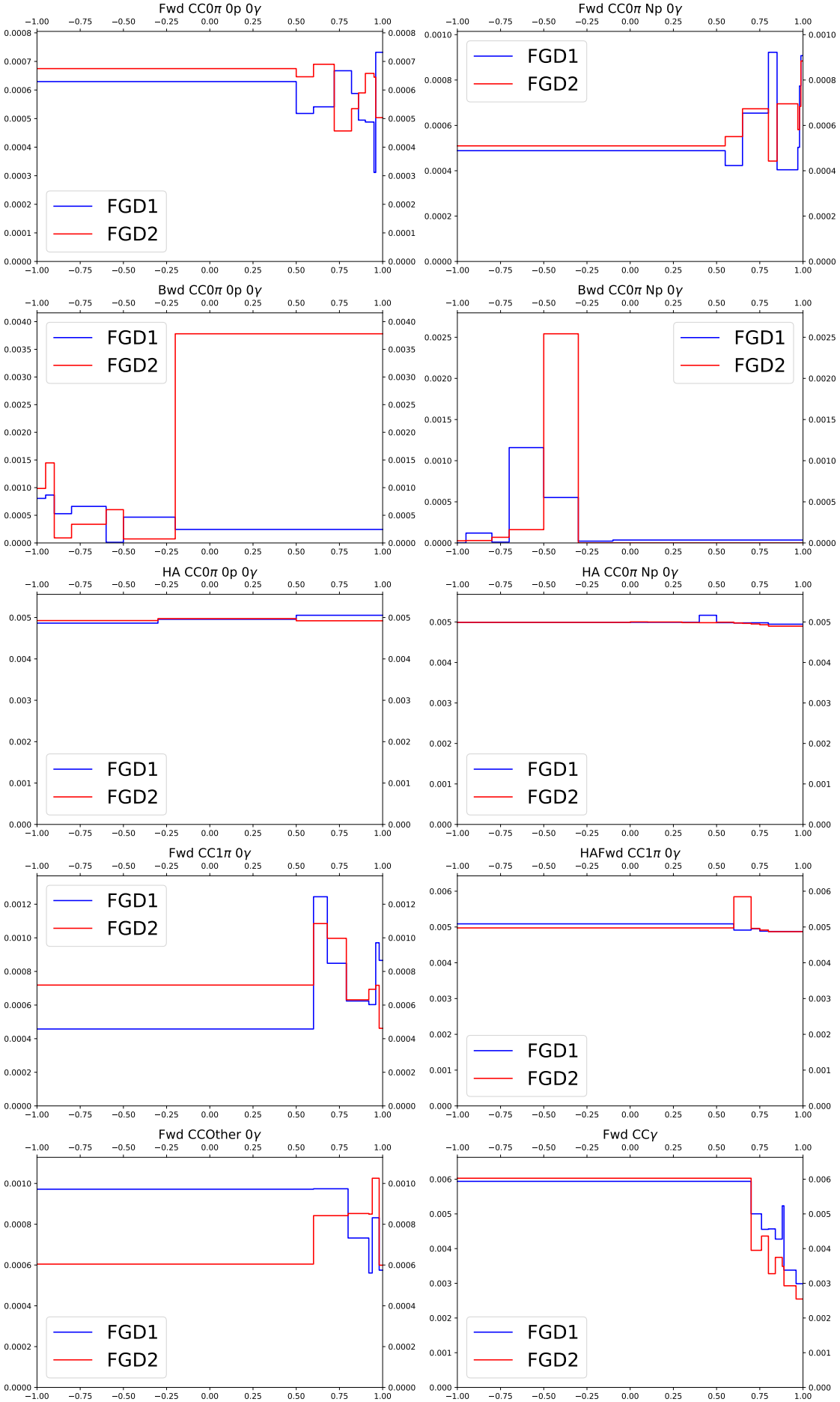

FIGURE C.25: The relative error caused by ECal PID, evaluated using highland2 propagation and parameters described before, as a function of muon $\cos\theta$ in different samples. The blue solid line stands for FGD1, and red line for FGD2.

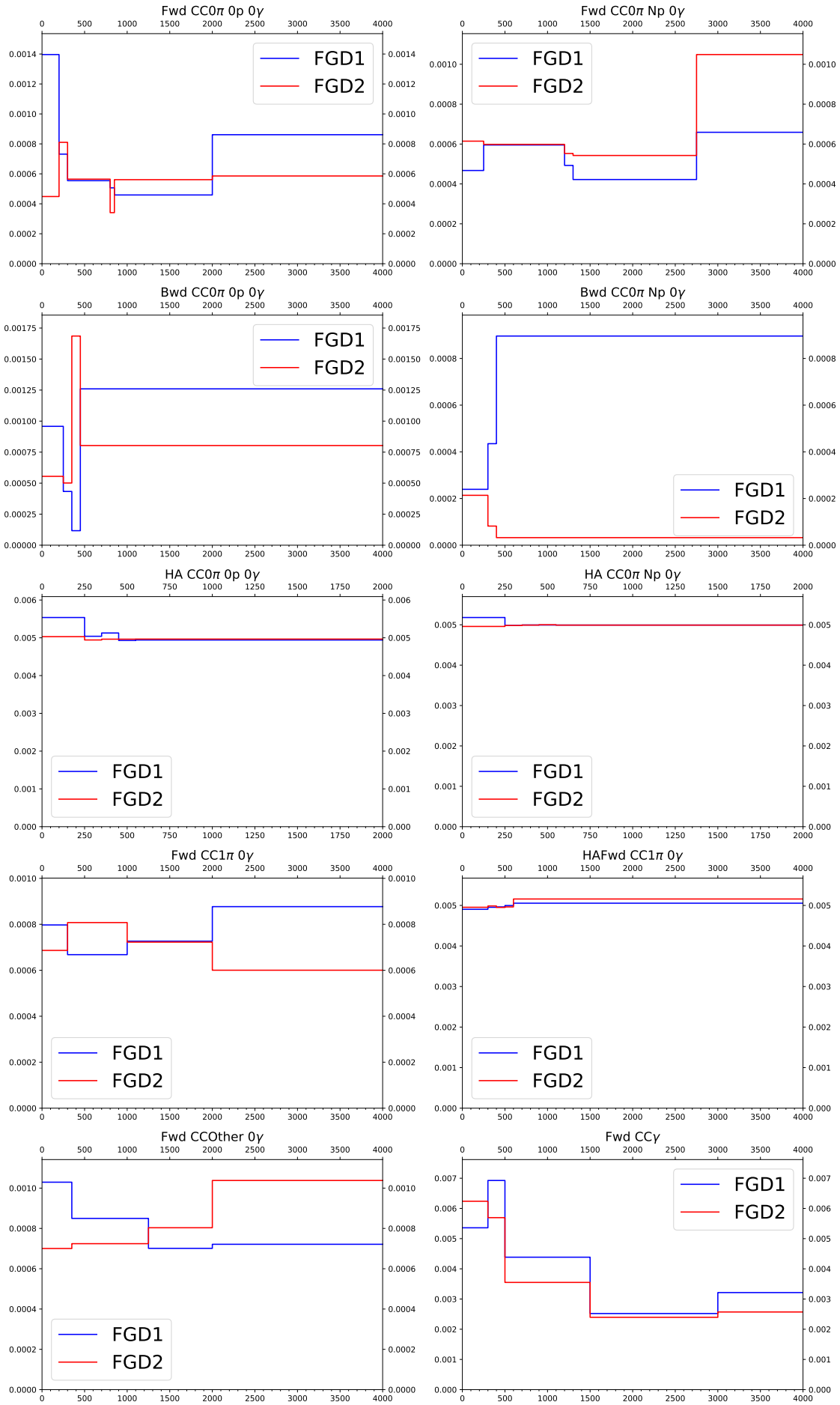

FIGURE C.26: The relative error caused by ECal PID, evaluated using highland2 propagation and parameters described before, as a function of muon $\cos\theta$ in different samples. The blue solid line stands for FGD1, and red line for FGD2.

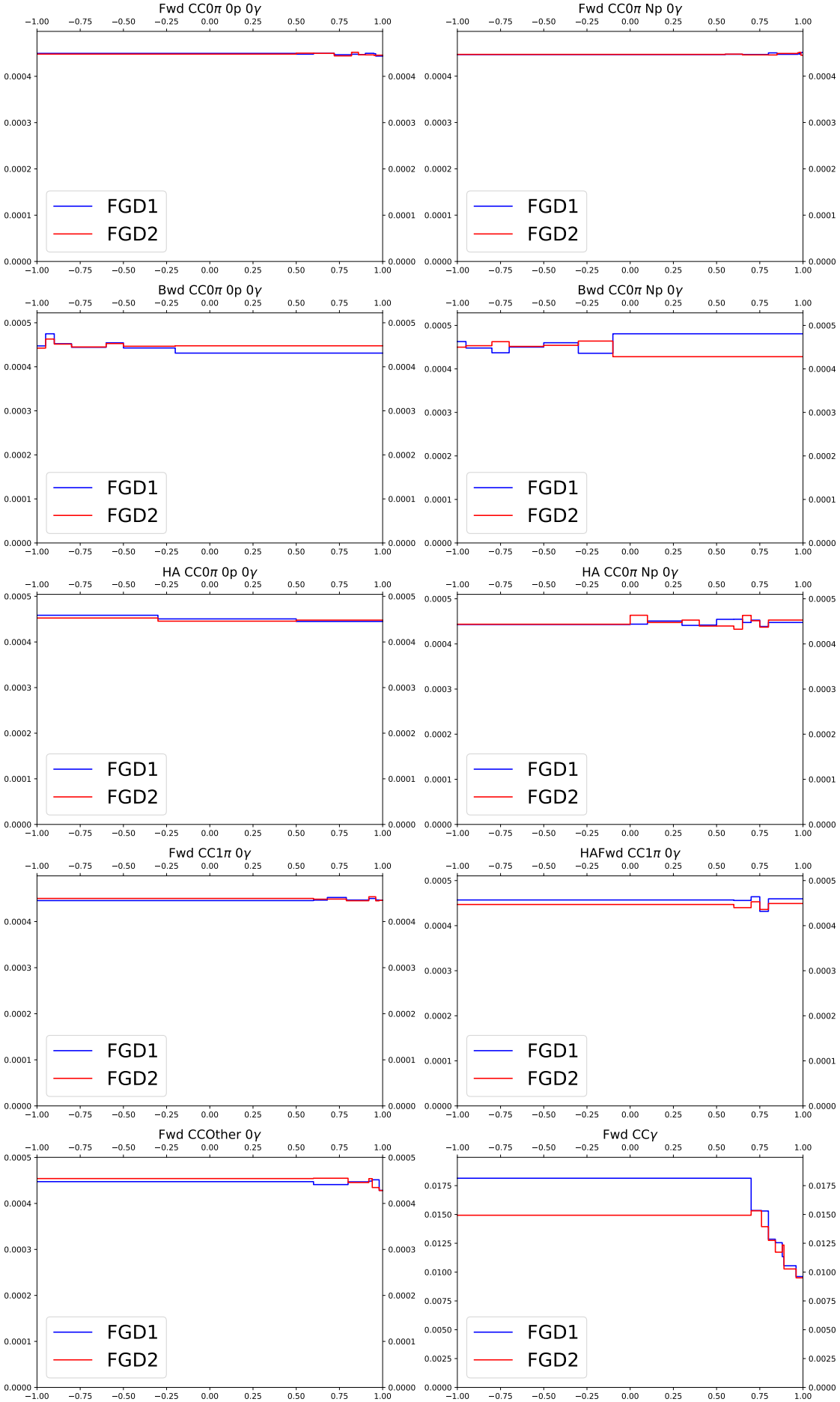

FIGURE C.27: The relative error caused by photon pile-up, evaluated using highland2 propagation and parameters described before, as a function of muon $\cos\theta$ in different samples. The blue solid line stands for FGD1, and red line for FGD2.

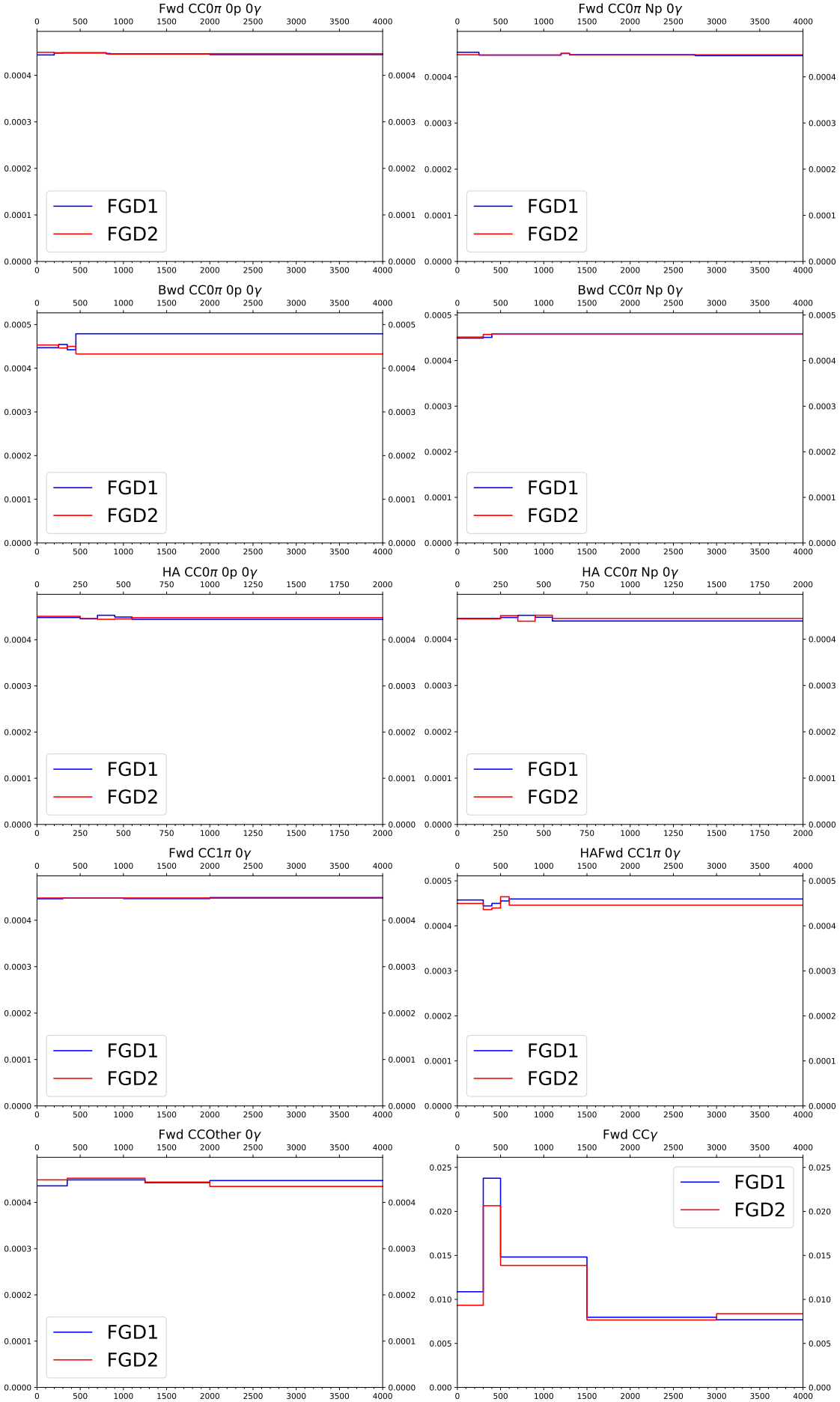

FIGURE C.28: The relative error caused by ECal photon pile-up, evaluated using highland2 propagation and parameters described before, as a function of muon $\cos\theta$ in different samples. The blue solid line stands for FGD1, and red line for FGD2.

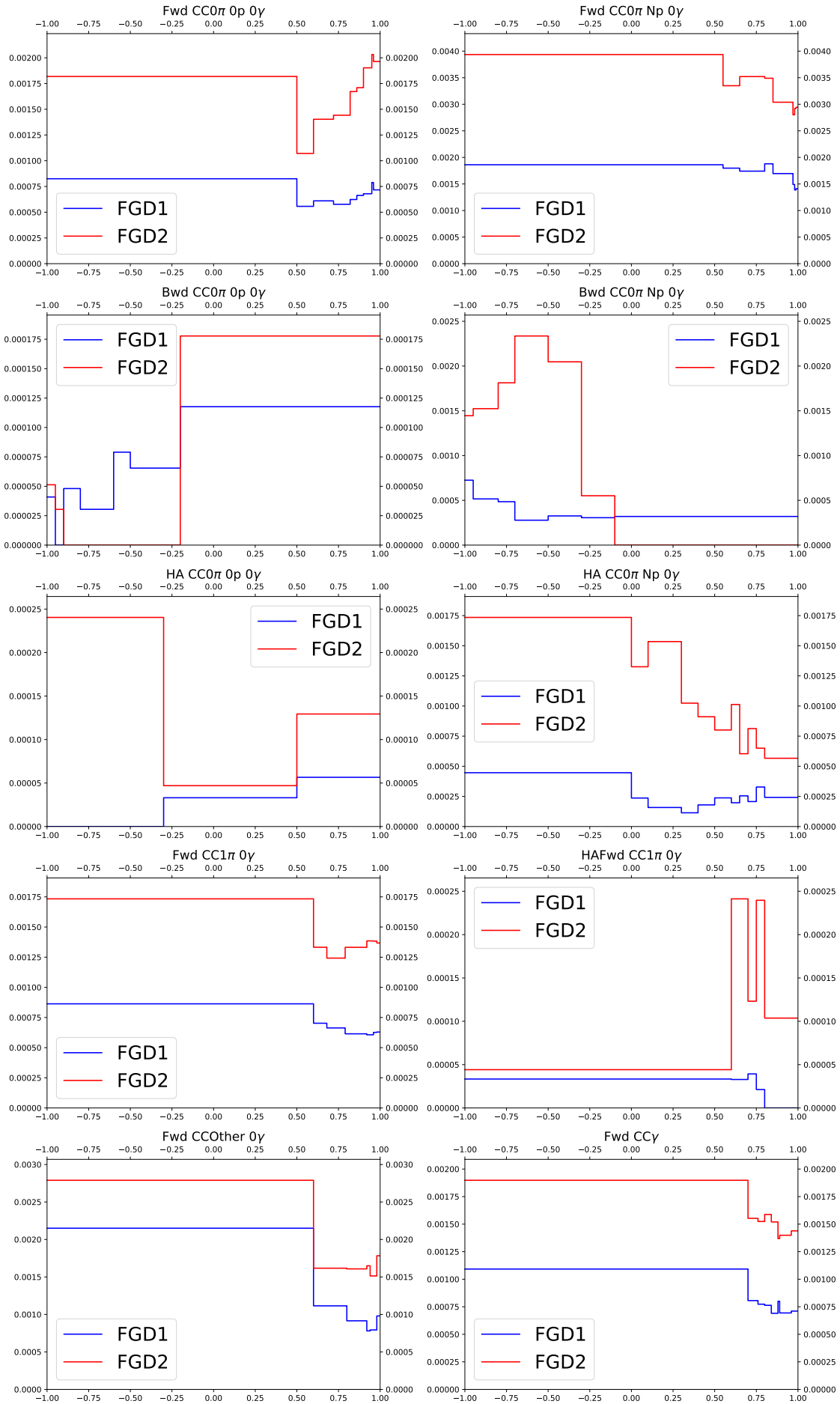

FIGURE C.29: The relative error caused by TPC-FGD matching efficiency, evaluated using highland2 propagation and parameters described before, as a function of muon $\cos\theta$ in different samples. The blue solid line stands for FGD1, and red line for FGD2.

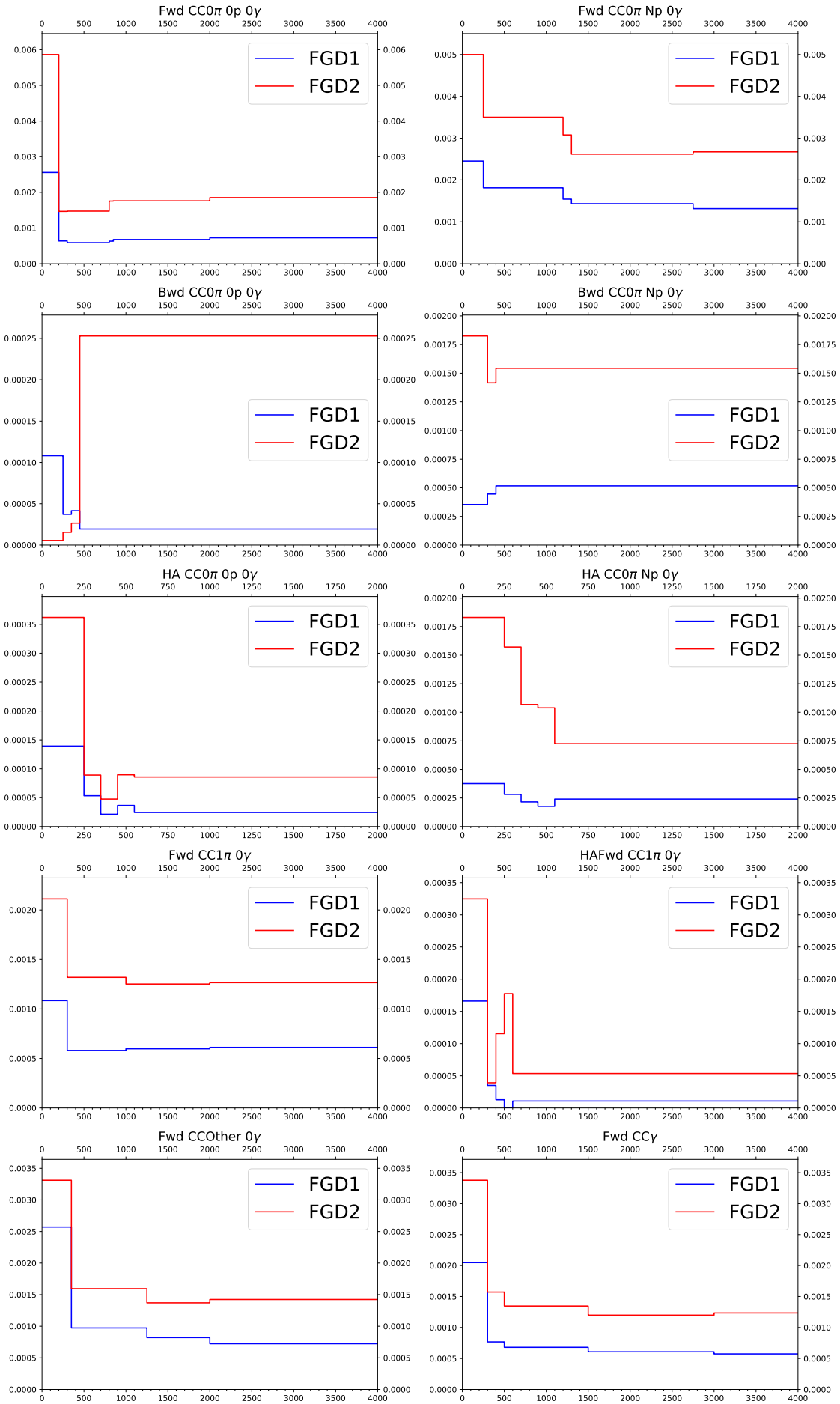

FIGURE C.30: The relative error caused by TPC-FGD matching efficiency, evaluated using highland2 propagation and parameters described before, as a function of muon $\cos\theta$ in different samples. The blue solid line stands for FGD1, and red line for FGD2.

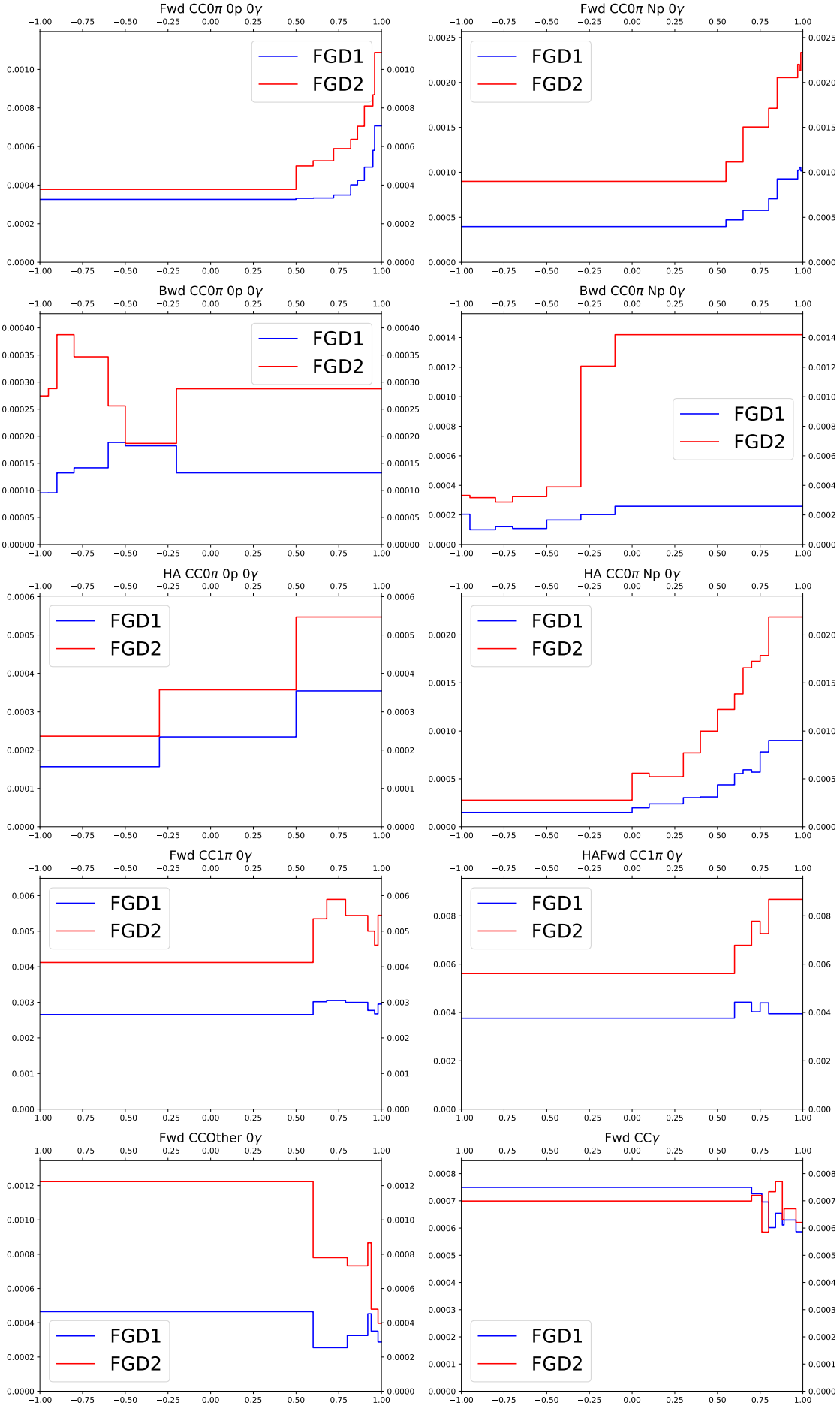

FIGURE C.31: The relative error caused by Michel electrons, evaluated using highland2 propagation and parameters described before, as a function of muon $\cos\theta$ in different samples. The blue solid line stands for FGD1, and red line for FGD2.

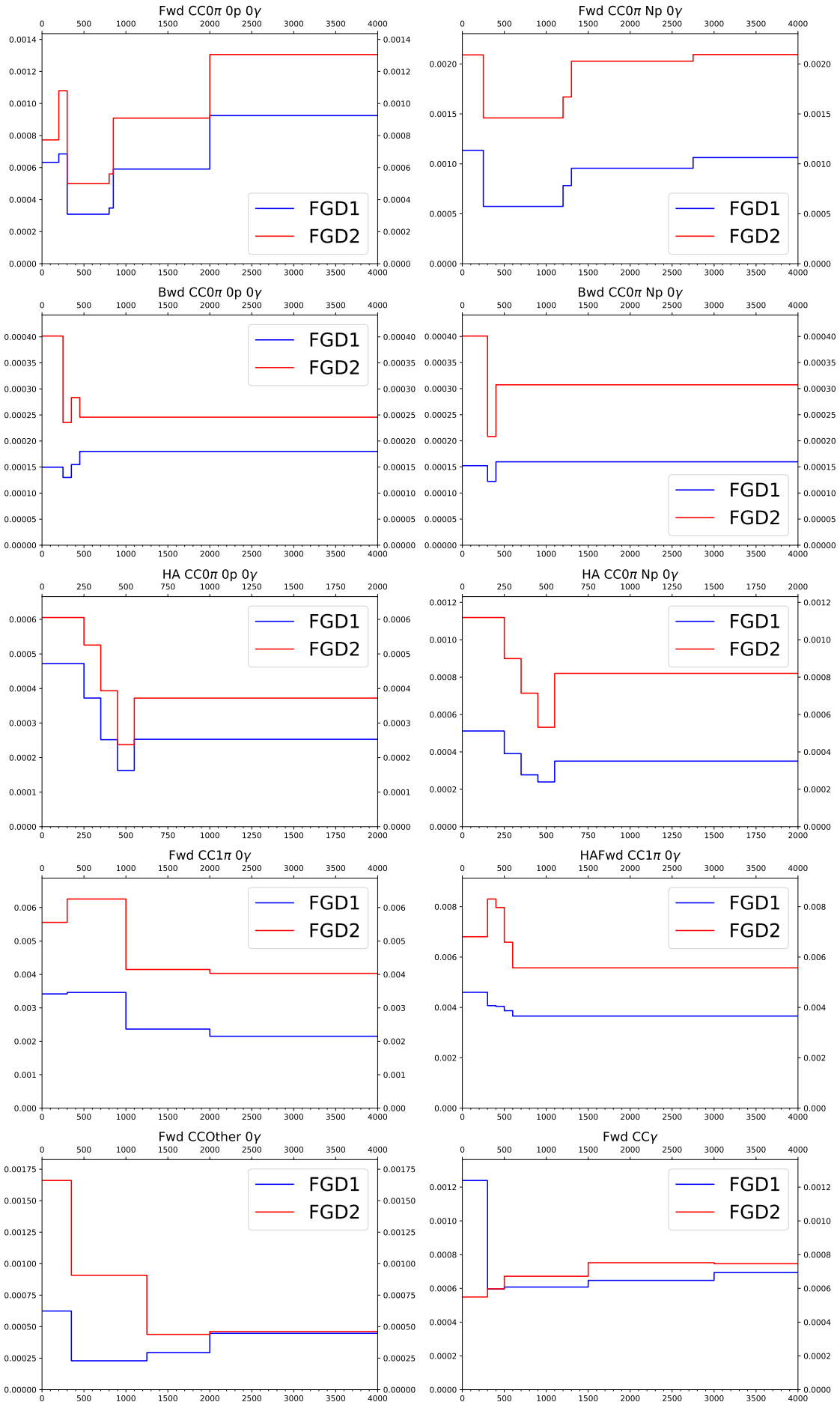

FIGURE C.32: The relative error caused by Michel electrons, evaluated using highland2 propagation and parameters described before, as a function of muon $\cos\theta$ in different samples. The blue solid line stands for FGD1, and red line for FGD2.

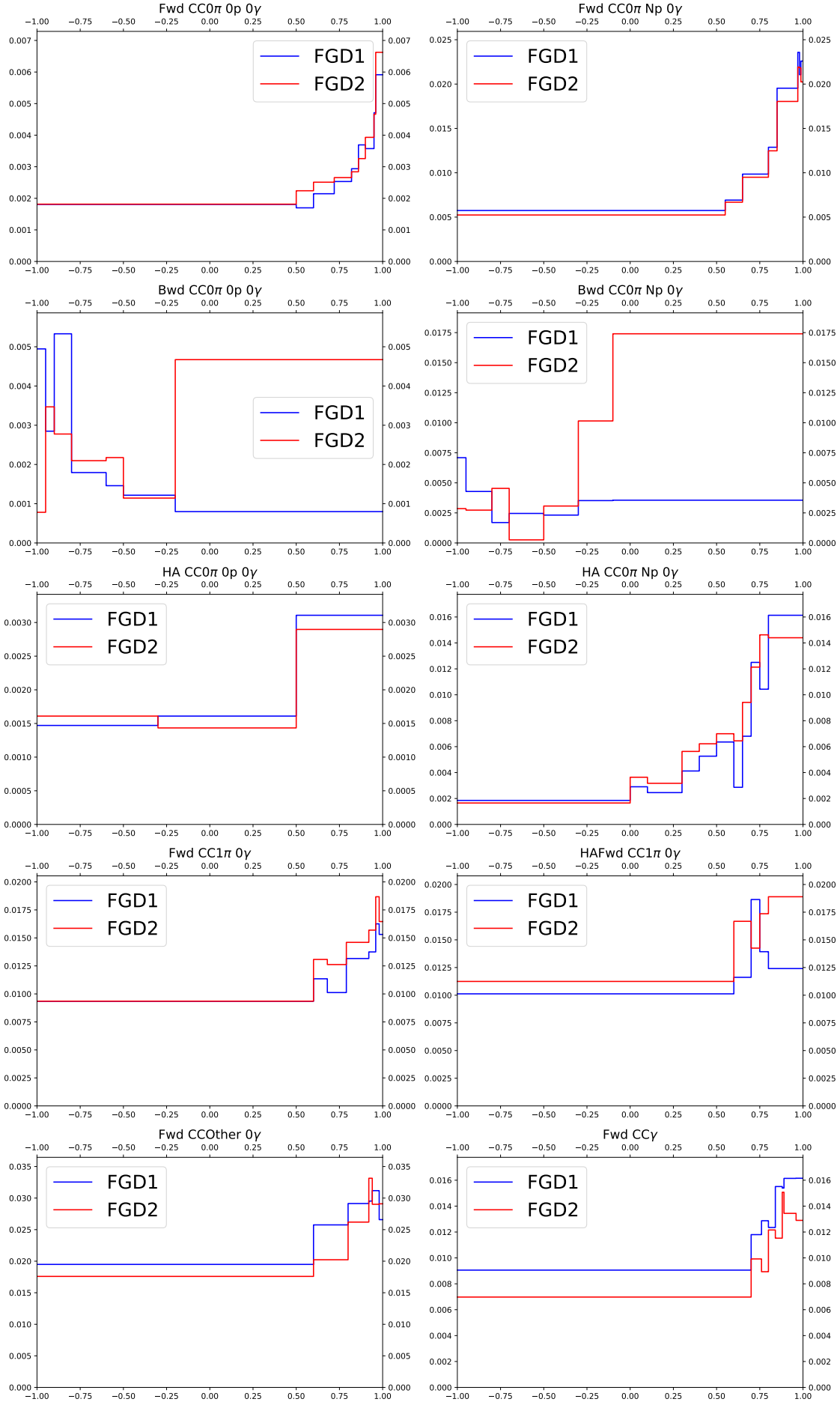

FIGURE C.33: The relative error caused by pion SI, evaluated using highland2 propagation and parameters described before, as a function of muon $\cos\theta$ in different samples. The blue solid line stands for FGD1, and red line for FGD2.

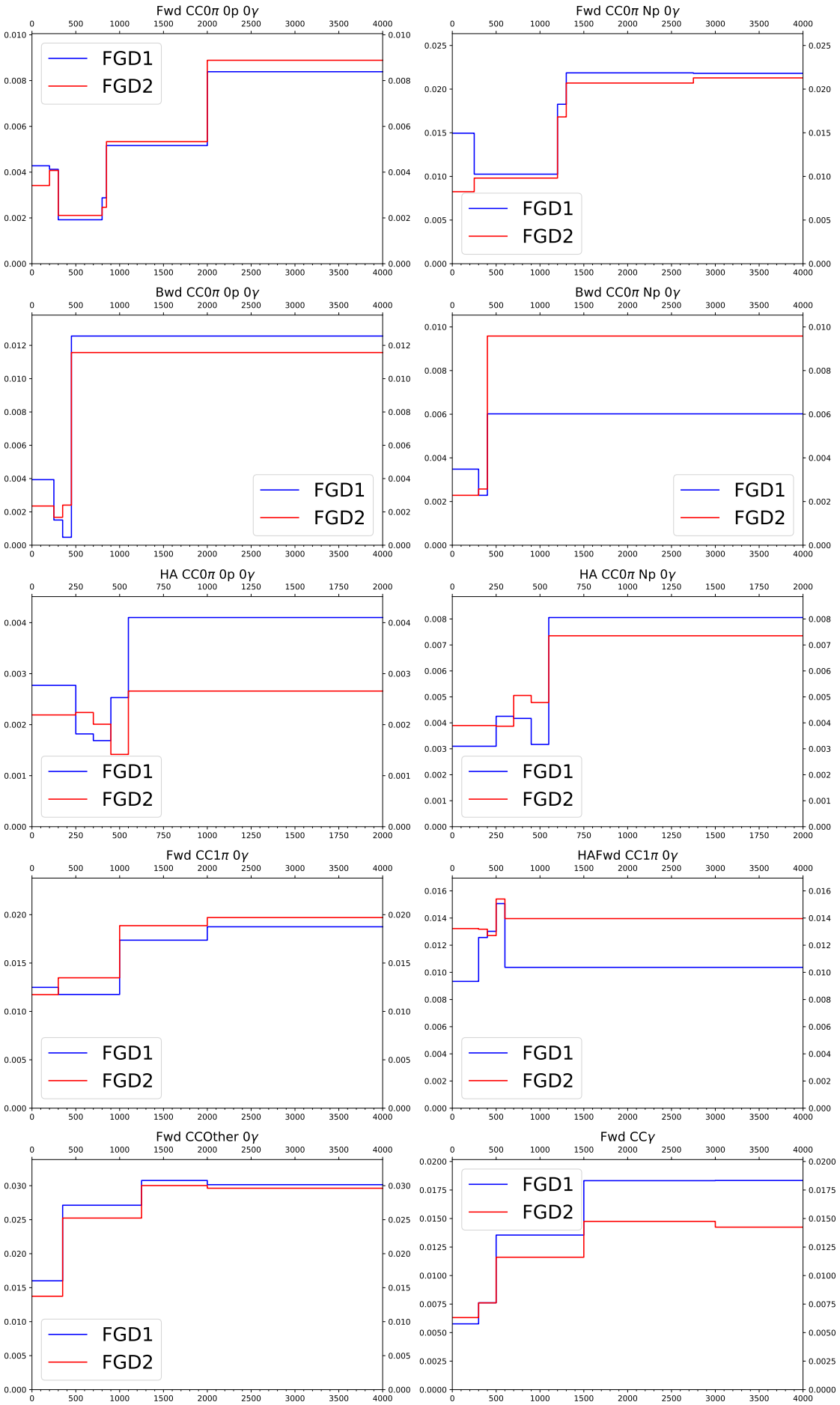

FIGURE C.34: The relative error caused by pion SI, evaluated using highland2 propagation and parameters described before, as a function of muon $\cos\theta$ in different samples. The blue solid line stands for FGD1, and red line for FGD2.

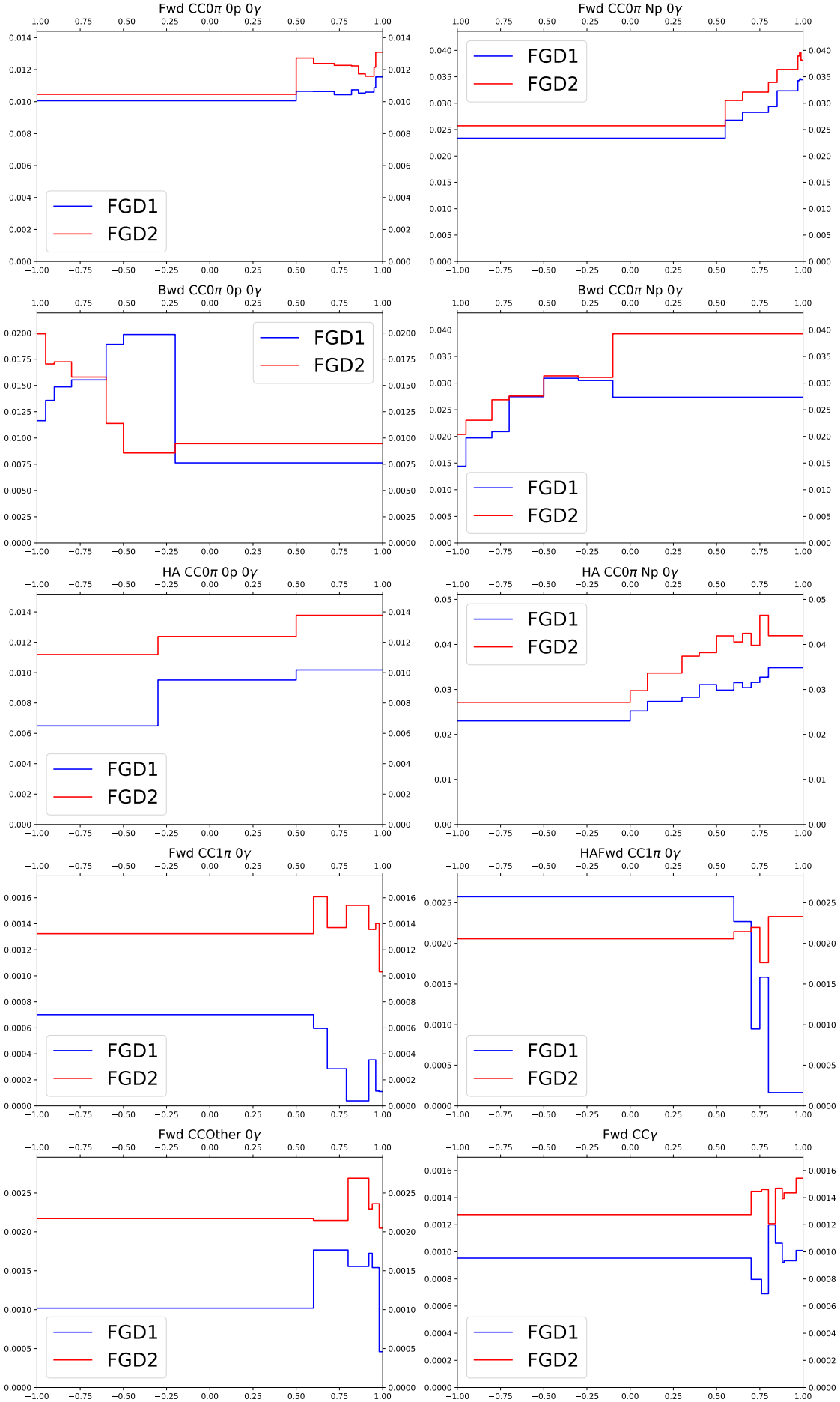

FIGURE C.35: The relative error caused by proton SI, evaluated using highland2 propagation and parameters described before, as a function of muon $\cos\theta$ in different samples. The blue solid line stands for FGD1, and red line for FGD2.

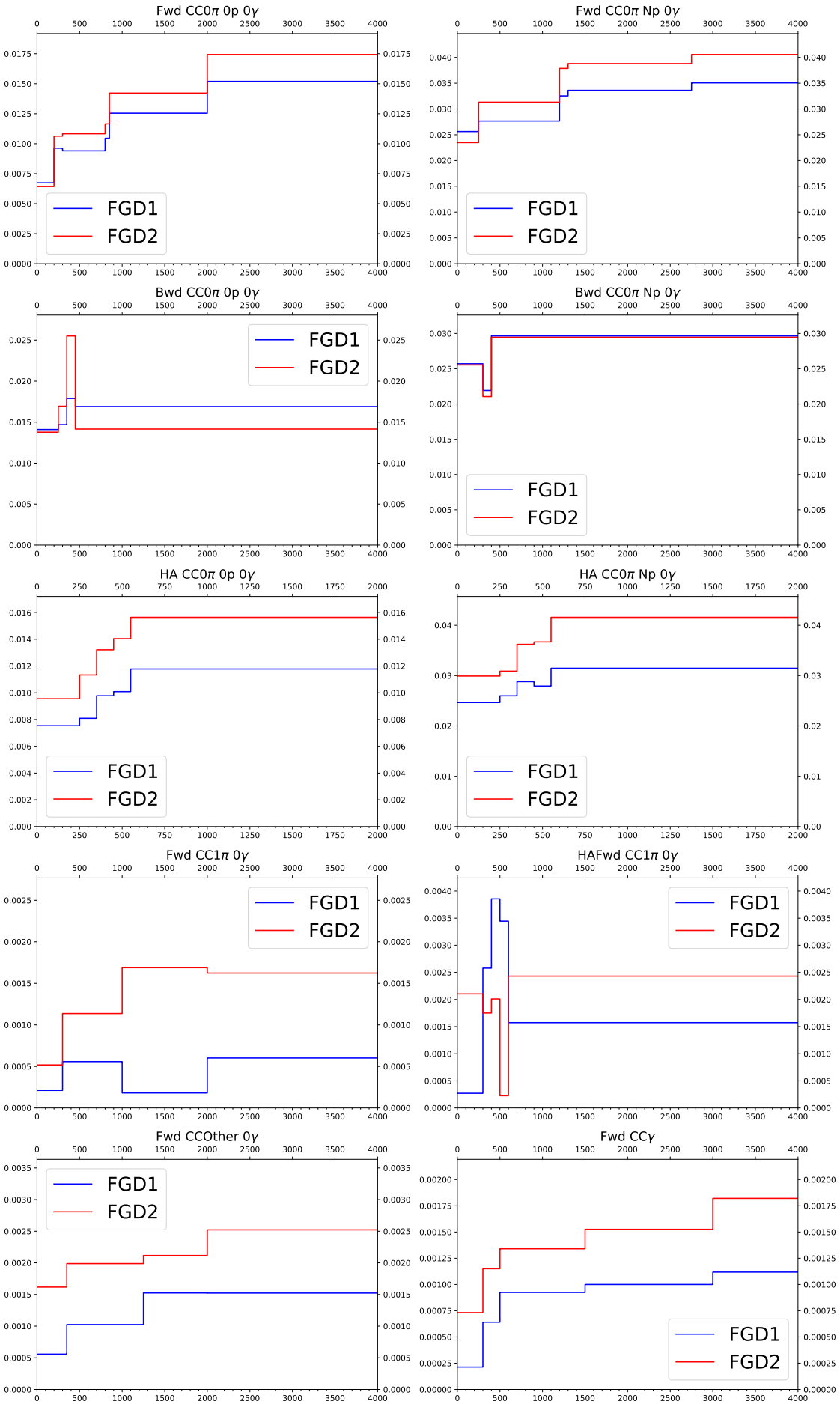

FIGURE C.36: The relative error caused by proton SI, evaluated using highland2 propagation and parameters described before, as a function of muon $\cos\theta$ in different samples. The blue solid line stands for FGD1, and red line for FGD2.

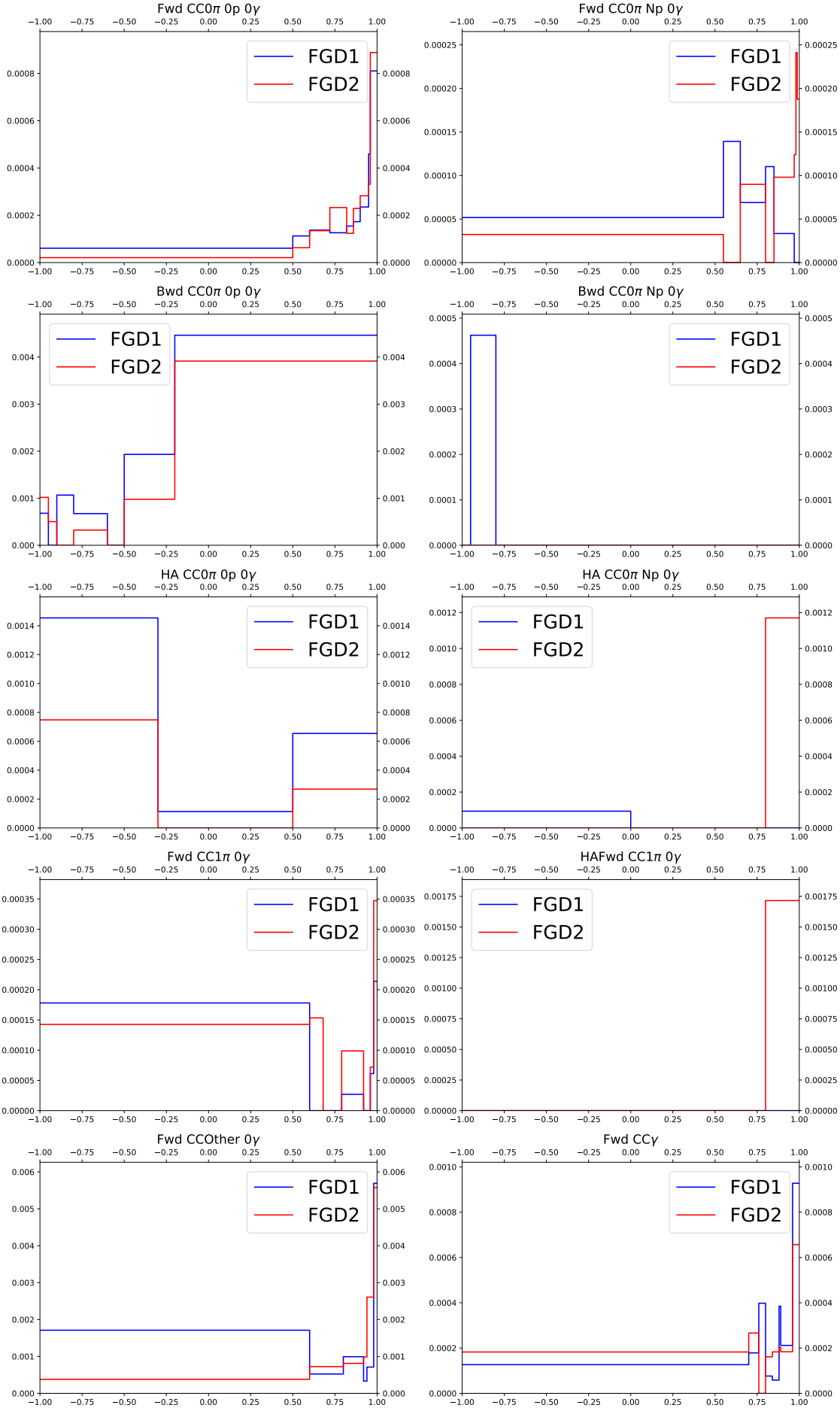

FIGURE C.37: The relative error caused by sand muons, evaluated using highland2 propagation and parameters described before, as a function of muon $\cos\theta$ in different samples. The blue solid line stands for FGD1, and red line for FGD2.

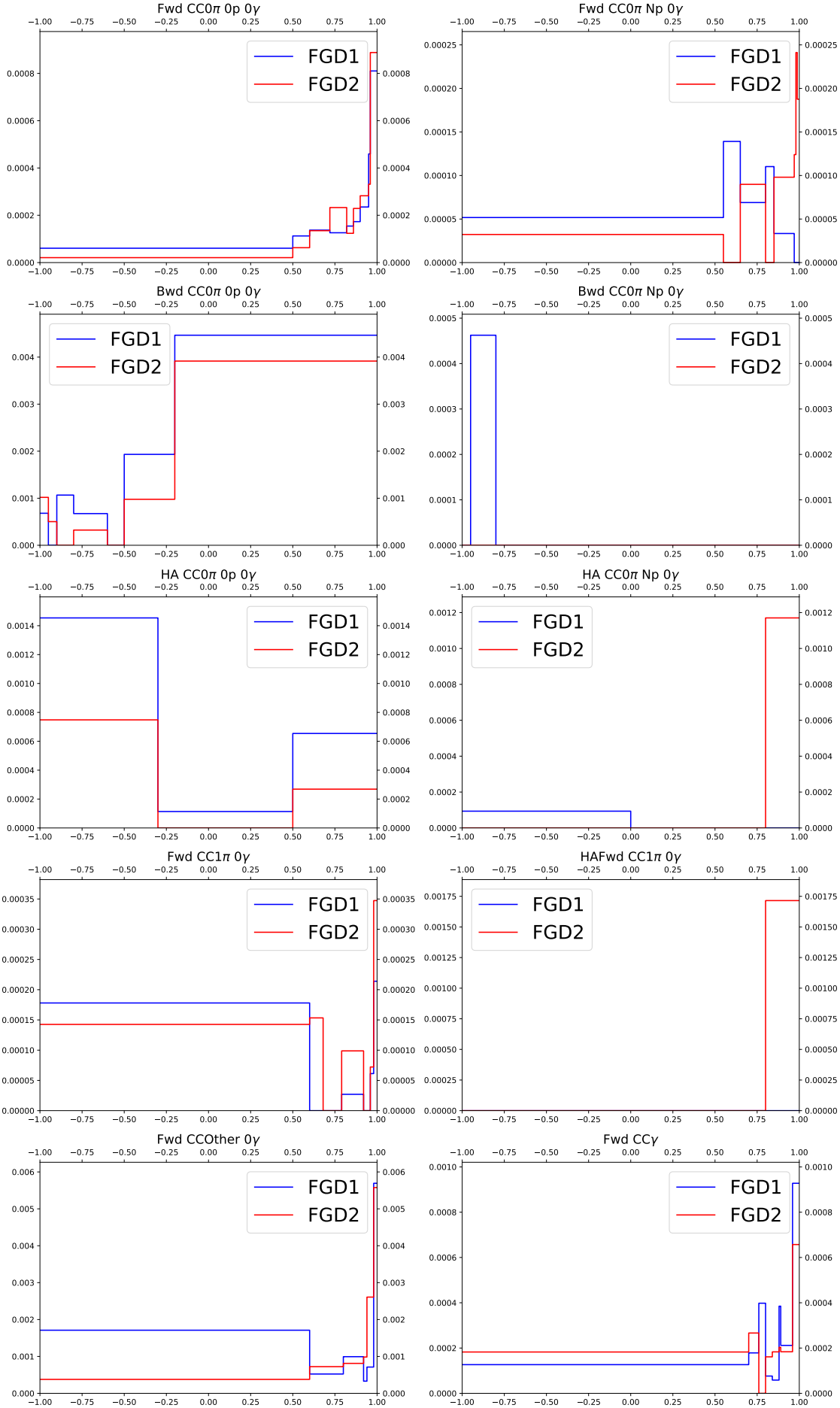

FIGURE C.38: The relative error caused by sand muons, evaluated using highland2 propagation and parameters described before, as a function of muon $\cos\theta$ in different samples. The blue solid line stands for FGD1, and red line for FGD2.

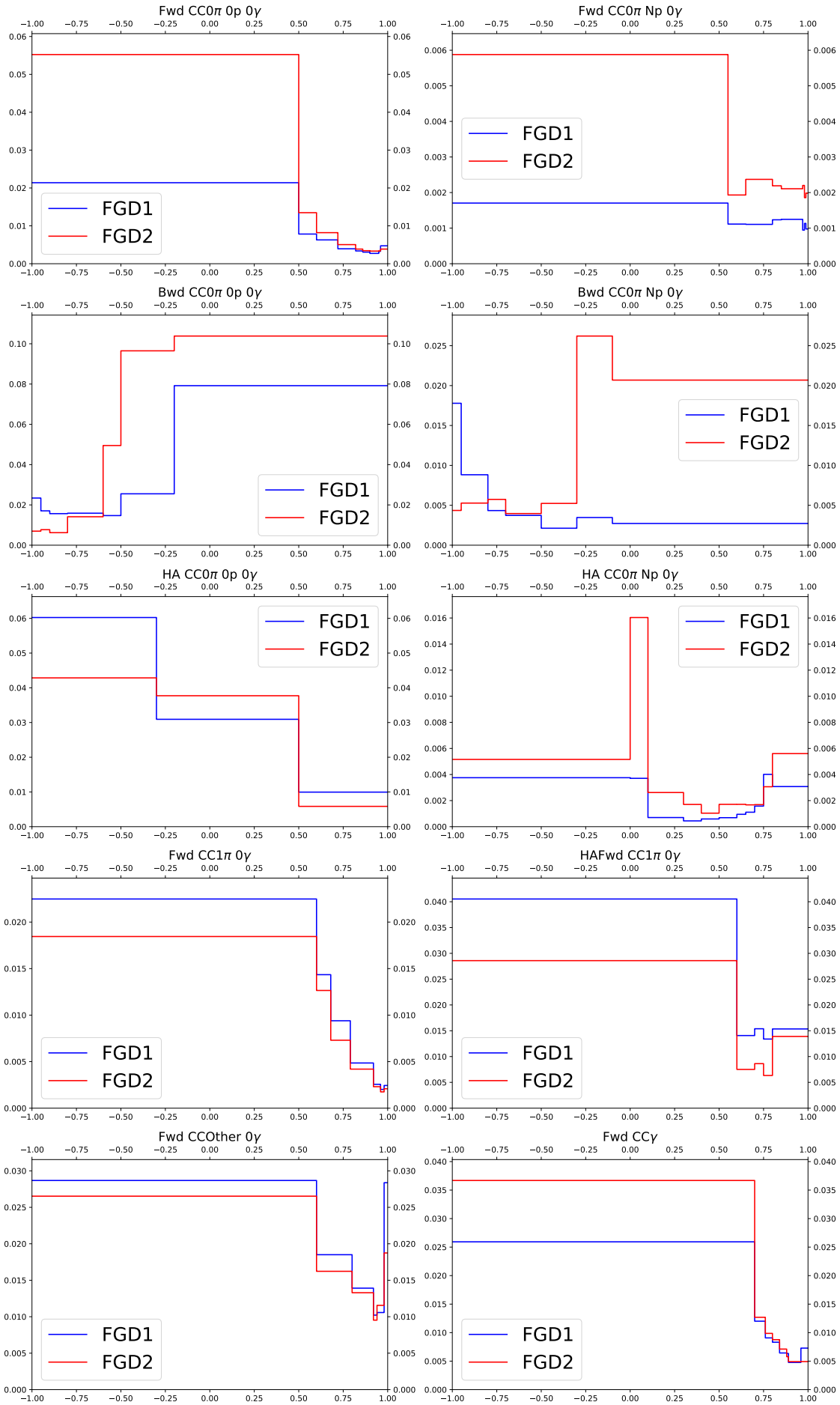

FIGURE C.39: The relative error caused by OOFV events, evaluated using highland2 propagation and parameters described before, as a function of muon $\cos\theta$ in different samples. The blue solid line stands for FGD1, and red line for FGD2.

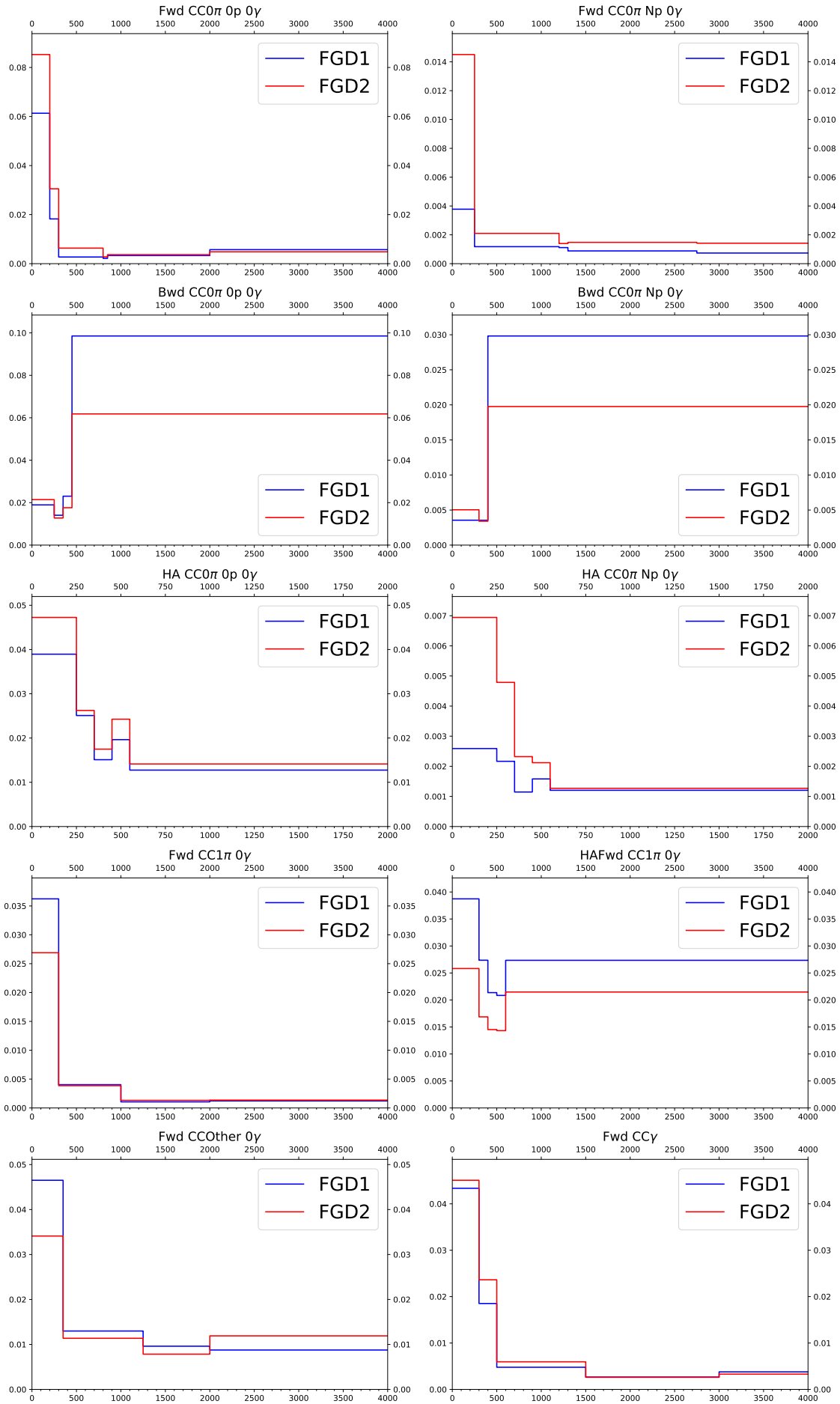

FIGURE C.40: The relative error caused by OOFV events, evaluated using highland2 propagation and parameters described before, as a function of muon $\cos\theta$ in different samples. The blue solid line stands for FGD1, and red line for FGD2.

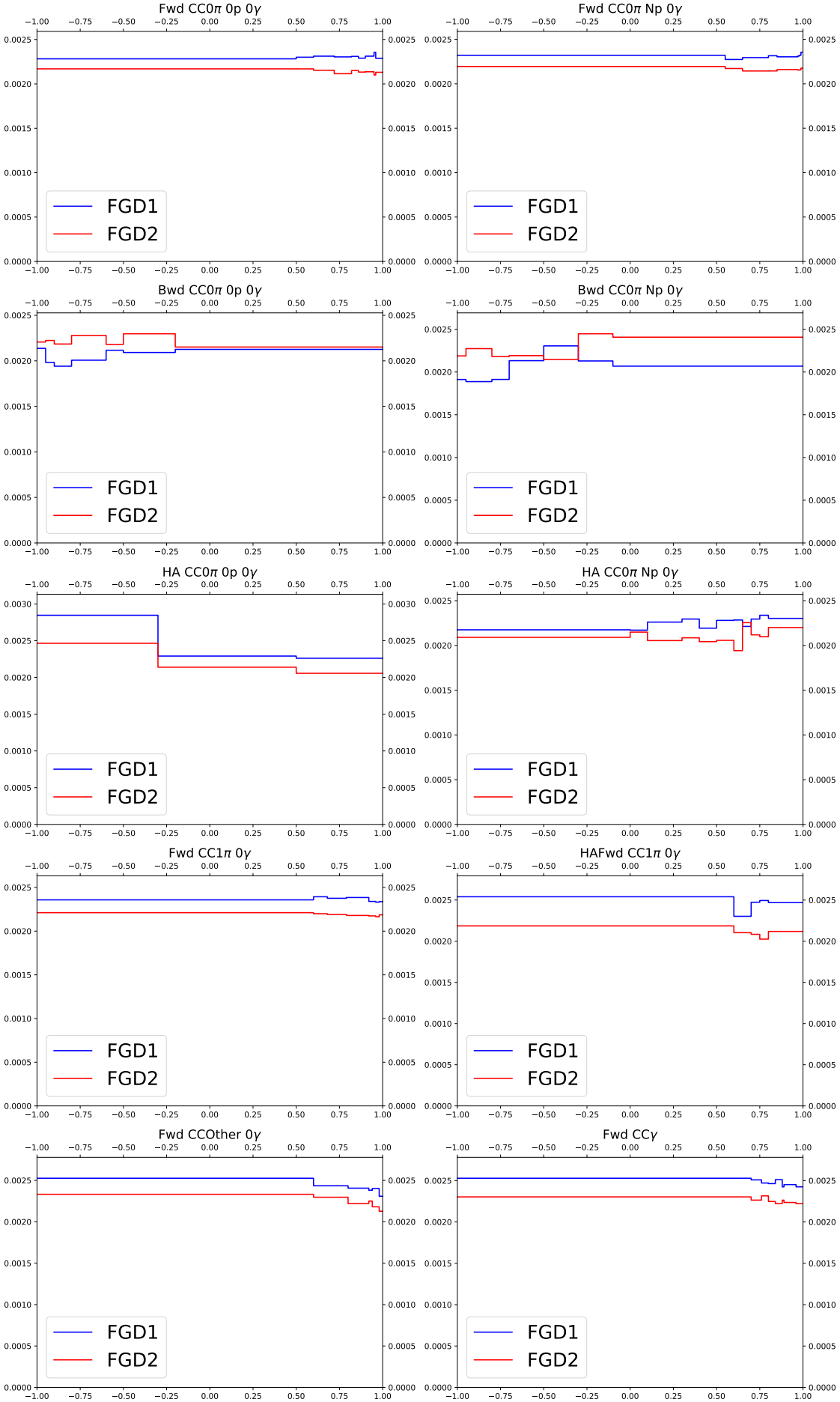

FIGURE C.41: The relative error caused by event pile-up, evaluated using highland2 propagation and parameters described before, as a function of muon $\cos\theta$ in different samples. The blue solid line stands for FGD1, and red line for FGD2.

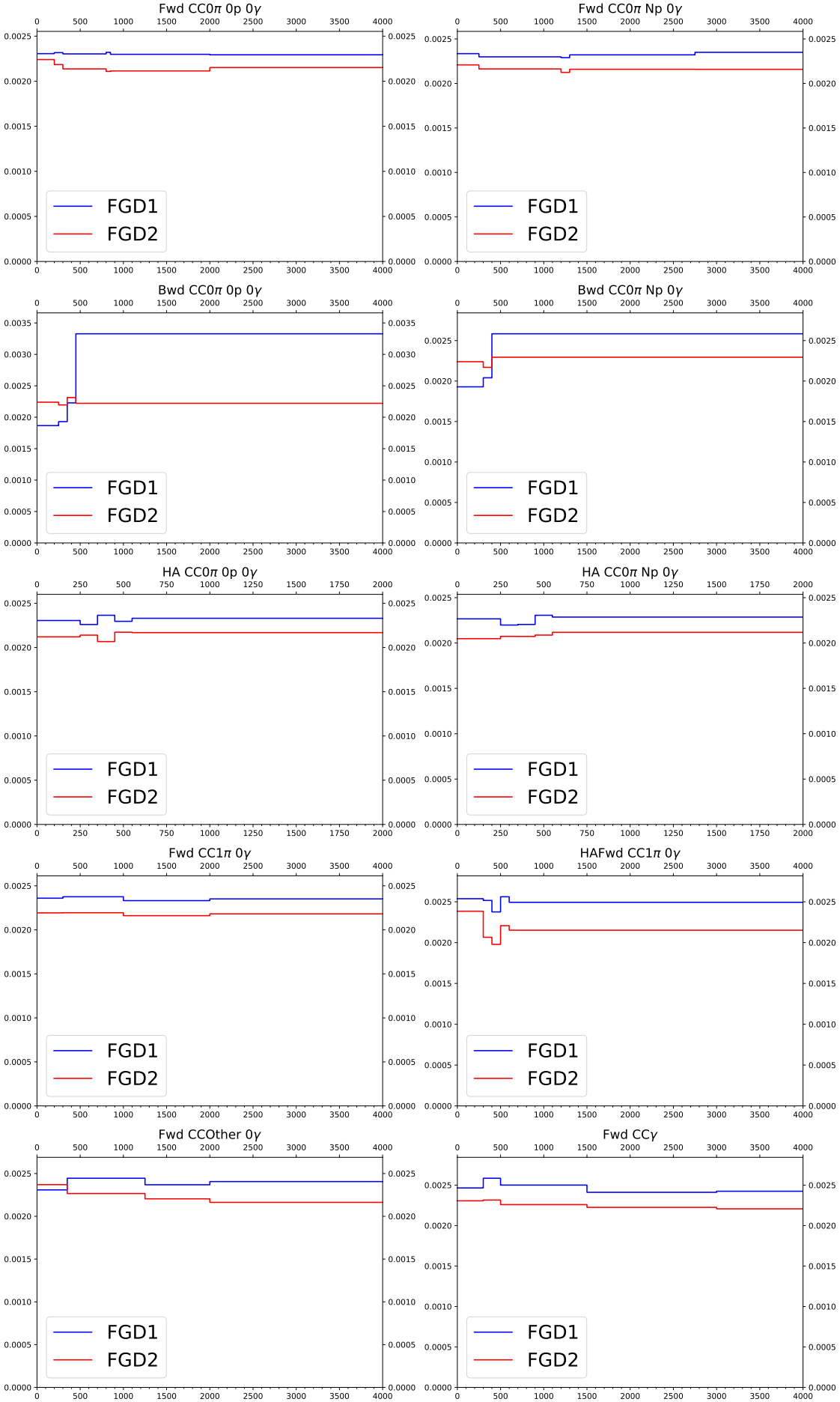

FIGURE C.42: The relative error caused by event pile-up, evaluated using highland2 propagation and parameters described before, as a function of muon $\cos\theta$ in different samples. The blue solid line stands for FGD1, and red line for FGD2.